Alma Mater Studiorum · Università di Bologna

Scuola di Scienze
Dipartimento di Fisica e Astronomia
Dottorato di ricerca in Astrofisica
Thesis in cotutela con l'UNIVERSIDAD NACIONAL DE COLOMBIA

Constraints on alternative cosmological models from clustering and redshift-space distortions

CANDIDATO:
Jorge Enrique García Farieta

RELATORE:
Prof. Lauro Moscardini

CO-RELATORE:
Prof. Rigoberto Casas Miranda

Coordinatore Dottorato:
Chair.mo Prof.
Francesco Rosario Ferraro

Esame finale anno 2019

Settore Concorsuale: 02/C1 - Astronomia, Astrofisica, Fisica della Terra e dei Pianeti Settore Scientifico Disciplinare: FIS/05 - Astronomia e Astrofisica

"*yo no dejo una religión por otra, un partido por otro, un sacrificio por otro. Yo soy un espíritu liberado, egoísta. Yo obro como yo siento.*"

Biófilo Panclasta.

"*It is in this gesture of 'going beyond', to be something in oneself rather than the pawn of a consensus, the refusal to stay within a rigid circle that others have drawn around one-it is in this solitary act that one finds true creativity. All others things follow as a matter of course.*"

Alexander Grothendieck.

«Если они знают мои работы, им не нужно мое CV. Если они нуждаются в моем CV, они не знают мои работы.»

Григорий Яковлевич Перельман.

«*Nessun ricercatore può essere misoneista, ma molti cultori di scienza possono, quasi direi debbono essere conservatori per la stessa loro missione di custodire con gelosa cura un certo patrimonio intellettuale ben consolidato, e di vagliare con severo spirito critico tutto ciò che importa variazione o alienazione del patrimonio stesso.*»

Tullio Levi Civita.

UNIVERSIDAD NACIONAL DE COLOMBIA

Abstract

Facultad de Ciencias
Departamento de Física

Doctor en Ciencias Física

Constraints on alternative cosmological models from clustering and redshift-space distortions

by Jorge Enrique García Farieta

In this Thesis I have exploited the most recent observational data from CMB, BAO and growth rate of LSS as well as N-body simulations of modified gravity, to investigate the spatial properties of the large scale structure of Universe by constraining cosmological parameters in the framework of alternative cosmologies. The research is focused on clustering and redshift space distortions as cosmological probe. In this context I have studied the degeneracies between modified gravity and massive neutrinos as well as the robustness of the methodology for constraining the linear growth rate including realistic systematics, implementing suitable parametrizations of the redshift-space distortions in the perspective of current and future galaxy surveys.

Spanish
En esta tesis se han utilizado los datos observacionales más recientes de CMB, BAO y tasa de crecimiento de LSS al igual que simulaciones tipo N-body de gravedad modificada, con el fin de investigar las propiedades espaciales de la estructura a gran escala del Universo a través de la restricción de parámetros cosmológicos en el marco de cosmologías alternativas. La investigación se centra en el clustering y las distorsiones del espacio de redshift como prueba cosmológica. En este contexto se ha estudiado la degenerancia de modelos de gravedad modificada y neutrinos masivos como también su robustez incluyendo errores sistemáticos realistas, e implementando parametrizaciones adecuadas de las distorsiones del espacio de redshift teniendo en cuenta los mapas de galaxias actuales y futuros.

Italian
In questa tesi sono stati sfruttati i dati osservativi più recenti di CMB, BAO e tasso di crescita di LSS, nonché simulazioni di N- body di gravità modificata per studiare le proprietà spaziali della struttura a grande scala dell'Universo vincolando i parametri cosmologici nel quadro di cosmologie alternative. La ricerca si concentra sul clustering e sulle distorsioni nello spazio dei redshift come test cosmologico, in questo contesto ho studiato le degenerazioni nella gravità modificata e nei neutrini massivi, nonché la loro robustezza, compresa i gli errori sistematici, e anche sono stati implementati parametrizzazioni delle distorsioni nello spazio dei redshift nella prospettiva di galaxy surveys attuali e future.

Contents

List of Figures

List of Tables

To my beloved parents Ana and Jorge,
to my siblings and
to Nastya.

CHAPTER 1

Introduction

The analysis of the large-scale structure of the Universe (LSS) represents one of the most active research fields from a theoretical, observational and computational point of view. The rise of precision cosmology is leaving a deeper understanding of the Universe. In the last two decades, many experiments have been developed to this aim, leading to the concordance model ΛCDM (Lambda cold dark matter) which describes the evolution and the components of the Universe. According to the ΛCDM model, the Universe is composed of $\approx 5\%$ of ordinary matter and radiation, while $\approx 25\%$ is filled by Dark Matter (DM) and the remaining ($\approx 70\%$) is associated with the so-called Dark Energy (DE), both components are physically unknown. This fact, together with a viable explanation of the accelerated expansion rate of the Universe represents a big issue for modern cosmology, and unveiling the nature of the dark sector of the Universe is one of the most ambitious challenges of fundamental physics in the recent years.

The open issues in the standard ΛCDM model have also motivated several theoretical efforts to find a satisfactory explanation of the dark sector, consequently different DE and DM models have been proposed in the literature, from simple scenarios with a constant equation of state $w(z)$ to models considering interactions between DM and DE or models based on modifications/extensions of general relativity. In this sense, a growing amount of observational evidence has been used to constrain cosmological parameters, in particular one of the most effective ways to test cosmological models on large scales, that is where the DM and DE arise, is to use the redshift-space distortions (RSD) (Sargent and Turner, 1977; Kaiser, 1987). Since RSD are directly related to the growth rate of cosmic structures, they have a leading role in both present and planned cosmological investigations (see e.g. Samushia, Percival, and Raccanelli, 2012; de la Torre et al., 2013; Beutler et al., 2014; Ross et al., 2007, and references therein). These measurements, together with other probes, are used to set constraints on several alternative cosmological models. Moreover, it is important to investigate how the

RSD affect the statistical properties related to the matter correlation function and power spectrum, which is essential to compare theoretical predictions to observations.

In this Thesis, we study the clustering properties of the spatial distribution of dark matter haloes in the framework of alternative cosmologies. The analysis is carried out to investigate *a)* the spatial properties of the LSS by improving the measurements of anisotropic clustering, focusing in particular on the multipole moments and clustering wedges of the two-point correlation function (2PCF) and *b)* parametrizing the RSD beyond the dispersion model (Reid and White, 2011), by implementing results based on LSS perturbation theory like Scoccimarro (2004) model and Taruya, Nishimichi, and Saito (2010) model to derive cosmological constraints.

The Thesis is organised as follows. In Chapter §2 a general overview on clustering is presented. First, we introduce briefly the current framework of the standard cosmological model giving a brief summary of general relativity, the definition of the background Universe, perturbation theory and structure formation. Then, in Chapter §3 the main topic of this Thesis, the redshift-space distortions (RSD), is introduced, providing details on the statistical description of random fields and the methods used to measure the clustering signal from discrete samples. The theoretical models used to parametrize RSD are also presented in this Chapter as well as its assumptions to derive cosmological constraints from them; a short introduction to some statistical measures of clustering is also given. In Chapter §4 a joint analysis from observational data, including growth rate, CMB, BAO measurements, is performed to set constraints on dynamical Dark Energy models. In Chapter §5 we investigate the clustering properties in modified gravity models with massive neutrinos using N-body simulations. The growth rate and bias parameters are constrained on intermediate scales making use of the Bayesian analysis that includes the clustering description in terms of its multipole moments. The implementation of models and the results obtained from a parametrization of RSD based on extensions of the linear perturbation theory are discussed in Chapter §6. In this Chapter the spatial distribution of the large-scale structure is studied in the standard scenario using high-resolution N-body simulations, and making use of both, the multipole description and clustering wedges of the 2PCF. Additionally, in this Chapter, the effect of dynamic distortions in galaxy redshift surveys is also studied. Finally, the main findings of this Thesis are summarized and discussed in Chapter §7.

CHAPTER 2

Landscape of modern cosmology

Until the first half of the 20th century, there was not enough physical evidence to make reasonable models about the origin and evolution of the Universe. Nowadays cosmology addresses these issues exploiting well understood physical phenomena and tested theories in a large range of scales and energies. The technology improvements on data acquisition, management, processing, and calibration, that have provided an increasing amount of observational/experimental data, together with the description of more refined theoretical models have led to establish a consensus about the best description of our Universe, commonly called standard cosmological model. The current standard cosmological model ΛCDM allows us to interpret with a high degree of precision many of the cosmological observations. In this context, the model was historically developed around three pillars of observational evidence (Kanipe, 1995; Dodelson, 2003): **1)** *the expansion of the Universe* (see e.g. galaxy surveys results Hubble, 1926; Hubble, 1934; Perlmutter et al., 1999; Riess et al., 1998; Cole et al., 2005; Guzzo et al., 2014; Alam et al., 2017), **2)** *the cosmic microwave background (CMB)* (Dicke et al., 1965; Penzias and Wilson, 1965; Hinshaw et al., 2013; Smoot, 1999; Smoot et al., 1992; Planck Collaboration et al., 2018a, see e.g.) and **3)** *the abundance of light-elements* (Alpher, Bethe, and Gamow, 1948; Copi, Schramm, and Turner, 1995; Walker et al., 1991; Cooke et al., 2014; Planck Collaboration et al., 2018b); in addition to two theoretical assumptions: *the cosmological principle* (Einstein, 1917; Bondi, 1948; Lemaître, 1927) and *General Relativity (GR) as the theory describing gravitational interactions on cosmological scales* (Einstein, 1917; Robertson, 1935; Friedmann, 1922).

The observational data collected during the last decade provided strong support to the concordance ΛCDM model, which, with only 6 free parameters, yields a consistent description of the main properties of the LSS (see e.g. Tonry et al., 2003; Bel et al., 2014; Hamana et al., 2015; Planck Collaboration et al., 2016a; Planck Collaboration et al., 2016b; Alam et al., 2017; Alsing, Heavens,

and Jaffe, 2017; Abbott et al., 2018; Planck Collaboration et al., 2018b; Pacaud et al., 2018; Joudaki et al., 2018; Di Valentino et al., 2018; Jones et al., 2018). In this framework, the Universe is currently dominated by DE, in the form of a cosmological constant, responsible for the late-time cosmic acceleration (Riess et al., 1998; Schmidt et al., 1998; Perlmutter et al., 1999), and by a Cold Dark Matter (CDM) component that drives the formation and evolution of cosmic structures. However, despite its great successes, some fundamental open issues have motivated efforts aimed at searching for possible expansions or alternative models beyond ΛCDM (Amendola et al., 2013; Frieman, Turner, and Huterer, 2008; Albrecht et al., 2006). In this way the main aspects that should be understood in the cosmological arena are related to the nature of the dark sector, DM (Zwicky, 1937) and DE (Perlmutter et al., 1999; Riess et al., 1998), cosmological tests of GR at large scales (Hut, 1977), fine-tuning of cosmological parameters (Weinberg, 2001; Quartin et al., 2008) and cosmic structures above the limit of homogeneity (Clowes et al., 2013).

2.1. The framework of General Relativity

According to GR, the gravitational attraction between masses is due to a curvature of spacetime and therefore to its geometry rather than instantaneous action-at-a-distance, in contrast to Newtonian gravity. After more than 100 years of being formulated by A. Einstein, GR has passed different tests, from the very well known perihelion precession of Mercury, the deflection of light by the Sun, and the gravitational redshift of light, until the most stringent tests today at laboratory scales including atom interferometry (Dimopoulos et al., 2007), low orbit scales precession in the Earth's perigee (Iorio, 2003), weak-field gravity at solar system distances with pulsar timing (Kramer et al., 2006), and, perhaps one of the most exciting during the last years, the first detection of gravitational waves observed, produced by the merger of binary compact object (Abbott et al., 2016).

The fundamental principles introduced in GR are the Einstein's equivalence principle which describes acceleration and gravity as distinct aspects of the same reality, the notion of curvature of spacetime and the principle of general covariance. GR can be expressed nowadays as a theory of a dynamical tensor field, in which the lengths of space-time intervals are defined in terms of the metric $g_{\mu\nu}$ on a manifold $\mathcal{M}$ as follows $ds^2 = g_{\mu\nu}dx^\mu dx^\nu$ being a covariant quantity under diffeomorphisms [1]. Consequently a gravitational phenomenon is described by the metric in a universal way and its dynamic does not depend on the chosen coordinates. Given a metric for any gravitational phenomenon, the Einstein field equations (EFE's) can be obtained by varying the so-called Einstein-Hilbert action with respect to the metric as

$$S = \int \left[\frac{c^4}{16\pi G}(R - 2\Lambda) + \mathcal{L}_m \right] \sqrt{-g} d^4x, \tag{2.1}$$

[1] The small Greek indices run from 0 to 3 and denote space-time dimensions, while small Latin indices run from 1 to 3.

being R the Ricci scalar, g the determinant of the metric, Λ the cosmological constant, c the speed of light in vacuum, G the Newton's gravitational constant and $\mathcal{L}_m$ corresponds to the matter-energy Lagrangian. By applying the principle of least action, the corresponding equation of motion are given by the EFE's written as

$$R_{\mu\nu} - \frac{1}{2}Rg_{\mu\nu} + \Lambda g_{\mu\nu} = \frac{8\pi G}{c^4}T_{\mu\nu} \qquad \text{with signature } (-,+,+,+). \tag{2.2}$$

Here $R_{\mu\nu}$ is the Ricci tensor and $T_{\mu\nu}$ the energy-momentum tensor (sometimes called stress-energy tensor), and commonly the Einstein tensor is defined as $G_{\mu\nu} \equiv R_{\mu\nu} - \frac{1}{2}g_{\mu\nu}R$. The Ricci tensor, obtained from the contraction of the Riemann tensor, is defined by

$$R_{\mu\nu} \equiv \Gamma^{\alpha}_{\mu\nu,\alpha} - \Gamma^{\alpha}_{\mu\alpha,\nu} + \Gamma^{\alpha}_{\mu\nu}\Gamma^{\beta}_{\alpha\beta} - \Gamma^{\alpha}_{\mu\beta}\Gamma^{\beta}_{\alpha\nu}, \tag{2.3}$$

being $\Gamma^{\mu}_{\nu\lambda} = \frac{1}{2}g^{\mu\alpha}\left(g_{\alpha\nu,\lambda} + g_{\alpha\lambda,\nu} - g_{\nu\lambda,\alpha}\right)$ the Christoffel symbols (also known as affine connections), where the derivative of the metric $g_{\alpha\nu}$ with respect to x^{λ} is represented by $g_{\alpha\nu,\lambda} \equiv \partial g_{\alpha\nu}/\partial x^{\lambda}$. The Ricci scalar (also called scalar curvature) is the simplest curvature invariant obtained from the full contraction of the Ricci tensor $R = g^{\mu\nu}R_{\mu\nu}$.

Equation (2.2) condenses essentially 16 coupled nonlinear partial differential equations that characterize completely the gravitational effects produced by a given mass, however, since the Einstein tensor is linear in the second partial derivatives of the metric, can be written as a symmetric order-2 tensor with 10 independent components in a 4-dimensional space. On the other hand, the energy-momentum tensor is equivalent to

$$T_{\mu\nu} = -2\frac{\partial \mathcal{L}_m}{\partial g^{\mu\nu}} + g_{\mu\nu}\mathcal{L}_m, \tag{2.4}$$

it contains all the information about the energy density, momentum and electromagnetic fields in the spacetime, and it can be interpreted as the source of the gravitational field in the EFE's. Moreover, the Bianchi identities, which state that the covariant divergence of the Einstein tensor is identically zero, automatically ensure the covariant conservation of the energy-momentum tensor in curved spacetimes:

$$\nabla_{\mu}T^{\mu\nu} = 0. \tag{2.5}$$

A particular form of this tensor is given by considering the approximation of perfect fluid, i.e., constant density and zero viscosity, to describe all the matter-energy components that constitute the fluid. In this case, the energy-momentum is given by

$$T_{\mu\nu} = \left(\rho + \frac{p}{c^2}\right)u_{\mu}u_{\nu} + pg_{\mu\nu}, \tag{2.6}$$

with p being the pressure of the fluid, ρ its density, both are functions of time,

and $u_\mu = (-1, 0, 0, 0)$ is the four-velocity of the fluid in comoving coordinates [2].

The equations (2.2) and (2.4) provide a precise formulation on the geometry of space-time, and therefore the dynamics of the metric, with properties of the matter itself. In this context, there are no better words to interpret the EFE's than the famous quote by Misner, Thorne, and Wheeler (Misner, Thorne, and Wheeler, 1973), "*Matter tells space-time how to curve and geometry tells matter how to move*".

2.2. The background Universe

The standard cosmological model assumes as valid the *cosmological principle*, which states that the mass distribution in the Universe is statistically homogeneous and isotropic on scales large enough, beyond hundreds of Mpc. This postulate allows to write the line element in an universe maximally symmetric by using Friedmann-Lemaître-Robertson-Walker (FLRW) metric

$$ds^2 = g_{\mu\nu} dx^\mu dx^\nu = -c^2 dt^2 + dl^2, \tag{2.7}$$

where $g_{\mu\nu}$ is a diagonal metric tensor, and the proper time t has been defined such that dl is identical in every space and time interval. The spatial metric dl can be expressed as product of a time-dependent term, the so-called scale factor $a(t)$, by one time-independent metric of the 3-dimensional space $d\sigma$, i.e., $dl^2 = a^2(t)\gamma_{ij} dx^i dx^j$. By assuming spherical polar coordinates

$$d\sigma^2 = \gamma_{ij} dx^i dx^j = \frac{dr^2}{1 - kr^2} + r^2 \left(d\theta^2 + \sin^2 \theta d\phi^2 \right), \tag{2.8}$$

where the spatial positions are denoted by the dimensionless coordinates (r, θ, ϕ), and $\gamma_{11} = (1 - kr^2)^{-1}$, $\gamma_{22} = r^2$, and $\gamma_{33} = r^2 \sin^2 \theta$. The coordinates are comoving with the expansion of the universe through the scale factor, this quantity is dimensionless and it is defined to be equal to 1 at the present epoch $[a(t_0) = 1]$. The value of the parameter k defines the geometry of the universe under consideration to be flat ($k = 0$), open ($k < 0$) or closed ($k > 0$) as sketched in the Fig. 2.1a. By using natural units $c = 1$, the FLRW metric is often expressed, without loss of generality, as

$$ds^2 = -dt^2 + a^2(t) \left[\frac{dr^2}{1 - kr^2} + r^2 d\theta^2 + r^2 \sin^2 \theta d\phi^2 \right]. \tag{2.9}$$

The equations of motion that describe the time evolution of $a(t)$ and the dynamic growth of the Universe are called *Friedmann equations*. This set of equations can be obtained from the EFE's, without any assumption on the geometry of the Universe, by evaluating the Einstein tensor in a FLRW spacetime

[2] The comoving coordinates correspond to fix values in a reference frame where an observer moves with the space expansion and perceives the Universe to be isotropic. The comoving distance between two bodies remains constant at all times i.e., fixed as the Universe expands.

and considering the energy-momentum tensor of the background matter as a perfect fluid. Tab. 2.1 shows the results of non-null elements of the Christoffel symbols, Ricci tensor, Ricci scalar and Einstein tensor in the FLRW metric described in Eq. (2.9). By evaluating the EFE's, assuming further that the matter and radiation content in the universe can be described as an ideal fluid with energy-momentum tensor $T^{\mu}_{\nu} = \mathrm{diag}(-\rho, p, p, p)$, we get a system of two ordinary differential equations, that describe the evolution of the scale factor $a(t)$ and correspond to the Friedmann equations for the (00) and (ii) components of the metric:

$$\left(\frac{\dot{a}}{a}\right)^2 = \frac{8\pi G}{3}\rho - \frac{k}{a^2} + \frac{\Lambda}{3}, \tag{2.10a}$$

$$2\frac{\ddot{a}}{a} + \left(\frac{\dot{a}}{a}\right)^2 = -8\pi G p - \frac{k}{a^2} + \Lambda, \tag{2.10b}$$

then, by eliminating the curvature term, they can be re-expressed as

$$\dot{\rho} = -3\frac{\dot{a}}{a}\left(\rho + p\right), \tag{2.11a}$$

$$\frac{\ddot{a}}{a} = -\frac{4\pi G}{3}\left(\rho + 3p\right) + \frac{\Lambda}{3}. \tag{2.11b}$$

The fact that Eq. (2.11a) corresponds to the continuity equation is not surprising since the energy-momentum tensor is covariant conserved. Moreover, this result is also equivalent to the first law of thermodynamics under adiabatic conditions, that can be understood as a continuity equation of energy. These equations lead to the definition of the Hubble parameter as $H \equiv \frac{\dot{a}}{a}$, which drives the expansion rate of the Universe, and usually is represented in terms of the dimensionless factor h, defined by the expression $H_0 = 100\ h\ km\ s^{-1}\ Mpc^{-1}$ at the present epoch. In order to have a full description of the background universe, it is necessary an equation of state (EoS) of the cosmic fluid, considering that the cosmic fluid has three principal components: baryonic matter, dark matter, and radiation (see Fig. 2.1b). In this sense, a first approximation consists in assuming a linear relationship between ρ and p, thus, the equation of state can be written as follows:

$$p = w\rho, \tag{2.12}$$

where w is a parameter that in principle can be time-dependent $w = w(t)$, but the simplest approach is to consider it as a constant. Under this assumption, Eq. (2.11a) is easy to solve, resulting $\rho(a) = a^{-3(1+w)}$.

The history of the Universe is commonly divided into two main epochs. The first epoch corresponds to the early universe, when radiation and relativistic particles were the dominant component of the energy density and the constant of proportionality in the EoS is $w = 1/3$, leading to $\rho \propto a^{-4}$. Then, as the universe expanded and cooled down, the energy density of the radiation decayed faster than the energy density of the non-relativistic matter. Thus, after a certain moment in the history of the Universe, the energy density of non-relativistic matter started to dominate the cosmic energy density and so the pressure of the fluid can now be neglected, which means $w = 0$, leading to the second epoch

$\Gamma^0_{ij} = a^2 H \gamma_{ij}$,	$\Gamma^i_{0j} = \Gamma^i_{j0} = H\delta^i_j$
$\Gamma^1_{11} = \frac{kr}{1-kr^2}$,	$\Gamma^1_{22} = -r\left(1-kr^2\right)$
$\Gamma^1_{33} = -r\left(1-kr^2\right)\sin^2\theta$,	$\Gamma^2_{33} = -\sin\theta\cos\theta$
$\Gamma^2_{12} = \Gamma^2_{21} = \Gamma^3_{13} = \Gamma^3_{25} = \frac{1}{r}$,	$\Gamma^3_{23} = \Gamma^3_{32} = \cot\theta$
$R_{00} = -3\left(H^2 + \dot{H}\right)$	
$R_{0i} = R_{i0} = 0$	
$R_{ij} = a^2\left(3H^2 + \dot{H} + 2k/a^2\right)\gamma_{ij}$	
$R = 6\left(2H^2 + \dot{H} + k/a^2\right)$	
$G^0_0 = -3\left(H^2 + k/a^2\right)$	
$G^0_i = G^i_0 = 0$	
$G^i_j = -\left(3H^2 + 2\dot{H} + k/a^2\right)\delta^i_j$	

Table 2.1: Summary of the results of non-null elements for the Christoffel symbols, Ricci tensor, Ricci scalar and Einstein tensor in a FLRW spacetime described by Eq. (2.9).

where $\rho \propto a^{-3}$. Since a universe in accelerated expansion is described by $\ddot{a} > 0$, thus from Eq. (2.11) and from the state equation Eq. (2.12) we have $w < -1/3$. The case with $w = -1$ corresponds to the so-called cosmological constant, it is obtained assuming a constant density energy so that the corresponding EoS is $p = -\rho$. It means a negative pressure related to dark energy (DE). The cosmological constant can be also associated with a vacuum energy density as following:

$$\rho_\Lambda = \frac{\Lambda}{8\pi G}. \tag{2.13}$$

On the other hand, the case of a flat universe ($k = 0$) is interesting because it is in agreement with many observational results (Planck Collaboration et al., 2018b), it also implies a special value of the matter density in the universe that allows to introduce naturally a critical density ρ_c in terms of the Hubble parameter as follows:

$$\rho_{cr} \equiv \frac{3H^2}{8\pi G}, \tag{2.14}$$

whose value at present-day can be easily computed in terms of the actual Hubble constant, $H_0 = 67.4 \pm 0.5$ km s^{-1}Mpc^{-1} constrained from Planck mission TT+TE+EE+lowP at 95% confidence level (Planck Collaboration et al., 2018b), to be $\rho_{cr,0} = 8.533 \times 10^{-27}$ kgm^{-3}. The critical density is also useful to define the dimensionless density parameter Ω_i for the various species i. We define the current contributions of radiation, matter, cosmological constant and curvature

in units of the critical density today ($a = 1$), as the following ratios:

$$\Omega_m \equiv \frac{\rho_{m,0}}{\rho_{cr,0}} = \frac{8\pi G\rho_{m,0}}{3H_0^2}, \tag{2.15}$$

$$\Omega_r \equiv \frac{\rho_{r,0}}{\rho_{cr,0}} = \frac{8\pi G\rho_{r,0}}{3H_0^2}, \tag{2.16}$$

$$\Omega_\Lambda \equiv \frac{\rho_{\Lambda,0}}{\rho_{cr,0}} = \frac{\Lambda}{3H_0^2}, \tag{2.17}$$

$$\Omega_k \equiv -\frac{k}{H_0^2}. \tag{2.18}$$

It is easy to verify that the sum of these parameters is equal to unity, as it can be expected from the Friedmann equations, in fact

$$\Omega_m + \Omega_r + \Omega_\Lambda + \Omega_k = 1, \tag{2.19}$$

is known as the *cosmic sum rule* and it is valid for any epoch of the universe. Therefore, a Friedmann universe can be described by the cosmological parameters ($H_0, \Omega_m,\ \Omega_r,\ \Omega_k,\ \Omega_\Lambda$) as defined above, such that the expansion rate as a function of the scale factor is given by

$$H^2(a) = H_0^2 \left[\Omega_r a^{-4} + \Omega_m a^{-3} + \Omega_k a^{-2} + \Omega_\Lambda\right]. \tag{2.20}$$

This equation is usually written as a dimensionless function defined by $E(a) = H(a)/H_0$. The last constraints on cosmological parameters obtained by the Planck satellite show that $w = -1.03 \pm 0.03$, consistent with a cosmological constant and $\Omega_m = 0.3153 \pm 0.0073,\ \Omega_\Lambda = 0.692 \pm 0.012,\ \Omega_k = 0.000 \pm 0.005$, where Ω_m contains the density of baryons (Ω_b) and cold dark matter (Ω_{CDM}). Additionally, in the last few years it became usual to include the energy density of neutrinos Ω_ν, they contributes to the radiation density at early times but behave as matter after the non-relativistic transition at late times (Lesgourgues and Pastor, 2012), so that for a flat universe the total energy density is given by $\rho = \rho_\gamma + \rho_{\rm CDM} + \rho_{\rm b} + \rho_\nu + \rho_\Lambda$. Fig. 2.1b shows the percentages, derived from Planck Collaboration et al. (2018b) data, in which each specie contributes to the total content of the Universe.

Since each component of the cosmic fluid scales in a different way with respect to the scale factor (see Eq. 2.20), the history of the Universe has been dominated by a specific component as previously mentioned. Fig. 2.2 shows the evolution of the density parameter ρ (in units of $\rho_{cr,0}$) and the dimensionless parameter Ω_i as functions of the scale factor a and redshift z defined as $z \equiv 1/a - 1$. The plot displays the periods of domination for the different species and the transition from one to another (radiation era, the matter era and the dark energy era). The transition from the radiation era to the matter era takes place at $a_{eq} \equiv \Omega_r/\Omega_m = 2.98 \times 10^{-4}$, then, since the DE remains constant while matter and radiation density drops as the Universe expands, the transition to the DE era occurs about $a_\Lambda = (\Omega_m/\Omega_\Lambda) = 0.47$, keeping the Universe expanding.

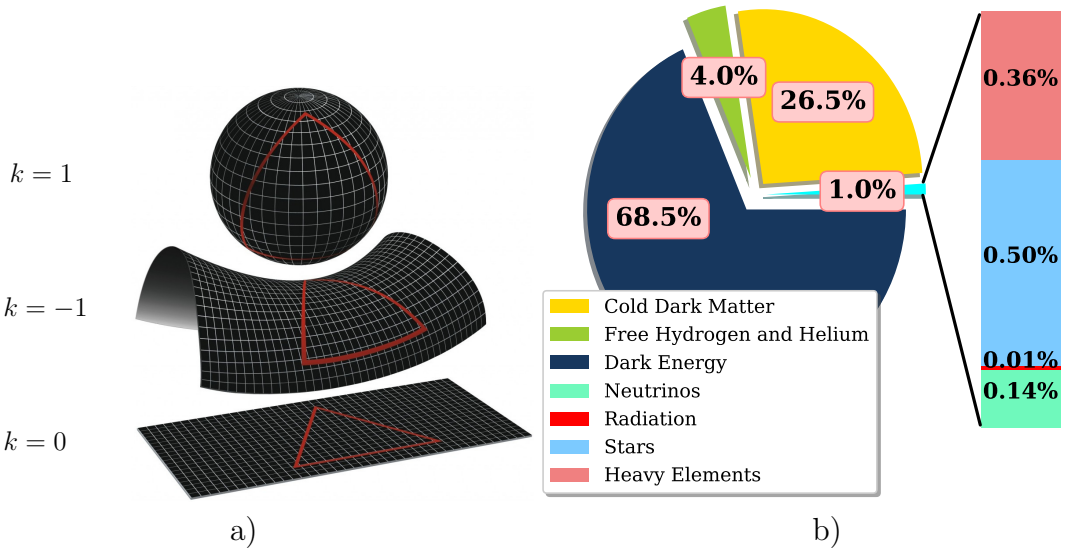

Figure 2.1: *a)* Spatial geometry of the Universe: Flat Universe ($k = 0$), Open Universe ($k = -1$) and Closed universe ($k = 1$), credit: NASA/WMAP Science Team. *b)* The current composition of the Universe derived from Planck data (Planck Collaboration et al., 2018b).

A fundamental aspect of the standard model ΛCDM is the measurement of distances. These depend on the geometry used and also on the content of matter-energy in the universe. As discussed above, the Friedmann equations depend primarily on the form of the field equations, so that the expressions for the distances will ultimately depend on the form of the metric and the field equations used. It is usual to express time through the cosmological redshift. Due to the expansion of the universe, the electromagnetic radiation emitted with a wavelength λ_{em} is observed, by a distant observer, having a wavelength $\lambda_{obs} > \lambda_{em}$. In other words, the electromagnetic signal has been redshifted by $z = (\lambda_{obs} - \lambda_{em})/\lambda_{em}$. This redshift is of particular importance in cosmology because it can be directly measured from the observations of spectra. If one neglects the peculiar motions that the source can have, i.e. its deviations from the Hubble flow, the redshift can be related to the expansion factor as following:

$$z + 1 = \frac{1}{a_{em}}, \tag{2.21}$$

where a_{em} is the scale factor at the emission time normalized to today's size. In an expanding Universe, it is important to obtain information about astrophysical tracers, either by detecting electromagnetic radiation or the recent gravitational waves, which allows to construct maps with the tracer position computed from the cosmological observations. In this sense, the *comoving distance*, $d_c(z)$, corresponds to the distance between observers that are both moving with the Hubble flow, it does not change with time, but it accounts for the expansion of

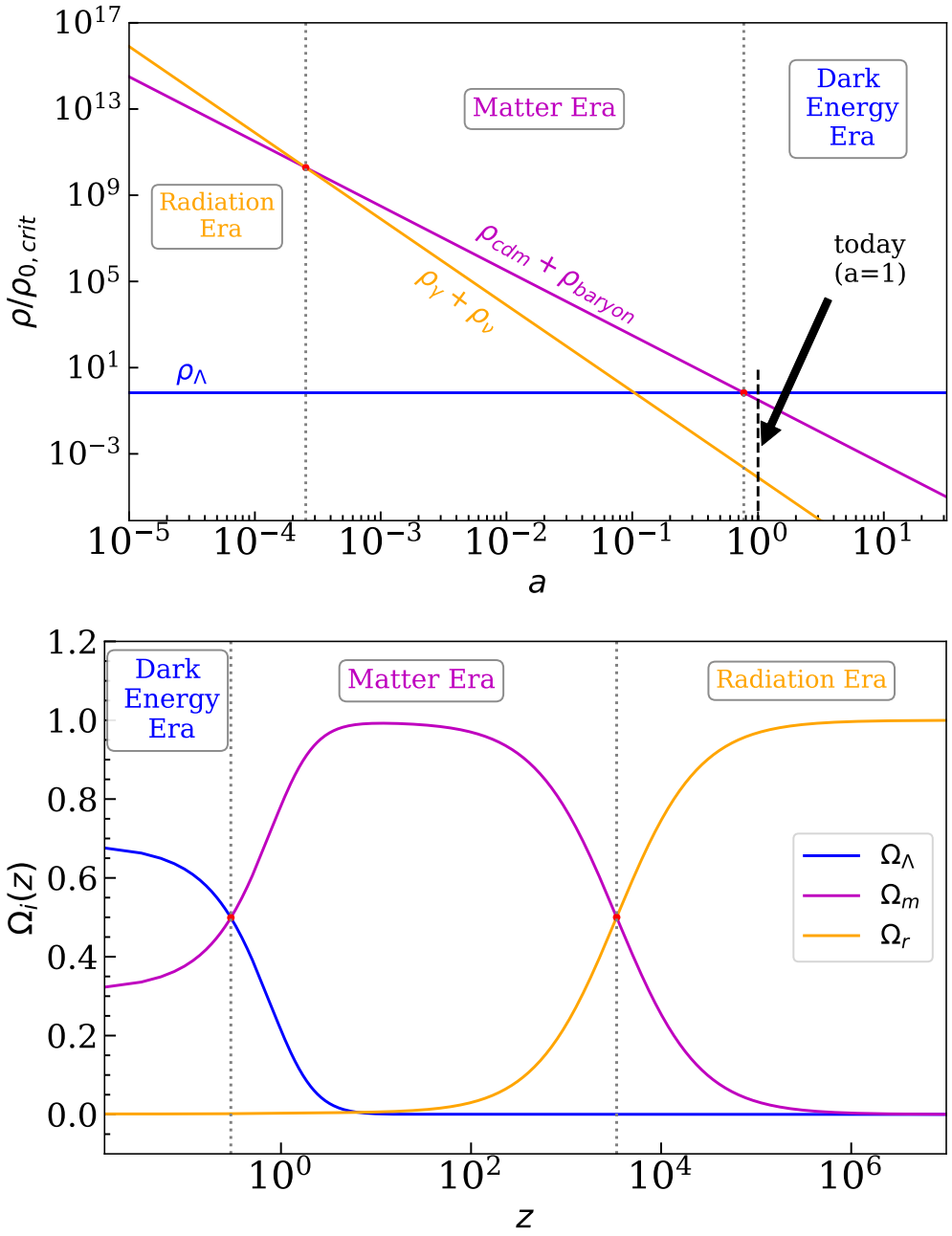

Figure 2.2: *Upper panel*: evolution of the energy density parameter ρ normalized to $\rho_{cr,0}$ as a function of the scale factor a. *Lower panel*: evolution of the dimensionless density parameter Ω_i for each specie (matter, radiation and DE) as a function of the redshift $z = 1/a - 1$. The intersections between lines split the cosmic history in three eras: radiation, matter and Dark Energy era.

the Universe. The comoving distance is defined as follows:

$$d_c(z) = c \int_0^z \frac{dz'}{H(z')}. \tag{2.22}$$

The *transverse comoving distance*, $d_M(z)$, i.e., the comoving distance between two events at the same redshift that is given by:

$$d_M(z) = \begin{cases} \frac{c}{H_0\sqrt{\Omega_k}} \sinh\left[\sqrt{\Omega_k} H_0 d_c/c\right] & \text{for } \Omega_k > 0, \\ d_c & \text{for } \Omega_k = 0, \\ \frac{c}{H_0\sqrt{|\Omega_k|}} \sin\left[\sqrt{|\Omega_k|} H_0 d_c/c\right] & \text{for } \Omega_k < 0. \end{cases} \tag{2.23}$$

The *luminosity distance*, $d_L(z)$, is related to the intrinsic luminosity of a distant object by measuring its flux, in terms of the redshift. It can be expressed as

$$d_L = (1+z) d_M(z). \tag{2.24}$$

The *angular diameter* distance, $d_A(z)$, is defined in terms of the angular size of an object as viewed from an observer, and can be written in terms of the transverse comoving distance as follows:

$$d_A = \frac{d_M}{1+z}. \tag{2.25}$$

Finally, Tab. 2.2 displays a summary of the notation used in this Thesis, as well as a short definition of the some derived quantities, useful for the reader in the following Chapters. For further details concerning the background Universe see Refs. (Peebles, 1993; Dodelson, 2003; Mukhanov, 2005).

2.3. Basics on cosmic structure formation

The observations have shown that the Universe contains a wide range of structures, from small galaxies to clusters of galaxies, superclusters and even to complex larger structures, but also, exist big regions with a very low density of galaxies known as "voids". The galaxy surveys have revealed that the universe becomes statistically homogeneous on very large scales, i.e., at distances larger than 100 Mpc/h, although the Universe appears to be inhomogeneous at small scales. This means that if the cosmic field is smoothed over large enough volumes, the homogeneity is recovered and it is still possible to describe the global dynamics of the universe using the Friedmann equations. In this sense the structures in the Universe can be understood from a cosmological point of view by considering the formation and evolution of galaxies (Coil, 2013). The most accepted description of structure formation is based on a homogeneous background universe perturbed by some mechanism in the early stages, these perturbations drive the formation and evolution of virialised large-scale structures that can be treated in the context of a perturbation theory.

Considering the Newtonian limit, we can assume a non-relativistic, homogeneous, dissipationless fluid without turbulent effects, described by a mass density ρ, pressure $p \ll \rho$, and velocity $\boldsymbol{u}$, in a Friedmann cosmology. The equations of motion of the fluid are then described by the hydrodynamical equations. The

Parameter	Physical meaning and/or definition
h	Dimensionless Hubble parameter
Ω_m	Dimensionless DM density parameter
Ω_Λ	Dimensionless DE density parameter to ΛCDM
Ω_k	Dimensionless curvature density parameter
σ_8	RMS matter fluctuations at 8Mpc/h in linear theory
ω	Constant EoS to ωCDM
$\omega(a) = \omega_0 + (1+a)\omega_1$	EoS of the Chevallier-Polarski-Linder (CPL) parametrization
ω_x, δ	EoS and dimensionless coupling term for Interacting Dark Energy model (*IDE*)
ω_0, Ω_e	EoS and asymptotic DE density term for Early Dark Energy model (*EDE*)
$H_0 = 100h$	Current expansion rate (Hubble parameter) in $Km.s^{-1}Mpc^{-1}$
t_0	Age of the Universe today (in Gyr)
$\Omega_b = 0.045$	Dimensionless baryon density parameter
$\Omega_r = \Omega_\gamma + \Omega_\nu$	Dimensionless radiation density parameter
$\Omega_\gamma = 2.469 \times 10^{-5} h^{-2}$	Dimensionless photon density parameter
Ω_ν	Dimensionless neutrino density parameter
$N_{eff} = 3.04$	Effective number of relativistic neutrino degrees of freedom
$\omega_m = \Omega_m h^2$	Physical DM density
$\omega_b = \Omega_b h^2$	Physical baryon density
$\rho_{cri} = 3H_0^2/8\pi G$	Critical density ($1.88 \times 10^{29} h^2 g/cm^3$)
Ω_X	Dimensionless DE density parameter
$\rho_X = \rho_{cri}\Omega_X$	Physical DE density
$\Lambda = 8\pi G \rho_\Lambda$	Cosmological constant where $\rho_\Lambda = \rho_{cri} 3H_0^2$
c_s	Sound speed
r_s	Comoving size of sound horizon
z_{drag}	Redshift at which baryon-drag optical depth equals unity
$r_{drag} = r_s(z_{drag})$	Comoving size of the sound horizon at z_{drag}
$r_s/D_v(z)$	BAO distance ratio scale
z_{cmb}	Redshift at decoupled photon-baryon
$R(z_{cmb})$	Scaled distance at recombination (z_{cmb})
$l_A(z_{cmb})$	Angular scale of sound horizon at recombination (z_{cmb})

Table 2.2: Notation and short overview of the cosmological parameters used in this Thesis. The upper block contains the main set of parameters usually consider as free in Bayesian analysis. The lower block displays the derived parameters from the upper block.

mass conservation implies the continuity equation

$$\partial_t \rho = -\nabla_{\boldsymbol{r}} \cdot (\rho \boldsymbol{u}), \tag{2.26}$$

where the vector position of a fluid element, at time t, is denoted by $\boldsymbol{r}$. The momentum conservation in a continuous system leads to the Euler equation

$$(\partial_t + \boldsymbol{u} \cdot \boldsymbol{\nabla}_{\boldsymbol{r}})\, \boldsymbol{u} = -\frac{\boldsymbol{\nabla}_r p}{\rho} - \nabla_{\mathbf{r}} \Phi, \tag{2.27}$$

where the gravitational potential Φ, is determined by the Poisson equation

$$\nabla_r^2 \Phi = 4\pi G \rho. \tag{2.28}$$

This set of equations, together with an equation of state, forms a closed non-linear system for ρ, $\boldsymbol{u}$, p and Φ. A first approach to get the evolution of small perturbations in a homogeneous background, is given by perturbing the fluid around its Hubble flow and by solving the hydrodynamical equations at the linear order in the perturbed quantities, i.e. , $\delta\rho$, $\delta\boldsymbol{u}$, δp and $\delta\Phi$. The quantities that correspond to the homogeneous background will be henceforth indicated by a bar ($\bar{\rho}$, $\bar{\boldsymbol{u}}$, $\bar{p}$ and $\bar{\Phi}$). Thus, assuming that the perturbations are small compared to the background, these quantities are given by

$$\rho(t, \boldsymbol{r}) = \bar{\rho}(t) + \delta\rho(t, \boldsymbol{r}), \tag{2.29}$$
$$\bar{\boldsymbol{u}}(t, \boldsymbol{r}) = \bar{\boldsymbol{u}}(t) + \delta\boldsymbol{u}(t, \boldsymbol{r}), \tag{2.30}$$
$$p(t, \boldsymbol{r}) = \bar{p}(t) + \delta p(t, \boldsymbol{r}), \tag{2.31}$$
$$\Phi(t, \boldsymbol{r}) = \bar{\Phi}(t) + \delta\Phi(t, \boldsymbol{r}). \tag{2.32}$$

In order to illustrate the procedure to get the evolution of the perturbations, first we consider the particular case of a static space in absent of gravity, then we introduce the gravitational potential to see how it affects the equations of motion as a source term. Finally we modify the equations for an expanding space with the Hubble flow, considering the usual relationship between physical coordinates $\boldsymbol{r}$ and comoving coordinates $\boldsymbol{x}$. In the first case we have $\Phi \equiv 0$, it implies that the solution for the background is given by $\bar{\rho} = const.$, $\bar{p} = const.$ and $\bar{\boldsymbol{u}} = 0$, whereas the evolution of the linearised equations for the fluctuations is reduced to

$$\partial_t \delta\rho = -\nabla_{\boldsymbol{r}} \cdot (\bar{\rho}\boldsymbol{u}), \tag{2.33a}$$
$$\bar{\rho}\partial_t \boldsymbol{u} = -\boldsymbol{\nabla}_{\boldsymbol{r}} \delta p, \tag{2.33b}$$

that, after some manipulations, leads to

$$\partial_t^2 \delta\rho - \nabla_{\boldsymbol{r}}^2 \delta p = 0. \tag{2.34}$$

Eq. (2.34) takes the form of a wave equation for the density perturbations, since it is proportional to the pressure in adiabatic regime, such that $\delta P = c_s^2 \delta\rho$ with

c_s being the speed of sound, whereby

$$\left(\partial_t^2 - c_s^2\nabla^2\right)\delta\rho = 0, \tag{2.35}$$

whose solution can be easily obtained in Fourier space by expanding $\delta\rho$. The result is given by a plane wave $\delta\rho = A\exp[i(\omega t - k\cdot r)]$, with $\omega = c_s k$, and $k \equiv |\boldsymbol{k}|$ the wave number, meaning that the fluctuations oscillate with a constant amplitude, as expected since gravity was ignored. If gravity is not ignored, Eq. (2.35) then gets a source term from the perturbed Poisson equation, $\nabla^2\delta\Phi = 4\pi G\delta\rho$, such as

$$\left(\partial_t^2 - c_s^2\nabla_r^2\right)\delta\rho = 4\pi G\overline{\rho}\delta\rho. \tag{2.36}$$

The solution of Eq. (2.36) is also described by a plane wave $\delta\rho = A\exp[i(\omega t - \boldsymbol{k}\cdot\boldsymbol{r})]$, however the natural frequency of the oscillations is given by $\omega^2 = c_s^2k^2 - 4\pi G\overline{\rho}$, which implies that there is a critical wavenumber k_J, the so-called *Jeans wavenumber*, for which the frequency of oscillations is equal to zero, see Eq. (2.37). The *Jeans wavenumber* sets a limit, in which for small scales, i.e. large wavenumber, $k > k_J$, the pressure dominates and the oscillations of the fluid are then described by Eq. (2.35). However, on large scales, when $k < k_J$, the gravitational effects are not negligible and the fluctuations grow exponentially. Naturally, there is a *Jeans length* associated to the *Jeans wavenumber* given by the following relationship

$$k_{\rm J} \equiv \frac{\sqrt{4\pi G\overline{\rho}}}{c_s} \quad \rightarrow \quad \lambda_{\rm J} = \frac{2\pi}{k_{\rm J}} = c_s\sqrt{\frac{\pi}{G\overline{\rho}}}. \tag{2.37}$$

Taking into account the expansion of the universe driven by $H(t)$, we can transform the equations of the evolution of perturbations into the comoving frame by using the usual relationship between physical coordinates $(t, \boldsymbol{r})$ and comoving coordinates $(t, \boldsymbol{x})$, to be

$$\boldsymbol{r}(t) = a(t)\boldsymbol{x}, \tag{2.38}$$

$$\boldsymbol{u}(t) = \dot{\boldsymbol{r}} = H\boldsymbol{r} + \boldsymbol{v}, \tag{2.39}$$

$$\boldsymbol{\nabla}_{\boldsymbol{r}} = \frac{1}{a}\boldsymbol{\nabla}_{\boldsymbol{x}}, \tag{2.40}$$

$$\left.\frac{\partial}{\partial t}\right|_{\boldsymbol{r}} = \left.\frac{\partial}{\partial t}\right|_{\boldsymbol{x}} - H\boldsymbol{x}\cdot\boldsymbol{\nabla}_{\boldsymbol{x}}, \tag{2.41}$$

where $H\boldsymbol{r}$ is the Hubble flow and $\boldsymbol{v} = a\dot{\boldsymbol{x}}$ is the peculiar velocity. Notice that in a static spacetime, the time and space derivates are independent, but are not in an expanding spacetime. Thus, by introducing density contrast defined as

$$\delta \equiv \frac{\delta\rho}{\overline{\rho}} = \frac{\rho - \overline{\rho}}{\overline{\rho}},$$

the equations that give the evolution of the perturbations in an expanding universe can be rewriting as follows:

$$\begin{cases} \dot{\delta} = -\dfrac{1}{a}\boldsymbol{\nabla}\cdot\boldsymbol{v} & \text{Continuity equation,} \quad (2.42a) \\ \dot{\boldsymbol{v}} + H\boldsymbol{v} = -\dfrac{1}{a\overline{\rho}}\boldsymbol{\nabla}\delta P - \dfrac{1}{a}\boldsymbol{\nabla}\delta\Phi & \text{Euler equation,} \quad (2.42b) \\ \boldsymbol{\nabla}^2\delta\Phi = 4\pi G a^2\overline{\rho}\delta & \text{Poisson equation.} \quad (2.42c) \end{cases}$$

By combining these equations, and considering that the expansion is adiabatic,

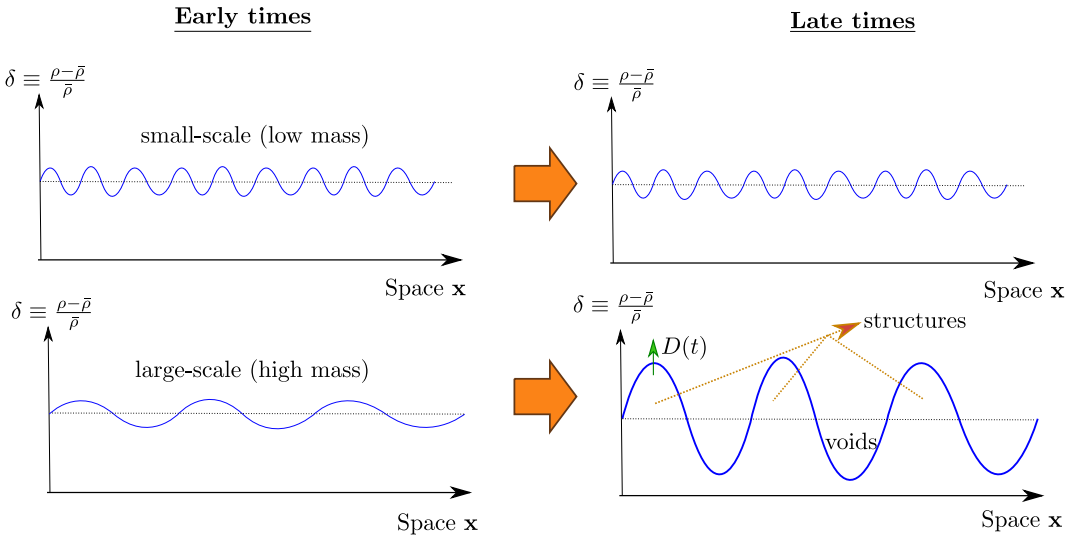

Figure 2.3: Schematic representation of the structure formation process. The plot shows the growth of the density fluctuations from the early universe depending on the Jeans limit, they can grow and propagate due to the effects of gravity and the expansion of the Universe. *Upper panel*: small scale, low mass density enhancements propagate over time due to pressure effects. *Lower panel*: large mass density enhancements grow due to gravitational effects which overcome the pressure effects.

we can get the differential equation that govern the evolution of the density contrast to characterize how the perturbations evolve during different cosmic epochs. This is given by

$$\ddot{\delta} + 2H\dot{\delta} - \frac{c_s^2}{a^2}\nabla^2\delta = 4\pi G\overline{\rho}\delta, \tag{2.43}$$

which is identical to the equation expected for linear acoustic waves in a static medium, apart of the Hubble damping and gravitational source term, but now the background density $\overline{\rho}(t)$ and sound speed $c_s(t)$ depends on time, even if the Jeans' length is the same as Eq. (2.37). As consequence of the damping term, $2H\dot{\delta}$, at scales below the Jeans' length $\lambda < \lambda_J$, the fluctuations oscillate with decreasing amplitude, whereas in the opposite case, above the Jeans' length $\lambda > \lambda_J$, the fluctuations behave as a power-law growth, rather than the exponential growth that we found for a static space. Moreover, since this is a second-order differential equation, it admits two independent solutions that can grow under certain conditions, thus the peculiar velocity field created by the

perturbations δ is immediately determined by means of Eq. (2.42a). The most general solution of the set of Eqs. (2.42) is a superposition of modes, commonly expressed as

$$\delta(t, \boldsymbol{x}) = \delta_+(\boldsymbol{x})D_+(t) + \delta_-(\boldsymbol{x})D_-(t), \tag{2.44}$$

where the subscript $+$ denotes the growing mode and $-$ the decaying mode. The functions $D_+(t)$ and $D_-(t)$ are independent, where the growing solution is often called linear growth function, normalized by definition such that $D_+(t_0) = 1$. Among these modes, only the adiabatic modes (i.e. that the cooling time is long compared with the age of the Universe) are interesting in the context of structure formation, so we will focus only on these in what follows. Fig. 2.3 shows schematically the process of the structure formation, considering that density fluctuations can grow and propagate due to the effects of gravity and the expansion of the Universe depending on the Jeans limit. Fig. 2.4 shows the evolution in redshift of the perturbations, in the ΛCDM model, for each component of the cosmic fluid: CDM, baryon and radiation. In the remaining of this Section, we summarise the main results of the modes obtained from the evolution of the matter fluctuations in each cosmic era.

Matter era: considering the linearised CDM fluctuations, by setting $c_s = 0$ since a non-linear effect produce a very small sound speed, the pressure term in Eq. (2.43) can be neglected, leading to

$$\ddot{\delta}_m + 2H\dot{\delta}_m - 4\pi G\overline{\rho}_m\delta_m = 0. \tag{2.45}$$

In a flat universe matter-dominated, the scale factor takes the form $a \propto t^{2/3}$, so that $H = 2/3t$, which in turn implies

$$\ddot{\delta}_m + \frac{4}{3t}\dot{\delta}_m - \frac{2}{3t^2}\delta_m = 0, \tag{2.46}$$

whose solutions can be obtained from $\delta_m \propto t^p$, giving the two modes as indicated by Eq. (2.47), where the growing mode of the dark matter fluctuations scales like the scale factor, clustering matter and forming later structures.

$$\delta_m \propto \begin{cases} t^{-1} \propto a^{-3/2} \\ t^{2/3} \propto a \end{cases} \tag{2.47}$$

Radiation era: during this epoch the main contribution to the total density fluctuation is given by matter and radiation species, $\delta\rho = \delta\rho_m + \delta\rho_r$, both under the effect of $\delta\Phi$, however from a full relativistic analysis of perturbation theory (see e.g., Mukhanov, 2005; Peacock, 1999; Peebles, 1993), can be shown that the fluctuations of radiation on scales smaller than the Hubble radius oscillate as sound waves, supported by large radiation pressure and the time-averaged density contrast that vanishes. This has as consequence the so-called *Meszaros effect* that establish that DM perturbations during radiation domain are basically frozen even for perturbations much larger than the Jeans length but inside the horizon (see e.g., Mukhanov, 2005). It implies that only CDM is responsible of

clustering during the acoustic oscillations of the radiation, furthermore, since $\bar{\rho}_m \ll \bar{\rho}_r$, it leads to $\ddot{\delta}_m \sim H^2\delta_m \sim \frac{8\pi G}{3}\bar{\rho}_r\delta_m \gg 4\pi G\bar{\rho}_m\delta_m$. We can therefore ignore the last term in Eq. (2.48) in comparison to the others terms, and to express the equation of the perturbations as

$$\ddot{\delta}_m + \frac{1}{t}\dot{\delta}_m - 4\pi G\bar{\rho}_m\delta_m \approx 0. \tag{2.48}$$

In this case, the modes are given by

$$\delta_m \propto \begin{cases} \text{const.} \\ \ln t \propto \ln a. \end{cases} \tag{2.49}$$

It means that the fast expansion due to radiation decreases the growing of δ_m to only logarithmic scales, moreover, in order to form structures the universe must make a transition from radiation domination to matter domination allowing that the density fluctuations of dark matter grow significantly.

Dark energy era: In this era the perturbations are even entirely frozen (see e.g., Mukhanov, 2005), since by definition the dark energy does not cluster, because ρ_Λ remains constant in all cosmic epochs as shown by Eq. (2.13). In this stage $H^2 \approx$ const. $\gg 4\pi G\bar{\rho}_m$, hence $\delta_m \approx 0$, that simplifies the equation of perturbations as following

$$\ddot{\delta}_m + 2H\dot{\delta}_m \approx 0. \tag{2.50}$$

whose solutions are given by

$$\delta_m \propto \begin{cases} \text{const.} \\ e^{-2Ht} \propto a^{-2}. \end{cases} \tag{2.51}$$

Since these solutions are not growing, it can be inferred that once dark energy starts to dominate the matter fluctuations stop growing and there is not structure formation anymore. Further details concerning scales larger than the Hubble radius, and a complete relativistic treatment on structure formation can be seen in Refs. (Padmanabhan, 1993; Peebles, 1993).

2.4. The linear growth factor and growth rate

In the matter dominated epoch, under the linear regime of the perturbation theory discussed previously, the density contrast δ of a pressureless fluid [see Eq. (2.43)], can be expressed like an equation of the amplitude of the growing mode $D(z)$, being scale independent and following the differential equation:

$$\ddot{D} + 2H(z)\dot{D} - \frac{3}{2}\Omega_{m,0}H_0^2(1+z)^3 D = 0. \tag{2.52}$$

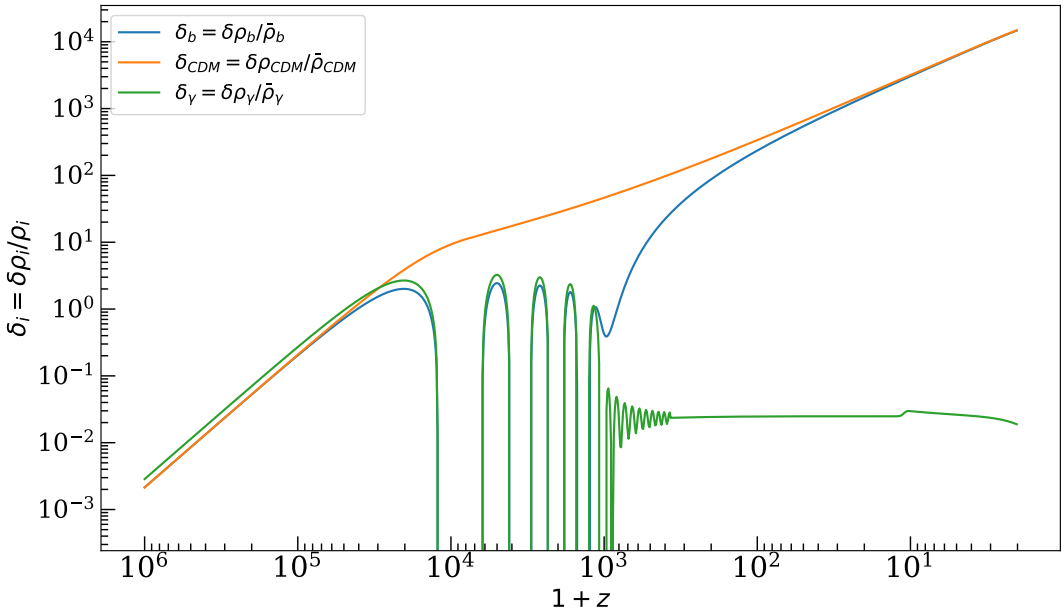

Figure 2.4: The evolution in redshift of the CDM (orange), baryon (blue) and radiation (green) perturbations for a wavenumber $k = 10^{-2}\,Mpc^{-1}$ by assuming the ΛCDM model. The baryon density fluctuates before recombination, i.e. about $z \sim 1000$, and grows afterwards. The baryon density eventually follows the CDM density perturbations, which starts growing before recombination. Figure created using CAMB.

By assuming a flat universe with cosmological constant ΛCDM-like, the solution of the differential equation can be written in its integral form as

$$D_1(z) = \frac{H(z)}{H_0}\int_z^\infty \frac{dz'\,(1+z')}{H^3\,(z')}\left[\int_0^\infty \frac{dz'\,(1+z')}{H^3\,(z')}\right]^{-1}, \tag{2.53}$$

where D_1 is the growing mode normalized so that $D_1(z=0) = 1$. Eq. (2.53) allows introducing the dimensionless linear growth rate $f(z)$, which is related to the growth factor in the follows form

$$f(z) \equiv -\frac{d\ln D}{d\ln(1+z)} \simeq \left[\Omega_{\rm m}(1+z)^3\frac{H_0^2}{H^2(z)}\right]^\gamma, \tag{2.54}$$

where the exponent $\gamma \simeq 0.55$ for GR (Linder, 2005). Eq. (2.54) is valid for a wide range of models in linear perturbation theory based on GR and for relevant values of cosmological parameters.

The dependence of the growth factor $D(z)$ with redshift is shown in Fig. 2.5 obtained by numerical integration of Eq. (2.53) for a flat universe with different cosmological parameters given by: WiggleZ (Blake et al., 2011), WMAP9 (Hinshaw et al., 2013), PLANCK18 (Planck Collaboration et al., 2018b) and Millennium simulation (Springel et al., 2005). Some significant deviations can be appreciated at low redshift due to the difference on the constrained parameters even if they are globally in agreement. This feature of the growth factor is highly important in the sense that allows to constrain several cosmological

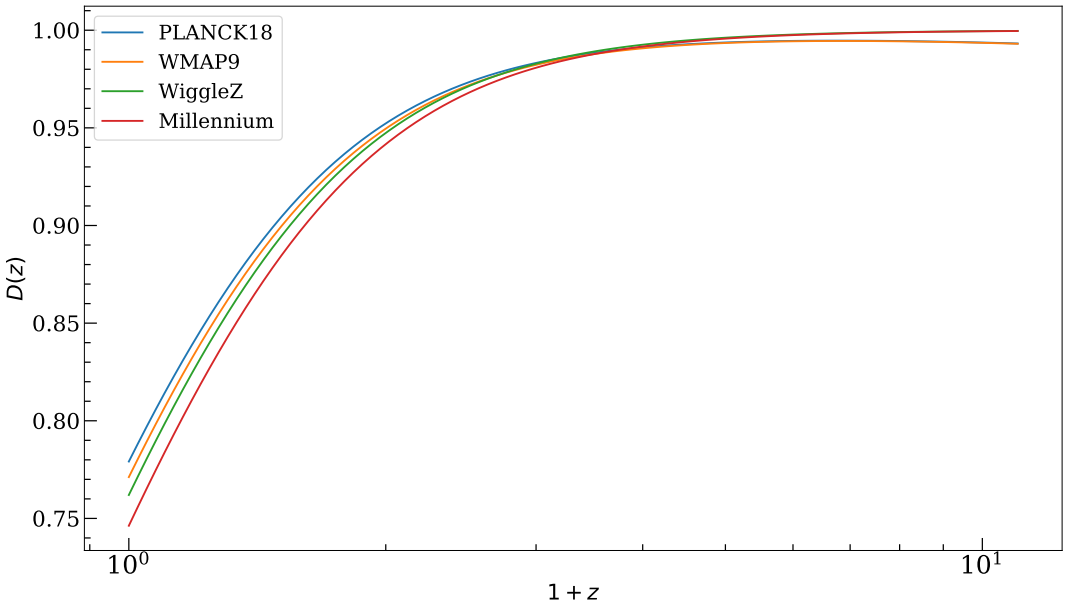

Figure 2.5: Evolution of the growth factor $D(z)$ in terms of redshift assuming a flat universe with different combinations of cosmological parameters as indicated by the labels.

models by evaluating the behaviour of its growth history. It means that an accurate estimate of the growth factor can constrain the value of Ω_m, Ω_Λ and the EoS w thanks to its dependence with the Hubble parameter $H(z)$. Usually the constraints are obtained by measuring the growth rate $f(z)$ instead of the growth factor, since its dependence with the cosmological parameters is more transparent. Additionally $f(z)$ can be used to find possible deviations from GR predictions, understood as a test of General Relativity at large scales, since this information is encoded in the γ exponent. In the literature, it is common to find the constraints expressed as $f(z)\sigma_8(z)$, where the σ_8 parameter corresponds to the linear density fluctuations smoothed on a scale of $8h^{-1}\,\mathrm{Mpc}$ computed from linear theory. This is done because at large scales the growth factor is fully degenerate with σ_8, and consequently, only the quantity $f\sigma_8$ can be constrained. Fig. 2.6 shows the evolution of $f\sigma_8$ in terms of redshift, obtained from surveys like the 2dfGRS (Percival et al., 2004a) and 6dFGS (Beutler et al., 2012), the GAMA (Blake et al., 2013b), the WiggleZ (Blake et al., 2012), the VVDS (Guzzo et al., 2008), and the VIPERS (de la Torre et al., 2013), as well as the measurements from the SDSS-I and -II main galaxy sample (Howlett et al., 2015, MGS) and the SDSS-II LRG sample (Oka et al., 2014, DR7).

2.5. Statistical description of the density field

As shown in the previous Section, the dynamics of the density contrast is described in the linear regime by a differential equation of the growth factor, that has been obtained after perturbing the density, velocity and potential fields. In particular, the density contrast have been decomposed into plane waves, that by Fourier transform, it produces a set of independent equations that can be solved

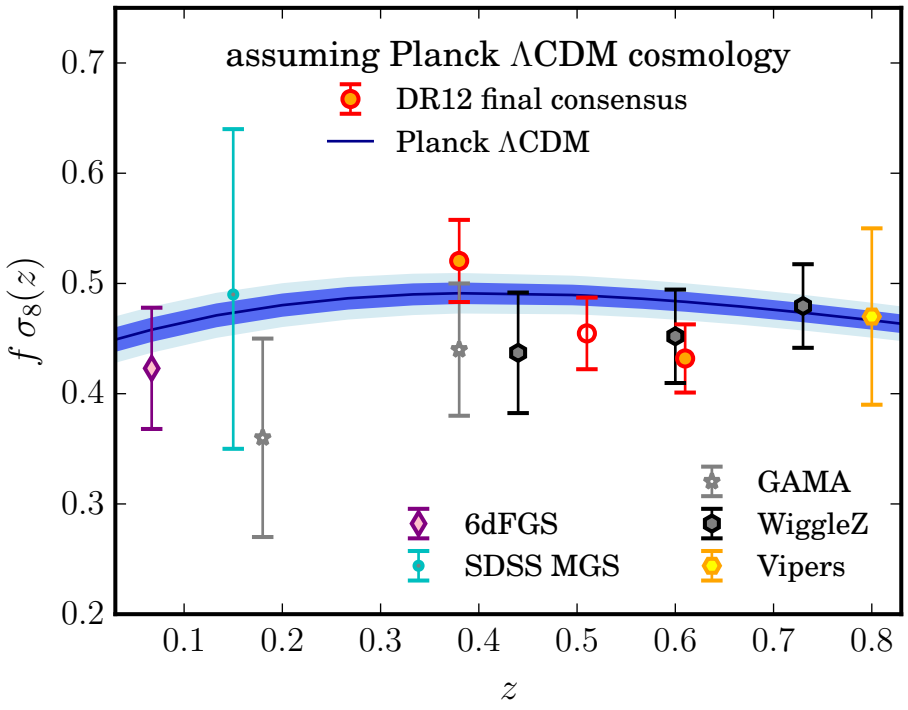

Figure 2.6: Redshift evolution of $f\sigma_8(z)$ assuming a Planck ΛCDM background cosmology, where $f(z)$ is the growth rate of matter fluctuations and $\sigma_8(z)$ is the rms amplitude of the density contrast δ smoothed on $8h^{-1}$Mpc in comoving scale. The $f\sigma_8(z)$ values are measured from the 2dfGRS (Percival et al., 2004a) and 6dFGS (Beutler et al., 2012), the GAMA (Blake et al., 2013b), the WiggleZ (Blake et al., 2012), the VVDS (Guzzo et al., 2008), and the VIPERS (de la Torre et al., 2013) surveys, as well as the measurements from the SDSS-I and -II main galaxy sample (Howlett et al., 2015, MGS) and the SDSS-II LRG sample (Oka et al., 2014, DR7). Figure taken from Alam et al. (2017).

independently for each mode $\mathbf{k}$. All the cosmological information is contained in the solutions of these equations when the linear theory applies. Naturally, solving the equations requires to specify a set of initial conditions to guarantee the uniqueness of the solution. In such a case, the initial conditions for the density field are not trivial, since they are related to the very early Universe, that is described nowadays by the inflationary paradigm [3]. Indeed, inflation does not predict the primordial density field $\delta(\mathbf{x}, t)$, but it makes predictions about the statistical properties of the density field, creating the seeds of the primordial Gaussian fluctuations imprinted in the density field at the end of the inflationary period (for a review on inflation see Turok, 2002).

From a statistical point of view, it is assumed that the observed Universe

[3]The inflationary theory (developed at the beginning of the 80's by A. Guth, A. Linde and A. Starobinsky), provides a mechanism to solve the horizon and flatness problems of the standard model of cosmology, by introducing an exponential expansion of universe just after the Big Bang. The inflation epoch occurs for a period around 10^{-36} seconds, where the Universe expands by 10^{24} orders of magnitude to fit the current observational constraints.

corresponds to a random realization of all the possible universes, which must be isotropic and homogeneous in order to comply the *cosmological principle*. This also implies that one part of the observable Universe can fairly represent the whole sample. Moreover, in order to describe the statistical properties of the Universe, it is not enough to evaluate the matter density contrast $\delta(\mathbf{x}) = \delta\rho(\mathbf{x})/\rho$ at a specific point $\mathbf{x}$, instead it can be associated to a Gaussian random field motivated in inflation as discussed above. In general, the distribution of the density fluctuations δ can not be exactly described by a Gaussian field, because it has to satisfy the condition $\delta > -1$, however since they have $\langle\delta\rangle = 0$ and under the approximation of a sufficiently small amplitude of the fluctuations, it is possible to describe them as Gaussian, this fact is also supported by the observations of the CMB anisotropies, which shows that possible deviations from Gaussianity in the primordial density field are very small. Besides that Gaussian random fields are crucially important in clustering, they have the virtue to describe their full statistical properties analytically; thus in what follows we discuss this statistic. A concise study on theory and observations of non-Gaussianity from inflation can be found in (Bartolo et al., 2004).

The simplest statistics, that quantifies completely the spatial distribution of cosmic tracers, is the two-point correlation function, defined in configuration space as follows

$$\xi(\mathbf{r}) \equiv \frac{\langle[\rho(\mathbf{x}) - \overline{\rho}][\rho(\mathbf{x}+\mathbf{r}) - \overline{\rho}]\rangle}{\overline{\rho}^2} = \langle\delta(\mathbf{x})\delta(\mathbf{x}+\mathbf{r})\rangle, \tag{2.55}$$

where the brackets denote the average over all possible realizations, or by evoking the *ergodic theorem*, over the entire Universe. The two-point correlation function measures the coherence of the density contrast field between all points on the sky separated by a distance r. Assuming that the random field is homogeneous and isotropic, the correlation function only depends on r i.e. $\xi(\mathbf{r}) \equiv \xi(r)$. Additionally, by considering the *spectral representation theorem* (for a description see e.g. Adler, 1981), if $\xi(r)$ is continuous at $r = 0$ there exists a spectral representation of the field, it means a representation in Fourier space with modes $\delta(\mathbf{k})$. The spatial Fourier transform of the density field $\delta(\mathbf{x})$ has the form

$$\delta(\mathbf{k}) = \frac{1}{(2\pi)^3}\int \delta(\mathbf{x})e^{-i\mathbf{k}\cdot\mathbf{x}}d\mathbf{x}, \tag{2.56}$$

with $\delta(\mathbf{x})$ being a real quantity and $\delta^*(\mathbf{k}) = \delta(-\mathbf{k})$. The variance of the density contrast in Fourier space defines the power spectrum $P(\mathbf{k})$ as follows

$$\langle\delta(\mathbf{k})\delta^*(\mathbf{k}')\rangle = (2\pi)^3\delta_D^{(3)}(\mathbf{k}-\mathbf{k}')\,P(k), \tag{2.57}$$

where $\delta_D^{(3)}$ is the three-dimensional Dirac Delta distribution, which ensures that modes of different wave vector $\mathbf{k}$ are uncorrelated in Fourier space and keeps the validity of cosmic homogeneity; furthermore, the isotropy condition makes the power spectrum independent of the direction of $\mathbf{k}$. Since this quantity is defined naturally in Fourier space, the power spectrum can be interpreted

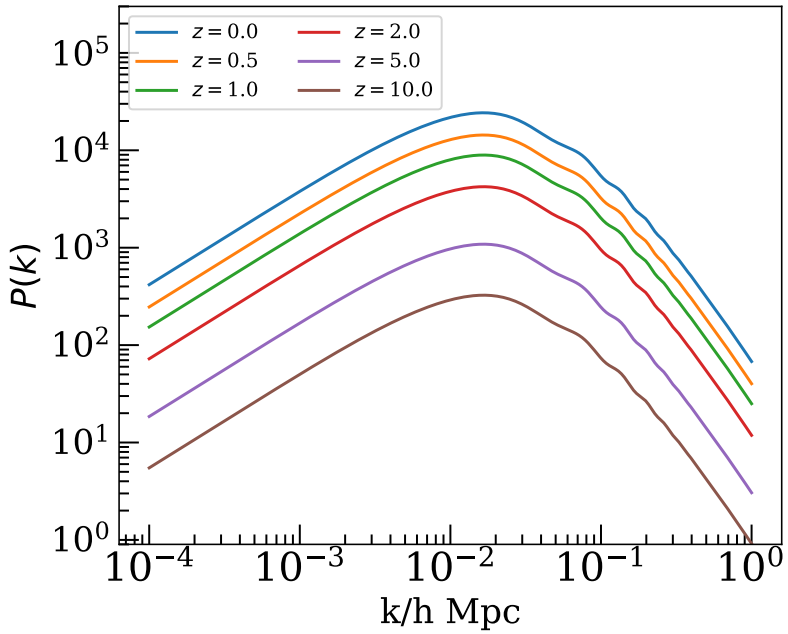

Figure 2.7: Linear matter power spectrum $P(k)$ computed with the CAMB code at different redshifts for a ΛCDM model with Planck Collaboration et al. (2018b) parameters.

as the contribution of modes of wave vector $\mathbf{k}$ to the total variance, per unit volume of wavenumber space, containing all the statistical information about the fluctuations. The determination of the matter power spectrum $P(k)$ in a wide range of scales, with high levels of precision and accuracy, is one of the big challenges in current cosmology. On the other hand, both, the power spectrum $P(k)$ and the two-point correlation function (hereafter 2PCF), encode the same information to describe the clustering, making them completely equivalent, perhaps a difference lies in that different Fourier coefficients are uncorrelated until the evolution of the perturbations remains linear, while the number of pairs at different separations become correlated because of gravity [4]. The power spectrum $P(k)$ can be computed from the 2PCF by Fourier transforming as follows

$$P(k) = \int d^3r\xi(r)e^{i\mathbf{k}\cdot\mathbf{r}} = 4\pi \int r^2\xi(r)\frac{\sin kr}{kr}dr, \tag{2.58}$$

whereas the inverse case in configuration space, i.e. getting the 2PCF given the power spectrum, follows

$$\xi(r) = \frac{1}{(2\pi)^3}\int P(k)e^{-i\mathbf{k}\cdot\mathbf{r}}d^3k = \frac{1}{2\pi^2}\int k^2P(k)\frac{\sin kr}{kr}dk. \tag{2.59}$$

Fig. 2.7 displays the evolution of the linear matter power spectrum for the ΛCDM model by assuming the final constraints on cosmological parameters from Planck Collaboration et al. (2018b). In literature is often used an alternative

[4]The correlation function is a dimensionless quantity, whereas the power spectrum $P(k)$ has units of volume. The density contrast $\delta(\mathbf{r})$ and $\delta(\mathbf{k})$ are dimensionless too.

definition of the power spectrum as given by

$$\Delta^2(k) \equiv k^3 P(k), \tag{2.60}$$

which is equivalent to $d\langle\delta^2\rangle / d\ln k$, where $\langle\delta^2\rangle = \xi(0)$ is the *zero-lag* correlation function. The quantity $\Delta^2(k)$ is called the dimensionless power spectrum and it measures the contribution of perturbations per unit of logarithmic interval at wavenumber k to the variance of the matter density fluctuations.

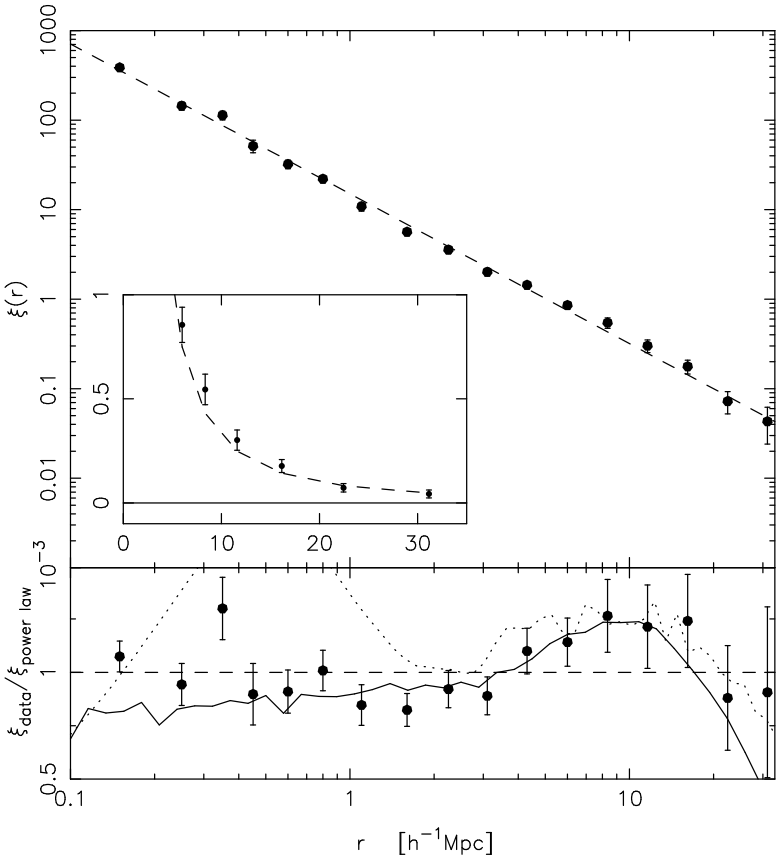

Figure 2.8: The correlation function measured from the 2dFGRS galaxy survey (Hawkins et al., 2003) in log-log scale. The dashed line is the best-fit power-law [$r_0 = 5.05h^{-1}Mpc$, $n = -1.33 \rightarrow$ exponent $\gamma = 1.67$]. The solid line is the result from the survey and the dashed line from an N-body simulation. Figure taken from (Hawkins et al., 2003).

2.6. The bias factor

In the previous Section, the clustering was described by introducing the concepts of power spectrum and correlation function of the total matter distribution. However, since its density is constituted mainly by CDM, the spatial distribution of observable galaxies, galaxy clusters, AGN etc., can not trace the clustering of the bulk of matter in the Universe. In a general sense, the observed matter density must be linked to the dark matter density field by introducing

a *tracer bias*, i.e. , a relationship between the spatial distribution of the tracer (galaxies, galaxy clusters, etc.), and the underlying dark matter density field as follows

$$\delta_{tr} = f(\delta_{DM}), \tag{2.61}$$

where δ_{tr} and δ_{DM} are the density fields of the tracer and dark matter, respectively. The bias is related to all the physical processes of the tracer history which cause the spatial distribution of baryons to differ from the expected of DM. It can depends on several factors such as scale, redshift or galaxy properties such as luminosity, morphology or color (Coil, 2013). The most simple and reasonably physical assumption is to assume a linear dependence of $f(\delta)$ with δ, parametrizing Eq. (2.61) by a *bias* factor b, so that

$$\delta_{tr} = b\delta_{DM} \qquad \rightarrow \qquad b = \delta_g/\delta_{DM}. \tag{2.62}$$

Since the bias factor is defined in terms of the density contrast, it encloses information about the level of clustering of the tracers; a bias $b > 1$ means a higher clustering of the tracers with respect to the underlying dark matter density field. In terms of the correlation function, the linear bias follows

$$\xi_{tr}(r) = b^2\xi_{DM}(r), \tag{2.63}$$

where the correlation function of both, matter and tracers, have positive values at small scales and it is well described by a power law relationship

$$\xi(r) = \left(\frac{r}{r_0}\right)^{-(3+n)}, \tag{2.64}$$

with n and r_0 being fitting parameters (see Fig. 2.8)[5]. From a theoretical and numerical point of view, the bias factor is complex to model because the tracer density can be a non-local and stochastic function adding extra variances (Scoccimarro, 2000). The linear approximation of the bias has shown to be valid on sufficiently large scales (Desjacques, Jeong, and Schmidt, 2018; Gaztañaga et al., 2005; Verde et al., 2002; Marulli et al., 2018).

2.7. Galaxy surveys - observational status

From an observational point of view, the study of the LSS has remote and diverse origins. Focused on modern science, the Edwin Hubble's observations in 1930 provided the elements to understand that galaxies are not randomly distributed (Schneider, 2007). Hubble used a catalog with 400 "extragalactic nebulae" to test the homogeneity of the Universe, finding that it is statistically uniform (Hubble, 1926). The following galaxy surveys such as Shapley-Ames in

[5]Motivated in the power law scaling of the correlation function, the 2 point statistic have been used also to find the homogeneity scale of the galaxy distribution. Early in the 90s, several authors extended this idea by using the fractal analysis. In the Appendix A are shown the details on how is performed this kind of analysis, and discuss the impact of observational holes on galaxy samples.

1932 for bright galaxies (Shapley and Ames, 1932), showed a "general inequality in the distribution" of projected galaxies in the celestial sphere with a difference by a factor 2 in the number of galaxies in each celestial hemisphere. For this galaxy sample, Hubble observed that at angular scales smaller than $\sim 10°$ there was an excess in the counts of galaxies above what would be expected for a Poisson distribution (Coil, 2013). This sample follows a Gaussian distribution at larger scales, wherewith the Universe seems to be homogeneous at large scales but exhibits a lumpy appearance defined by the clustering of galaxies at small scales (Hubble, 1934).

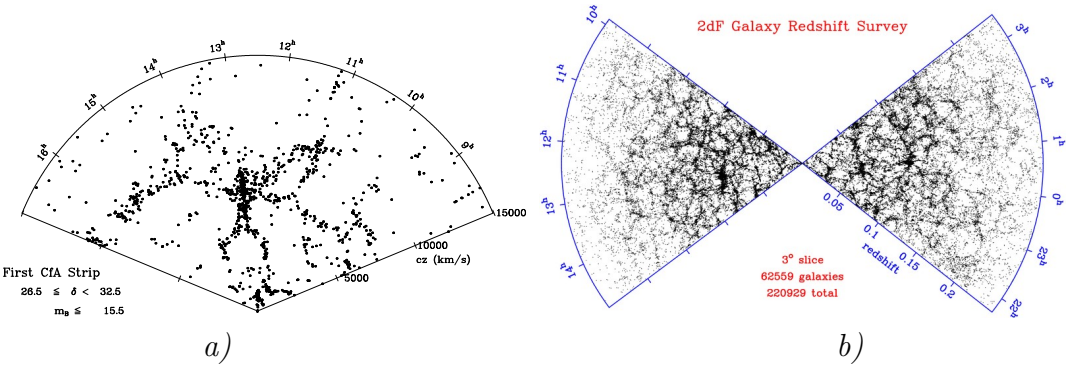

a) *b)*

Figure 2.9: *a)* CfA slice with 249 galaxies distributed in declination $10° < \delta < 20°$ (Figure taken from https://www.cfa.harvard.edu/~dfabricant/huchra/zcat/); *b)* 62559 galaxies distributed in a 3° thick slice through the *2dF Galaxy Redshift Survey* (Figure taken from Eke et al., 2004 - http://www.2dfgrs.net/).

Advances in the study of LSS were significant with the Lick catalog of galaxies by Shane, Wirtanen, and Steinlin, 1959 and the analysis performed by Seldner et al., 1977 that showed in much more detail that the galaxy distribution is not fully uniform. The samples from this catalog and from the Zwicky and Herzog, 1966 catalog were analyzed by Peebles and Groth, 1975 and Hawley and Peebles, 1975 showing that the angular two-point correlation function follows approximately a power law in the range $\sim 0.1° - 5°$. Since 1980 maps of galaxy distribution have been made in three dimensions. These galaxy surveys show a matter configuration with cosmic structures at large-scales. Some of the first galaxy redshift surveys were the *KOS survey* (Kirshner et al., 1983) with 164 galaxies in a field of 15 deg^2; *CfA* (Davis et al., 1982; Davis and Peebles, 1983) with approximately 5800 galaxies, that revealed the structure so-called "Great Wall", a supercluster of galaxies that extends over 170 Mpc/h (see Fig. 2.9a), and the 2dF -"Two-degree-Field Galaxy Redshift Survey" operated by the Anglo-Australian Observatory (AAO), which showed a wall structure of 766.5 Mpc (see Fig. 2.9b).

Nowadays galaxy surveys have progressed rapidly with the development of multi-object spectrographs and fiber-optic systems allowing simultaneous observations of hundreds of galaxies, making it possible to have deeper samples with objects at high redshift. Two examples are: *a)* the Baryon Oscillation Spectroscopic Survey (BOSS), one of the projects managed by the Sloan Digital

Sky Survey III (SDSS-III), consisting of approximately 1000 optical fibers with an effective volume of ∼6 $h^{-3}Gpc^3$ in a field of ∼10000 deg^2, and a sample close to 1.5 million galaxies until a redshift of 0.7 (Delubac et al., 2015); and *b)* the VIMOS Public Extragalactic Redshift Survey (VIPERS), a completed ESO Large Program that has mapped in detail the spatial distribution of normal galaxies over an unprecedented volume at $z \sim 1$ using a spectrograph at the 8 m Very Large Telescope to measure spectra for more than 90000 galaxies (Guzzo et al., 2014). Advances in observational techniques and instrumentation allow to use these surveys for cosmological purposes, such as WiggleZ Dark Energy Survey, VIPERS, BOSS, Dark Energy Spectroscopic Instrument (DESI) and the Euclid mission that will use specific tracers to probe the underlying structure on large scales with the latest technology, representing the next step in the study of observational cosmology. Figure 2.10 shows a comparison of the effective volume V_{eff} $(h^{-3}Gpc^{-3})$ for galaxy redshift surveys operating at optical and radio wavelengths.

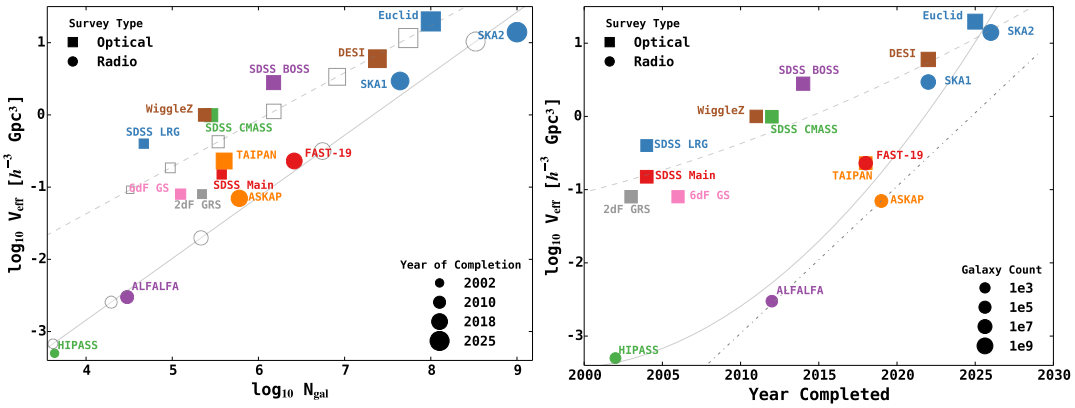

Figure 2.10: *a)* Effective volume of several galaxy surveys as a function of total galaxy count for telescopes at optical and radio wavelengths. Symbol size indicates the approximate year in which the survey is finished or will finish; *b)* effective volume of several galaxy surveys as a function of the year it was completed for both optical and radio facilities. Symbol size indicates the approximate number of objects sampled. Fits to a power law of the effective volume are shown in gray curves based on the completed year and the number of observed galaxies. Credit: Duffy, 2014.

Since the study of the dark sector and the RSD includes mainly large-scale surveys, the European Space Agency (ESA) has developed the Euclid mission[6]. Euclid is a space mission approved in October 2011, and will be launched to the L2 Sun-Earth Lagrange point in 2022, for a mission of 7 years to investigate the nature of dark energy, dark matter and gravity by tracking their observational signatures on the geometry of the Universe and on the history of structure formation. To accomplish this task, Euclid will use two main probes, weak lensing and galaxy clustering, including Baryon acoustic oscillations (BAO) and RSD, to measure about 10 billion sources, from which around 1 billion will

[6]Euclid Consortium http://www.euclid-ec.org

be used for weak lensing, and tens of million redshifts will be used for galaxy clustering (Laureijs et al., 2012; Amendola et al., 2018). Euclid will use a 1.2 m mirror telescope operating in both visible and infrared wavelengths, which will cover an area of about 15000 deg^2 in the redshift range $0.5 < z < 2.0$, when the cosmic speed-up its supposed to start. Euclid seems promising, and a big scientific effort has been made until now (and for sure in the forthcoming years) to provide the best map of the structure on a large scale and allow us to expand our knowledge of the fundamental open questions about the structure of the Universe.

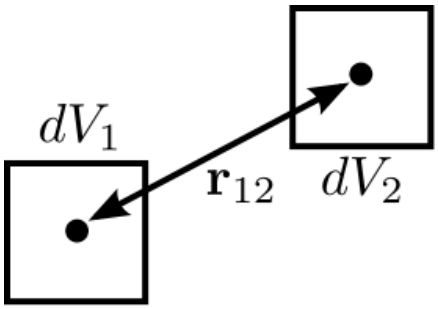

Figure 2.11: The two-point correlation function (2PCF) described as the excess of probability (compared with that expected for a random distribution) of finding a pair of objects in the volumes dV_1 and dV_2 separated by $\mathbf{r}_{12}$.

2.8. Clustering measurements of discrete samples

Regarding the clustering measurements, the 2PCF can be also defined as the joint probability dP_{12}, compared with that is expected for a random distribution, of finding a pair of objects at certain spatial separation r in the infinitesimally small volume elements dV_1 and dV_2 (see Fig. 2.11):

$$dP_{12} = \overline{n}^2[1 + \xi(r)]\mathrm{d}V_1\mathrm{d}V_2, \tag{2.65}$$

where $\bar{n}$ is the mean number density of the tracer and the product $\bar{n}dV_i$ represents the stochastic probability of finding an object in dV_i. Fig. 2.12 shows the coordinate convention used in this Thesis to estimate the clustering. If the tracers are distributed randomly, i.e. uncorrelated, Eq. (2.65) is reduced to $dP_{12} = \overline{n}^2\mathrm{d}V_1\mathrm{d}V_2$, otherwise $\xi(r) > 0$ means a positive correlation while $-1 < \xi(r) < 0$ means negative correlation. This probabilistic definition provides a method to estimate the 2PCF by counting pairs that can be summarized as follows: given the limited volume, like a galaxy survey or an N-body simulation, finding the count of pairs separated by a distance between r and $r + dr$, and then compare it to the count of pairs expected if the tracers were randomly distributed. Usually the estimation of $\xi(r)$, considering edge effects, is performed in a sample of objects within a window W of the entire volume $V(W)$, as illustrated in Fig. 2.13, so that the centres for counting pairs correspond only to objects within an inner window W_{in}, leading to

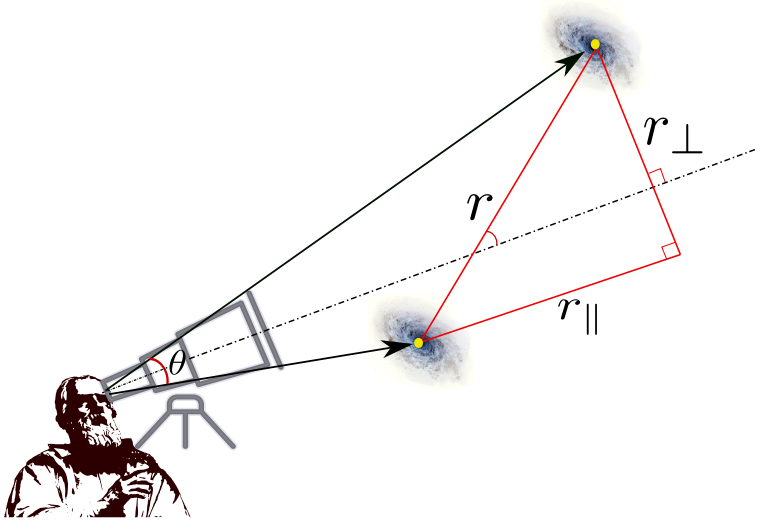

Figure 2.12: Sketch that describes the coordinate convention used in this Thesis for the 2PCF. Two tracers (galaxies) separated by a distance r, which is decomposed in terms of the line-of-sight of the observed as a transverse $r_\perp$ and parallel $r_\perp$ components, with $\theta = r_\parallel / r$.

$$\hat{\xi}(r) = \frac{V(W)}{NN_{in}} \sum_{i=1}^{N_i n} \frac{n_i(r)}{V_{sh}} - 1, \tag{2.66}$$

where $\hat{\xi}(r)$ is the so-called minus-estimator of $\xi(r)$ and V_{sh} is the volume of the shell of width dr,

$$V_{\rm sh} = \frac{4\pi}{3}\left[(r+dr)^3 - r^3\right], \tag{2.67}$$

than can be approximated by $4\pi r^2 dr$ if dr is small enough, on the other hand, based on this estimator several edge-corrections to estimate the 2PCF have been proposed to avoid underestimations (Martínez and Saar, 2002). Now, by denoting the number of pairs in the catalogue of N tracers (by example galaxies, haloes, etc.) as $DD(r)$; the number of pairs in an auxiliary random sample with N_{rd} points as $RR(r)$; and the number of pairs between the data and the random sample as $RR(r)$; the *Peebles-Hauser* (PH) unbiased estimator (Peebles and Hauser, 1974), sometimes called *natural estimator*, can be defined as follows

$$\hat{\xi}_{PH}(r) = \left(\frac{N_{rd}}{N}\right)^2 \frac{\langle DD\rangle}{\langle RR\rangle} - 1, \tag{2.68}$$

being a statistics based on discrete counts of stochastic variables; its variance scale as Poissonian variance, i.e. as the inverse of number of pairs. The *Davis-Peebles* (DP) estimator (Davis and Peebles, 1983) is defined as follows:

$$\hat{\xi}_{DP}(r) = \frac{N_{rd}}{N}\frac{\langle DD\rangle}{\langle DR\rangle} - 1, \tag{2.69}$$

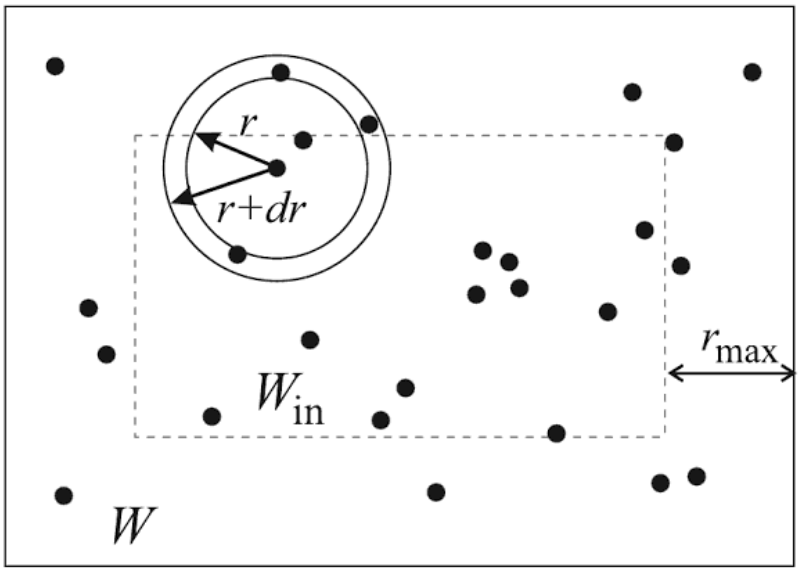

Figure 2.13: Sketch of the inner window method used in the minus-estimator of the 2PCF. Only points within W_{in} are considered as centres to perform the pair counting. Figure taken from (Martínez and Saar, 2002).

the *Hamilton* (HAM) estimator (Hamilton, 1993) as follows:

$$\hat{\xi}_{HAM}(r) = \frac{\langle DD\rangle\langle RR\rangle}{\langle DR\rangle^2} - 1, \tag{2.70}$$

and finally the *Landy-Szalay* (LS) estimator (Landy and Szalay, 1993) as follows:

$$\hat{\xi}_{LS}(r) = \left(\frac{N_{rd}}{N}\right)^2 \frac{\langle DD\rangle}{\langle RR\rangle} - 2\frac{N_{rd}}{N}\frac{\langle DR\rangle}{\langle RR\rangle} + 1. \tag{2.71}$$

The latter estimator is almost unbiased with minimum variance, this is reason why the Landy-Szalay estimator is preferred over the other ones, being widely used in investigations on clustering (Kerscher, Szapudi, and Szalay, 2000).

CHAPTER 3

Redshift space distortions

The large-scale structure provides a powerful tool to study many of the current issues in cosmology, such as to test gravity theories on large scales, to explore the dark sector and the origin of the accelerated expansion of the Universe, as well as it provides a probe to constrain alternative cosmological models. Over many decades, galaxy surveys have measured the position of these objects using different technologies that have been improved over the years. Nevertheless, the galaxy distances that contains cosmological information as shown in Chapter 2, are mostly obtained through their redshift, impacting the shape of the clustering signal.

3.1. Real and redshift space

Let us consider the case of a redshift survey where the position of each galaxy is expressed in terms of its angular position in the sky and its redshift, that is denoted in equatorial coordinates as Right Ascension (RA), Declination (DEC), and redshift z. The position of a galaxy in *real-space*, i.e. as a function of its actual distance, is then given by

$$\mathbf{r} = |\mathbf{r}|(\sin\theta\cos\phi,\ \ \sin\theta\sin\phi,\ \ \cos\theta), \tag{3.1}$$

which corresponds to a position in *redshift-space*, i.e. , as a function of its redshift, given by

$$\mathbf{s} = d_L(z)(\sin\theta\cos\phi,\ \ \sin\theta\sin\phi,\ \ \cos\theta), \tag{3.2}$$

with d_L being the luminosity distance as a function of the redshift as described by Eq. (2.24). This expression can be simplified in the low-redshift limit $z \ll 1$, where the Hubble relation is linear, so that $s = cz/H$, however it ignores the peculiar velocities of galaxies. Indeed, this is not completely exact because inhomogeneities in the matter density field induce galaxies to have peculiar velocities that distort the Hubble flow. Actually, the measured redshift has

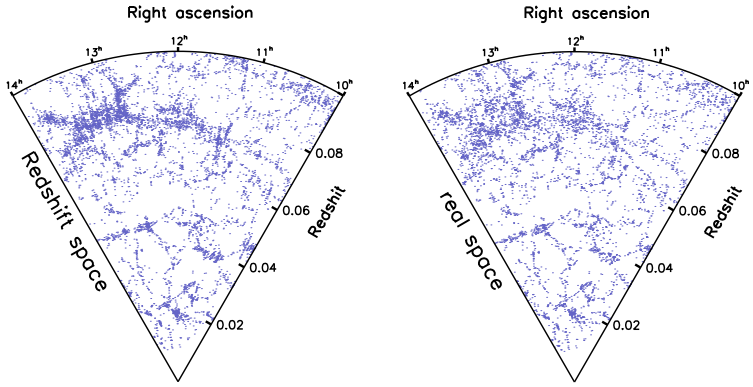

Figure 3.1: Representation of the redshift space distortions from a galaxy catalogue of the SDSS DR7 in a 4° slice with right ascensions in the range from $14^{\rm h}$ to $10^{\rm h}$ and with redshift $0.01 \leq z \leq 0.1$. The left panel shows the galaxy distribution in redshift-space, where the redshift space distortions can be appreciated a long the line-of-sight. The right panel shows the equivalent of the galaxy distribution in real-space. Figure taken from (Shi et al., 2016).

two contributions: the Hubble expansion velocity and the line-of-sight (LOS) projection of the peculiar velocity, so that $cz = Hr + \mathbf{v} \cdot \mathbf{r}$. Therefore, the interpretation of the distance as cz/H, contains the extra term $v/H \equiv \mathbf{v} \cdot \hat{\mathbf{r}}/H$ due to the peculiar velocity, in such a way, the redshift-space distortions can be understood as displacements of galaxies relative to their true positions in redshift-space when they have a peculiar velocity along the LOS of the observer. In terms of the measurements performed by spectroscopic surveys, it means, that they observe a combination of the density and velocity fields in *redshift-space*, where the observed redshift of an extragalactic source, z_{obs}, encloses the cosmological redshift, z_c, and the term related to the peculiar velocities along the LOS, as follows

$$z_{\rm obs} = z_c + (1 + z_c)\frac{\mathbf{v} \cdot \hat{\mathbf{r}}}{c}\,, \tag{3.3}$$

where $\hat{\mathbf{r}}$ is a unit vector along the LOS, so that the contribution of peculiar motions is given by $v_{\parallel} = \mathbf{v} \cdot \hat{\mathbf{r}}$. In fact, by taking into account the peculiar velocities, the positions in *redshift-space* appear distorted with respect to the ones in real-space (see Fig. 3.1), being described by the following relationship

$$\mathbf{s} = \mathbf{r} + (1 + z_c)\,\frac{v_{\parallel}}{H\,(z_c)}\hat{\mathbf{r}}. \tag{3.4}$$

This shift in the position causes the so-called redshift-space distortions (RSD), that can be appreciated in Fig. 3.1, where the spatial distribution of galaxies appears squashed and distorted when their positions are plotted in redshift-space rather than in real-space. Fig. 3.2 shows schematically how the RSD look like in redshift-space for a symmetric radial distribution of galaxies represented by dots. All galaxies in the real space (represented by the black circle) have the same total peculiar velocity and they are falling towards the center, such that for an observer the galaxies will appear, in redshift-space, with positions represented by the red ellipse due to the effect caused by peculiar velocities. Coherent infall

velocities of galaxies between the center of the distribution and the observer will add to the Hubble expansion, while velocities of galaxies behind the center of the density contrast will subtract from the Hubble flow. On large scales the distortion tends to be small because the gravitational pull is relatively weak, so the distribution appears squashed along the LOS, this result is called *Kaiser effect* (Kaiser, 1987). At smaller scales, the peculiar motions of galaxies can even surpass the Hubble flow velocity thus producing a smearing effect known as *Fingers of God* (FoG) (Jackson, 1972). There is an intermediate point between those regimes where the peculiar velocities are cancelled exactly out the Hubble flow velocity (Hamilton, 1998).

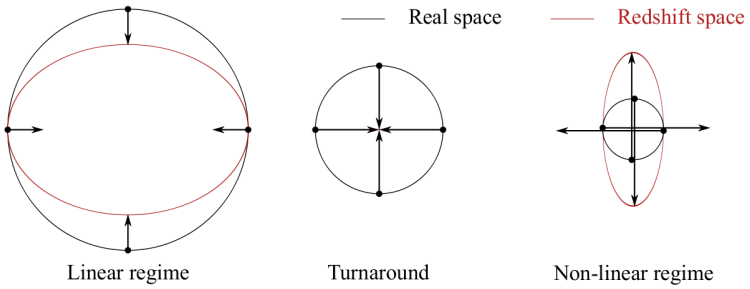

Figure 3.2: Schematic diagram showing how real-space structures look in redshift-space due to peculiar motions. In the linear regime, a spherical density contrast appears squashed along the line of sight. At smaller scales velocities tend to be larger appearing to be turned inside out. There is an intermediate point of turnaround where the density contrast shell appears collapsed (Marcondes, 2016).

The RSD have been used over the years as a powerful tool to constrain the growth factor $f(z)$, which is directly related to the mass density parameter Ω_m (e.g. Kaiser, 1987; Cole, Fisher, and Weinberg, 1995; Hamilton, Tegmark, and Padmanabhan, 2000; Peacock et al., 2001; Scoccimarro, 2004; Guzzo et al., 2008; Cabré and Gaztañaga, 2009; Blake et al., 2013b; Hawkins et al., 2003; Ross, Shanks, and Cruz da Ângela, 2007; da Ângela, Outram, and Shanks, 2005). Since the RSD destroy the statistical homogeneity (Hamilton, 1998), they were considered for a while, as a source of "noise" to be marginalized over (Seo and Eisenstein, 2003; Seo and Eisenstein, 2007), nevertheless, the interest on RSD grew rapidly when it was realized that they can constrain the cosmological parameters if not marginalized over (Amendola, Quercellini, and Giallongo, 2005; Guzzo et al., 2008; Zhang et al., 2008). Nowadays, RSD represent one of the most useful and promising techniques in cosmology to discriminate between dark energy (DE) scenarios and models based on modified gravity theories to explain the cosmic acceleration, being used in many investigations that involve forecasts (see e.g. Linder, 2008; Wang, 2008; Song and Percival, 2009) and galaxy clustering of several datasets (Cabré and Gaztañaga, 2009; Blake et al., 2011). Moreover, by modelling the clustering anisotropies derived from the RSD, it is possible to characterize the statistical properties of the LSS by constraining the linear growth rate of cosmic structures, as it has been shown successfully in many spectroscopic galaxy surveys (see e.g. Guzzo et al., 2014). In the last

few years, the RSD have also been used in different contexts, such as, constraining interacting dark energy models (Marulli, Baldi, and Moscardini, 2012; Costa et al., 2017), constraints on the neutrino mass in DE scenarios (Marulli et al., 2011; Upadhye, 2019), investigations on the effect of vector perturbations (Tansella et al., 2018; Bonvin et al., 2018) and baryons on RSD (Hellwing et al., 2016), RSD around cosmic voids (Hamaus et al., 2015; Cai et al., 2016; Hamaus et al., 2017), as well as in astrophysical scenarios as shown in (Ursino et al., 2011; Turner et al., 2017). Recently, the RSD have been exploited by first time to investigate the degeneracy between modified gravity and massive neutrinos (García-Farieta et al., 2019; Wright et al., 2019).

3.2. Clustering in redshift-space

Although the galaxy distribution in redshift-space induces a bias in the measurements derived from the density field, such as the power spectrum or the 2PCF, it also contains valuable information on the growth of cosmic structures as mentioned above. Indeed, the peculiar motions of galaxies, or tracers in general, are related to the gravitational collapse of density fluctuations, being influenced by the growth of the perturbations and changing the observed clustering signal. Regarding the linear perturbation theory, the effect of peculiar velocities does not change the number of galaxies, thus the number density conservation requires $\delta^s d^3s = \delta d^3r$, where the superscript s refers to the quantities in redshift-space. Taking into account the relation between the redshift position and real position, it implies that

$$\delta^s(\mathbf{s}) = [1 + \delta(\mathbf{r})] \left| \frac{d^3s}{d^3r} \right|^{-1} - 1. \tag{3.5}$$

This equation can be linearised by assuming that the separations are much smaller than the distances from the observer to the sources, i.e. $kr \gg 1$, which is commonly known as the plane-parallel approximation, being valid for many surveys that do not have a wide angular depth. This approximation simplifies the Jacobian of the coordinate transformation between real and redshift-space as follows

$$\left| \frac{d\mathbf{s}}{d\mathbf{r}} \right| = 1 - f\partial_\parallel u_\parallel, \tag{3.6}$$

where the velocity along the LOS of the observer has been normalized to $u_\parallel(\mathbf{r}) = -v_\parallel(\mathbf{r})/[faH(a)]$, being f the growth rate and H the Hubble parameter. In this framework, the velocity divergence field is defined as $\theta(\boldsymbol{r}) \equiv \nabla \cdot \boldsymbol{v}(\boldsymbol{r})$, such that the density contrast in redshift-space, Eq. (3.5), follows

$$\delta^s(\mathbf{s}) = \left[\delta(\boldsymbol{r}) + f\partial_\parallel^2 \Delta^{-1}\theta(\boldsymbol{r})\right] \left[1 - f\partial_\parallel^2 \Delta^{-1}\theta(\boldsymbol{r})\right]^{-1}, \tag{3.7}$$

where Δ denotes the Laplacian operator. If μ is the cosine of the angle between the line-of-sight and the wave vector $\mathbf{k}$ ($\mu = \cos\theta$, see Fig. 2.12), in Fourier

space the derivative of the Laplacian term takes the form

$$\partial_{\parallel}^2 \Delta^{-1} = \left(k_{\parallel}/k\right)^2 = \mu^2.$$

By replacing this expression in Eq. (3.7), the density contrast is equivalent to

$$\delta^s(k,\mu) = \int \frac{d^3s}{(2\pi)^3} e^{-i\boldsymbol{k}\cdot s}\delta^s(\boldsymbol{s}) = \int \frac{d^3\boldsymbol{x}}{(2\pi)^3} e^{-i\boldsymbol{k}\cdot\boldsymbol{r}} e^{-ik\mu f u_{\parallel}} \left[\delta(\boldsymbol{x}) + \mu^2 f\theta(\boldsymbol{x})\right]. \quad (3.8)$$

Finally, this expression can be written in terms of the power spectrum using the fact that $P(k) = \left\langle |\delta_{\mathbf{k}}|^2 \right\rangle$, as defined in the previous Chapter, allowing to recover the expression given in (Scoccimarro, Couchman, and Frieman, 1999), that is

$$P^s(k,\mu) = \int \frac{d^3\boldsymbol{r}}{(2\pi)^3} e^{-i\boldsymbol{k}\cdot\boldsymbol{r}} \left\langle e^{-ik\mu f\Delta u_{\parallel}} \times \left[\delta(\boldsymbol{x}) + \mu^2 f\theta(\boldsymbol{x})\right] \left[\delta\left(\boldsymbol{x}'\right) + \mu^2 f\theta\left(\boldsymbol{x}'\right)\right] \right\rangle, \quad (3.9)$$

where $\Delta u_{\parallel} = u_{\parallel}(\boldsymbol{x}) - u_{\parallel}\left(\boldsymbol{x}'\right)$ is the relative difference in the velocity field and $\boldsymbol{r} = \boldsymbol{x} - \boldsymbol{x}'$. This result makes evident the dependency of the signal from RSD on the non-linear density and the velocity field. Furthermore, as shown by (Scoccimarro, Couchman, and Frieman, 1999; Bernardeau et al., 2002), in a more general case, by considering the impact of the rotational term in the velocity field, which is quite important at smaller scales since it describes completely the clustering anisotropies of the density field at each separation, the result obtained previously can be generalized using only the plane-parallel approximation:

$$P^s(k,\mu) = \int \frac{d^3\boldsymbol{r}}{(2\pi)^3} e^{-i\boldsymbol{k}\cdot\boldsymbol{r}} \left\langle e^{-ik\mu f\Delta u_{\parallel}} \times \left[\delta(\boldsymbol{x}) + f\partial_{\parallel}u_{\parallel}\right] \left[\delta\left(\boldsymbol{x}'\right) + f\partial_{\parallel}u_{\parallel}\right] \right\rangle. \quad (3.10)$$

On the basis of the previous discussion, by assuming the distant observer approximation in linear regime, Kaiser (1987) showed that the power spectrum in redshift-space, $P^s(k,\mu)$, can be modelled in terms of the isotropic one in real-space, $P(k)$, by the following relation:

$$P^s(k,\mu) = \left(1 + 2f\mu^2 + f^2\mu^4\right) P(k), \quad (3.11a)$$

$$= \left(1 + f\mu^2\right)^2 P(k). \quad (3.11b)$$

Moreover, in the case of galaxies by considering a linear bias term so that $\delta_{\mathrm{g}} = b\delta$, the linear growth rate f in Eq. (3.11) can be replaced by a distortion parameter defined as $\beta \equiv f/b$, such that the redshift power spectrum is described by

$$P_g^s(k,\mu) = \left(1 + 2\beta\mu^2 + \beta^2\mu^4\right) b^2 P(k), \quad (3.12a)$$

$$= \left(1 + \beta\mu^2\right)^2 b^2 P(k), \quad (3.12b)$$

where $P_g^s(k,\mu)$ is the galaxy power spectrum in redshift-space and $P(k)$ is the

linear matter power spectrum in real-space. Note that the anisotropic term originates from the velocity and therefore it does not depend on the bias, this explains why the RSD measurements are often parametrized in terms of $f\sigma_8$. In order to examine how significant is the RSD correction, the redshift power spectrum can be expanded in the orthonormal basis of the Legendre polynomials, as shown by (Hamilton, 1992), such that

$$P^s(k,\mu) = \sum_\ell P_\ell(k)\mathcal{L}_\ell(\mu), \tag{3.13}$$

where $\mathcal{L}_\ell(\mu)$ is the Legendre polynomial of degree l, and each coefficient $P_l(k)$ corresponds to the l-th multipole moment obtained from the orthonormality condition as follows

$$P_\ell(k) = \frac{2\ell+1}{2}\int_{-1}^{1} d\mu P^s(k,\mu)\mathcal{L}_\ell(\mu). \tag{3.14}$$

Since the Kaiser formula, Eq. (3.12), contains terms only up to μ^4, only the monopole ($l=0$), quadrupole ($l=2$), and hexadecapole ($l=4$), moments are non-vanishing, (for details see e.g. , Percival and White, 2009), it reduces to

$$P(k,\mu) = P_0(k)\mathcal{L}_0(\mu) + P_2(k)\mathcal{L}_2(\mu) + P_4(k)\mathcal{L}_4(\mu)\ , \tag{3.15}$$

where, explicitly, the multipole moments are given by

$$P^s_{\ell=0}(k) = \left(1 + \frac{2}{3}\beta + \frac{1}{5}\beta^2\right) b^2 P(k) \tag{3.16}$$

$$P^s_{\ell=2}(k) = \left(\frac{4}{3}\beta + \frac{4}{7}\beta^2\right) b^2 P(k) \tag{3.17}$$

$$P^s_{\ell=4}(k) = \frac{8}{35}\beta^2 b^2 P(k). \tag{3.18}$$

The monopole moment can be understood as a spherical average in the k-space of the galaxy power spectrum, see Eq. (3.12), while the other multipole moments contributes to the anisotropic part of the power spectrum. Tab. 3.1 shows the functions to which the three first even Legendre polynomials correspond and their polar representation. In configuration space these equations can been obtained by computing the corresponding Fourier transform of the power spectrum (for a detailed description see e.g. , Kaiser, 1987; Lilje and Efstathiou, 1989; McGill, 1990; Hamilton, 1992; Fisher and Nusser, 1996). Thus, the 2PCF in redshift-space can be written as

$$\xi(s_\perp, s_\parallel)_{\rm lin} = \xi_0(s)\mathcal{L}_0(\mu) + \xi_2(s)\mathcal{L}_2(\mu) + \xi_4(s)\mathcal{L}_4(\mu)\ , \tag{3.19}$$

where $\mu = \cos\theta = s_\parallel/s$ and $s = \sqrt{s_\perp^2 + s_\parallel^2}$, furthermore the multipole moments of the correlation function can be expressed in terms of the multipole moments of the power spectrum, as shown by Eq. (3.14), such that

$$\xi_\ell(s) = \frac{i^\ell}{2\pi^2}\int P_l(k)\mathcal{L}_\ell(k) j_\ell(ks) k^2 dk, \tag{3.20}$$

$\mathcal{L}_0(\mu) = 1$	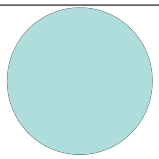
$\mathcal{L}_2(\mu) = \frac{1}{2}\left(3\mu^2 - 1\right)$	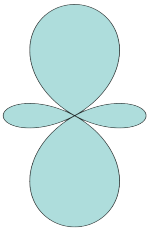
$\mathcal{L}_4(\mu) = \frac{1}{8}\left(35\mu^4 - 30\mu^2 + 3\right)$	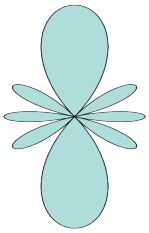

Table 3.1: Three first three even Legendre polynomials and their polar representation, where the radial coordinate is described by $r = \mathcal{L}_l(\mu)$ with $\mu = \cos\theta$.

where $j_l(ks)$ is the spherical Bessel function at l-th order; or to be computed from the full 2D 2PCF as

$$\xi_\ell(s) = \frac{2l+1}{2}\int_{-1}^{1} d\mu \xi(s,\mu)\mathcal{L}_l(\mu). \tag{3.21}$$

In their explicit form, the three first non-null multipole moments of $\xi(s_\perp, s_\parallel)$ can be written as follows:

$$\xi_0(s) = \left(1 + \frac{2\beta}{3} + \frac{\beta^2}{5}\right)\xi(r)\ , \tag{3.22}$$

$$\xi_2(s) = \left(\frac{4\beta}{3} + \frac{4\beta^2}{7}\right)\left[\xi(r) - \overline{\xi}(r)\right]\ , \tag{3.23}$$

$$\xi_4(s) = \frac{8\beta^2}{35}\left[\xi(r) + \frac{5}{2}\overline{\xi}(r)\ , -\frac{7}{2}\overline{\overline{\xi}}(r)\right], \tag{3.24}$$

where $\xi(r)$ is the real-space *undistorted* correlation function, and the *barred* functions are defined by

$$\overline{\xi}(r) \equiv \frac{3}{r^3}\int_0^r dr'\xi(r')r'^2\ , \tag{3.25}$$

$$\overline{\overline{\xi}}(r) \equiv \frac{5}{r^5}\int_0^r dr'\xi(r')r'^4\ . \tag{3.26}$$

Fig. 3.3 shows the RSD effects on the iso-correlation curves of the 2D two-point correlation function (2PCF) in the plane $(r_\perp, r_\parallel)$, where $r_\perp$ and $r_\parallel$ coordinates are respectively the perpendicular and parallel components along

the line-of-sight of the observer. The 2PCF has been computed from a N-body simulation, in real-space (*left panel*), and for the corresponding sample in redshift-space (*right panel*). The contours are draw at the iso-correlation levels $\xi(s_\perp, s_\parallel) = 0.3, 0.5, 1.0, 1.4, 2.2, 3.6, 7.2, 21.6$. In real-space the correlation function is undistorted, describing circular curves in this plane, as discussed in previous Section. In redshift-space (*left panel*), the effect caused by the RSD are clearly visible on small scales, where the 2PCF is stretched in the direction of $r_\parallel$ (Finger-of-God effect), and the infall effect on large scales, the contours are squashed along the perpendicular direction (Kaiser effect).

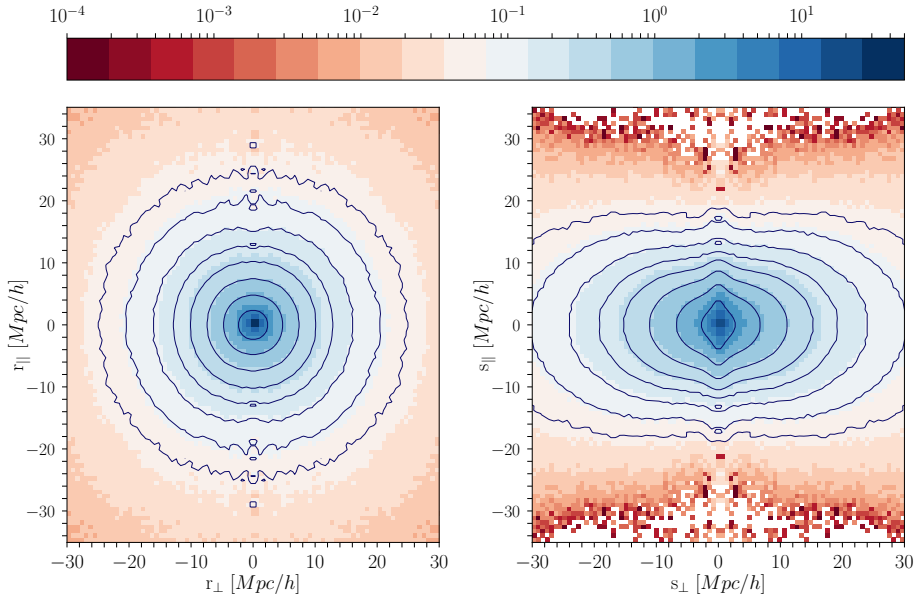

Figure 3.3: Contours of the 2D two-point correlation function (2PCF) in the plane $(r_\perp, r_\parallel)$, the $r_\perp$ and $r_\parallel$ coordinates are respectively the perpendicular and parallel components along the line-of-sight of the observer. The 2PCF has been computed from a N-body simulation, in real-space (*left panel*), and for the corresponding sample in redshift-space (*right panel*). The contours are draw at the iso-correlation levels $\xi(s_\perp, s_\parallel) = 0.3, 0.5, 1.0, 1.4, 2.2, 3.6, 7.2, 21.6$ as indicated by the color bar. Both the effect of redshift space distortions on small scales (Finger-of-God effect) and the infall effect at large scales (Kaiser effect) are clearly visible in the *left panel*. On small scales the 2PCF is stretched in the direction of $r_\parallel$, and on large scales the contours are squashed along the perpendicular direction.

Measuring independently the monopole and the quadrupole moments of the 2PCF, it is possible to get an estimation on the distortion parameter β. In particular two relationships can be defined, the first one by calculating the ratio of the monopole in redshift-space to the real-space correlation function $R(s)$, and the second one, by the quadrupole-to-monopole ratio $Q(s)$. By assuming

the linear regime, these quantities are given by

$$R(s) \equiv \frac{\xi_0(s)}{\xi_0(r)} = 1 + \frac{2\beta}{3} + \frac{\beta^2}{5}, \tag{3.27}$$

$$Q(s) \equiv \frac{\xi_2(s)}{\xi_0(s) - \frac{3}{s^3}\int_0^s ds'\xi(s')s'^2} = \frac{\frac{4}{3}\beta + \frac{4}{7}\beta^2}{1 + \frac{2\beta}{3} + \frac{\beta^2}{5}}, \tag{3.28}$$

where ξ_0 and ξ_2 are the monopole and quadrupole of the 2PCF, respectively, and β is the linear distortion parameter defined as $\beta \equiv f(z)/b(z)$.

An alternative description of the anisotropies in the correlation function is given by the clustering wedges, introduced by (Kazin, Sánchez, and Blanton, 2012), that correspond to the angle average of the $\xi(s_\perp, s_\parallel)$ over wide bins of μ. It can be interpreted as a projection of $\xi(s_\perp, s_\parallel)$ into wide bins of the LOS, expressed as

$$\xi_w(s) = \frac{1}{\Delta\mu}\int_{\mu_1}^{\mu_2} \xi(s,\mu)\mathrm{d}\mu, \tag{3.29}$$

being μ_1 and μ_2 the lower and upper limits of non-intersecting wedges, such that $\Delta\mu = \mu_2 - \mu_1$ is the wedge width. In this Thesis we will focus on two clustering wedges of $\Delta\mu = 0.5$, that in the literature are labelled as transverse wedge $\xi_\perp(s) \equiv \xi_{1/2}(0 \leq \mu \leq 0.5, s)$ and radial (or line-of-sight) wedge $\xi_\parallel(s) \equiv \xi_{1/2}(0.5 \leq \mu \leq 1, s)$ for the ranges $0 \leq \mu < 0.5$ and $0.5 \leq \mu \leq 1$, respectively.

From the definitions given in Eq. (3.29) and (3.19), clustering wedges are related to the multipole moments through the following relationship

$$\xi_w(r) = \sum_l \xi_l(s)\bar{L}_l, \tag{3.30}$$

with $\bar{L}_l$ being the average value of the Legendre polynomials over the interval $[\mu_1, \mu_2]$. Moreover, considering multipole contributions up $l = 2$ and wedges width $\Delta\mu = 0.5$, this relation can be expressed through the following transformation

$$\begin{pmatrix} \xi_\parallel \\ \xi_\perp \end{pmatrix} = \begin{pmatrix} 1 & \frac{3}{8} \\ 1 & -\frac{3}{8} \end{pmatrix} \begin{pmatrix} \xi_0 \\ \xi_2 \end{pmatrix}. \tag{3.31}$$

In real-space the two wedges, radial $\xi_\parallel$ and transverse $\xi_\perp$, are identical between them and equal to the monopole signal $\xi_0(r)$ because there are no distortions in any direction.

3.3. Redshift space distortions beyond Kaiser model

The Kaiser formula is a good description of the RSD only at very large scales, where non-linear effects can be neglected. Thus, with the aim of extracting information from the RSD signal at non-linear regime and considering the increasing

precision of recent and upcoming surveys, many more approaches have been proposed. There is a vast literature that shows the efforts to model the RSD beyond the linear Kaiser model, (for a review see by e.g. Scoccimarro, Couchman, and Frieman, 1999; Scoccimarro, 2004; Taruya, Nishimichi, and Saito, 2010; Reid and White, 2011), some of them making use of a phenomenological description of the velocity field, others instead, taking into account higher orders in perturbation theory since, in principle, there is no reason to stop at linear order. Other approaches do a combination of both frameworks. In the remaining part of this Section, three of the most important models that have provided a satisfactory representation of the redshift-space distortions in recent years are discussed.

■ Dispersion model (Peacock and Dodds, 1996): although the Kaiser formula reproduces the apparent enhancement of the clustering at large scales, it does not describe accurately the non-linear regime. Thus, it is possible to model the redshift-space 2PCF at small scales, extending the Kaiser formula, by adding a phenomenological damping factor that plays the role of a pairwise velocity distribution. It can account for both linear and non-linear dynamics. For convenience, the model is written in Fourier space knowing in advance that the 2PCF can be obtained by Fourier transforming, as follows

$$P^s(k,\mu) = D_{FoG}\left(k,\mu,\sigma_{12}\right)\left(1+\frac{f}{b}\mu^2\right)^2 b^2 P_{\delta\delta}(k), \tag{3.32}$$

where $D_{FoG}(k,\mu,\sigma_{12})$ is a damping factor, which depends on the σ_{12} parameter assumed to be scale-independent and usually can be interpreted as the dispersion in the pairwise random peculiar velocities. In particular, the damping factor has been described by Gaussian or Lorentzian distributions (Cole, Fisher, and Weinberg, 1995; Peacock and Dodds, 1996) since both have the same behaviour to first order, so that

$$D_{FoG}(k\,\mu,\sigma_{12}) = \begin{cases} e^{-k^2\mu^2\sigma_{12}^2}, \\ \frac{1}{1+k^2\mu^2\sigma_{12}^2}. \end{cases} \tag{3.33}$$

In configuration space, the redshift-space correlation function is expressed as the convolution of the linearly-distorted function with the distribution function of pairwise velocities $f(v)$, the latter is obtained by Fourier transform of Eq. (3.33), resulting

$$\xi(s_\perp, s_\parallel) = \int_{-\infty}^{\infty} dv f(v) \xi\left(s_\perp, s_\parallel - \frac{v(1+z)}{H(z)}\right)_{\rm lin}, \tag{3.34}$$

with the pairwise velocity v expressed in physical coordinates and $f(v)$ given by

$$f(v) = \begin{cases} \frac{1}{\sigma_{12}\sqrt{\pi}} \exp\left(-\frac{v^2}{\sigma_{12}^2}\right), \\ \frac{1}{\sigma_{12}\sqrt{2}} \exp\left(-\frac{\sqrt{2}|v|}{\sigma_{12}}\right). \end{cases} \tag{3.35}$$

Since the exact form of σ_{12}, and therefore of the damping factor, depends on several features of the galaxy population (Jing and Börner, 2004; Li et al., 2007), it is common in RSD analysis, to regard it as a free parameter that quantifies the cumulative effect of small scale random motions. The *dispersion model* can be also extended by replacing the linear power spectrum by its non-linear version computed from an analytic approximation, for example by using `HALOFIT` which is currently implemented in several codes like CAMB. By adopting the notation of this model presented in (Vargas-Magaña et al., 2018; Xu et al., 2012; Xu et al., 2013), the non-linear redshift-space power spectrum of matter density, $P(k,\ \mu)$, can be expressed as

$$P(k,\mu) = (1+\beta\mu^2)^2 D_{FoG}(k,\mu,\sigma_{12}) P_{\rm NL}(k). \tag{3.36}$$

■ Scoccimarro model: the previous models ignore the fact that the velocity divergence field θ deviates from linear theory on large scales, in this direction Scoccimarro (2004) proposed an extension of the matter power spectrum from linear theory. It considers the density and velocity divergence fields separately to account for the non-linear mode coupling between them in order to explain the mildly non-linear regime, moreover it consider an exponential pre-factor that can be decoupled from the Kaiser term, so that its impact on the clustering is limited only to small scales. Usually the exponential pre-factor can be replaced, without loss of generality, by a damping factor similar to the one already used in the dispersion model (Pezzotta et al., 2017), leading to

$$P^s(k,\mu) = D\left(k\mu\sigma_{12}\right)\left(b^2 P_{\delta\delta}(k) + 2fb\mu^2 P_{\delta\theta}(k) + f^2\mu^4 P_{\theta\theta}(k)\right), \tag{3.37}$$

where $P_{\delta\delta}$, $P_{\delta\theta}$ and $P_{\theta\theta}$ denote the auto-power spectrum of density, the cross-power spectrum and the velocity-divergence auto-spectrum, respectively. In Fourier space these power spectra are defined as

$$\langle\delta(\mathbf{k})\delta\left(\mathbf{k}'\right)\rangle \equiv (2\pi)^3\delta^D\left(\mathbf{k}+\mathbf{k}'\right) P_{\delta\delta}(k), \tag{3.38}$$

$$\langle\delta(\mathbf{k})\theta\left(\mathbf{k}'\right)\rangle \equiv (2\pi)^3\delta^D\left(\mathbf{k}+\mathbf{k}'\right) P_{\delta\theta}(k), \tag{3.39}$$

$$\langle\theta(\mathbf{k})\theta\left(\mathbf{k}'\right)\rangle \equiv (2\pi)^3\delta^D\left(\mathbf{k}+\mathbf{k}'\right) P_{\theta\theta}(k), \tag{3.40}$$

moreover, at scales close to linear-regime $P_{\delta\theta}$ and $P_{\theta\theta}$ tend to $P_{\delta\delta}$.

■ TNS model: even considering the contribution of the velocity divergence, there are strong bias dependences in the shape of the redshift space correlation function as shown by (Reid and White, 2011). Taruya, Nishimichi, and Saito (2010) proposed a model on the basis of the cosmological perturbation theory (hereafter PT), that besides taking into account the non-linear mode coupling between the density and velocity divergence fields, involves additional terms to correct systematics at small scales. For this model the power spectrum is

written as follows

$$P^s(k,\mu) = D(k\mu\sigma_{12})\Big(b^2 P_{\delta\delta}(k) + 2fb\mu^2 P_{\delta\theta}(k) + f^2\mu^4 P_{\theta\theta}(k) + \\ + C_A(k,\mu,f,b) + C_B(k,\mu,f,b)\Big). \tag{3.41}$$

In general, the $P_{\delta\delta}$, $P_{\delta\theta}$ and $P_{\theta\theta}$ terms can be computed from perturbation theory (Eulerian, Lagrangian or Time renormalization), but also from fitting formulae (see e.g. Jennings, 2012; Pezzotta et al., 2017; Bel et al., 2019). In this Thesis we adopt the full description given by the standard perturbation theory (SPT), that consists of expanding the statistics of interest as a sum of infinite terms, where every term corresponds to a n-loop correction. We consider corrections up 1-loop order, where the power spectrum is written as Eq. (3.42).

$$P^{\rm SPT}(k) = P^{(0)}(k) + P^{(1)}(k) = P^{(0)}(k) + 2P_{13}(k) + P_{22}(k). \tag{3.42}$$

It is well known that the 0-loop correction term in SPT corresponds to the linear power spectrum, $P^{(0)}(k) = P_{lin}(k)$, whereas the 1-loop term is expressed as a sum of 2 different terms $P_{13}(k)$ and $P_{22}(k)$. For a detailed description on the perturbation theory approach for the power spectrum for massive haloes in redshift space see e.g., Gil-Marín et al. (2012). Following Taruya, Nishimichi, and Saito (2010) and de la Torre and Guzzo (2012), we can express the corrections terms derived from SPT of the TNS model, C_A and C_B, in terms of the basic quantities of the density δ and of the velocity divergence $\theta(\mathbf{k}) \equiv [-i\mathbf{k}\cdot\mathbf{v}(\mathbf{k})]/[af(a)H(a)]$, specifically they are rewritten as

$$C_A(k,\mu) = (k\mu f)\int \frac{d^3\boldsymbol{p}}{(2\pi)^3}\frac{p_z}{p^2} \\ \times [B_\sigma(\boldsymbol{p},\boldsymbol{k}-\boldsymbol{p},-\boldsymbol{k}) - B_\sigma(\boldsymbol{p},\boldsymbol{k},-\boldsymbol{k}-\boldsymbol{p})] \tag{3.43}$$

$$C_B(k,\mu) = (k\mu f)^2\int \frac{d^3\boldsymbol{p}}{(2\pi)^3}F(\boldsymbol{p})F(\boldsymbol{k}-\boldsymbol{p}) \tag{3.44}$$

$$F(\boldsymbol{p}) = \frac{p_z}{p^2}\left[P_{\delta\theta}(p) + f\frac{p_z^2}{p^2}P_{\theta\theta}(p)\right] \tag{3.45}$$

where B_σ is the cross-bispectrum defined by

$$\left\langle \theta(\boldsymbol{k}_1)\left\{\delta(\boldsymbol{k}_2) + f\frac{k_{2z}^2}{k_2^2}\theta(\boldsymbol{k}_2)\right\}\left\{\delta(\boldsymbol{k}_3) + f\frac{k_{3z}^2}{k_3^2}\theta(\boldsymbol{k}_3)\right\}\right\rangle \\ = (2\pi)^3\delta_D(\boldsymbol{k}_1+\boldsymbol{k}_2+\boldsymbol{k}_3)\,B_\sigma(\boldsymbol{k}_1,\boldsymbol{k}_2,\boldsymbol{k}_3)\,. \tag{3.46}$$

Note that the C_A and C_B terms are proportional to b^3 and b^4, respectively, actually they can be re-written as a power series expansion of b, f and μ and their respective contributions to the total power spectrum. For a detailed explanation about perturbation theory calculations for these correction terms see the appendix A of (Taruya, Nishimichi, and Saito, 2010), and for what concern the correlation functions and the dependence of the spatial bias of the

considered tracers see appendix A of (de la Torre and Guzzo, 2012).

CHAPTER 4

Constraints on Dynamical Dark Energy models

As mentioned above, in the ΛCDM model DM is composed by collisionless non baryonic particles and DE is described in terms of the cosmological constant Λ, traditionally presented as responsible of the present cosmic acceleration, with an EoS $w = -1$. The predictions made by this model reproduce remarkably well the observations of the anisotropies in the Cosmic Microwave Background (CMB) radiation, baryonic acoustic oscillations (BAO), Supernovae Ia (SNIa), etc. Although this framework offers a simple description of the LSS in terms of few free parameters, the dark sector (DM and DE) remains not well understood both from the theoretical and the observational points of view (Frieman, Turner, and Huterer, 2008; Albrecht et al., 2006). Currently no direct detection of a dark matter particle has been achieved, and the theoretical basis of the observed cosmological constant is not clearly established, especially with respect to the issue of gravitational effects of quantum vacuum energy (Tutusaus et al., 2016). The lack of a full comprehension of the fundamental nature of these two components has demanded to further test the GR to understand if it is the effective theory of gravity at large scales, and consequently to get a complete cosmological model that explains fully the astrophysical and cosmological observations at those scales (Martino, De Laurentis, and Capozziello, 2015).

The coincidence problem is one out of many theoretical arguments against a cosmological constant. It is related to the order of magnitude of DE and DM densities in the current era, i.e., $\Omega_m \sim \Omega_\Lambda$. A second issue is associated with the required fine tuning of the value of Λ, which is quite far from particle physics predictions (Weinberg, 1989; Copeland, Sami, and Tsujikawa, 2006). To alleviate these tensions, different DE models with dynamical EoS have been proposed in literature (Frieman, Turner, and Huterer, 2008). The Chevallier-Polarski-Linder (CPL) is one of the most popular parametrizations of the EoS (Chevallier and Polarski, 2001; Linder, 2003). Another alternative is to include

a scalar field that mimics the DE component, such as quintessence (Caldwell, Dave, and Steinhardt, 1998; Ratra and Peebles, 1988), phantom (Caldwell, 2002; Chiba, Okabe, and Yamaguchi, 2000; Parker and Raval, 1999), quintom (Xu and Zhang, 2016) and k-essence fields (Armendariz-Picon, Mukhanov, and Steinhardt, 2000; Armendariz-Picon, Mukhanov, and Steinhardt, 2001; Chiba, Okabe, and Yamaguchi, 2000). Besides these models, more ambitious proposals have been done by considering interactions between DE and DM. Some of these alternatives are the so-called Interacting Dark Energy (IDE) (Caldera-Cabral, Maartens, and Ureña-López, 2009), Early Dark Energy (EDE) (Doran and Robbers, 2006; Pettorino, Amendola, and Wetterich, 2013; Poulin et al., 2019), the Holographic DE (HolDE) (Cohen, Kaplan, and Nelson, 1999; Susskind, 1995; 't Hooft, 1993; 't Hooft, 2001; Zhang, Li, and Noh, 2010), modified gravity (MG) (Dvali, Gabadadze, and Porrati, 2000) and Braneworld models (García-Aspeitia, Magaña, and Matos, 2012). A typical classification of the cosmological models is done in terms of the value assumed by the EoS, so that, models are considered as phantom if EoS $w < -1$, or quintessence if $w > -1$. In the first case a fluid multicomponent is required with at least one phantom constituent, which has been shown to suffer serious theoretical problems, and in the second case, general relativity needs to be extended to a more general theory at cosmological scales (Nesseris and Perivolaropoulos, 2007).

In this Chapter we constrain the main set of parameters in some of the well established models of DE by combining recent observational data from CMB, BAO and growth rate of LSS. These original results are based on our research (Bonilla and García-Farieta, 2019). In order to discern which one of the DE models considered is the most favoured by current observations, we have used statistical tools like the Akaike and Bayesian Information Criteria (Shi, Huang, and Lu, 2012; Akaike, 1974; Schwarz, 1978), to indicate the level of agreement with the observational data taking into account the number of free parameters and the data points of each model. Data from SNIa, CMB and BAO have been used to determine $H(z)$ directly through the redshift dependence with cosmological distances, e.g. by the angular diameter distance $d_A(z)$. A dynamical test, has been also implemented using the linear growth factor of matter density perturbations $D(a)$, that can be obtained from the redshift distortion parameter from redshift surveys $[A(z) \equiv f(z)\sigma_8(z)]$.

4.1. The cosmological tests

In the following Sections we present the details about the observational datasets and the methodology employed. In order to do a forecast on the main set of parameters of each cosmological model (ΛCDM , wCDM, CPL, IDE and EDE), we implement a Bayesian analysis taking into account the following data: the CMB by using the so-called *shift parameter* R, which is related to the position of the first acoustic peak in the power spectrum of the temperature anisotropies; the baryon acoustic oscillations (BAO), by a combination of the radial and angular signal that defines the Distance Ratio Scale $D_v(z)/r_s$, being

$D_v(z)$ the so-called dilation scale and r_s the comoving sound horizon[1]; and the growth rate of LSS through Growth Parameter $A(z) \equiv f(z)\sigma_8(z)$.

4.1.1. CMB data

From the CMB information provided by the Planck satellite final release (Planck Collaboration et al., 2018c), it is possible to explore the early stages of the expansion history in each model considered here. A useful test to achieve this is given by the angular scale of sound horizon at decoupling time ($z_{cmb} \approx 1090$), which is encoded in the location of the first acoustic peak of the CMB power spectrum. Following (Chen, Huang, and Wang, 2019), the χ^2 for the CMB data is constructed as

$$\chi^2_{CMB} = X^T_{Planck18} C^{-1}_{cmb} X_{Planck18}, \tag{4.1}$$

such that

$$X_{Planck18} = \begin{pmatrix} R - 1.7502 \\ l_A - 301.471 \\ \omega_b - 0.02236 \end{pmatrix}, \tag{4.2}$$

where $\omega_b = \Omega_b h^2$ is the physical baryon density parameter. The acoustic scale l_A is defined in terms of the angular diameter distance $d_A(z_{cmb})$ as

$$l_A = \frac{\pi d_A(z_{cmb})(1 + z_{cmb})}{r_s(z_{cmb})}, \tag{4.3}$$

where z_{cmb} corresponds to the redshift at decoupling time given by (Hu and Sugiyama, 1996),

$$z_{cmb} = 1048[1 + 0.00124(\Omega_b h^2)^{-0.738}][1 + g_1(\Omega_m h^2)^{g_2}], \tag{4.4}$$

$$g_1 = \frac{0.0783(\Omega_b h^2)^{-0.238}}{1 + 39.5(\Omega_b h^2)^{0.763}}, \quad g_2 = \frac{0.560}{1 + 21.1(\Omega_b h^2)^{1.81}}. \tag{4.5}$$

The shift parameter R is defined as follows (Bond, Efstathiou, and Tegmark, 1997):

$$R = \frac{\sqrt{\Omega_m}}{c} d_A(z_{cmb})(1 + z_{cmb}). \tag{4.6}$$

The inverse of the covariance matrix for (R, l_A, ω_b), denoted as C^{-1}_{cmb} in Eq. (4.1), takes the form $C^{-1}_{cmb^{Planck18}} = \sigma_i \sigma_j C_{NorCov_{i,j}}$ by assuming Planck 2018 data, where $\sigma_i = (0.0046, 0.090, 0.00015)$ contributes with three data points to the statistical analysis, so that the normalised covariance matrix is given by (Chen, Huang,

[1]The BAO feature in the LSS correlation function is the consequence of acoustic waves in the pre-recombination baryon-photon plasma, caused by the opposing forces of gravity and radiation pressure (Peebles and Yu, 1970). The sound horizon r_s is related to the distance between the wavefront of the acoustic waves after decoupling between baryons and photons, while the dilation scale $D_v(z)$ can be understood as an angle-weighted average of $D_A(z)$ and $D_H(z)$, which is the best determined quantity in measurements of BAO from galaxy surveys.

and Wang, 2019) as follows:

$$C_{NorCov_{i,j}} = \begin{pmatrix} 1.00 & 0.46 & -0.66 \\ 0.46 & 1.00 & -0.37 \\ -0.66 & -0.33 & 1.00 \end{pmatrix}. \tag{4.7}$$

4.1.2. BAO data

A remarkable feature that appears in the large-scale correlation function measured from several galaxy surveys (e.g. 2dF, SDSS, WiggleZ, 6dF, etc), is the BAO scale represented as a hump in the 2PCF at a distance around $100h^{-1}Mpc$ in comoving coordinates, or equivalently in Fourier space as a series of decaying wiggles in the matter power spectrum (Cole et al., 2005; Eisenstein et al., 2005). As mentioned earlier, the BAO correspond to fluctuations in the density field, as expanding acoustic waves, imprinted in the primordial plasma before the matter-radiation decoupling; they have been widely used as standard rule to characterize the properties of DE (Bassett and Hlozek, 2010; White, 2005). In order to set constraints on dynamical dark energy models, we consider data from WiggleZ, SDSS-MGS, SDSS-BOSS LOWZ, SDSS BOSS-Ly$_\alpha$, 6dF, which leads to a total of effective measurements of 12 data points and whose χ^2 is given by

$$\begin{aligned}\chi^2_{BAO} = \chi^2_{WiggleZ} + \chi^2_{SDSS} + \chi^2_{6dF} + \chi^2_{SDSS-MGS} + \chi^2_{BOSS-LOWZ} \\ +\chi^2_{BOSS-Ly_\alpha}.\end{aligned} \tag{4.8}$$

Now we describe each one of these contributions. Following (Blake et al., 2011), the WiggleZ BAO data is given by

$$\chi^2_{WiggleZ} = (\bar{A}_{obs} - \bar{A}_{th})C^{-1}_{WiggleZ}(\bar{A}_{obs} - \bar{A}_{th})^T, \tag{4.9}$$

where $\bar{A}_{obs} = (0.447, 0.442, 0.424)$ is the data vector at $z = (0.44, 0.60, 0.73)$ and $\bar{A}_{th}(z, \Theta^m_i)$ is the theoretical prediction given by Eisenstein et al. (2005) at redshift z for a set of cosmological parameters Θ^m_i in each model m, with

$$\bar{A}_{th} = D_V(z)\frac{\sqrt{\Omega_m H_0^2}}{cz}, \tag{4.10}$$

assuming the distance scale $D_V(z)$ defined traditionally as

$$D_V(z) = \frac{1}{H_0}\left[(1+z)^2 d_A(z)^2 \frac{cz}{E(z)}\right]^{1/3}. \tag{4.11}$$

Moreover, the inverse covariance matrix $C^{-1}_{WiggleZ}$ for the WiggleZ dataset is given by

$$C^{-1}_{WiggleZ} = \begin{pmatrix} 1040.3 & -807.5 & 336.8 \\ -807.5 & 3720.3 & -1551.9 \\ 336.8 & -1551.9 & 2914.9 \end{pmatrix}. \tag{4.12}$$

Similarly, the SDSS DR7 - BAO distance measurements contributes to the total χ^2 as (Percival et al., 2010)

$$\chi^2_{SDSS} = (\bar{d}_{obs} - \bar{d}_{th}) C^{-1}_{SDSS} (\bar{d}_{obs} - \bar{d}_{th})^T, \tag{4.13}$$

where $\bar{d}_{obs} = (0.1905, 0.1097)$ is measured at $z = 0.2$ and $z = 0.35$, whereas $\bar{d}_{th}(z, \Theta^m_i)$ denotes the distance ratio

$$\bar{d}_{th} = \frac{r_s(z_{drag})}{D_V(z)}, \tag{4.14}$$

being z_{drag} the redshift at the baryon drag epoch[2] and $r_s(z)$ the comoving sound horizon given by

$$r_s(z) = c \int_z^\infty \frac{c_s(z')}{H(z')} dz', \tag{4.15}$$

and $c_s(z)$ is the sound speed

$$c_s(z) = \frac{1}{\sqrt{3(1 + \bar{R}_b/(1+z))}}, \tag{4.16}$$

where $\bar{R}_b$ is defined in terms of the fractional energy densities of baryons and photons at the present-day, so that $\bar{R}_b \equiv 3\Omega_{b0}/4\Omega_{\gamma 0} = 31500 \Omega_b h^2 (T_{CMB}/2.7\text{K})^{-4}$ and $T_{CMB} = 2.726K$ is the today's CMB temperature. The redshift z_{drag} at the baryon drag epoch is fitted using the Eisenstein and Hu (1998) formula as

$$z_{drag} = \frac{1291(\Omega_m h^2)^{0.251}}{1 + 0.659(\Omega_m h^2)^{0.828}} [1 + b_1 (\Omega_b h^2)^{b_2}], \tag{4.17}$$

where $b_1 = 0.313(\Omega_m h^2)^{-0.419}[1 + 0.607(\Omega_m h^2)^{0.674}]$ and $b_2 = 0.238(\Omega_m h^2)^{0.223}$. For the SDSS dataset, the inverse of the covariance matrix C^{-1}_{SDSS} is given by

$$C^{-1}_{SDSS} = \begin{pmatrix} 30124 & -17227 \\ -17227 & 86977 \end{pmatrix}. \tag{4.18}$$

The 6dFGS - BAO data (Beutler et al., 2011), contributes to the analysis with only one point at $z = 0.106$, so that the χ^2 is computed by

$$\chi^2_{6dFGS} = \left(\frac{d_{th} - 0.336}{0.015} \right)^2. \tag{4.19}$$

To complement the analysis, we have included measurements from the Main Galaxy Sample of Data Release 7 of Sloan Digital Sky Survey (SDSS-MGS) (Anderson et al., 2014) ($r_s/D_V(0.57) = 0.0732 \pm 0.0012$), the LOWZ and CMASS galaxy samples of the Baryon Oscillation Spectroscopic Survey (BOSS) (Anderson et al., 2014) ($D_V/r_s(0.32) = 8.47 \pm 0.17$), the distribution of the LymanForest

[2]The drag epoch is defined as the time, when the recombination process occurs, at which baryons are released from the Compton drag of the photons in terms of a weighted integral over the Thomson scattering.

in BOSS (BOSS - Ly_α) (Font-Ribera et al., 2014) ($D_A/r_s(2.36) = 10.08 \pm 0.4$) and BOSS DR12 galaxy sample ($D_V/r_s(0.38) = 1477 \pm 16$, $D_V/r_s(0.51) = 1877 \pm 19$, $D_V/r_s(0.61) = 2140 \pm 22$).

4.1.3. Growth Rate of LSS

Following the description given in Chapter §2 on perturbation theory and structure formation, we characterize the growth of the structures by using the linear structure growth factor $D(a)$, obtained numerically from Eq. (2.52) (Nesseris et al., 2011; Uzan, 2006; Stabenau and Jain, 2006)

$$\ddot{D} + 2H(z)\dot{D} - \frac{3}{2}\Omega_{m,0}H_0^2(1+z)^3 D = 0.. \tag{2.52}$$

The observational estimates on the growth rate $f(z)$ can be obtained from the linear growth factor $D(z)$, where by convention we define the parameter $A(z) \equiv f(z)\sigma_8(z)$ to constrain cosmological models by minimizing

$$\chi^2_G = \sum_{i=1}^{n} \frac{(A(z) - A_{obs}(z_i))^2}{\sigma_i^2}, \tag{4.20}$$

where the subscript G refers to the growth rate measurements, $\sigma_8(z)$ to the RMS mass fluctuation on spheres of $8Mpch^{-1}$ and $A_{obs}(z_i)$ to the observed growth parameter with measurement error σ_i, that includes the Alcock-Paczynski effect [3] in redshift-space distortions. Since $\sigma_8(z) = \sigma_8^0 D(z)/D(0)$, we adopt σ_8^0 as free parameter in our analysis. The growth parameter data have been obtained from the following projects: PSCz, 2dF, VIPERS, SDSS, 2MASS, GAMA, WiggleZ and FastSound galaxy surveys. The Tab. 4.1 displays the complete dataset of the observed growth parameter and the corresponding references.

In addition, the Supernovae data (SNIa) from the project Union2.1 (Suzuki et al., 2012) and also information from the Observational Hubble Parameter Data (OHD) (Meng et al., 2015) have been included to complement our analysis. The Union 2.1 compilation is part of The Union2.1 Supernova Cosmology Project (Suzuki et al., 2012), which contains a sample of 833 SNIa, of which 580 pass usability cuts. The luminosity distance is obtained by the relationship $d_L(z) = (1+z)^2 d_A(z)$ [see Eq. (2.24)], and it is fitted to a cosmological model by minimizing the χ^2 function, that by convenience has been expanded up quadratic terms (for a detailed description on this method see e.g. Nesseris and Perivolaropoulos, 2005), such as

$$\chi^2_{SNIa} = \mathsf{A} - \frac{\mathsf{B}^2}{\mathsf{C}} \tag{4.21}$$

[3] The Alcock-Paczynski (AP) effect consists in the apparent distortion of the clustering when the distances are derived from a wrong cosmological model. The Alcock-Paczynski test is a method of determining the geometry of the universe despite this effect, by adjusting the cosmological model to ensure that angular and radial clustering match constrains.

Index	z	$A_{obs}(z_i)$	Refs.
1	0.02	0.360 ± 0.040	(Hudson and Turnbull, 2012)
2	0.067	0.423 ± 0.055	(Beutler et al., 2012)
3	0.17	0.510 ± 0.060	(Percival, 2004b; Song and Percival, 2009)
4	0.18	0.360 ± 0.090	(Blake, 2013a)
5	0.25	0.351 ± 0.058	(Samushia, Percival, and Raccanelli, 2012)
6	0.37	0.460 ± 0.038	(Samushia, Percival, and Raccanelli, 2012)
7	0.38	0.440 ± 0.060	(Blake et al., 2013b)
8	0.41	0.450 ± 0.040	(Blake et al., 2011)
9	0.60	0.550 ± 0.120	(Pezzotta et al., 2017)
10	0.60	0.430 ± 0.040	(Blake et al., 2011)
11	0.78	0.380 ± 0.040	(Blake et al., 2011)
12	0.57	0.427 ± 0.066	(Reid et al., 2012)
13	0.30	0.407 ± 0.055	(Tojeiro et al., 2012)
14	0.40	0.419 ± 0.041	(Tojeiro et al., 2012)
15	0.50	0.427 ± 0.043	(Tojeiro et al., 2012)
16	0.60	0.433 ± 0.067	(Tojeiro et al., 2012)
17	0.86	0.400 ± 0.110	(Pezzotta et al., 2017)
18	1,40	0.484 ± 0.116	(Okumura et al., 2016)

Table 4.1: Summary of the observed growth rate measurements and their corresponding references.

where

$$\mathsf{A} = \sum_{i=1}^{580} \frac{[\mu_{th}(z_i, \Theta_i^m) - \mu_{obs}(z_i)]^2}{\sigma_{\mu_i}^2},$$

$$\mathsf{B} = \sum_{i=1}^{580} \frac{\mu_{th}(z_i, \Theta_i^m) - \mu_{obs}(z_i)}{\sigma_{\mu_i}^2}, \tag{4.22}$$

$$\mathsf{C} = \sum_{i=1}^{580} \frac{1}{\sigma_{\mu_i}^2},$$

with $\mu(z) \equiv 5\log_{10}[d_L(z)/Mpc] + 25$ being the theoretical expectation of the distance modulus, and we have marginalized over the nuisance parameter μ_{obs}.

Regarding the Hubble parameter, it has been used widely in literature together with other probes to constrain the cosmic growth and expansion history of the Universe and to test gravity (see e.g. Moresco and Marulli, 2017; Linder, 2017). In our analysis, the observational Hubble parameter data (OHD) used to constrain the free parameters of the models under consideration, it have been obtained by considering that the differential evolution of early type passive galaxies provides model-independent information about the Hubble parameter $H(z)$ from direct observations. We used 36 OHD in the redshift range

$0.0708 \leq z \leq 2.36$, obtained from (Meng et al., 2015), where 26 of them are deduced from the differential age method, and the remaining 10 belong to the radial BAO method. Other constraints on the Hubble parameter can be found in (Moresco, 2015; Moresco et al., 2016). The corresponding χ^2 is given by

$$\chi^2_{H(z)}(H_0, \Theta_i^m) = \sum_{i=1}^{36} \frac{[H_{obs}(z_i) - H_{th}(z_i, H_0, \Theta_i^m)]^2}{\sigma_H^2(z_i)}, \tag{4.23}$$

where $H_{th}(z_i, H_0, \Theta_i^m)$ is the theoretical expectation on the Hubble parameter at redshift z_i. To marginalize over H_0, we assume a Gaussian prior distribution, in such a way the posterior likelihood function $\mathcal{L}_H(\Theta_i^m)$ depends only of the free parameters Θ_i^m, as

$$\mathcal{L}_H(\Theta_i^m) = \int \pi_H(H_0) exp\left[-\chi^2_H(H_0, \Theta_i^m)\right] dH_0, \tag{4.24}$$

where

$$\pi_H(H_0) = \frac{1}{\sqrt{2\pi}\sigma_{H_0}} exp\left[-\frac{1}{2}\left(\frac{H_0 - \bar{H}_0}{\sigma_{H_0}}\right)^2\right], \tag{4.25}$$

is a prior probability function widely used in the literature. Finally, we minimize $\chi^2_{H(z)}(\Theta_i^m) = -2\ln \mathcal{L}_H(\Theta_i^m)$ with respect to the free parameters Θ_i^m to obtain the best-fit model.

4.2. Methodology

In order to get the best-fit values of the free parameters for a given dark energy model, a Bayesian analysis is performed by minimizing the negative log-likelihood for the vector of parameters Θ_i^m. Since the likelihood $\mathcal{L}$ has a Gaussian error distribution (Andrae, Schulze-Hartung, and Melchior, 2010), the minimized χ^2 can be expressed as

$$\chi^2_{min}(\Theta_i^m) = -2\ln \mathcal{L}_{max}(\Theta_i^m), \tag{4.26}$$

that by combining the different observational datasets and by considering the properties of χ^2, the final constraint of parameters is obtained from the total posterior distribution, such as

$$\chi^2_{min} = \chi^2_{CMB} + \chi^2_{BAO} + \chi^2_G + \chi^2_{SNIa} + \chi^2_{H(z)}. \tag{4.27}$$

The uncertainties are computed by using the Fisher matrix formalism, which is widely used to constrain the parameter space from joint analysis (Albrecht et al., 2009; Wolz et al., 2012). The coefficients of the Fisher matrix encode the Gaussian uncertainties of the parameters Θ_i^m, being computed in terms of the best-fit χ^2_{min} as

$$F_{ij} = \frac{1}{2}\frac{\partial^2 \chi^2_{min}}{\partial\Theta_i \partial\Theta_j}, \tag{4.28}$$

where Θ_i and Θ_j are the set of free parameters in each model. In its extended form the Fisher matrix is given by

$$[F] = \frac{1}{2}\begin{bmatrix} \frac{\partial^2}{\partial\Theta_1^2} & \frac{\partial^2}{\partial\Theta_1\partial\Theta_2} & \cdot & \cdot & \cdot & \frac{\partial^2}{\partial\Theta_1\partial\Theta_n} \\ \frac{\partial^2}{\partial\Theta_2\partial\Theta_1} & \frac{\partial^2}{\partial\Theta_2^2} & \cdot & \cdot & \cdot & \frac{\partial^2}{\partial\Theta_2\partial\Theta_n} \\ \cdot & \cdot & \cdot & & & \cdot \\ \cdot & \cdot & & \cdot & & \cdot \\ \cdot & \cdot & & & \cdot & \cdot \\ \frac{\partial^2}{\partial\Theta_n\partial\Theta_1} & \frac{\partial^2}{\partial\Theta_n\partial\Theta_2} & \cdot & \cdot & \cdot & \frac{\partial^2}{\partial\Theta_n^2} \end{bmatrix} \chi^2_{min}(\Theta_1, \Theta_2, ..., \Theta_n). \tag{4.29}$$

On the other hand, the covariance matrix C_{cov} corresponds to the inverse of the Fisher matrix, see Eq. (4.30), where its coefficients σ_i and σ_j are the uncertainties related to each parameter Θ_i^m and Θ_j^m, with 1σ of statistical confidence. The uncertainties are obtained as $\sigma_i = \sqrt{Diag\,[C_{cov}]_{ij}}$.

$$[C_{cov}] = [F]^{-1} = \begin{bmatrix} \sigma_1^2 & \sigma_{12} & \cdot & \cdot & \cdot & \sigma_{1n} \\ \sigma_{21} & \sigma_2^2 & \cdot & \cdot & \cdot & \sigma_{2n} \\ \cdot & \cdot & \cdot & & & \cdot \\ \cdot & \cdot & & \cdot & & \cdot \\ \cdot & \cdot & & & \cdot & \cdot \\ \sigma_{n1} & \sigma_{n2} & \cdot & \cdot & \cdot & \sigma_n^2 \end{bmatrix}. \tag{4.30}$$

After obtaining tight constraints on the set of parameters in each model, we applied two criteria to discern among them, which model is the most favoured by the observations. The best-fit results are compared by using the Akaike information criterion (AIC), (Akaike, 1974) and the Bayesian Information Criterion (BIC)(Schwarz, 1978), both of them allow to compare cosmological models considering the degrees of freedom, with respect to the observational evidence and the set of parameters used (Liddle, 2004). The AIC and BIC criteria can be computed as

$$AIC = -2\ln\mathcal{L}_{max} + 2k, \tag{4.31}$$

$$BIC = -2\ln\mathcal{L}_{max} + k\ln N, \tag{4.32}$$

where $\mathcal{L}_{max}$ is the maximum likelihood and k is the number of parameters of the model in consideration. Since the BIC criterion takes into account the number of data points N used in the fit, it imposes a strict penalty against extra parameters for any set of data $\ln N > 2$. Thus, the most favoured model corresponds to the one that minimizes AIC and BIC, that is easy to check by calculating their relative values among the different models, instead of their absolute values. Therefore the weight of the evidence can be quantified by $\Delta AIC_i = AIC_i - AIC_{min}$ and $\Delta BIC_i = BIC_i - BIC_{min}$, where the subindex i runs over the models and AIC_{min} (BIC_{min}) is the lowest value of the corresponding criterion among all the models (Anderson and Burnham, 2004; Kass and Raftery, 1995). Tabs. 4.2 and 4.3 summarize the convention adopted by each criterion in terms of their relative difference. In the analysis we have considered a total of $N = 639$ data points from independent cosmological probes: CMB (3), BAO (12), G (18),

SNIa (580), $H(z)$ (36). In next Section the main results obtained for each model are presented, with a comparative analysis based on the AIC and BIC criteria that display the hierarchy of the models preferred by the observations given their phenomenology related to DE.

ΔAIC	Level of Empirical Support For Model i
$0-2$	Substantial
$4-7$	Considerably Less
>10	Essentially None

Table 4.2: ΔAIC criterion.

ΔBIC	Evidence Against Model i
$0-2$	Not Worth More Than A Bare Mention
$2-6$	Positive
$6-10$	Strong
>10	Very Strong

Table 4.3: ΔBIC criterion.

4.3. Cosmological models and data analysis

In order to apply the Bayesian analysis, first of all, we calculated the predicted angular diameter distance in a FLRW metric to compare it with the observations. The angular diameter distance described in Chapter §2, given by Eq. (2.25), is only valid for a flat universe; since we are interested in estimating also the curvature parameter in each model, the general form of Eq. (2.25) is considered instead, such as for a source at redshift z, the angular diameter distance is given by

$$d_A(z,\Theta_i^m) = \frac{3000h^{-1}}{(1+z)}\frac{1}{\sqrt{\mid \Omega_k \mid}}\sin\varsigma\left(\int_0^z \frac{\sqrt{\mid \Omega_k \mid}}{E(z,\Omega_i)}dz\right), \tag{4.33}$$

where h is the dimensionless Hubble parameter and the function $\sin\varsigma(x)$ is defined as $\sinh(x)$ if $\Omega_k > 0$, $\sin(x)$ if $\Omega_k < 0$ and x if $\Omega_k = 0$ (Hogg, 1999). Currently, all the evidence about DE comes from measurements of the expansion rate $H(z)$, providing a detailed description on the expansion history of the Universe. As discussed in Chapter §2, in a standard FLRW cosmology, the expansion rate as a function of the redshift $H(z)$ is given by the Friedmann equation as

$$E^2(z,\Omega_i) = \Omega_r(1+z)^4 + \Omega_m(1+z)^3 + \Omega_k(1+z)^2 + \Omega_X e^{3\int_0^z \frac{dz'}{1+z'}(1+w(z'))} \tag{4.34}$$

where $E(z,\Omega_i) \equiv H(z)/H_0$, H_0 is the Hubble parameter today, and the relationship between redshift and scale factor is given by $1+z = a^{-1}$. As already introduced, Ω_i in the equation (4.34) corresponds to the today's energy density normalised to the critical density $\rho_{cri} = 3H_0^2/8\pi G$, for radiation ($\Omega_r$), matter ($\Omega_m$), curvature ($\Omega_k$) and DE ($\Omega_X$). The EoS of DE is characterised by the ratio pressure to energy-density $w(a) = p(a)/\rho(a)$, what allows to classify the models into two groups: one with constant energy density and the other with dynamic energy density. For all models studied, the density parameter of curvature Ω_k is free, and each one of them is described in terms of its vector of parameters $\Theta_i^m = \{\theta_i, \Omega_i\}$, where $\theta_i = \{h, \sigma_8^0\}$ while $\Omega_i = \{\Omega_r, \Omega_m, \Omega_k, \Omega_x\}$ represents the components of the cosmic fluid.

Since the Hubble parameter $H(z)$ provides a natural description about of kinematics of the cosmic expansion, it is possible to characterize whether the Universe is currently accelerating or decelerating, by introducing the deceleration parameter $q(z) \equiv -\ddot{a}(z)/a(z)H(z)^2$. In particular, if $q(z) > 0$, it means $\ddot{a}(z) < 0$, then the expansion decelerate as expected due to the gravitational collapse. The information derived from the dynamics of the expansion history is quite useful when expressed by means of the deceleration parameter, since it helps to clarify the issues related to the cosmological constant and to constrain, from a phenomenological point of view, the possible deviations from the standard ΛCDM model. In a general FLRW cosmology the deceleration has the following form

$$q(z) = -1 + \frac{(1+z)}{E(z)}\frac{dE(z)}{dz}, \tag{4.35}$$

it depends explicitly on the cosmological model studied and its matter-energy content through $E(z)$. In general, if $\Omega_X \neq 0$ is large enough, i.e. $\Omega_X > \Omega_m$, then $q(z) < 0$ and $\ddot{a}(z) > 0$, it corresponds to an accelerated expansion as shown by observational data (Perlmutter et al., 1999; Riess et al., 1998), with a cosmological constant different from zero. If the acceleration is driven by a perfect fluid with nonlinear equation of state, it is important to identify the signs that determine the dynamics of the energy density of the fluid; this is achieved by considering the EoS parameter, that can be written as (Saini et al., 2000)

$$w(z) = \frac{-1 + \frac{2(1+z)}{3}\frac{d\ln H(z)}{dz}}{1 - \frac{\Omega_m(1+z)^3}{E^2(z)}}. \tag{4.36}$$

Clearly, the EoS $w(z)$ has a dynamical nature given its dependence on redshift, as mentioned earlier, depending on its value the models can be classified as quintessence if $-1 < w(z) < -1/3$ or phantom if $w(z) < -1$. In quintessence models, the accelerated expansion related to DE implies a negative pressure, whose simplest case is given by cosmological constant so that $w(z) = -1$. In phantom models, the Einstein's field equations are modified and the new equations combined with the assumption of homogeneity and isotropy lead to a generalized Friedman equation, but $w(z)$ can not be interpreted as a perfect fluid. In this context, the parameter $w(z)$ determines not only the gravitational properties of DE but also its evolution.

4.3.1. ΛCDM model

As reference, we consider the standard baseline ΛCDM model. As it is well known, in this scenario DE is consistent with a cosmological constant Λ with EoS $w = -1$ (see Fig. 4.9). The dimensionless Hubble parameter $E^2(z, \Theta)$ is given by

$$E^2(z, \Theta) = \Omega_r(1+z)^4 + \Omega_m(1+z)^3 + \Omega_k(1+z)^2 + \Omega_X, \tag{4.37}$$

where Ω_m and $\Omega_X = \Omega_\Lambda = 1 - \Omega_m - \Omega_k - \Omega_r$ are the density parameters for matter and DE respectively and Ω_r corresponds to the radiation parameter. The

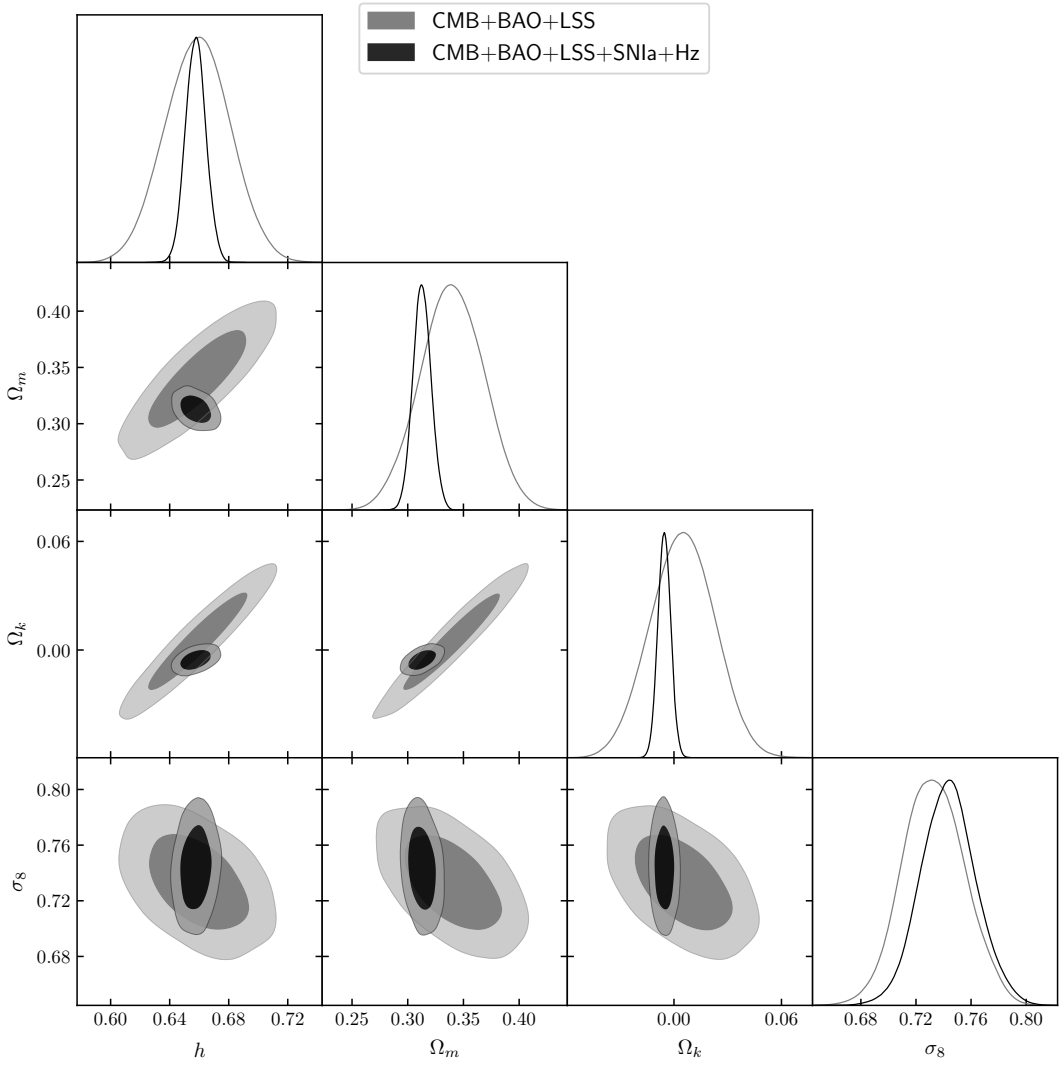

Figure 4.1: 2D contour plots at 1σ and 2σ levels and 1D posterior distributions, with CMB+BAO+G (Gray) and CMB+BAO+SNIa+G+Hz (Black) for the ΛCDM model.

vector of parameters is given by $\Theta_i^{\Lambda CDM} = \{h, \sigma_8, \Omega_m, \Omega_k\}$ and the corresponding best-fit values after minimizing the χ^2 are shown in Tab. 4.4 for two cases, *a)* by combining CMB, BAO and the growth factor data (CMB+BAO+G); *b)* by combining CMB, BAO, SNIa and OHD data (CMB+BAO+G+SNIa+Hz).

In Tab. 4.4 we present a summary of the best-fit values for the ΛCDM model, including the reduced χ^2 that is defined as $\chi^2_{red} = \chi^2_{min}/\nu$, being ν the number of degrees of freedom such that $\nu \equiv N - k$ with $N = 639$ and k is the number of free parameter in the model. As shown in Tab. 4.4, we find that the RMS mass fluctuations $\sigma_8 = 0.744 \pm 0.021$ with 68% confidence level. This result is compatible with the one obtained from Planck Collaboration et al. (2018c), which report a lower uncertainty. Additionally the best-fit value for the DE density normalised to the critical density today is $\Omega_\Lambda = 0.687 \pm 0.009$ at 68%, that also agrees with the limits reported by Planck 2018 ($\Omega_\Lambda = 0.6847 \pm 0.0073$

Θ_i	*CMB+BAO+G*	*CMB+BAO+G+SNIa+Hz*
h	0.658 ± 0.022	0.6576 ± 0.0068
Ω_m	0.339 ± 0.028	0.3126 ± 0.0081
Ω_k	0.004 ± 0.018	-0.0054 ± 0.0035
σ_8	0.733 ± 0.022	0.744 ± 0.019
χ^2_{min}	28.894	621.624
χ^2_{red}	0.046	0.980

Table 4.4: Summary of the best-fit values for the ΛCDM model.

at 68% using TT,TE,EE+LowE+lensing)(Planck Collaboration et al., 2018c). Moreover, the analysis gives a positive cosmological constant, whose value in physical units corresponds to $\Lambda c^{-2} = (1.517 \pm 0.009) \times 10^{-35}\mathrm{s}^{-2}$, which agrees with measurements obtained by the High-Z Supernova Team and the Supernova Cosmology Project (Perlmutter et al., 1999; Carmeli and Kuzmenko, 2001). As complement we computed the derived parameters for this model as shown in Tab. 4.11, while Fig. 4.1 displays the 2D confident contours at 1σ and 2σ levels and 1D posterior distributions with CMB+BAO+G (gray) and CMB+BAO+SNIa+G+Hz (black). From Tab. 4.4 it is worth noting the impact of adding the SNIa and Hz datasets to CMB + BAO + G, which evidently improves the constraints on the parameters.

4.3.2. wCDM model

A natural extension of the standard model is given by considering an EoS constant but in theory different from $w = -1$. In this case the dimensionless Hubble parameter $E^2(z, \Theta)$ for a universe with curvature reads as

$$E^2(z, \Theta) = \Omega_r(1+z)^4 + \Omega_m(1+z)^3 + \Omega_k(1+z)^2 + \Omega_X(1+z)^{3(1+w)}, \quad (4.38)$$

where $\Omega_X = 1 - \Omega_m - \Omega_k - \Omega_r$. For this model the set of free parameters is given by $\Theta_i^{wCDM} = \{h, \sigma_8, \Omega_k, \Omega_m, w\}$, and the best-fit values after marginalizing over are displayed in Tab. 4.5. Fig. 4.2 shows the 2D contour plots at 1σ and 2σ confidence levels and the 1D posterior distribution using CMB+BAO+G (gray) and CMB+BAO+SNIa+G+Hz (magenta) for the wCDM model. From the contours, it can be appreciated that the ΛCDM model, $w = -1$, is allowed at 1σ with CMB+BAO+G and combining all datasets, and it is consistent with a cosmological constant (see Tab. 4.5). The result obtained by Shi, Huang, and Lu (2012), $w = -0.990 \pm 0.041$, is consistent with our results within the errors. The constraints by (Planck Collaboration et al., 2018c) for the $wCDM$ model gives $w_0 = -1.03 \pm 0.03$, being also in agreement with our marginalization at 1σ and 2σ. From Tab. 4.5, the EoS corresponds to a quintessence model when used CMB+BAO+G (see Fig. 4.9) and it has a phantom behaviour when SNIa and Hz are added.

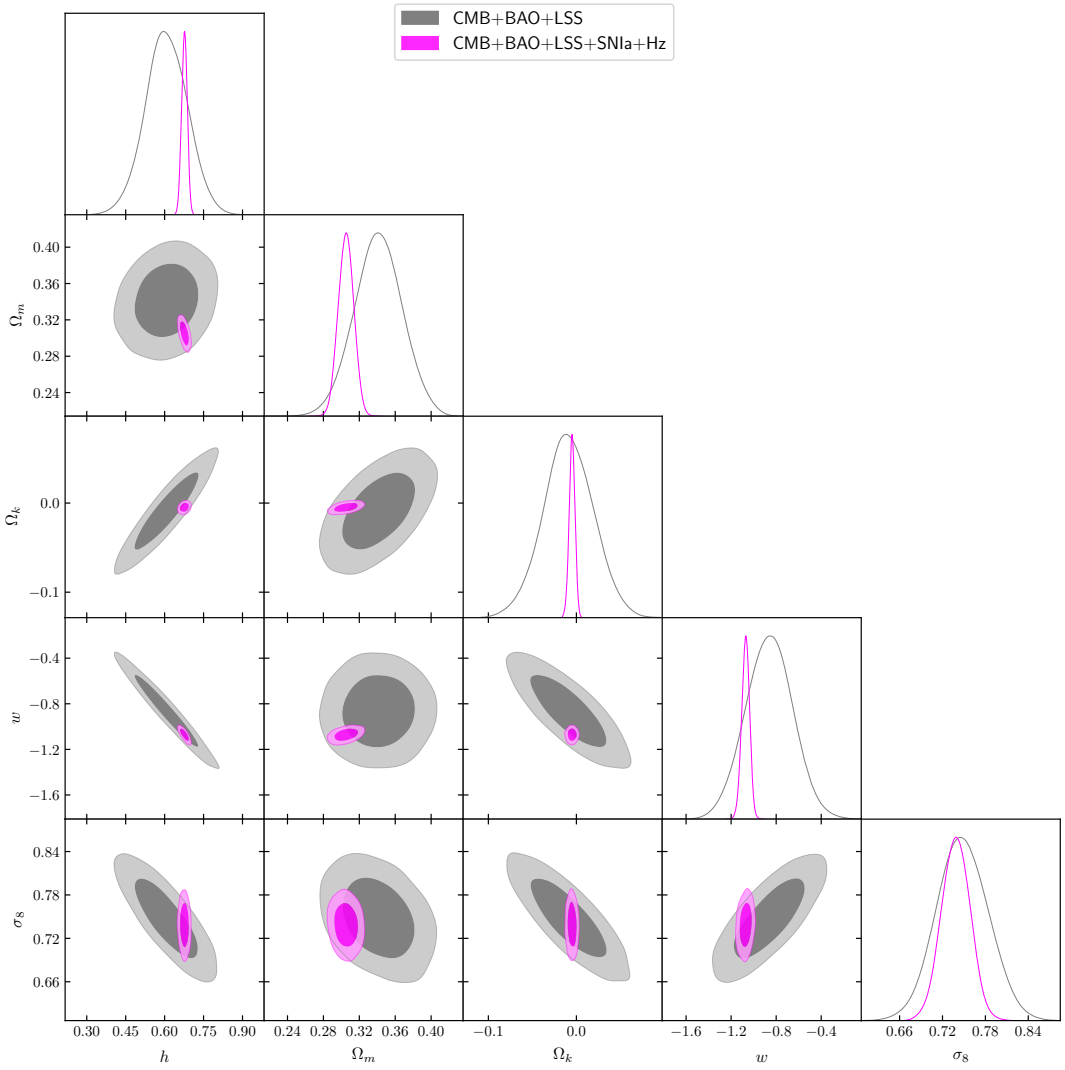

Figure 4.2: 2D contour plots at 1σ and 2σ levels and 1D posterior distributions, with CMB+BAO+G (Gray) and CMB+BAO+SNIa+G+Hz (Magenta) for the wCDM model.

4.3.3. Chevalier-Polarski-Linder model

The Chevalier-Polarski-Linder (CPL) parametrization corresponds to an extension of the standard scenario by generalizing the EoS of DE considering w as a linear function of the scale factor, or equivalently of the inverse of redshift, (Chevallier and Polarski, 2001; Linder, 2003), satisfying

$$w(z) = w_0 + w_1 \frac{z}{1+z}, \tag{4.39}$$

where w_0 and w_1 are free parameters to be fitted. The dimensionless Hubble parameter $E(z)$ for the CPL parametrization is written as

$$E^2(z,\Theta) = \Omega_r(1+z)^4 + \Omega_k(1+z)^2 + \Omega_m(1+z)^3 + \Omega_X X(z), \tag{4.40}$$

Θ_i	*CMB+BAO+G*	*CMB+BAO+G+SNIa+Hz*
h	0.606 ± 0.083	0.676 ± 0.011
Ω_m	0.341 ± 0.026	0.3054 ± 0.0087
Ω_k	-0.009 ± 0.029	-0.0048 ± 0.0033
w	-0.86 ± 0.21	-1.070 ± 0.036
σ_8	0.747 ± 0.037	0.738 ± 0.020
χ^2_{min}	39.366	629.191
χ^2_{red}	0.062	0.990

Table 4.5: Summary of the best-fit values for the wCDM model.

being $\Omega_X = (1 - \Omega_k - \Omega_m - \Omega_r)$ and $X(z) = (1+z)^{3(1+w_0+w_1)} \exp\left[-\frac{3w_1 z}{1+z}\right]$. The vector of free parameters is given by $\Theta_i^{CPL} = \{h, \sigma_8, \Omega_k, \Omega_m, w_0, w_1\}$ and the corresponding best-fit values obtained from the observational data are shown in Tab. 4.6.

Θ_i	*CMB+BAO+G*	*CMB+BAO+G+SNIa+Hz*
h	0.57 ± 0.11	0.678 ± 0.011
Ω_m	0.306 ± 0.079	0.303 ± 0.010
Ω_k	-0.025 ± 0.065	-0.0054 ± 0.0034
w_1	0.57 ± 2.79	0.02 ± 0.53
w_0	-0.92 ± 0.89	-1.091 ± 0.092
σ_8	0.777 ± 0.034	0.735 ± 0.020
χ^2_{min}	27.353	616.376
χ^2_{red}	0.043	0.973

Table 4.6: Summary of the best-fit values for the CPL model.

The confidence contour plots at 1σ and 2σ levels and the posterior distributions for the CPL parametrization are shown in Fig. 4.3, for the joint analysis of CMB+BAO+G (Gray) and CMB+BAO+SNIa+G+Hz (Purple). At 1σ of confidence using all cosmological data, the constraints on h, Ω_m and σ_8 are compatible with the values obtained by Shi, Huang, and Lu (2012) and Planck Collaboration et al. (2018c), however, there is a clear degeneracy between the curvature parameter Ω_k and the equation of state w_0. The final results by Planck Collaboration et al. (2018c) combining only CMB+SNe+BAO information gives $w_0 = -0.961 \pm 0.077$, which is inside the statistical confidence of our estimates. Since the CPL model is reduced to the ΛCDM one when $w_0 = -1$ and $w_a = 0$, it is possible to appreciate that a cosmological constant is not discarded from this analysis as shown in Fig. 4.3. The set of derived physical parameters for this model is displayed in Tab. 4.11, being in general very close to the reference ΛCDM model. From Tab. 4.6, the EoS corresponds to a quintessence model for CMB+BAO+G and phantom when the full dataset is used. On the other hand, in Fig. 4.9 it can be seen that the evolution of EoS with CMB+BAO+G does not cross the phantom line at late times.

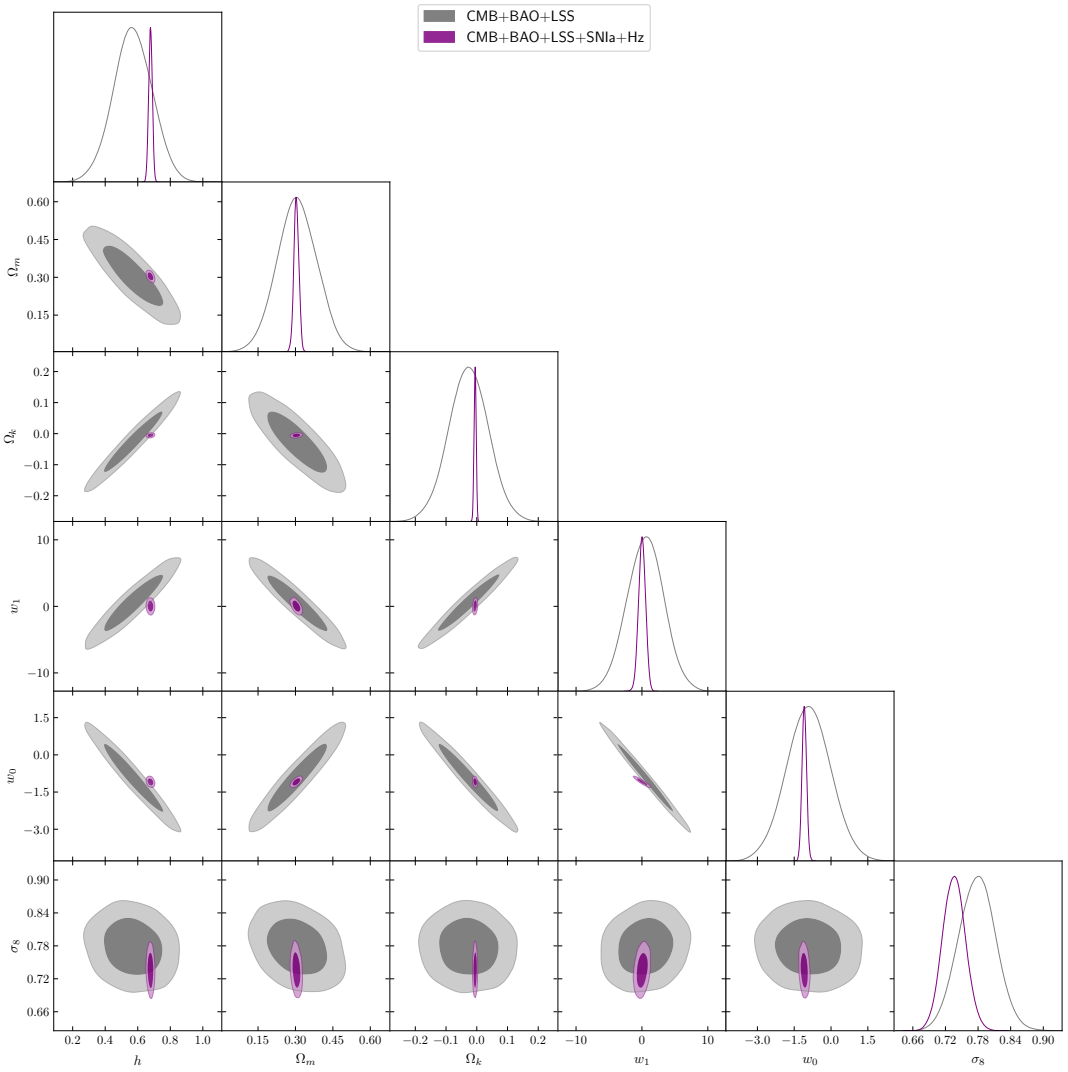

Figure 4.3: 2D contour plots at 1σ and 2σ confidence levels and 1D posterior distributions, with CMB+BAO+G (Gray) and CMB+BAO+SNIa+G+Hz (Purple) for CPL model.

4.3.4. Interacting Dark Energy model

In interacting dark energy (IDE) scenarios there is a coupling between the DE density ρ_x with the DM density ρ_m that could alleviate the cosmic coincidence problem. A general approach is to introduce an interacting term in the right side of the continuity equation (Amendola, 2000; Caldera-Cabral, Maartens, and Ureña-López, 2009; Cai and Wang, 2005; Dalal et al., 2001; Guo, Ohta, and Tsujikawa, 2007), such as

$$\begin{aligned} \dot{\rho}_m + 3H\rho_m &= \delta H \rho_m, \\ \dot{\rho}_x + 3H\left(1 + w_x\right)\rho_x &= -\delta H \rho_m, \end{aligned} \tag{4.41}$$

where w_x is the equation of state of DE and δ denotes the term of interaction to be fitted with the observations. Thus, the dimensionless Hubble parameter for

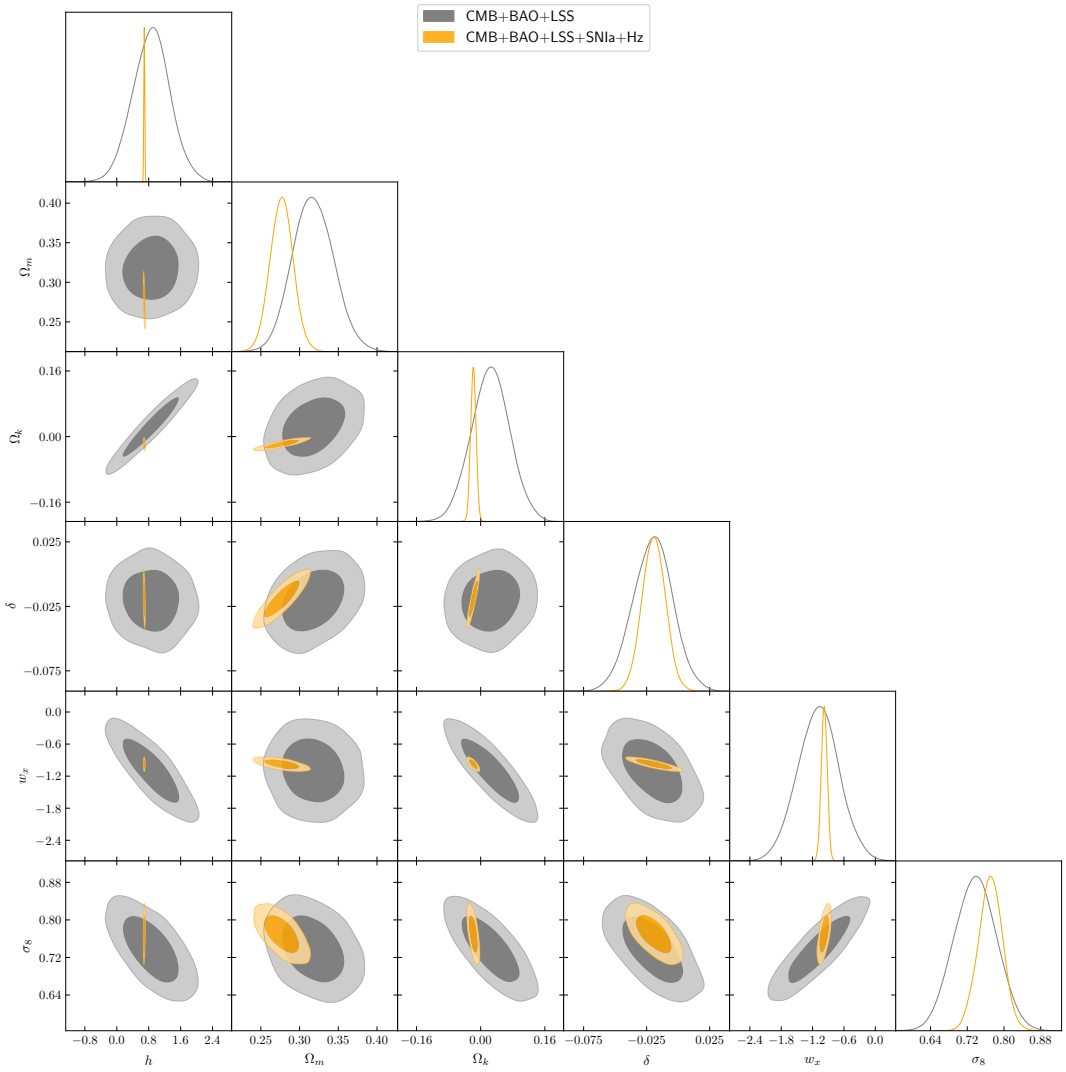

Figure 4.4: 2D contour plots at 1σ and 2σ confidence levels and 1D posterior distributions, with CMB+BAO+G (Gray) and CMB+BAO+SNIa+G+Hz (Orange) for the IDE model.

this interacting model is described by

$$E^2(z,\Theta) = \Omega_r(1+z)^4 + \Omega_k(1+z)^2 + \Omega_m\Psi(z) + \Omega_X(1+z)^{3(1+w_x)}, \quad (4.42)$$

with $\Omega_X = (1-\Omega_m-\Omega_k-\Omega_r)$ and

$$\Psi(z) = \frac{\left(\delta(1+z)^{3(1+w_x)} + 3w_x(1+z)^{3-\delta}\right)}{\delta + 3w_x}. \quad (4.43)$$

This model is characterised by six parameters so that $\Theta_i^{IDE} = \{h, \sigma_8, \Omega_k, \Omega_m, w_x, \delta\}$, their best-fit values are shown in Tab. 4.7. Fig. 4.4 shows the contour plots at 1σ and 2σ confidence level and the posterior distributions for the IDE model using data from CMB+BAO+G (gray) and from CMB+BAO+SNIa+G+Hz (orange). From this model, the ΛCDM scenario can be recovered when $w_x = -1$ and $\delta = 0$, however, the constraints obtained show that the ΛCDM model is

ruled out at least 1σ level in our analysis with all datasets, as it can be seen in Tab. 4.7. Furthermore, if the coupling term in Eq. (4.41) takes a negative value so that $\delta < 0$, thus there is a transfer from DM to DE, whereas a positive coupling, i.e. $\delta > 0$, implies a transfer from DE to DM, the latter case is favoured according to the constraints obtained in this work. According to the classification of the EoS of DE, the analysis points to a phantom behaviour $w_x <$ -1 when the CMB+BAO+G dataset is used. A similar result has been previously reported by Shi, Huang, and Lu (2012), with an agreement at 1σ confidence level. However, with the joint analysis of CMB+BAO+G+SNIa+Hz data the central values of w_x, as shown in Tab. 4.7, point to a quintessence behaviour. Indeed, in Fig. 4.9 it can be appreciated the evolution of EoS with CMB+BAO+G, which crosses the limit of phantom models at $z \sim 0.64$, making a transition from a quintessential behaviour at early times to a phantom behaviour at late times.

Θ_i	*CMB+BAO+G*	*CMB+BAO+G+SNIa+Hz*
h	0.87 ± 0.46	0.688 ± 0.012
Ω_m	0.317 ± 0.026	0.276 ± 0.014
Ω_k	0.024 ± 0.046	-0.0183 ± 0.0068
w_x	-1.09 ± 0.38	-0.976 ± 0.057
δ	-0.020 ± 0.015	-0.0192 ± 0.0093
σ_8	0.737 ± 0.045	0.769 ± 0.027
χ^2_{min}	28.669	612.756
χ^2_{red}	0.045	0.968

Table 4.7: Summary of the best-fit values for the IDE model.

4.3.5. Early Dark Energy model

In early dark energy (EDE) scenarios, the energy density of DE is assumed to be significant at high redshift, unlike in a cosmological constant scenario, where the fraction of DE is negligible at high redshift. This kind of models are attractive since they can alleviate the current Hubble tension, as it has been stated recently by Poulin et al. (2019). Moreover this phenomenon is allowed if the DE tracks the dynamics of the background fluid density (Steinhardt, Wang, and Zlatev, 1999; Wetterich, 1988), what could also ameliorate the coincidence problem of the cosmological constant. A relevant quantity in the EDE model is the Ω_e parameter, which measures the amount of dark energy present at early epochs. We adopt a general EDE model proposed by (Doran and Robbers, 2006) adding a curvature term, what leads to the dimensionless Hubble parameter

$$E^2(z,\Theta) = \frac{\Omega_r(1+z)^4 + \Omega_m(1+z)^3 + \Omega_k(1+z)^2}{1-\Omega_X}, \tag{4.44}$$

with Ω_X given by

$$\Omega_X = \frac{\Omega_{X_0} - \Omega_e\left[1-(1+z)^{3w_0}\right]}{\Omega_{X_0} + f(z)} + \Omega_e\left[1-(1+z)^{3w_0}\right] \tag{4.45}$$

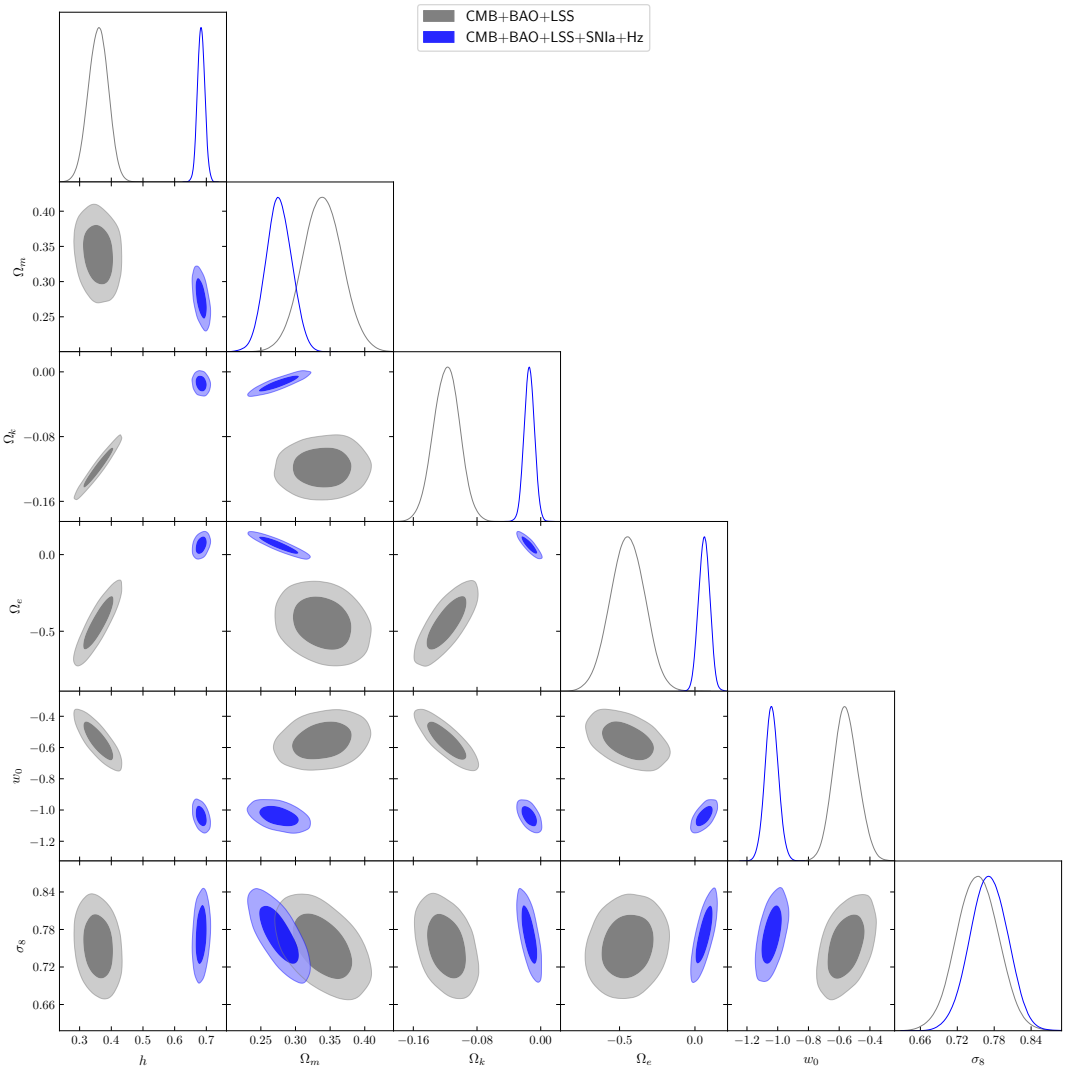

Figure 4.5: 2D contour plots at 1σ and 2σ levels and the posterior distributions, with CMB+BAO+G (Gray) and CMB+BAO+SNIa+G+Hz (Blue) for EDE model.

and

$$f(z) = \Omega_m(1+z)^{-3w_0} + \Omega_r(1+z)^{-3w_0+1} + \Omega_k(1+z)^{-3w_0-1}, \tag{4.46}$$

such that $\Omega_{X_0} = 1 - \Omega_m - \Omega_k - \Omega_r$ is the current DE density. This model has five free parameters $\Theta_i^{EDE} = \{h, \sigma_8, \Omega_k, \Omega_m, \Omega_e, w_0\}$, whose best-fit values are shown in Tab. 4.8. After applied the Bayesian analysis with the full dataset we found that $\Omega_e = 0.061 \pm 0.037$, which is in agreement at 2σ confidence level with Doran and Robbers (2006), who reported $\Omega_e < 0.04$ at 95% confidence level by using a combination of data from WMAP+VSA+CBI+BOOMERANG+SDSS+SNIa, and it is also in agreement with Pettorino, Amendola, and Wetterich (2013), reporting a constraint of $\Omega_e < 0.015$ at 95%. From Fig. 4.5 it is clear that the ΛCDM model ($\Omega_e = 0$, $w_0 = -1$) is favoured at least at 2σ confidence level by the join analysis of the full dataset, but it is out of the confidence region for the combination CMB+BAO+G. In addition, some tensions are found between h and the rest of parameters, in particular when SNIa+Hz data are

included in the χ^2 thus significant deviations appear in the limits of the posterior distribution. Tab. 4.8 shows that the EoS (w_0) is quintessence for CMB+BAO+G and phantom by adding SNIa+Hz. Fig. 4.9 displays the evolution of the EoS with CMB+BAO+G which crosses the phantom line at $z \sim 0.49$, passing from a phantom behaviour at early times to a quintessential behaviour at late times.

Θ_i	*CMB+BAO+G*	*CMB+BAO+G+SNIa+Hz*
h	0.359 ± 0.029	0.683 ± 0.011
Ω_m	0.338 ± 0.026	0.275 ± 0.018
Ω_k	-0.117 ± 0.012	-0.0144 ± 0.0064
w_0	-0.5587 ± 0.0091	-1.039 ± 0.043
Ω_e	-0.44 ± 0.10	0.061 ± 0.037
σ_8	0.752 ± 0.033	0.771 ± 0.030
χ^2_{min}	30.912	613.638
χ^2_{red}	0.049	0.969

Table 4.8: Summary of the best-fit values for the EDE model.

4.3.6. History of the expansion

After constraining the main set of parameters of each model, it is possible to reconstruct the history of the expansion as well as the main features of the corresponding cosmology as a function of the redshift. Fig. 4.6 shows the evolution of the Hubble parameter $H(z)$ as a function of redshift, as evaluated by considering the models with the central values of the posterior distribution obtained using CMB+BAO+G+SNIa+Hz data. The relative differences in the lower panel of Fig. 4.6 have been computed with respect to the ΛCDM model; at high redshift $z > 1$ the dynamical DE models have a similar behaviour with deviations smaller than 2%, so that the wCDM mimics the CPL one, whereas the EDE model reproduces the ΛCDM evolution with negligible deviations at these redshifts. The IDE model behaves as the ΛCDM one with almost a constant deviation smaller than 1%, at $z > 1$. On the contrary, at $z < 1$, all dynamical DE models deviate from ΛCDM , in particular at $z \approx 0$, wCDM and CPL models differ by about 3%, the EDE model by 4% and the IDE one beyond this value.

Model	χ^2_{min}	Parameters
ΛCDM	25.71	$h = 0.7497$, Ω_m=0.3202, Ω_k=-0.1462
wCDM	15.29	$h = 0.6133$, Ω_m=0.3067, Ω_k=-0.6021, w=-0.6548
CPL	13.62	$h = 1.9489$, Ω_m=0.2829, Ω_k=-0.4470, w_a=0.8145, w_0=-0.8927
IDE	15.29	$h = 0.6245$, Ω_m=0.3064, Ω_k=-0.6024, w_x=-0.6554, δ=-0.0027
EDE	15.43	$h = 0.3885$, Ω_m=0.3419, Ω_k=-0.2887, w_0=-0.4582, Ω_e= -0.5558

Table 4.9: Best-fit values obtained from the Bayesian analysis using BAO and growth factor datasets for each model considered in this work.

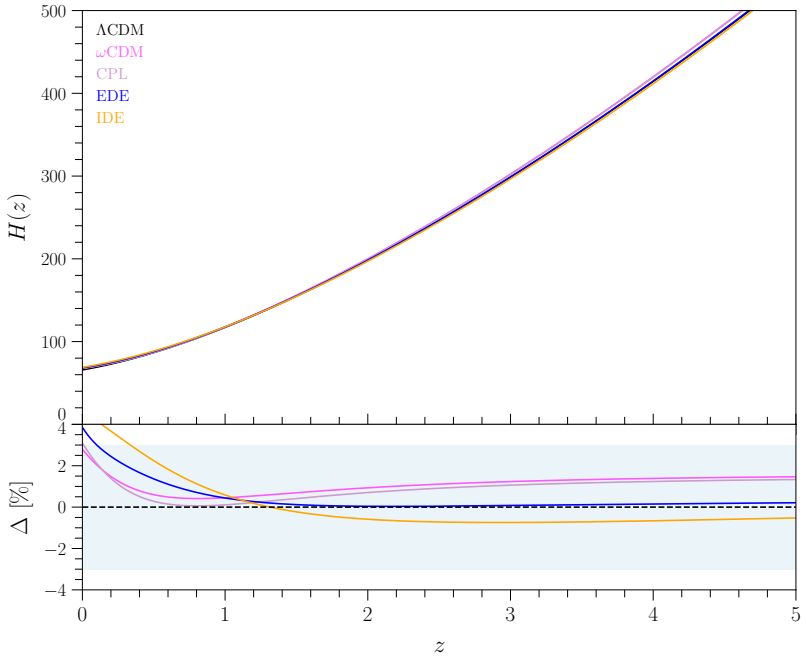

Figure 4.6: The Hubble parameter $H(z)$ as a function of redshift. The shaded region in the lower panel represents a 3% deviation around the ΛCDM model prediction. The best-fit parameters from CMB+BAO+G+SNIa+Hz constraints have been used for each model.

Fig. 4.7 shows the behaviour of the deceleration parameter $q(z)$ as a function of redshift using the BAO and Growth factor datasets; the central values of the free parameters are shown in Tab. 4.9. As expected, the models studied display $q(z) < 0$ at late times and $q(z) > 0$ at earlier epoch, it means that the history of the expansion is slowed down in the past and accelerated today. All models have a transition, at redshift z_t, between the two periods, however, the models that include a dynamical DE term display an interesting behaviour of slowing down of acceleration at low redshift, i.e., late times, when only BAO+G datasets are used. This effect have been reported previously by Cárdenas, Bernal, and Bonilla (2013), Magaña, Cárdenas, and Motta (2014), Wang et al. (2016), Magaña et al. (2017), and Zhang and Xia (2018), and it can be characterised through the change of sign of the jerk parameter $j(z)$, that can be interpreted as the slope at each point of the $q(z)$ function indicating a change in the acceleration (Bonilla and Castillo, 2018), so that, in CPL: $j(z_{low}) \to 0$, when $z_{low} \sim 0.25$; IDE: $j(z_{low}) \to 0$, when $z_{low} \sim -0.09$; EDE: $j(z_{low}) \to 0$, when $z_{low} \sim 0.24$. This result is consistent with the one presented by Barrow, Bean, and Magueijo (2000), who raise the possibility of a scenario consistent with the current accelerating Universe and does not imply an accelerated eternal expansion. For an extensive analysis exploring this possibility see e.g. Bolotin, Erokhin, and Lemets (2012). This can be also related to a clear behaviour of a dynamical DE at low redshift in these models with variation of the density of DE over time.

Fig. 4.8 shows the distance-redshift relation $D_v(z)/r_s$ using the best-fit values

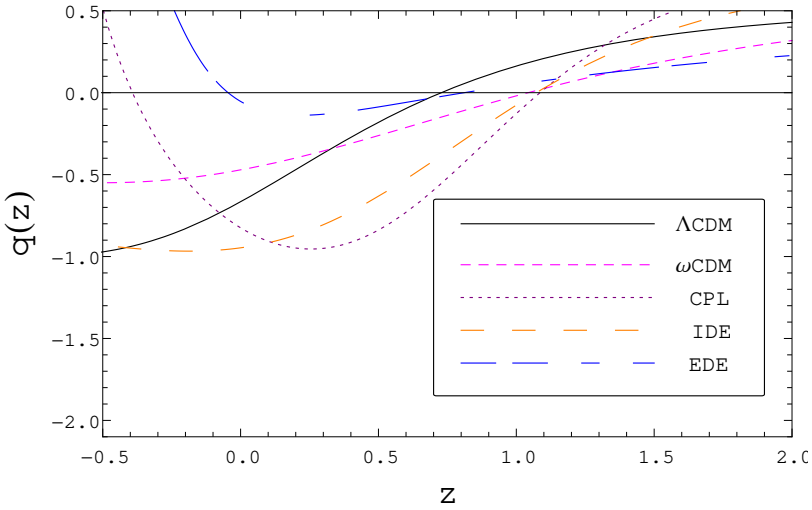

Figure 4.7: The deceleration parameter as a function of redshift using BAO and growth factor datasets. The transition from a decelerated to an accelerated phase occurs at redshift z_t such that $q(z_t) = 0$ and the current value of the deceleration parameter is denoted by q_0. For the models investigated these values are: $z_t \approx 0.73$, $q_0 = -0.67$ for ΛCDM; $z_t \approx 1.07$, $q_0 = -0.50$ for $wCDM$; $z_t \approx 1.07$, $q_0 = -0.79$ for CPL; $z_t \approx 1.07$, $q_0 = -0.95$ for IDE and $z_t \approx 0.84$, $q_0 = -0.06$ for EDE. Note the behaviour of the deceleration parameter to later times for dynamical DE models (CPL, IDE, EDE).

obtained from BAO+CMB+G measurements for each model considered in this analysis. The differences have been quantified by means of the exclusion analysis since all models present a high confidence with respect to the measurements. By using the same posterior parameters, in Fig. 4.9, we show the evolution of the equation of state $w(z)$ as a function of redshift; in fact, the IDE and EDE models are the only ones that cross the phantom limit, making a transition at $z \sim 0.57$ (IDE) and at $z \sim 0.77$ (EDE). The other models behave as expected, following the corresponding parametrization of the EoS.

The measurements of the growth parameter $A(z)$ have been used to constrain independently the amplitude of density fluctuations σ_8. This method allows to break the $\Omega_m - \sigma_8$ degeneracy, by means of Eq. (2.52) to thereby achieve a good independent constraint. Fig. 4.10 displays the growth rate measurements and the theoretical prediction by using the best fit values from BAO+CMB+G. Fig. 4.11 shows the evolution of the normalised growth factor computed by using Eq. (2.52) for each model considered in our research. Deviations around 3% with respect to ΛCDM can be appreciated in the lower panel, where all models are in well agreement at low redshift. In particular, the deviations increase above 1% from redshift 0.5 at all redshifts considered, where the transition to an accelerated stage occurs, i.e., $q(z) < 0$. As the growth factor evolves as a function of redshift, the wCDM and CPL models remain close to ΛCDM. Finally, in Tab. 4.11 we report the main derived parameters from the constraints in this work, by considering the full observational data samples.

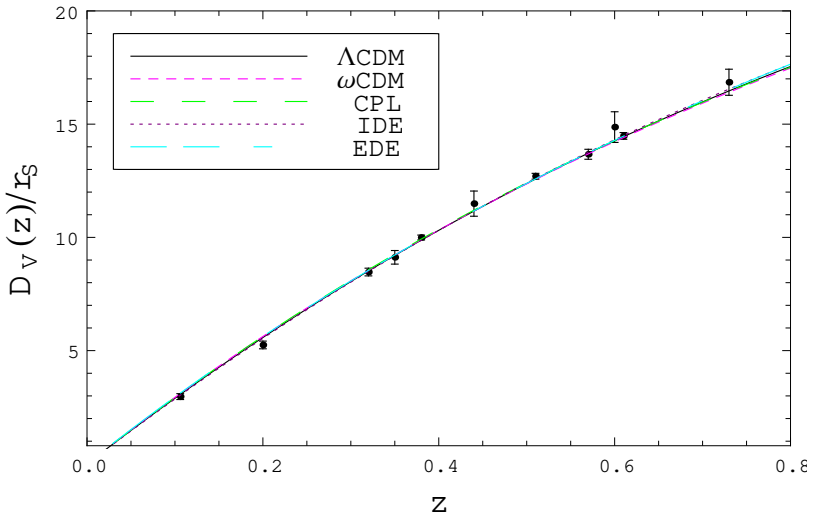

Figure 4.8: The distance-redshift relation using best-fit values for BAO+CMB+G and BAO measurements $D_v(z)/r_s$ for each model considered in this analysis.

4.3.7. Exclusion analysis

In order to discern the most favoured model in terms of its statistical confidence and the number of parameters used in the Bayesian analysis, we compute the AIC/BIC criteria for each model. The exclusion criteria have been quantified by the absolute and relative differences of the AIC/BIC weights. Tab. 4.10 shows the values of ΔAIC and ΔBIC for DE models from the full cosmological tests. The IDE model gives the lowest value of ΔAIC and ΔBIC, therefore, we conclude this is the most favoured model by the observational data employed, as it can also inferred from Tab. 4.11. The ΔAIC and ΔBIC weights for the other models are measured with respect to IDE one. Following Shi, Huang, and Lu (2012), the DE models can be classified in two groups: *1*) models that show a substantial level of empirical support to IDE, EDE and positive evidence for ΛCDM; *2*) models with a considerably low level of empirical support and positive evidence against CPL and $wCDM$ models.

Model	k	χ^2_{red}	AIC	ΔAIC	BIC	ΔBIC
ΛCDM	4	0.980	631.624	6.868	653.924	2.409
wCDM	5	0.990	637.191	12.435	655.031	3.516
CPL	6	0.973	628.376	3.620	655.135	3.620
IDE	6	0.968	624.756	0.000	651.515	0.000
EDE	6	0.969	625.638	0.882	652.397	0.882

Table 4.10: Comparison of the different cosmological models with the ΔAIC y ΔBIC criteria using the joint analysis of CMB+BAO+G+SNIa+Hz data, where $N = 639$ and $\chi^2_{red} = \chi^2_{min}/\nu$, being ν the number of degrees of freedom such that $\nu \equiv N - k$ with k the number of free parameter in each model.

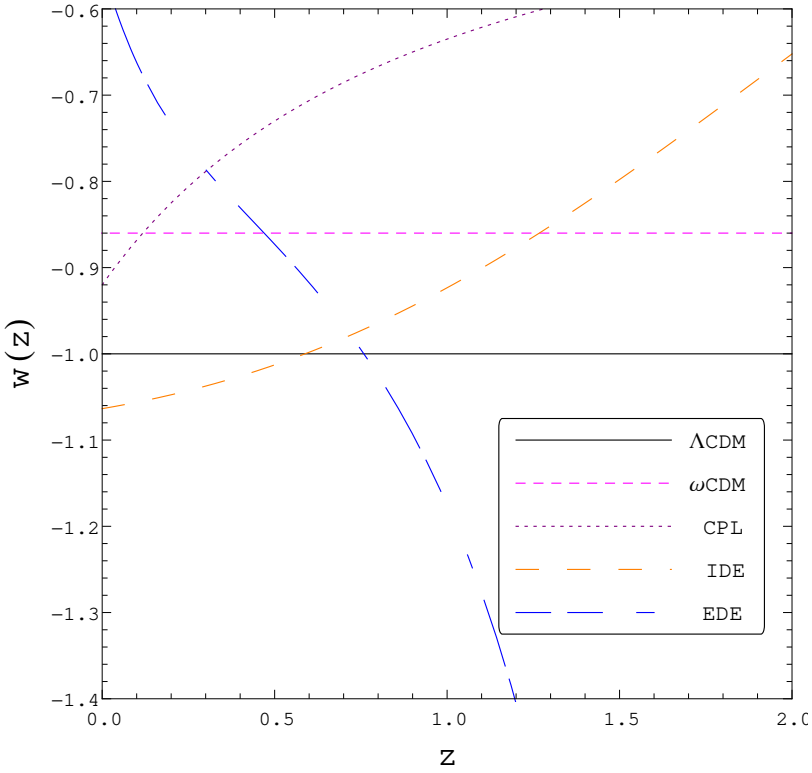

Figure 4.9: Evolution of the equation of state $w(z)$ as a function of redshift for ΛCDM, wCDM, CPL, IDE ($z \sim 0.57$) and EDE ($z \sim 0.77$) models, where the redshift between parenthesis corresponds to the transition in the phantom line. The color lines correspond to the predictions for each model using the best-fit values from the BAO+CMB+G dataset.

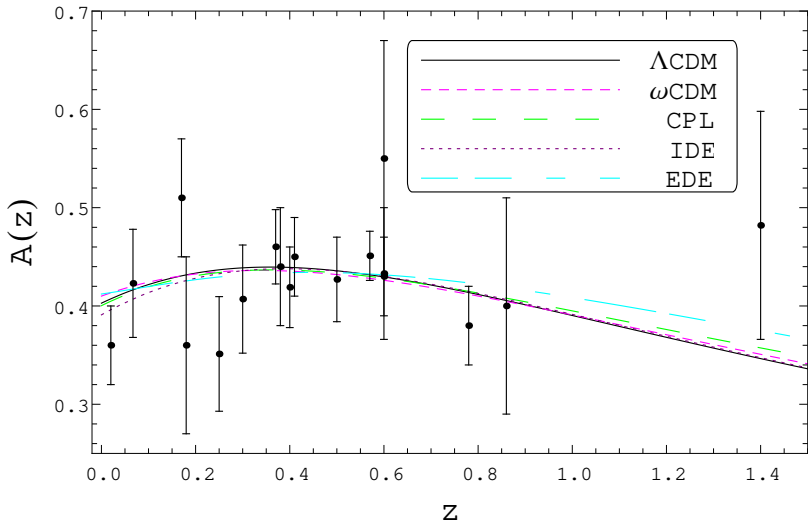

Figure 4.10: Growth rate measurements $A_{obs}(z_i)$ and theoretical expectations for different cosmological models using the fit values for BAO+CMB+G.

4.4. Discussion

In this Chapter we have investigated different dark energy models by constraining its main set of cosmological parameters, including a comparison between

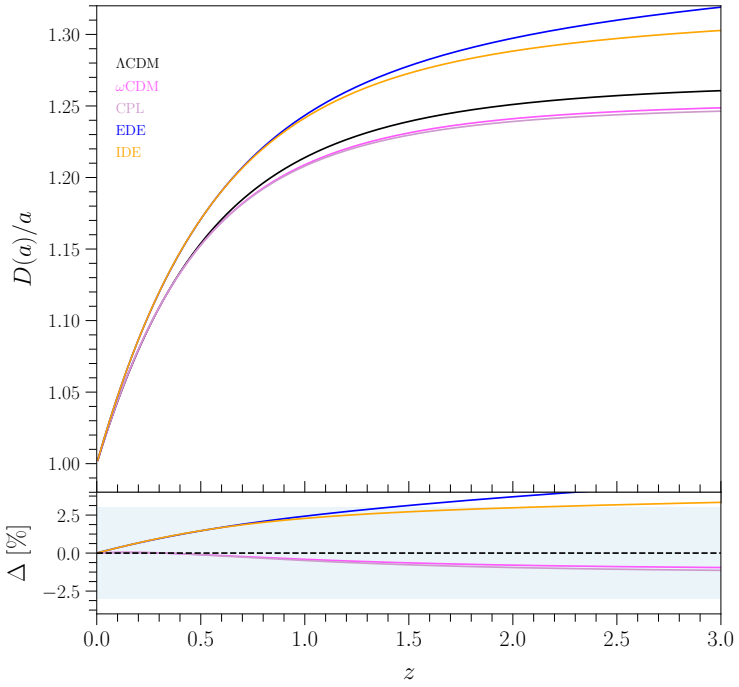

Figure 4.11: Normalised growth factor ratio $D(a)/a$ as a function of redshift. The shaded region in the lower panel represents a 3% deviation around the ΛCDM model prediction. Best-fit parameters from CMB+BAO+G+SNIa+Hz constraints have been use for each model.

them through the best-fit to observational data.

In particular, the cosmic expansion history of dynamical dark energy models has been revisited using a Bayesian analysis, considering the most recent information from CMB and LSS. The cosmological models studied (ΛCDM , wCDM, CPL, IDE and EDE) have been evaluated by a robust exclusion analysis in terms of their confidence with the observational data and the number of degree of freedom. We studied the cosmic expansion through the deceleration parameter $q(z)$ with data from LSS, using BAO distance, ratio scale $r_s/D_v(z)$ and the growth factor, providing new support to some results stated in previous works (Bonilla and Castillo, 2018), such as the behaviour of the deceleration parameter $q(z)$ at late times ($z_{low} < 0.5$). Our findings show a change in the sign of the jerk parameter $j(z)$, from positive to negative values, which is more evident in the dynamical dark energy models that indicate a possible decelerated stage as shown by Fig. 4.7. This effect raises the possibility that an accelerated expansion does not imply an eternal accelerated expansion, even in presence of DE. This particular behaviour is present only in models with DE density varying with time, and it is possibly due to the dynamics of the DE density which in principle can be a way to distinguish it from a cosmological constant.

Based on the best fit parameters obtained from the χ^2 minimization, the models have been classified following the information criteria provided by ΔAIC and ΔBIC, giving a favorability weight of the models by the data employed. The exclusion analysis shows that the IDE model is preferred by the Bayesian and Akaike criterion, but although ΛCDM, $wCDM$, EDE and CPL models are less favoured, they are not discarded. In fact, the evolution of the normalised growth factor and Hubble parameter show deviations up 3% at high redshift. The deviations at low z are very interesting, since models with interactions offer a natural alternative to alleviate some of the current tensions in cosmology such as those of H_0 with different observational tests.

Parameter	ΛCDM	$wCDM$	CPL	IDE	EDE
H_0	65.76 ± 0.68	67.6 ± 1.1	67.8 ± 1.1	68.8 ± 1.2	68.3 ± 1.1
t_0	14.879 ± 0.154	14.474 ± 0.235	14.432 ± 0.234	14.222 ± 0.248	14.326 ± 0.231
$10^{-5}\Omega_{r_0}$	9.66 ± 0.20	9.140 ± 0.297	9.086 ± 0.294	8.824 ± 0.307	8.953 ± 0.288
$10^{-5}\Omega_{\gamma_0}$	5.709 ± 0.181	5.403 ± 0.176	5.371 ± 0.174	5.216 ± 0.182	5.292 ± 0.170
$10^{-5}\Omega_{\nu_0}$	3.950 ± 0.082	3.737 ± 0.122	3.715 ± 0.120	3.608 ± 0.125	3.661 ± 0.117
ω_{m_0}	0.1351 ± 0.0044	0.140 ± 0.006	0.139 ± 0.006	0.131 ± 0.008	0.128 ± 0.009
ω_{b_0}	0.0211 ± 0.0004	0.0223 ± 0.0007	0.0224 ± 0.0007	0.0230 ± 0.0008	0.0227 ± 0.0007
Ω_{X_0}	0.693 ± 0.011	0.699 ± 0.012	0.702 ± 0.013	0.742 ± 0.021	0.739 ± 0.024
$10^{-30}\rho_{cri_0}$	8.130 ± 0.168	8.591 ± 0.279	8.642 ± 0.280	8.898 ± 0.310	8.770 ± 0.282
$10^{-30}\rho_{X_0}$	5.632 ± 0.137	6.001 ± 0.211	6.069 ± 0.217	6.604 ± 0.268	6.483 ± 0.268
c_s	0.452 ± 0.002	0.447 ± 0.003	0.447 ± 0.002	0.444 ± 0.003	0.446 ± 0.003
z_{drag}	1017.13 ± 1.29	1020.26 ± 2.02	1020.53 ± 2.01	1021.16 ± 2.21	1020.19 ± 2.05
r_{drag}	153.123 ± 1.482	151.767 ± 2.044	152.726 ± 2.136	148.238 ± 3.771	149.85 ± 4.14
z_{cmb}	1093.12 ± 0.53	1091.71 ± 0.73	1091.5 ± 0.8	1089.82 ± 0.89	1090.1 ± 1.0

Table 4.11: Derived parameters for different cosmological DE models. We assume $\Omega_{b_0} = 0.045$ (Kirkman et al., 2003) and $N_{eff} = 3.04$ (Planck Collaboration et al., 2018c) for all cosmological models.

CHAPTER 5

Constraints on $f(R)$ gravity with and without massive neutrinos from redshift-space distortions

In the previous Chapter we explored different cosmological models, all of them including DE and DM components, following the dynamics derived from the general relativity (GR) framework solving the corresponding modified Friedmann equations. In this Chapter we go one step beyond, by considering models where the theory of gravity is a modification of GR, keeping as usual the standard model ΛCDM as reference.

From first principles it is well known that a theory of gravity is needed to describe the spatial properties and dynamics of the LSS of the Universe. The observational data collected for several decades provide strong support to the concordance ΛCDM model, which yields a consistent description of the main properties of the LSS as already discussed in the previous Chapters (see e.g. Tonry et al., 2003; Bel et al., 2014; Hamana et al., 2015; Planck Collaboration et al., 2016a; Planck Collaboration et al., 2016b; Alam et al., 2017; Alsing, Heavens, and Jaffe, 2017; Abbott et al., 2018; Planck Collaboration et al., 2018b; Pacaud et al., 2018; Joudaki et al., 2018; Di Valentino et al., 2018; Jones et al., 2018). However, since cosmological observations have entered in an unprecedented precision era, one of the current aims is to test some of the most fundamental assumptions of the concordance model of the Universe. In this sense, the ΛCDM model assumes: GR as the theory describing gravitational interactions at large scales, the standard model of particles and the cosmological principle. Moreover, in this framework, the Universe is currently dominated by DE, in the form of a cosmological constant, responsible for the late-time cosmic acceleration (Riess et al., 1998; Schmidt et al., 1998; Perlmutter et al., 1999), and by a CDM component that drives the formation and evolution of cosmic structures.

Recently, several shortcomings have been found, like a possible critical tension in the ΛCDM scenario consisting in the discrepancy observed in H_0 and σ_8 measurements when different probes at high and low redshifts are used (see Planck Collaboration et al., 2016c; Riess et al., 2016; Bernal, Verde, and Riess, 2016; Planck Collaboration et al., 2018b). This has motivated the interest on theoretical models beyond GR. Between them, models based on $f(R)$ gravity are the favourite ones because of their generality and rich phenomenology (Sotiriou and Faraoni, 2010; De Felice and Tsujikawa, 2010). Moreover, modified gravity (MG) models represent one of the most viable alternatives to explain cosmic acceleration (for a review see e.g. Joyce, Lombriser, and Schmidt, 2016), that require satisfying simultaneously solar system constraints and to be consistent with the measured accelerated cosmic expansion and large-scale constraints (see e.g. Uzan, 2011; Will, 2014; Pezzotta et al., 2017; Collett et al., 2018, and references therein).

An extra motivation to study MG models, is given by the fact that massive neutrinos, the only (hot) dark matter candidates we actually know to exist, can affect these observables and have several cosmological implications (e.g. Lesgourgues and Pastor, 2006; Wong, 2008; Wong, 2011; Marulli et al., 2011; Costanzi et al., 2014; Battye and Moss, 2014; Villaescusa-Navarro et al., 2014; Enqvist et al., 2015; Roncarelli, Carbone, and Moscardini, 2015; Zennaro et al., 2018; Poulin et al., 2018). As has been recently shown in literature, exists a strong observational degeneracy between some modified gravity (MG) models and the total neutrino mass (Motohashi, Starobinsky, and Yokoyama, 2013; He, 2013; Baldi et al., 2014; Giocoli, Baldi, and Moscardini, 2018), giving rise to an intrinsic limitation of the discriminating power of many standard cosmological statistics (Peel et al., 2018a; Hagstotz et al., 2018).

Considering the impact of MG and massive neutrinos in the clustering, a powerful cosmological test to discriminate among these scenarios is provided by the redshift-space galaxy clustering on different scales (see e.g. Arnouts et al., 1999; Blake and Glazebrook, 2003; Percival et al., 2007; Guzzo et al., 2008; Blake et al., 2011; Marulli, Baldi, and Moscardini, 2012; Marulli et al., 2012; de la Torre et al., 2013; Beutler et al., 2014; Alam et al., 2017; Sánchez et al., 2017; Satpathy et al., 2017; Pezzotta et al., 2017). In this context, the present Chapter is based on our paper (García-Farieta et al., 2019), where we investigated the spatial properties of the LSS of the Universe focusing on models derived from the Hu and Sawicki (2007) $f(R)$ gravity. The RSD have been used as cosmological test since it is well known that the large-scale velocity field is more sensitive to modifications of gravity as compared to the matter density distribution (Jennings et al., 2012) and it can increase the possible signal associated with a deviation from GR. In this sense, recently some kinematic information encoded by the velocity power spectrum and by the velocity dispersion around massive clusters have been extracted from a new suite of MG cosmological simulations – the DUSTGRAIN-*pathfinder* simulations (Giocoli, Baldi, and Moscardini, 2018) – in order to discuss and possibly break the $f(R)$-massive neutrino degeneracy (Hagstotz et al., 2019). Here, we investigate the information gain coming from

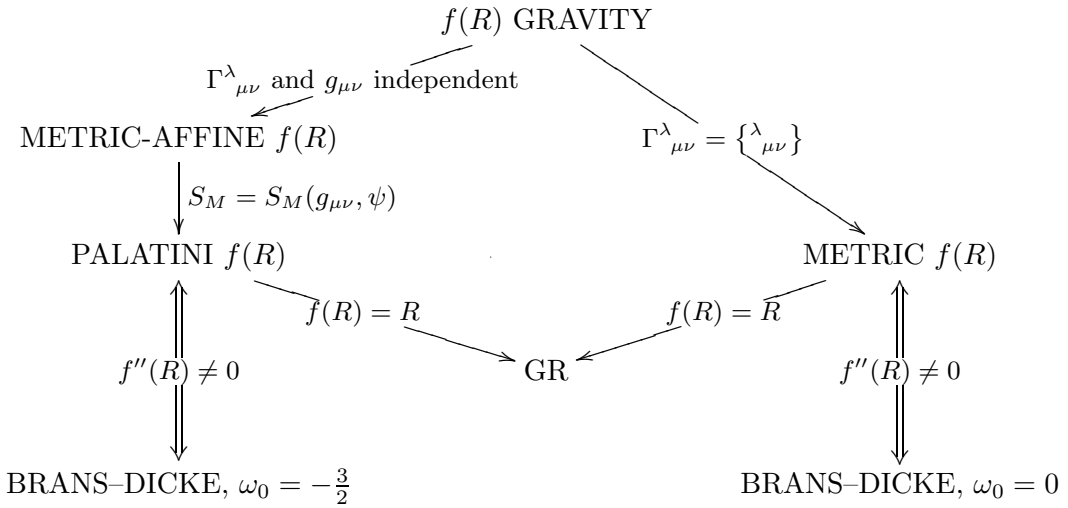

Figure 5.1: Classification of $f(R)$ theories of gravity and the assumptions needed to arrive to the various versions of $f(R)$ gravity and GR. Taken from (Sotiriou, 2006).

the large-scale velocity field through the redshift-space distribution of biased tracers, such as CDM haloes expected to host galaxies and galaxy clusters. In the following Sections, we present the analysis of the real-space and redshift-space clustering properties of CDM halo catalogues extracted from the DUSTGRAIN-*pathfinder* simulations, with the aim of exploring the possible degeneracies introduced by massive neutrinos, by constraining $b\sigma_8$ and $f\sigma_8$ from the multipole moments of the 2PCF.

5.1. Modified gravity models

Among the proposed extensions of GR, we consider the one based on the following modified Einstein-Hilbert action:

$$S = \int \mathrm{d}^4x \sqrt{-g} \left(\frac{R + f(R)}{16\pi G} + \mathcal{L}_m \right) , \tag{5.1}$$

where R is the Ricci scalar, G is the Newton's gravitational constant, g is the determinant of the metric tensor $g_{\mu\nu}$, and $\mathcal{L}_m$ is the Lagrangian density of all matter fields[1]. Fig. 5.1 shows a short classification of $f(R)$ theories of gravity and the assumptions needed to arrive to different versions of $f(R)$ gravity and GR. For a general $f(R)$ model, by considering a spatially flat FLRW universe with metric $ds^2 = -dt^2 + a^2(t)d\mathbf{x}^2$ and varying the above action with respect to $g_{\mu\nu}$ one can get the general form of the modified Einstein field equations

$$G_{\mu\nu} + f_R R_{\mu\nu} - g_{\mu\nu} \left(\frac{1}{2} f(R) - \Box f_R \right) - \nabla_\mu \nabla_\nu f_R = 8\pi G T^{\mathrm{m}}_{\mu\nu}, \tag{5.2}$$

where $R_{\mu\nu}$ and $G_{\mu\nu}$ are the Ricci tensor and Einstein tensor respectively, while ∇_μ denotes the covariant derivative, $\Box = \nabla^\mu \nabla_\mu$ the d'Alambertian, $T^m_{\mu\nu}$

[1]We use natural units $c = 1$. The Greek indices, μ and ν, run over 0, 1, 2, 3.

the energy-momentum tensor for matter and $f_R \equiv df(R)/dR$ is the so-called *scalaron* field. The amplitude of the latter quantity determines the deviation from GR, so that a large $|f_R|$ means a strong deviation. The corresponding modified Friedmann equations are obtained by following the procedure detailed in Chapter §2, such that for the action given by Eq. (5.1) these are

$$3H^2(1+f_R) = 8\pi G\left(\rho_m + \rho_{rad}\right) + \frac{1}{2}(f_R R - f) - 3H\dot{f}_R \tag{5.3}$$

$$-2(1+f_R)\dot{H} = 8\pi G\left(\rho_m + \frac{4}{3}\rho_{rad}\right) + \ddot{f}_R - H\dot{f}_R\,, \tag{5.4}$$

where $R = 6(2H^2 + \dot{H})$, the over-dot denotes a derivative with respect to the cosmic time t. In general, the background evolution of a viable $f(R)$ is not simple as it has been shown by Boisseau et al. (2000), Nojiri, Odintsov, and Sáez-Gómez (2009), and Cognola et al. (2009). However it is possible to get an approximation in a way analogous to the DE models, by neglecting the higher derivative and the non-linear terms. Thus, the equation that describes the growth of matter perturbations in terms of the density contrast δ in a $f(R)$ model is approximated by (Boisseau et al., 2000):

$$\ddot{\delta} + 2H\dot{\delta} - 4\pi G_{eff}\rho_m\delta = 0, \tag{5.5}$$

where G_{eff} is the effective gravitational constant, that can be written as (Tsujikawa, 2007)

$$G_{eff} = G\left(1 + \frac{1}{3}\frac{k^2/a^2}{k^2/a^2 + 1/(3f_{RR})}\right), \tag{5.6}$$

where we introduced the derivative of the scalaron with respect to the scalar curvature $f_{RR} \equiv d^2f(R)/dR^2$, whereas k corresponds to the wave number, meaning that the evolution of matter density perturbations depends on this (Fu, Wu, and Yu, 2010; Narikawa and Yamamoto, 2010). By defining the growth rate as usual $f \equiv d\ln\delta/d\ln a$, it leads to

$$\frac{df}{d\ln a} + f^2 + \frac{1}{2}\left(1 - \frac{d\ln\Omega_m}{d\ln a}\right)f = \frac{3}{2}\frac{G_{\rm eff}}{G_N}\Omega_m\,, \tag{5.7}$$

with $\Omega_m(a) = H_0^2\Omega_0 a^{-3}/H^2$. Besides, if the background expansion in the $f(R)$ model is well approximated by the ΛCDM model, the following relations must be satisfied

$$\begin{cases} \dfrac{\dot{H}}{H^2} = -\dfrac{3}{2}\Omega_m(a), & (5.8) \\ \dfrac{d\Omega_m(a)}{d\ln a} = -3\Omega_m(a)\left(1-\Omega_m(a)\right), & (5.9) \end{cases}$$

allowing to re-write Eq. (5.7) as (Narikawa and Yamamoto, 2010):

$$-3\Omega_m(a)\left(1-\Omega_m(a)\right)\frac{df}{d\Omega_m(a)} + f^2 + \left(2 - \frac{3}{2}\Omega_m(a)\right)f = \frac{3}{2}\frac{G_{\rm eff}}{G}\Omega_m(a). \tag{5.10}$$

A plausible $f(R)$ function able to satisfy the solar system constraints, to mimic the ΛCDM model at high-redshift regime where it is well tested by the CMB, and at the same time, to accelerate the expansion of the universe at low redshift but without a cosmological constant (Hu and Sawicki, 2007), suggests that

$$\lim_{R\to\infty} f(R) = \text{ const}, \qquad \lim_{R\to 0} f(R) = 0, \tag{5.11}$$

that can be satisfied by a broken power law function such that

$$f(R) = -m^2 \frac{c_1 \left(\frac{R}{m^2}\right)^n}{c_2 \left(\frac{R}{m^2}\right)^n + 1}\,, \tag{5.12}$$

where the mass scale m is defined as $m^2 \equiv H_0^2 \Omega_{\rm M}$, and c_1, c_2 and n are non-negative free parameters of the model (Hu and Sawicki, 2007). For this $f(R)$ model, the background expansion history is consistent with the ΛCDM case by choosing $c_1/c_2 = 6\Omega_\Lambda/\Omega_{\rm M}$, where Ω_Λ and $\Omega_{\rm M}$ are the dimensionless density parameters for vacuum and matter, respectively. The scalar field f_R adds an additional degree of freedom to the model, whose dynamic in the limit of $|f_R| \ll 1$ and $|f/R| \ll 1$ can be expressed in terms of perturbations of the scalar curvature, δR, and matter density, $\delta\rho$ as

$$\nabla^2 f_R = \frac{1}{3}\left(\delta R - 8\pi G \delta\rho\right)\,. \tag{5.13}$$

Comparing to the ΛCDM model expansion history, and under the condition $c_2(R/m^2)^n \gg 1$, the scalar field can be approximated by:

$$f_R \approx -n \frac{c_1}{c_2^2} \left(\frac{m^2}{R}\right)^{n+1}\,. \tag{5.14}$$

Thus, for $n = 1$ the model is fully specified by only one free parameter c_2, which in turn can be expressed in terms of the dimensionless scalar at present epoch, f_{R0}, given by:

$$f_{R0} \equiv -\frac{1}{c_2}\frac{6\Omega_\Lambda}{\Omega_M}\left(\frac{m^2}{R_0}\right)^2\,. \tag{5.15}$$

Under these assumptions, the modified Einstein's field equations for $f(R)$ gravity lead to a dynamical gravitational potential, $\Phi = \Phi_N - \delta R/6$, that satisfies the following equation:

$$\nabla^2\Phi = -\frac{16\pi G}{3}\delta\rho - \frac{1}{6}\delta R\,, \tag{5.16}$$

being Φ_N the Newtonian potential.

Nowadays it is generally accepted that some MG theories such as the Hu and Sawicki $f(R)$ are strongly degenerated in a wide range of their observables with the effects of massive neutrinos (see e.g. Baldi et al., 2014; He, 2013; Motohashi, Starobinsky, and Yokoyama, 2013; Wright, Winther, and Koyama, 2017). This represents a serious challenge constraining cosmological models from current

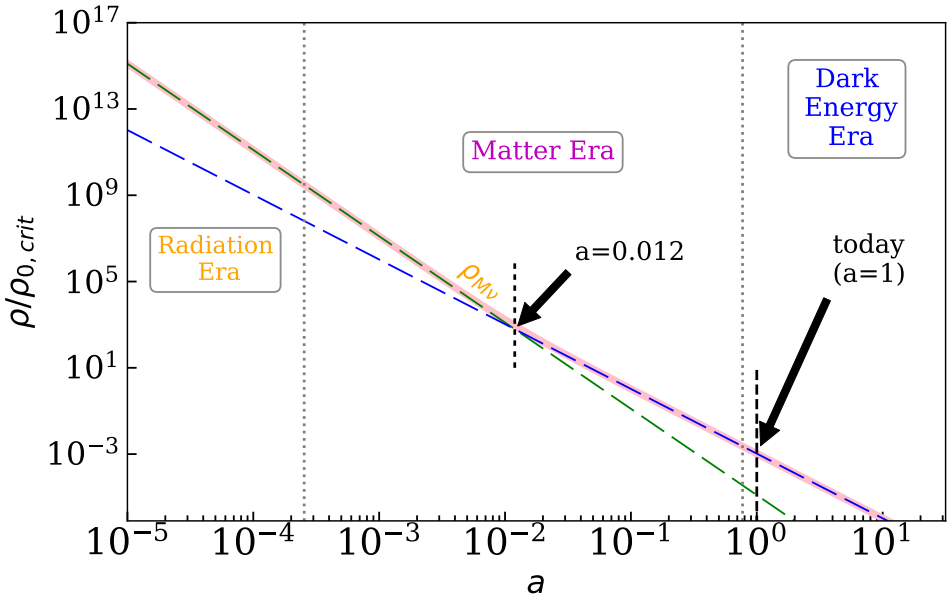

Figure 5.2: Evolution of the massive neutrino density, normalised with respect today's critical density, as a function of the scale factor a, for a neutrino mass $m_\nu = 0.1$ eV. The pink solid line shows the correct solution for $\rho_\nu(a)$, while the green and blue dashed lines show the limit at early and late time respectively. The early time limit is proportional to a^4, underlining that at early times neutrinos are relativistic and behave like radiation. The late time limit, instead, is proportional to a^3, following the same evolution of matter. The short vertical dashed line (black) marks the non-relativistic transition for neutrinos of this given mass. The figure was computed by using the CAMB code.

and future galaxy surveys requiring robust and reliable methods to disentangle both phenomena. Furthermore, for some specific combinations of the $f(R)$ gravity parameter f_{R0} and of the total neutrino mass $m_\nu \equiv \Sigma m_{\nu,i}$, standard statistics such as the matter auto-power spectrum, the lensing convergence power spectrum, and the halo mass function may be hardly distinguishable from their standard ΛCDM expectations (see Baldi et al., 2014; Peel et al., 2018a; Giocoli, Baldi, and Moscardini, 2018). In addition, since the degeneracy is mostly driven by the non-linear behaviour of both the MG and the massive neutrinos effects on the LSS, the linear tools are not suitable to properly disentangle the combined parameter space (Giocoli, Baldi, and Moscardini, 2018).

5.2. Massive neutrinos and the large-scale structure

Motivated by the apparent violation of energy, momentum and spin in β-decay processes, Pauli proposed the existence of neutrinos in 1930 to keep the conservation laws safe. Eventually, twenty six years after been theoretically postulated, the neutrinos were detected for the first time by Cowan et al. (1956). Neutrinos are classified in three 'flavour' in the standard model of particles, they were considered to be massless for some time until the discovery of the neutrino

oscillation phenomena, i.e. related to the change of flavour (Cleveland et al., 1998). Since then, it is known that at least two of the three neutrino families are massive, in contrast to the particle standard model assumption, however measuring the absolute masses of the neutrinos is not easy, which makes this a very active field of research today, both for cosmology and particle physics. In a cosmological context, the neutrinos leave detectable imprints on observations that can then be used to constrain their properties, in particular, the presence of massive neutrinos impacts the background evolution of the universe and the growth of structures (for a detailed and updated review see Lesgourgues et al., 2013; Lesgourgues and Pastor, 2014). In the early universe, massive neutrinos are relativistic and indistinguishable from the massless ones, behaving like photons, meaning that their energy density drops like $\propto a^{-4}$. In this stage, neutrinos are in thermal equilibrium and their momentum follows the standard Fermi-Dirac distribution

$$n(p)\mathrm{d}p = \frac{4\pi g_\nu}{(2\pi\hbar c)^3}\frac{p^2\mathrm{d}p}{e^{\frac{p}{k_B T_\nu}}+1}, \tag{5.17}$$

where $n(p)$ is the number of cosmic neutrinos with momentum between p and $p+dp$, g_ν is the number of neutrino spin states, $T_\nu(z)$ is the neutrino temperature at redshift z and k_B is the Boltzmann constant. In principle, in the momentum distribution function the chemical potential should be also included, however it has been shown to be negligible for cosmological neutrinos (see for example Dolgov et al., 2002; Wong, 2002; Abazajian, Beacom, and Bell, 2002). The temperature of the cosmic neutrino background and the one from CMB are related by $T_\nu(z=0) = \left(\frac{4}{11}\right)^{1/3} T_\gamma(z=0)$ (for details see e.g. Weinberg, 2008), such that the temperature of the neutrino background at certain redshift z is given by $T_\nu(z) \cong 1.95(1+z)$ K. Then, when the average momentum of neutrinos drops below a certain mass, they become non-relativistic and their energy density drops like $\propto a^{-3}$ behaving like baryons and cold dark matter. Fig. 5.2 shows the evolution of the massive neutrino density, normalised to the today's critical density, as a function of the scale factor from its early stage to the late universe.

After neutrinos with mass m_ν decouple from the rest of the plasma at redshift z_{nr}, as shown by Eq. (5.18)

$$1 + z_{nr}\,(m_\nu) \simeq 1890\left(\frac{m_\nu}{1\mathrm{eV}}\right), \tag{5.18}$$

the number density per flavour is fixed by the temperature, so that the Universe is currently filled by a relic neutrino background, uniformly distributed, with a density of 113 part/cm^3 per species and average temperature of 1.95K. As neutrinos are non-relativistic particles at late times, they contribute to the total matter density of the Universe Ω_M, so that $\Omega_M = \Omega_{\mathrm{CDM}} + \Omega_b + \Omega_\nu$, where Ω_{CDM}, Ω_b and Ω_ν are the dimensionless density parameters for CDM, baryons and neutrinos, respectively. The density background is affected by massive neutrinos such that a perturbation in the density field is well described by (Lesgourgues

et al., 2013; Castorina et al., 2014) as follows:

$$\delta_m = (1 - f_\nu)\delta_{CDM} + f_\nu \delta_\nu, \qquad \text{where} \qquad f_\nu \equiv \frac{\Omega_\nu}{\Omega_{CDM} + \Omega_\nu}, \tag{5.19}$$

being δ_ν the neutrino perturbations and Ω_ν the density contribution related to massive neutrinos that can be expressed in terms of the total neutrino mass, $m_\nu \equiv \sum_i m_{\nu_i}$, as follows:

$$\Omega_\nu = \frac{\Sigma_i m_{\nu_i}}{93.14\ h^2\text{eV}}\,. \tag{5.20}$$

Several astronomical observations provide upper limits on the total neutrino mass, that results around $0.1-0.3$ eV, under the assumption of standard GR (see e.g. Seljak, Slosar, and McDonald, 2006; Riemer-Sørensen et al., 2013; Lu et al., 2015; Lu et al., 2016; Cuesta, Niro, and Verde, 2016; Kumar and Nunes, 2016; Yèche et al., 2017; Poulin et al., 2018). Currently, one of the most important goals of precision cosmology is to extract robust, model-independent constraints on neutrino masses.

Among the main features that neutrinos imprint on cosmological observables, is well established that massive neutrinos suppress the clustering below their thermal free-streaming scale and change the matter-radiation equality time (Lesgourgues and Pastor, 2006). They also affect the non-linear matter power spectrum (Brandbyge et al., 2008; Saito, Takada, and Taruya, 2008; Saito, Takada, and Taruya, 2009; Brandbyge and Hannestad, 2009; Brandbyge and Hannestad, 2010; Agarwal and Feldman, 2011; Wagner, Verde, and Jimenez, 2012), the halo mass function (Brandbyge et al., 2010; Marulli et al., 2011; Villaescusa-Navarro et al., 2013), the clustering properties of CDM haloes and redshift-space distortions (Viel, Haehnelt, and Springel, 2010; Marulli et al., 2011; Villaescusa-Navarro et al., 2014; Castorina et al., 2014; Castorina et al., 2015; Zennaro et al., 2018), and the scale-dependent bias (Chiang, LoVerde, and Villaescusa-Navarro, 2018). Given these effects, it is thus crucial to investigate whether the cosmological effects of massive neutrinos might be degenerate with MG models, which would severely affect the constraints. Indeed, cosmological probes able to distinguish between these two effects are required to achieve tight constraints on both MG and massive neutrinos (He, 2013; Motohashi, Starobinsky, and Yokoyama, 2013; Baldi et al., 2014; Bellomo et al., 2017; Wright, Winther, and Koyama, 2017; Peel et al., 2018a; Giocoli, Baldi, and Moscardini, 2018).

5.3. N-body simulations and halo samples

Since the formation and evolution of cosmic structures is based on the growth of small fluctuations in the density field, it is expected that the amplitude of these initial perturbations have the correct value at late times to match the observed clustering today. As reviewed in Chapter §2, an analytical development based on perturbation theory makes possible to follow the growth of structures to a certain extent using the linear approximation, being valid as long as $\delta\rho \ll \rho$.

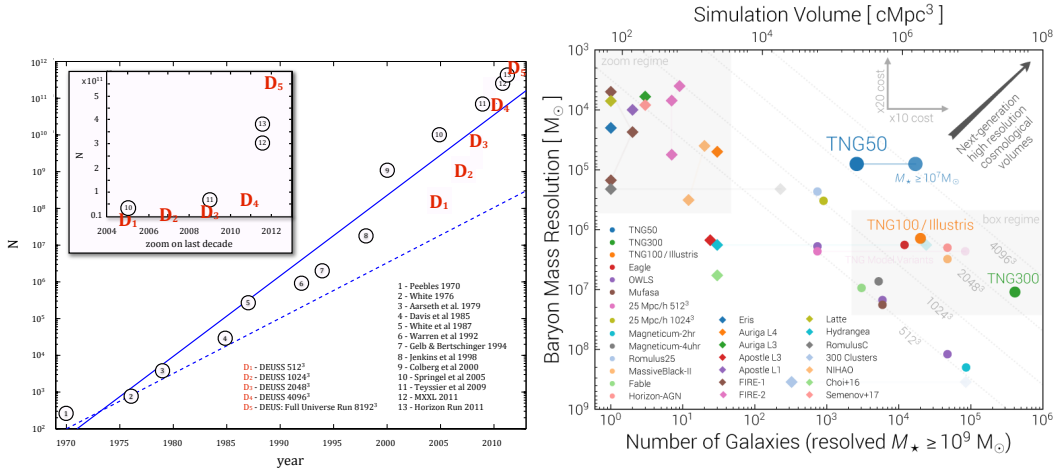

Figure 5.3: *Left panel*: Evolution of the number of particles used in cosmological N-body simulations as a function of time until 2010. Taken form (Alimi et al., 2012). *Right panel*: Resolution of hydrodynamical simulations as a function of the number of resolved galaxies (lower axis) and simulation volume (upper axis) from the `IllustrisTNG project` www.tng-project.org/.

Nevertheless, these calculations are limited and can not be extrapolated to explain completely the observational data, they break down on a scale where the density contrast $\delta \sim 1$. Moreover, beyond the linear regime, the observed structures have a density contrast in a wide range from cosmic voids with $\delta \sim -1$ to $\delta \sim 10^6$ and larger. It makes necessary a more elaborated description of the perturbations in the non-linear regime, which can be achieved using higher order perturbation theory or numerical simulations (Yepes, 2001).

Over the past three decades, cosmological simulations have played a key role in exploring the cosmic structure landscape, becoming a powerful tool for testing theoretical predictions and to lead observational projects. In this context, the formation and evolution of cosmic structures can be understood as a dynamical system of many particles, that trace the underlying mass distribution in a certain cosmological model. The N-body simulations, methods and algorithms have progressed continuously achieving a high-resolution to resolve finer structures with millions of particles, reducing the gap between theory and observations. For a detailed description on fundamentals of cosmological simulations see e.g. Yepes (2001), Knebe (2005), Moscardini and Dolag (2011), and Dolag et al. (2008). The *left panel* of Fig. 5.3 shows the evolution of the number of particles in N-body simulations as a function of time in years until 2010 (Alimi et al., 2012). The solid blue line is the mean evolution of the simulation size from Springel (2005) and the dashed blue line is an analogous of the Moore's Law which shows that the volume increases by a factor of two every 18 months. The marks 'D' in red correspond to the simulations of the project AMA-DEUS - A Multiple purpose Application for Dark Energy Universe Simulation - (Alimi et al., 2012). The *right panel* of Fig. 5.3 shows the state of art of hydrodynamical simulations from the IllustrisTNG project, where the resolution is plotted as a function of the number of resolved galaxies and volume.

To investigate the clustering in the modified gravity context with massive neutrinos, we used a subset of the DUSTGRAIN-*pathfinder* (Dark Universe Simulations to Test GRAvity In the presence of Neutrinos) cosmological N-body simulations, which is part of a numerical project aimed at investigating possible cosmic degeneracies. In a series of recent papers, these simulations have been exploited to investigate several features related to weak-lensing statistics (Giocoli, Baldi, and Moscardini, 2018; Peel et al., 2018a), to the abundance of massive haloes (Hagstotz et al., 2018) and to explore cosmic degeneracies using machine learning techniques (Peel et al., 2018b; Merten et al., 2018). The DUSTGRAIN-*pathfinder* runs have been performed using the MG-Gadget code (Puchwein, Baldi, and Springel, 2013), which is a modified version of GADGET (Springel, 2005) implementing the Hu and Sawicki (2007) $f(R)$ gravity model, with a mixture of cold and hot DM components, the latter made up of massive neutrinos. The simulations were carried out in a box of (750 Mpc/h)^3 volume, with periodic boundary conditions, and 768^3 DM particles. The cosmological parameters assumed for all the considered models at $z = 0$ are consistent with Planck 2015 constraints (Planck Collaboration et al., 2016b): $\Omega_{\rm M} \equiv \Omega_{\rm CDM} + \Omega_{\rm b} + \Omega_\nu = 0.31345$, $\Omega_{\rm b} = 0.0481$, $\Omega_\Lambda = 0.68655$, $H_0 = 67.31$ km s^{-1} Mpc^{-1}, $\mathcal{A}_{\rm s} = 2.199 \times 10^{-9}$, $n_s = 0.9658$ and $\sigma_8 = 0.847$.

We identify haloes in the particle distribution using the Spherical Overdensity (SO) algorithm termed `Denhf` (Tormen, 1998; Tormen, Moscardini, and Yoshida, 2004; Giocoli, Tormen, and van den Bosch, 2008; Despali et al., 2016). This method has been chosen over the Friends-of-Friends (FoF) group finding algorithm by Davis et al. (1985), because it appears to be slightly closer to physical models of halo formation, and because of its resemblance to the definition of the mass in observational data sets. Specifically, for each particle we compute the local DM density by calculating the distance $d_{i,10}$ to the tenth nearest neighbour. In this way, we assign to each particle a local density $\rho_i \propto d_{i,10}^{-3}$. Next, we sort the particles by density and define the position of the densest particle as the centre of the first halo. Around this centre, the algorithm grows a sphere with a certain average density, that in this work has been chosen to be 200 times the critical density of the Universe. At this point we assign all particles within the sphere to the newly identified halo, removing them from the global list of particles. Subsequently, the densest particle of the remaining distribution is chosen and the process is repeated several times, until none of the remaining particles has a local density large enough to be the centre of a 10 particle halo. The particles that are not assigned to any haloes are called 'field' or 'dust' particles. In numerical simulations containing massive neutrinos, we assume that they contribute only to the expanding cosmological background metric (Castorina et al., 2014) and thus, when identifying the haloes, we link together only DM particles.

Tab. 5.1 presents an overview of the main parameters of each simulation, such as the f_{R0} values, the total neutrino mass, the total CDM density contrast, $\Omega_{\rm CDM}$, and the mass of the DM particles. In all cases, the scalar at present

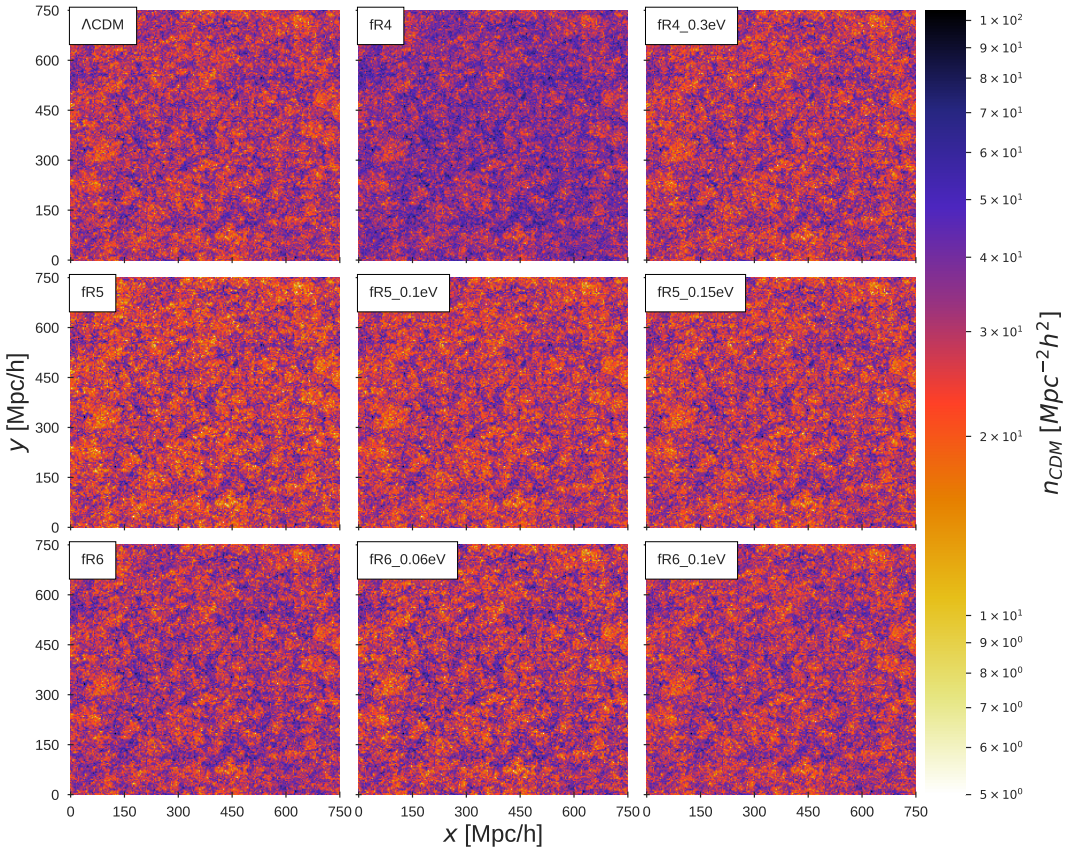

Figure 5.4: Maps of the projected number density of CDM haloes in the mass range $[4 \times 10^{12},\ 7 \times 10^{14}]\ \mathrm{M}_\odot/h$ extracted from the DUSTGRAIN-*pathfinder* simulations at $z = 0$. The boxes have been divided into 300×300 pixels and the colorbar indicates the normalised number of CDM haloes n_{CDM} per unit area ($2.5 \times 2.5\ \mathrm{Mpc}^2 h^{-2}$).

epoch, $|f_{R0}|$, is in the range $10^{-4} - 10^{-6}$, as suggested by Hu and Sawicki (2007), to be consistent with distance-based measurements of the expansion history. The total neutrino masses considered in this work are $m_\nu = 0,\ 0.06,\ 0.1,\ 0.15,\ 0.3$ eV. As shown in Fig. 5.4 at $z = 0$, the density distributions of CDM haloes predicted by the MG models considered show notable differences, as it can be appreciated, for instance, comparing $f(R)$ and $f(R) + m_\nu$ models. For the clustering analysis presented in the following Sections, we make use of halo samples from each of the nine models presented in Tab. 5.1, restricting our analysis in the mass range $M_{\mathrm{min}} < M < M_{\mathrm{max}}$, where $M_{\mathrm{min}} = 4 \times 10^{12} \mathrm{M}_\odot/h$ and $M_{\mathrm{max}} = 7 \times 10^{14},\ 4 \times 10^{14},\ 3 \times 10^{14},\ 2 \times 10^{14},\ 10^{14} \mathrm{M}_\odot/h$ at $z = 0,\ 0.5,\ 1,\ 1.4,\ 1.6$, respectively. In particular we focus on the halo clustering modelled through DM N-body simulations that include simultaneously both effects.

Simulation name	Gravity model	f_{R0}	m_ν [eV]	$\Omega_{\rm CDM}$	Ω_ν	$m^p_{\rm CDM}$ [$\rm M_\odot/h$]	m^p_ν [$\rm M_\odot/h$]	σ_8
ΛCDM	GR	–	0	0.31345	0	8.1×10^{10}	0	0.842
$fR4$	$f(R)$	-1×10^{-4}	0	0.31345	0	8.1×10^{10}	0	0.963
$fR5$	$f(R)$	-1×10^{-5}	0	0.31345	0	8.1×10^{10}	0	0.898
$fR6$	$f(R)$	-1×10^{-6}	0	0.31345	0	8.1×10^{10}	0	0.856
$fR4\_0.3eV$	$f(R)$	-1×10^{-4}	0.3	0.30630	0.00715	7.92×10^{10}	1.85×10^{9}	0.887
$fR5\_0.15eV$	$f(R)$	-1×10^{-5}	0.15	0.30987	0.00358	8.01×10^{10}	9.25×10^{8}	0.859
$fR5\_0.1eV$	$f(R)$	-1×10^{-5}	0.1	0.31107	0.00238	8.04×10^{10}	6.16×10^{8}	0.872
$fR6\_0.06eV$	$f(R)$	-1×10^{-6}	0.06	0.31202	0.00143	8.07×10^{10}	3.7×10^{8}	0.842
$fR6\_0.1eV$	$f(R)$	-1×10^{-6}	0.1	0.31107	0.00238	8.04×10^{10}	6.16×10^{8}	0.831

Table 5.1: Summary of parameters used in the DUSTGRAIN-*pathfinder* simulations considered in this work: f_{R0} represents the modified gravity parameter, m_ν is the neutrino mass in electronvolt, $\Omega_{\rm CDM}$ and Ω_ν are the CDM and neutrino density parameters, $m^p_{\rm CDM}$ and m^p_ν are the CDM and neutrino particle masses (in $\rm M_\odot/h$), respectively. The value in the last column displays the σ_8 parameter at $z = 0$, which corresponds to the linear density fluctuations smoothed on a scale of $8h^{-1}\,$Mpc, computed from linear theory. In particular, for the $f(R)$ models we have computed σ_8 from linear theory using MG-CAMB, while for the combined models of massive neutrinos plus $f(R)$ we joined together the predictions of CAMB for massive neutrinos with those of MG-CAMB.

5.4. The halo mass function

As CDM haloes form from collapsing regions that detaches from the background density field, their abundance can be related to the volume fraction of a Gaussian density smoothed on a radius R above a critical collapse threshold δ_c (Press and Schechter, 1974). The comoving number density of the haloes is strictly related to underlining cosmological model, such that within a mass interval $[M,\ M + dM]$, the halo mass function is given by

$$\frac{\mathrm{d}n(M,z)}{\mathrm{d}M} = f(\sigma(M,z))\frac{\overline{\rho}}{M}\frac{\mathrm{d}\ln\sigma(M,z)^{-1}}{\mathrm{d}M}, \tag{5.21}$$

where $f(\sigma)$ is the multiplicity function, σ the RMS variance of the linear density field smoothed on scale $R(M)$ and $\overline{\rho}$ is the mean matter density. The product $f(\sigma(M,z))\overline{\rho}$ quantifies the amount of mass contained in fluctuations of typical mass $M = \frac{4}{3}\pi R^3\overline{\rho}$. The simplest argument to compute analytically the multiplicity function $f(\sigma)$ comes from the spherical collapse theory, following the Press and Schechter (1974) formalism, such that a perturbation is supposed to collapse when it reaches the threshold $\delta_c \simeq 1.68$, by assuming that the probability distribution for a perturbation on a scale M is a Gaussian function with variance σ_M^2, resulting

$$f(\sigma(M)) = \sqrt{\frac{2}{\pi}}\frac{\delta_c}{\sigma(M)}\exp\left(-\frac{\delta_c^2}{2\sigma^2(M)}\right). \tag{5.22}$$

Another approach to determine $f(\sigma)$ is given by accurate fitting functions, like the proposed by Tinker et al. (2008), which extends phenomenologically the results of Press and Schechter (1974). For Tinker et al. the function $f(\sigma)$ is expected to be universal to the changes in redshift and cosmology, and is parametrized as follows:

$$f(\sigma) = A\left[\left(\frac{\sigma}{b}\right)^{-a} + \sigma^{-c}\right]\exp\left(-d/\sigma^2\right), \tag{5.23}$$

where A is an amplitude of the mass function and a, b, c, and d are free parameters that depend on halo definition. The variance σ^2 is usually given by

$$\sigma^2(R(M),z) = \int \frac{P(k,z)}{2\pi^2}W^2(kR(M))k^2\mathrm{d}k, \tag{5.24}$$

where $P(k)$ is the linear matter power spectrum as a function of the wave number k, and W is the Fourier transform of the real-space top-hat window function of radius R. A fundamental feature of the mass function is that it decreases monotonically with increasing masses, furthermore, its dependency on cosmology is encoded in the variance σ^2, as shown by the integrand of Eq. (5.24). From the point of view of N-boby simulations, an approach to compute the mass function is given straightforward from Eq. (5.21), by counting the number of haloes N_h

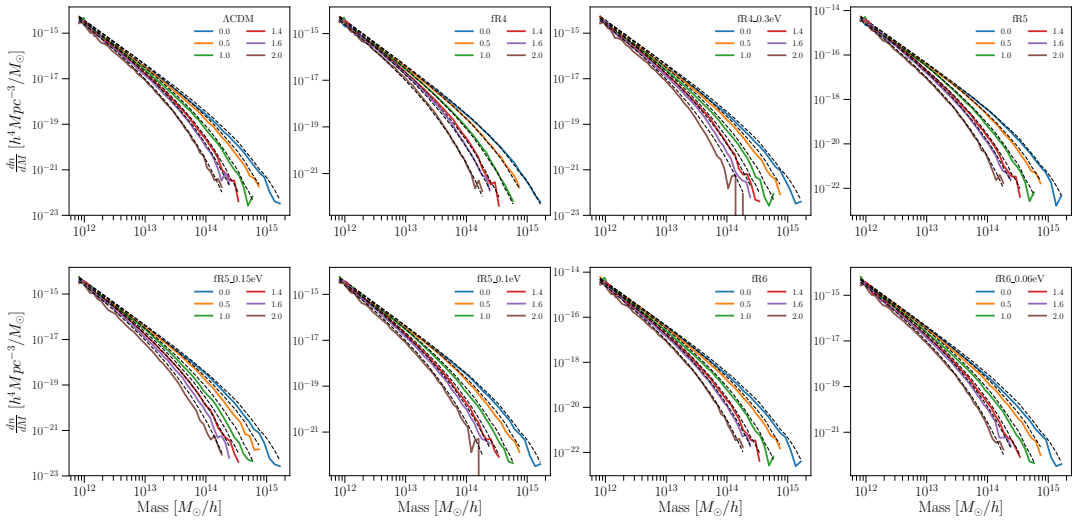

Figure 5.5: The mass function of CDM haloes per each model of the DUSTGRAIN-*pathfinder* project at six different redshifts $z = 0, 0.5, 1, 1.4, 1.6, 2$ as labelled. Each panel corresponds to one model as labelled, and the dashed line represents the theoretical expectation by Tinker et al. (2008) assuming a flat ΛCDM model.

above a certain mass threshold M_{min} in a comoving volume V such as

$$N_h = A \int_{z_{min}}^{z_{max}} \int_{M_{min}}^{\infty} \frac{\mathrm{d}V}{\mathrm{d}z} n(M, z) \mathrm{d}M \mathrm{d}z, \tag{5.25}$$

where A is the area, z_{min} and z_{max} are the redshift boundaries and dV/dz is the comoving volume element.

Fig. 5.5 shows the mass function of CDM haloes measured for all models of the DUSTGRAIN-*pathfinder* runs at six different redshifts $z = 0, 0.5, 1, 1.4, 1.6, 2$. Each panel contains the mass function, per each model as labelled, to track its evolution in redshift. As reference, the black dashed line represents the theoretical expectation by Tinker et al. (2008) for a flat ΛCDM model. As expected, massive haloes are less abundant with respect to smaller ones in a fixed comoving volume. The mass function decreases with redshift, since at earlier times the density field is smoother than at late times. The plot is logarithmic, meaning that the number density of large mass haloes falls off by several orders of magnitude over the range of redshifts shown. The $f(R)$ models both with and without neutrinos reproduce in very well agreement this pattern, but only at really high masses significant differences appear.

Fig. 5.6 compares the halo mass functions of the different DUSTGRAIN-*pathfinder* simulations, computed at $z = 0$ (left column), $z = 1$ (central column) and $z = 1.6$ (right column). The lower panels show the percentage difference with respect to the ΛCDM model. It is possible to see that the effect of $f(R)$ and massive neutrinos on the dynamical evolution of the matter density field results in different halo formation epochs and different number density of collapsed systems. In particular, the $fR4$ model (blue) is the most deviated model from

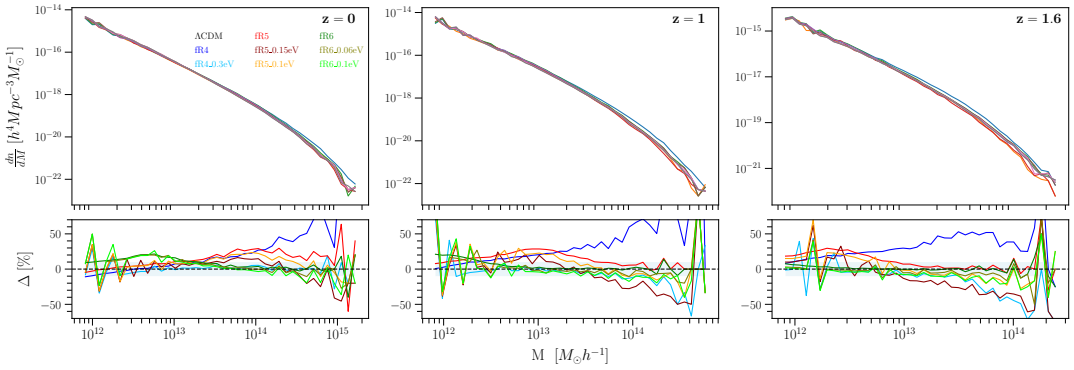

Figure 5.6: The mass function of CDM haloes for all the models of the DUSTGRAIN-*pathfinder* at three different redshifts: $z = 0$ (left column), $z = 1$ (central column), $z = 1.6$ (right column). The lower panels show the percentage difference with respect to the ΛCDM model. As in Fig. 5.5 the dashed line represents the theoretical prediction by Tinker et al. (2008).

the standard scenario whereas the $fR6$, $fR6\_0.06eV$ and $fR6\_0.1eV$ models mimic the ΛCDM behaviour over a wide range of masses.

5.5. Clustering in real space

In the first part of this Section, we present the methodology used to quantify the halo clustering in real space, focusing on the first multipole moment of the 2PCF, that is the monopole. In the second part, the halo biasing function derived from the previous mass functions is studied.

All the numerical computations in the current Section and in the following ones have been performed with the CosmoBolognaLib, a large set of *free software* libraries that provide all the required tools for the data analysis presented in this Thesis, including the measurements of all statistical quantities and the Bayesian inference analysis[2] (Marulli, Veropalumbo, and Moresco, 2016).

5.5.1. The two-point correlation function

To measure the 2D 2PCF, $\xi(r, \mu)$, we used the Landy and Szalay (1993) estimator given by

$$\hat{\xi}(r, \mu) = \frac{DD(r, \mu) - 2DR(r, \mu) + RR(r, \mu)}{RR(r, \mu)}\,, \tag{5.26}$$

where μ is the cosine of the angle between the line of sight and the comoving halo pair separation, r; $DD(r, \mu)$, $RR(r, \mu)$, and $DR(r, \mu)$ represent the normalised

[2]Specifically, we used CosmoBolognaLib V5.0. The CosmoBolognaLib are entirely implemented in C++. They also provide the possibility to be converted in Python modules through wrappers. Both the software and its documentation are freely available at the public GitHub repository: https://github.com/federicomarulli/CosmoBolognaLib.

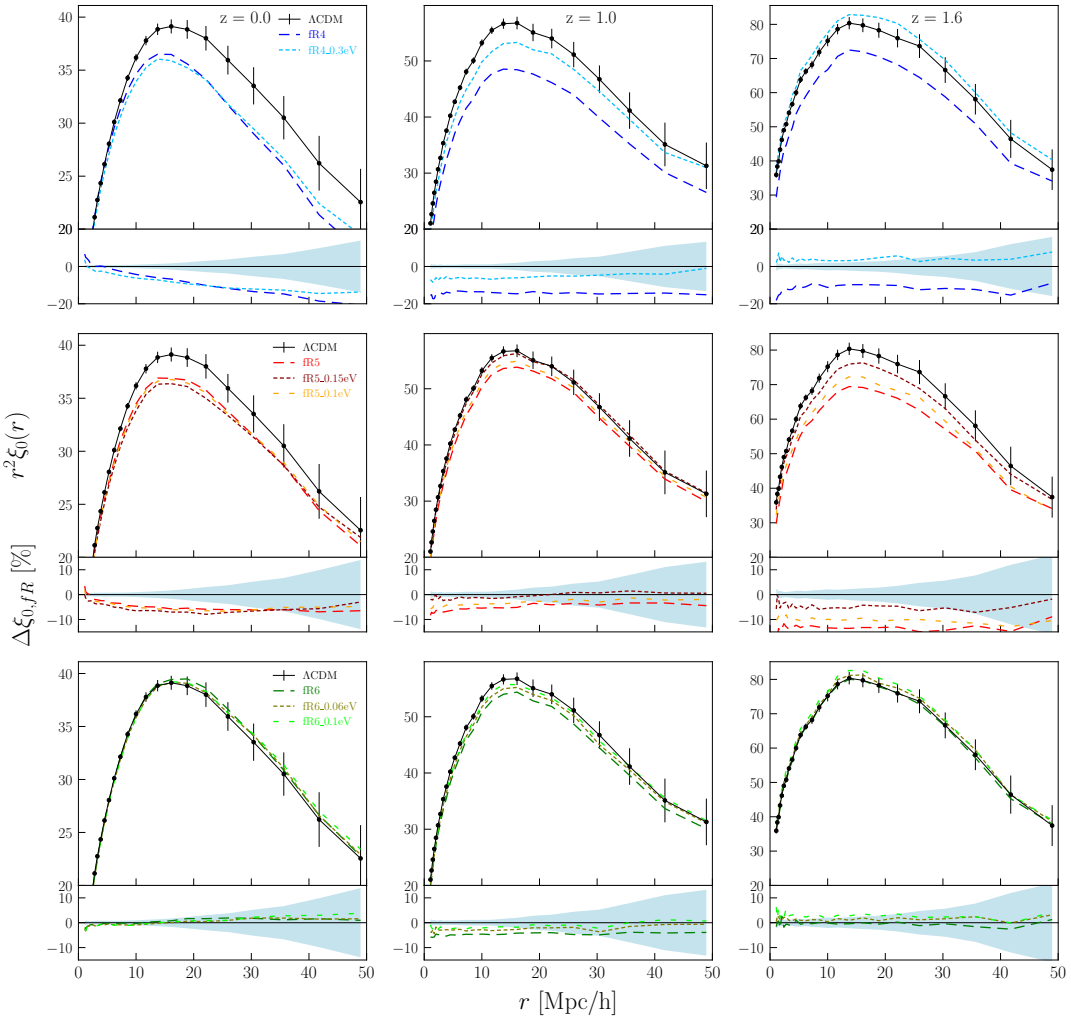

Figure 5.7: The real-space 2PCF $r^2\xi_0$ of CDM haloes for all the models of the DUSTGRAIN-*pathfinder* project at three different redshifts: $z = 0$ (left column), $z = 1$ (central column), $z = 1.6$ (right column). From top to bottom, the panels show the $fR4$, $fR5$ and $fR6$ models, respectively, compared to the results of the ΛCDM model. The error bars, shown only for the ΛCDM model for clarity reasons, are the diagonal values of the bootstrap covariance matrices used for the statistical analysis. Percentage differences between $f(R)$, $f(R) + m_\nu$ and ΛCDM predictions are in the subpanels, while the shaded regions represent the deviation at 1σ confidence level.

number of data-data, random-random and data-random pairs, respectively, in ranges of r and μ. We consider intermediate scales from $1h^{-1}\,\mathrm{Mpc}$ to $50h^{-1}\,\mathrm{Mpc}$, in 25 linear bins. The random samples used are ten times larger than the halo ones. The 2PCF uncertainties are estimated with the bootstrap method, by dividing the original data sets into 27 sub-samples, which are then re-sampled in 100 data sets with replacement, measuring $\xi(r,\mu)$ in each one of them (Efron, 1979; Barrow, Bhavsar, and Sonoda, 1984; Ling, Frenk, and Barrow, 1986).

For the reasons discussed in Chapter §4, it is convenient to expand the 2D 2PCF in terms of Legendre polynomials, $L_l(\mu)$, as follows:

$$\xi(s,\mu) \equiv \xi_0(s)L_0(\mu) + \xi_2(s)L_2(\mu) + \xi_4(s)L_4(\mu)\,, \tag{5.27}$$

where each coefficient corresponds to the l^{th} multipole moment:

$$\xi_l(r) = \frac{2l+1}{2}\int_{-1}^{+1} d\mu\,\xi(r,\mu)L_l(\mu)\,. \tag{3.21}$$

The clustering multipoles are computed with the *integrated estimator* (e.g. Kazin, Sánchez, and Blanton, 2012), which consists in calculating $\xi(r,\mu)$ in 2D bins and then integrating it as follows:

$$\hat{\xi}_l(r) = \frac{2l+1}{2}\int_{-1}^{+1} d\mu L_l(\mu)\frac{DD(r,\mu) - 2DR(r,\mu) + RR(r,\mu)}{RR(r,\mu)}\,. \tag{5.28}$$

In real space the full clustering signal is contained in the monopole moment $\xi_0(r)$. Fig. 5.7 shows $\xi_0(r)$ of the CDM haloes for all models considered in the DUSTGRAIN-*pathfinder* project, at three different redshifts $z = 0, 1, 1.6$. Subpanels show the percentage difference between MG models [$f(R)$ with and without massive neutrinos], and the ΛCDM model, computed as $\Delta\xi_{\mathrm{fR}} = 100(\xi_{\mathrm{fR}} - \xi_{\Lambda\mathrm{CDM}})/\xi_{\Lambda\mathrm{CDM}}$.

The clustering properties of $fR4$ and $fR4\_0.3eV$ models at $z = 0$ are the ones that deviate the most from ΛCDM, with a significant clustering suppression at scales larger than 10 $h^{-1}\,\mathrm{Mpc}$. This is expected, as the f_{R0} value of these models is the most extreme one considered, marginally compatible with the constraints from solar system observations (Hu and Sawicki, 2007). At higher redshifts the $fR4\_0.3eV$ monopole gets closer to the ΛCDM one, due to the effect of massive neutrinos. A similar, though less significant, effect is found also for $fR5$, $fR5\_0.15eV$ and $fR5\_0.1eV$ models. The clustering suppression is further reduced in the $fR6$, $fR6\_0.06eV$ and $fR6\_0.1eV$ models, so that they appear highly degenerate with ΛCDM at all the scales and redshifts considered, with deviations smaller than 2%.

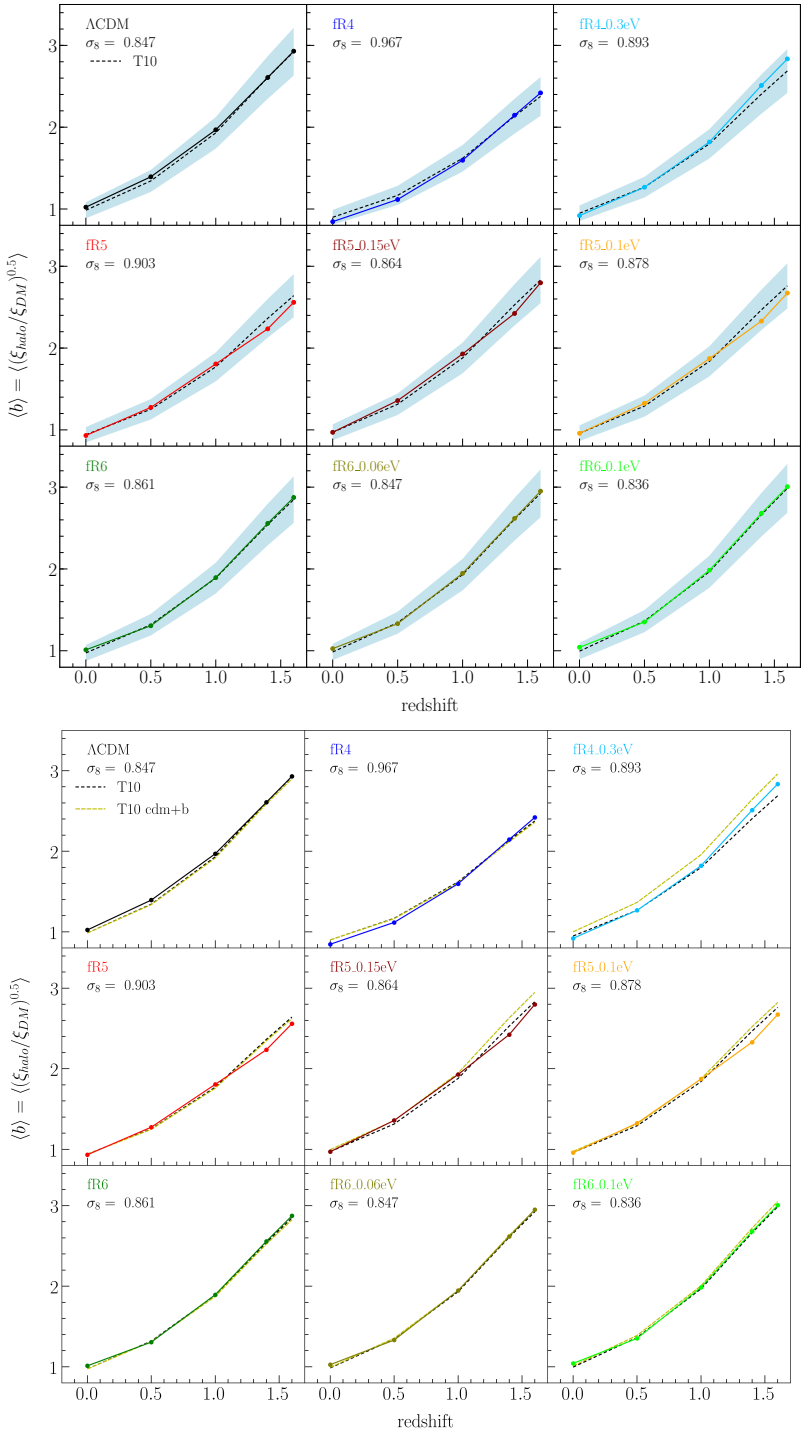

Figure 5.8: The coloured solid lines represent the *apparent* effective halo bias, $\langle b \rangle$, as a function of redshift, averaged in the range $10h^{-1}\,\mathrm{Mpc} < r < 50h^{-1}\,\mathrm{Mpc}$. Black lines show the theoretical ΛCDM effective bias predicted by Tinker et al. (2010) (dashed), normalised to the σ_8 values of each DUSTGRAIN-*pathfinder* simulation, while the cyan shaded areas show a 10% error. The *upper set of panels* shows the results considering the total power spectrum, while the *lower set of panels* shows the results when the CDM+baryon power spectrum is used instead.

5.5.2. The halo bias

We estimate the effective halo bias to characterise the relation between the halo clustering and the underlying mass distribution. In the linear regime, the bias is approximately independent of the scale, depending only on halo masses and redshifts. In our mass-selected samples, this quantity can be computed as follows, averaging in a given scale range:

$$\langle b(z) \rangle = \left\langle \sqrt{\frac{\xi_{\rm halo,fR}}{\xi_{\rm DM,\Lambda CDM}}} \right\rangle , \tag{5.29}$$

where $\xi_{\rm halo,fR}$ and $\xi_{\rm DM,\Lambda CDM}$ are the CDM halo 2PCF of the DUSTGRAIN-*pathfinder* models and the CDM 2PCF estimated in ΛCDM, respectively. Eq. (5.29) is obtained by Fourier transforming the non-linear matter power spectrum computed with CAMB, including HALOFIT (Lewis, Challinor, and Lasenby, 2000; Smith et al., 2003). The latter simulates the *apparent* bias that would be assessed in a $f(R)$ Universe if a ΛCDM model was wrongly assumed to predict the DM clustering (see Marulli, Baldi, and Moscardini, 2012, for more details). The *apparent* effective bias is then estimated by averaging the bias $b(M, z)$ over a set of CDM haloes with given mass M_i:

$$b(z) = \frac{1}{N_{\rm halo}} \sum_{i=1}^{N_{\rm halo}} b(M_i, z) \, , \tag{5.30}$$

where $N_{\rm halo}$ is the number of haloes enclosed in the sample volume and $b(M_i, z)$ is their linear bias computed using the theoretical Tinker et al. (2008) mass function. Then, in order to compare measurements in $f(R)$ and $f(R) + m_\nu$ scenarios with the ΛCDM ones, we consider the theoretical effective bias proposed by Tinker et al. (2010), computed with the so-called *CDM prescription* (Villaescusa-Navarro et al., 2014), that is, using the linear CDM+baryons power spectrum[3], and replacing ρ_m with $\rho_{\rm CDM}$ (Castorina et al., 2014). It implies, as shown by Costanzi et al. (2013), that the effect of neutrinos on the cluster abundance is well captured by rescaling the smoothed density field such that

$$\sigma^2 \rightarrow \sigma^2_{\rm CDM}(z) = \int \frac{P_{\rm CDM}(k, z)}{2\pi^2} W^2(kR) k^2 {\rm d}k \tag{5.31}$$

with the CDM power spectrum obtained by rescaling the total matter power spectrum with the corresponding transfer functions, T_{CDM} and T_b, weighted by the density of each species so that

$$P_{\rm CDM}(k, z) = P_{\rm m}(k, z) \left(\frac{\Omega_{\rm CDM} T_{\rm CDM}(k, z) + \Omega_{\rm b} T_{\rm b}(k, z)}{T_{\rm m}(k, z) \, (\Omega_{\rm CDM} + \Omega_{\rm b})} \right)^2 . \tag{5.32}$$

However the CDM prescription has a minor impact on the results presented in this work as it can be appreciated in the lower panel of Fig. 5.8. Comparing to the

[3]Both $P_{lin}^{\rm CDM+b}(k)$ and $P_{lin}^{m}(k)$ can be directly obtained with CAMB, since $P_{lin}^{\rm CDM}(k) = T^2_{\rm CDM}/T^2_m P_{lin}^m(k)$, where $T_{\rm CDM}(k)$ and $T_b(k)$ are the corresponding transfer functions.

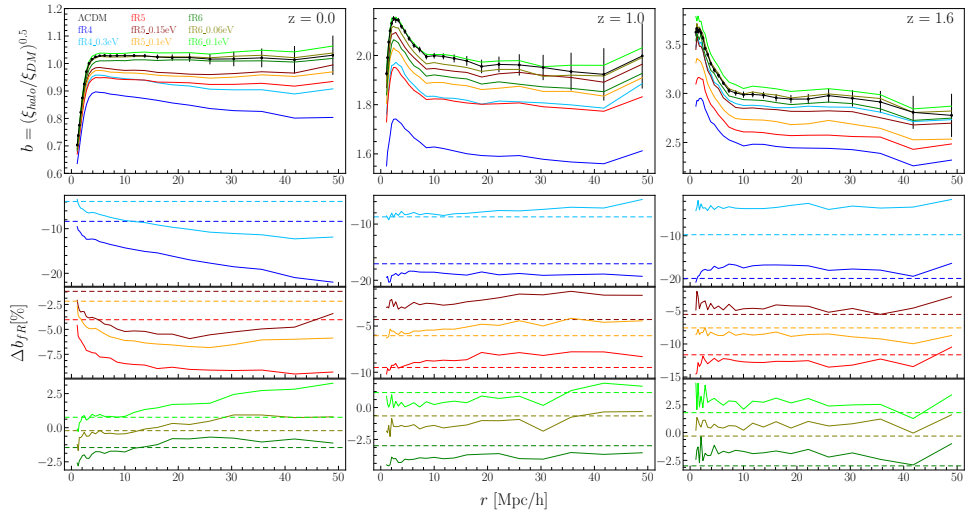

Figure 5.9: The *apparent* effective halo bias as a function of scale, for three different redshifts ($z = 0,\ 1$ and 1.6, columns from left to right), for all models, as indicated by the labels. Dotted and dashed horizontal lines show theoretical predictions, as in Fig. 5.8.

results obtained with the total matter power spectrum, we found deviations on the estimated halo bias smaller than 1% for $fR5+m_\nu$ and $fR6+m_\nu$ models, and of about 3% for $fR4+m_\nu$ model. Fig. 5.8 shows the mean *apparent* effective bias as a function of redshift, averaged over the range $10h^{-1}\,\mathrm{Mpc} < r < 50h^{-1}\,\mathrm{Mpc}$, whereas Fig. 5.9 shows how it changes as a function of scale. The error bars are computed by propagating the 2PCF uncertainties obtained with the bootstrap method (for details see Section 5.5.1). Dashed lines represent the theoretical expectations by Tinker et al. (2010), while the shaded region shows a 10% difference with respect to the central value. The effective bias increases as a function of redshift, as expected (Matarrese et al., 1997; Ma, 1999). The predicted effective bias of all the models considered appears quite indistinguishable from the ΛCDM case, when it is normalised to the σ_8 values of the DUSTGRAIN-*pathfinder* cosmologies, that is assuming $\xi_{DM,f(R)} = \xi_{DM,\Lambda\mathrm{CDM}(\sigma_8)}$, where $\xi_{DM,\Lambda\mathrm{CDM}(\sigma_8)}$ is computed by setting the amplitude of the primordial curvature perturbations to the values required to have the σ_8 values of the $f(R)$ models (see e.g. Marulli et al., 2011; Marulli et al., 2012). The largest deviation occurs at $z = 1.6$ for the $fR4\_0.3eV$ model, though it is in any case not statistically significant (between 5% and 7%, averaging over different distances larger than $10h^{-1}\,\mathrm{Mpc}$). As a counterpart, the most degenerate model is $fR6$, both with and without massive neutrinos, which is in agreement with ΛCDM better than 2% at all scales.

5.6. Clustering in redshift-space

In a realistic case, spectroscopic surveys observe a combination of density and velocity fields in redshift space. Specifically, the observed redshift, $z_{\rm obs}$, of extragalactic sources is a combination of the cosmological redshift, z_c, due to the Hubble flow, and an additional term caused by the peculiar velocities along

the line of sight:

$$z_{\rm obs} = z_c + (1 + z_c)\frac{\mathbf{v}\cdot\hat{\mathbf{r}}}{c}\,, \tag{3.3}$$

where $\hat{\mathbf{r}}$ is a unit vector along the line of sight, so that the contribution of peculiar motions is given by $v_\parallel = \mathbf{v}\cdot\hat{\mathbf{r}}$. As a consequence, redshift-space catalogues appear distorted with respect to the real-space ones. Since in N-body simulations both positions and peculiar velocities are known, the distorted mass distribution in redshift space can be derived directly. Specifically, we first convert the comoving coordinates of each CDM halo, {x, y, z}, into polar real-space coordinates {R.A., Dec, z_c}, relative to a given virtual observer placed at random, where R.A. and Dec are the Right Ascension and Declination, respectively. Then, we estimate the observed redshifts using Eq. (3.3). Finally, we convert back {R.A., Dec, $z_{\rm obs}$} into *distorted* comoving coordinates {x', y', z'}, mimicking the redshift space.

Redshift-space distortions turned out to be one of the most powerful cosmological probes to test the gravity theory on the largest scales (Kaiser, 1987; Guzzo et al., 2008; Simpson and Peacock, 2010; Jennings et al., 2012; Raccanelli, Percival, and Samushia, 2012; He et al., 2018). In redshift space, the spatial statistics of cosmic tracers, such as the 2PCF and power spectrum, are anisotropic due to the dynamic distortions along the line of sight (Hamilton, 1998; Scoccimarro, 2004): at large scales the matter density distribution appears squashed along the line of sight, while an opposite stretching distortion is present at small scales, the so-called *fingers of God* (FoG) effect (Jackson, 1972).

The effect of redshift-space distortions on the 2PCF is shown conveniently by decomposing the pair comoving distances into their parallel and perpendicular components to the line of sight, that is $\vec{s} = (s_\parallel, s_\perp)$. Hereafter, we will use s to indicate redshift-space coordinates. The anisotropic redshift-space 2PCFs, $\xi(s_\perp, s_\parallel)$, of all our DUSTGRAIN-*pathfinder* halo catalogues at $z = 1.6$ are shown in Fig. 5.10. Similarly to the real-space case, the 2PCF predicted by the $f(R)$ model with $|f_{R0}| = 10^{-6}$, both with and without massive neutrinos, is quite similar to the ΛCDM one. On the other hand, the $|f_{R0}| = 10^{-4}$ model with massless neutrinos predicts a lower signal on all scales.

As described in Section 5.5.1, the 2D 2PCF can be conveniently expressed in the Legendre multipole base. For simplicity, we focus here only on the first two even multipoles of the 2PCF, that is the monopole, ξ_0, and the quadrupole, ξ_2. The signal in the other even multipoles of the redshift-space 2PCF of CDM halo in the considered simulations is negligible, while odd multipoles vanish by symmetry. Fig. 5.11 shows the monopole and quadrupole of the redshift-space 2PCF of all the halo catalogues considered in this work. As expected, the $\{|f_{R0}| = 10^{-4}, m_\nu = 0.3eV\}$ model is the one that differs the most from ΛCDM. This is particularly evident in the monopole. On the other hand, the quadrupole appears less sensitive to the effect of the alternative cosmologies considered, both with and without massive neutrinos. The percentage differences with respect to the ΛCDM case are shown in the lower panels. For the quadrupole they are

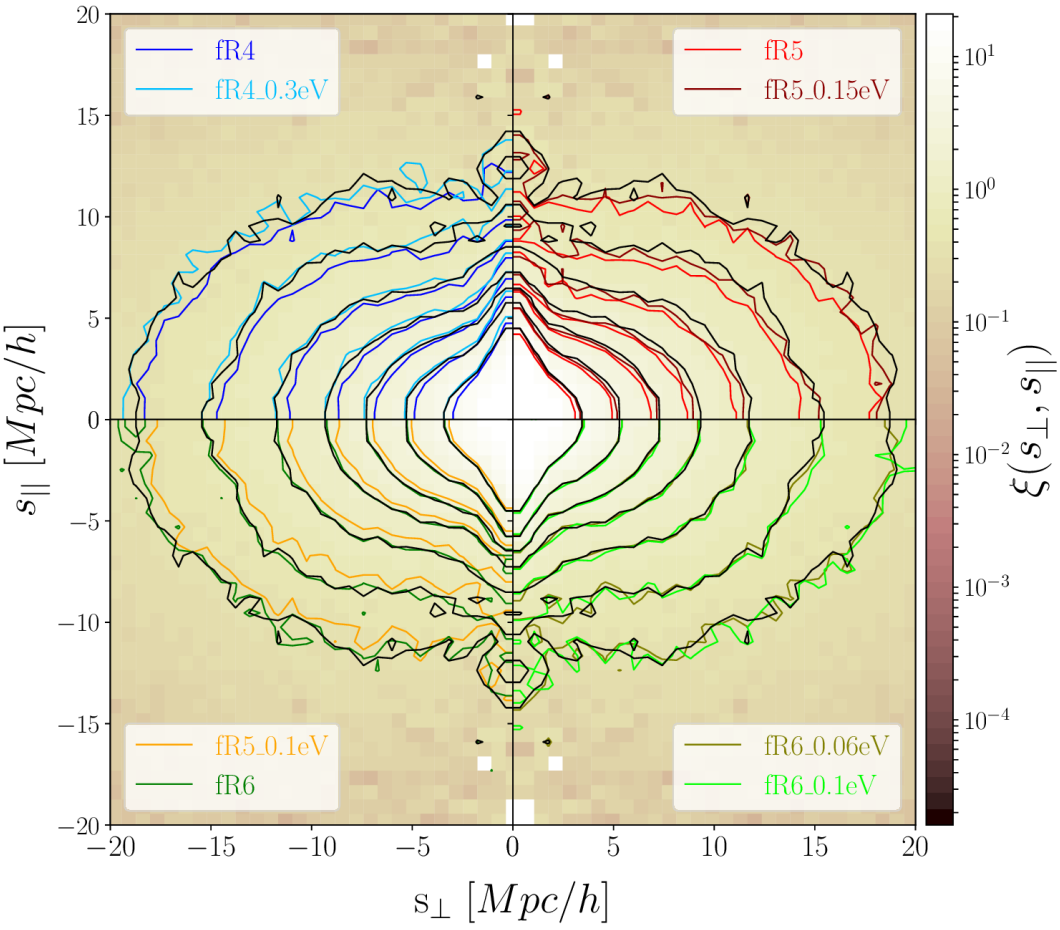

Figure 5.10: Contour lines of the 2D 2PCF of the DUSTGRAIN-*pathfinder* simulations at $z = 1.6$. Each quadrant refers to a different set of models, as labelled in the plot. The iso-curves plotted are $\xi(s_{\perp}, s_{\parallel}) = \{0.3,\ 0.5,\ 1.0,\ 1.4,\ 2.2,\ 3.6,\ 7.2,\ 21.6\}$.

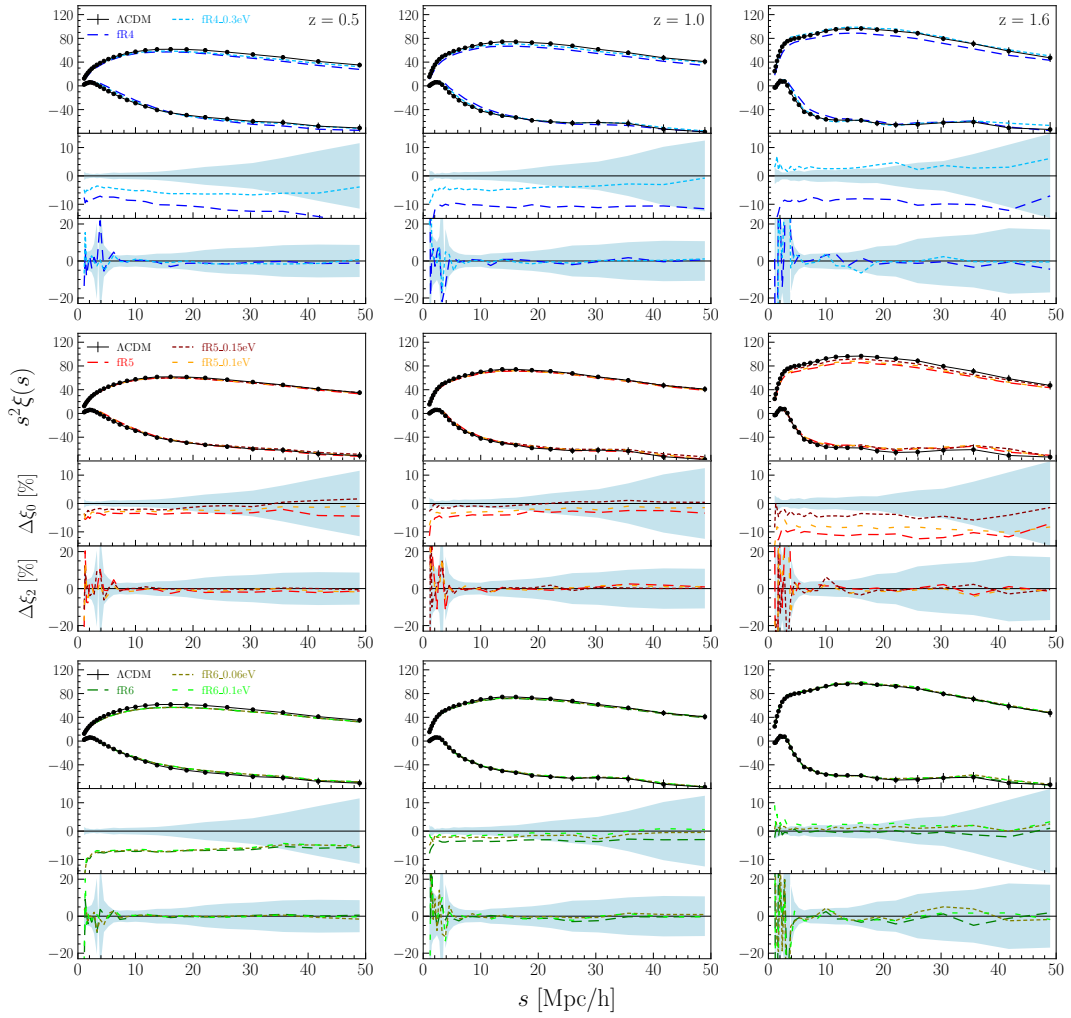

Figure 5.11: The redshift-space monopole (upper curves) and quadrupole (lower curves) moments of the 2PCF of the DUSTGRAIN-*pathfinder* simulations at three different redshifts: $z = 0.5$ (left column), $z = 1$ (central column), and $z = 1.6$ (right column). Black lines show the ΛCDM predictions compared to the results of different models (coloured lines, as labelled). The percentage differences between $f(R)$, $f(R) + m_\nu$ and ΛCDM predictions are in the subpanels. The cyan shaded regions represent the deviations at $\pm 1\sigma$ confidence level.

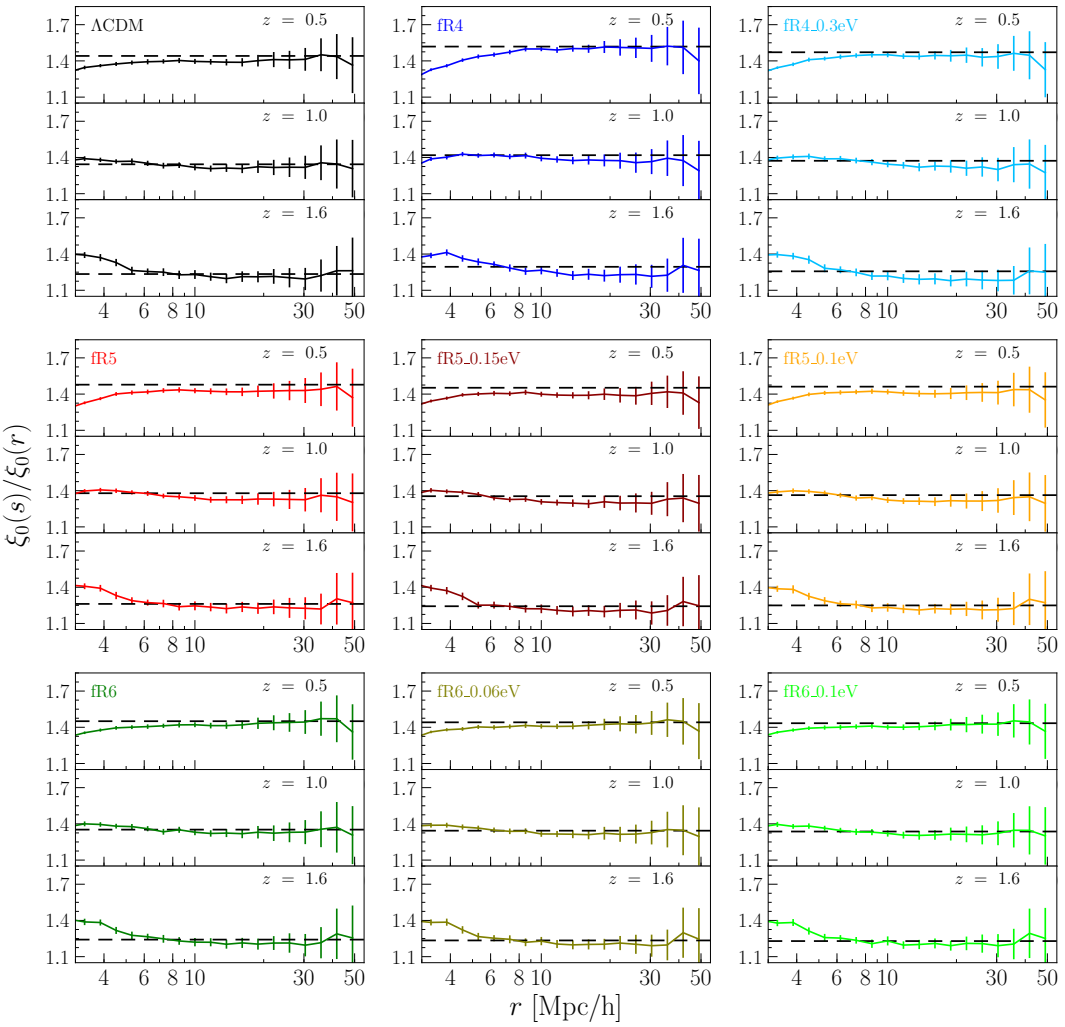

Figure 5.12: Ratio between the redshift-space and real-space 2PCF monopoles at redshifts $z = 0.5$ (left column), $z = 1$ (central column), $z = 1.6$ (right column). From top to bottom, the panels show the results for the $fR4$, $fR5$ and $fR6$ models, respectively. Horizontal dashed lines show the theoretical predictions by Tinker et al. (2010), normalised to the σ_8 values of each DUSTGRAIN-*pathfinder* simulation.

always smaller than 5%, whereas for the monopole they can reach up to 10%.

5.7. Modelling the redshift-space distortions

Until now, we have characterised statistically the samples of mock catalogues constructed from the DUSTGRAIN-*pathfinder* runs. In this Section we provide a description of the implemented model to derive cosmological constraints from the clustering signal.

In order to quantify the effects of $f(R)$ gravity and massive neutrinos on redshift-space clustering distortions, we perform a statistical analysis aimed at extracting constraints on the growth rate of matter perturbation from the

monopole and quadrupole of the redshift-space 2PCF of CDM haloes. Following Marulli et al. (2012), we start analysing the ratio between the redshift-space and real-space monopoles, which depends directly on the linear distortion parameter, β:

$$\frac{\xi_0(s)}{\xi_0(r)} = 1 + \frac{2}{3}\beta + \frac{1}{5}\beta^2 \,. \tag{5.33}$$

The linear distortion parameter is defined as follows:

$$\beta \equiv \frac{f(\Omega_m)}{b} \simeq \frac{\Omega_m(z)^\gamma}{b} \,, \tag{5.34}$$

where $f(\Omega_m) \equiv d\ln D/d\ln a$ is the linear growth rate, D is the linear density growth factor, b is the linear CDM halo bias and γ is the gravitational growth index, which depends on the gravity theory. In GR, it can be demonstrated that $\gamma \sim 0.545$ (Wang and Steinhardt, 1998; Linder, 2005).

The results of this analysis are shown in Fig. 5.12, at three different redshifts, for all the models considered. The horizontal lines in each panel show the ΛCDM predictions computed with the linear biases by Tinker et al. (2010), normalised at the σ_8 values of each model (Marulli et al., 2012). Thanks to the latter normalisation, all the considered models agree remarkably well with the ΛCDM predictions, particularly at scales beyond $10h^{-1}\,\mathrm{Mpc}$. These results show that the effect of $f(R)$ gravity models, with or without massive neutrinos, on the redshift-space monopole of the halo 2PCF is strongly degenerate with σ_8, similarly to what was previously found in real space (see Fig. 5.8). This result also confirms what found by Marulli et al. (2012) for cDE models with massless neutrinos. Similar conclusions have been reached by Villaescusa-Navarro et al. (2018), who investigated the redshift-space clustering in massive neutrino cosmologies.

The redshift-space 2PCF monopole alone is not sufficient to discriminate among these alternative cosmological frameworks due to the σ_8-degeneracy. Thus, in order to break the degeneracy, the full 2D clustering information has to be extracted. As explained in Section 5.6, it is enough though to consider only the first two even multipoles, that is the monopole and the quadrupole (see Fig. 5.11), which contain the anisotropic clustering information. To construct the likelihood, we consider the so-called *dispersion model* (Peacock and Dodds, 1994). Though it has been shown that it can introduce systematics in the linear growth rate measurements (see e.g. Bianchi et al., 2012; de la Torre and Guzzo, 2012; Marulli et al., 2017, and references therein), the dispersion model is accurate enough for the purposes of the present work, that consists in quantifying the relative differences between $f(R)$ models and ΛCDM.

In the following, we briefly summarise the main equations of the dispersion model (see e.g. de la Torre and Guzzo, 2012, for more details) implemented in the CosmoBolognaLib. Assuming the plane-parallel approximation, the redshift-space power spectrum of matter density fluctuations, $P^{\rm zs}(k,\mu)$, can be parametrised

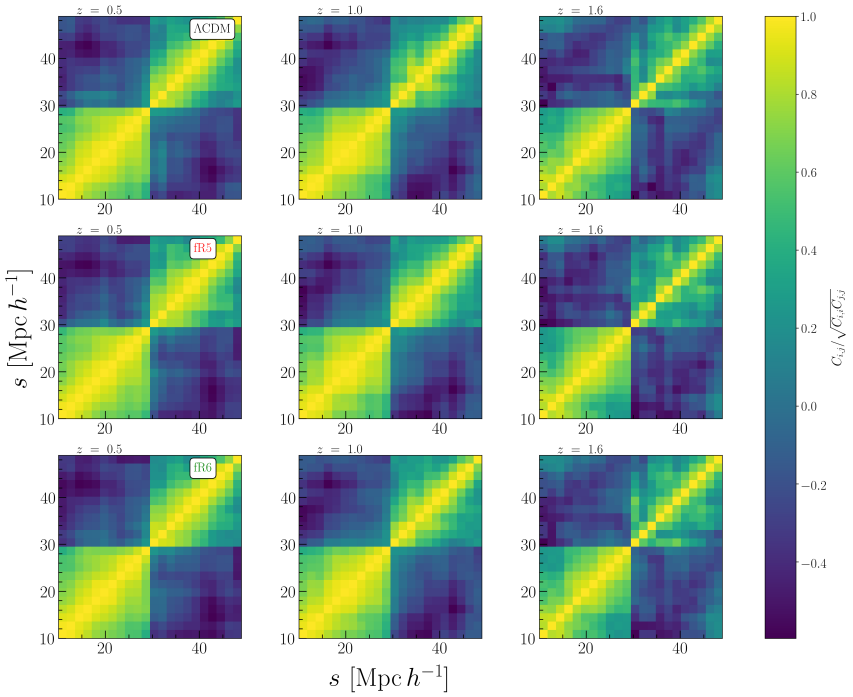

Figure 5.13: Covariance matrices from the analysis of the redshift-space monopole and quadrupole moments of CDM haloes with Bootstrap errors. The models correspond to: ΛCDM (upper panels), $fR4$ (central panels) and $fR5$ (bottom panels), at three different redshifts $z = 0.5, 1.0$ and 1.6 from left to right.

as follows:

$$P^{\rm zs}(k,\mu) = \left(1 + \frac{f}{b}\mu^2\right)^2 F(k,\mu,\Sigma_s) b^2 P(k)\,, \tag{5.35}$$

where the first term on the right-hand side is the linear Kaiser term, b is the linear bias and $P(k,\mu)$ is the matter density power spectrum in real space. $F(k,\mu,\Sigma_s)$ is a damping function used to describe the FoG at small scales given by:

$$F(k,\mu,\Sigma_s) = \frac{1}{(1 + k^2\mu^2\Sigma_s^2)}\,, \tag{5.36}$$

where the streaming scale Σ_s is a free model parameter (Kaiser, 1987; Hamilton, 1992; Fisher and Nusser, 1996). The model for the 2PCF multipoles are obtained by Fourier transforming the power spectrum multipoles, $P_l(k)$, as follows:

$$P_l(k) = \frac{2l+1}{2}\int_{-1}^{+1} d\mu P(k,\mu) L_l(\mu)\,, \tag{5.37}$$

$$\xi_l(s) = \frac{i^l}{2\pi^2}\int dk k^2 P_l(k) j_l(ks)\,, \tag{5.38}$$

where j_l are the l^{th}-order spherical Bessel functions (for more details see e.g. Pezzotta et al., 2017).

For the Bayesian analysis, the dispersion model (Eqs. 5.35, 5.36) can be

written in terms of three free parameters, $f\sigma_8$, $b\sigma_8$ and Σ_S, that we constrain by minimising numerically the negative log-likelihood:

$$-2\ln\mathcal{L} = \sum_{i,j=1}^{N}\left[\xi_l^D(s_i) - \xi_l^M(s_i)\right]C_l(s_i,s_j)^{-1}\left[\xi_l^D(s_j) - \xi_l^M(s_j)\right] , \tag{5.39}$$

with N being the number of bins at which the multipole moments are estimated, and the superscripts D and M referring to data and model, respectively. The covariance matrix $C_l(s_i, s_j)$ is computed from the data with the bootstrap method:

$$C_l(s_i,s_j) = \frac{1}{N_R-1}\sum_{n=1}^{N_R}\left[\xi_l^n(s_i) - \bar{\xi}_l(s_i)\right]\left[\xi_l^n(s_j) - \bar{\xi}_l(s_j)\right] , \tag{5.40}$$

where the indices i and j run over the 2PCF bins, $l = 0,\ 2$ correspond to the multipole moments considered, $\bar{\xi}_l = 1/N_R\sum_{n=1}^{N_R}\xi_l^n$ is the average multipole of the 2PCF, and $N_R = 100$ is the number of realisations obtained by resampling the catalogues with the bootstrap method. Fig. 5.13 shows the normalised covariance matrices $(C_{i,j}/\sqrt{C_{i,i}C_{j,j}})$ of the redshift-space monopole and quadrupole moments of CDM haloes with Bootstrap errors resampling at three different redshifts $z = 0.5, 1.0$ and 1.6. As it can be appreciated, the covariance matrices represent how the scatter propagates into the likelihood and on the final posterior probabilities of the parameters.

Then, to assess the posterior distributions of the three model parameters, we perform a MCMC analysis. The fitting analysis is limited to the scale range $10 \leq r\ [\mathrm{Mpc}\,h^{-1}] \leq 50$, assuming flat priors in the ranges $0 \leq f\sigma_8 \leq 2$, $0 \leq b\sigma_8 \leq 3$ and $0 \leq \Sigma_S \leq 2$.

As an illustrative example, Fig. 5.14 shows the $f\sigma_8$-$b\sigma_8$ posterior constraints, marginalised over Σ_s, obtained from the MCMC analysis of ξ_0, ξ_2 and $\xi_0 + \xi_2$. The *upper panel* shows the constraints for all models considered in this work at $z = 1.0$ using the monopole (orange), quadrupole (green) and monopole plus quadrupole (blue), while the *lower panel* corresponds to a zoom of the intersection region of a ΛCDM halo mock sample at $z = 0.5$. As it is well known, a joint analysis of the redshift-space monopole and quadrupole is required to break the degeneracy between $f\sigma_8$ and $b\sigma_8$, as it is shown in the Figure. We apply this analysis to all the DUSTGRAIN-*pathfinder* mock catalogues. Fig. 5.15 shows the monopole and quadrupole measurements compared to best-fit model predictions. The latter are obtained by assuming the dispersion model, with ΛCDM power spectrum, normalised to the σ_8 values of each DUSTGRAIN-*pathfinder* simulation. As in all previous plots, this method simulates the statistical analysis that would be performed if the real cosmological model of the Universe was one of the $f(R)$ assumed scenarios, with or without massive neutrinos, while a ΛCDM model was instead erroneously assumed to predict the DM clustering.

Fig. 5.16 shows the $f\sigma_8$-$b\sigma_8$ posterior contours, at $1-2\sigma$, for all models

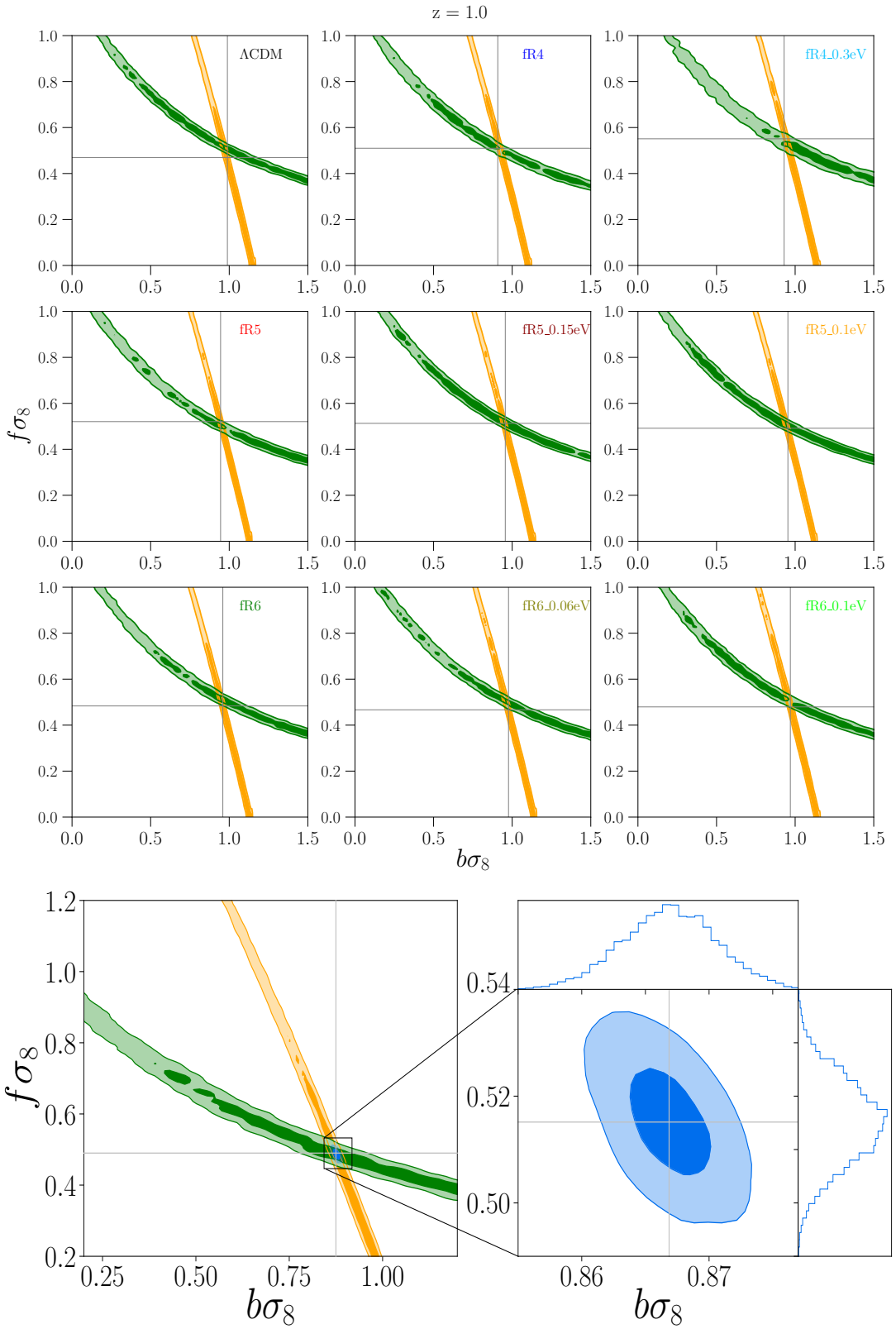

Figure 5.14: Contours at $1-2\sigma$ confidence level of the $f\sigma_8 - b\sigma_8$ posterior distributions, obtained from the MCMC analysis in redshift-space for 2PCF multipoles of CDM haloes. *Upper panel* shows the results for all models considered in this work at $z = 1.0$: monopole (orange), quadrupole (green) and monopole plus quadrupole (blue). *Lower panel* corresponds to a zoom of the region of interest for the ΛCDM model at $z = 0.5$. The joint modelling of monopole and quadrupole breaks the degeneracy in the $\{f\sigma_8, b\sigma_8\}$ space.

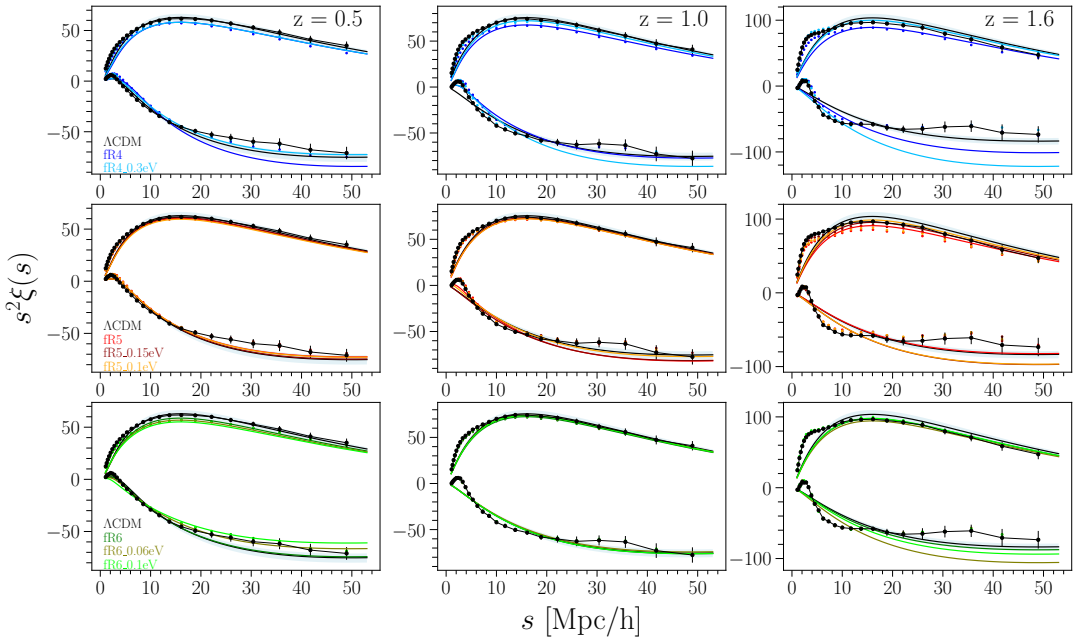

Figure 5.15: The measured redshift-space 2PCF multipole moments for the ΛCDM (points with errorbars) model compared to the best-fit posterior models, at three different redshifts ($z = 0.5,\ 1$ and 1.6, columns from left to right), for the different MG models (as labelled in the plot).

and redshifts considered. This represents the main result: the alternative MG models considered in this work can be clearly discriminated at $z \gtrsim 1$, also in the presence of massive neutrinos whose masses are chosen to introduce strong degeneracies in linear real-space statistics.

In Fig. 5.17 we show the theoretical behaviour of the linear distortion parameter and the growth factor as a function of the redshift for each family of models assuming a flat ΛCDM model. A final summary of all our $f\sigma_8$, $b\sigma_8$ and Σ_s cosmological constraints is presented in Fig. 5.18. At low redshifts, the $f\sigma_8$ posteriors of almost all the $f(R)$ models considered appear statistically indistinguishable from ΛCDM (as already evident in Fig. 5.16). Nevertheless, at higher redshifts they are clearly no more degenerate. This is an interesting result, given that the next-generation dark energy experiments, such as the ESA Euclid mission (Laureijs, 2011a), will mainly probe the high redshift ($z > 1$) Universe.

An additional issue we investigated is related to how much our estimated uncertainties on $\Delta f\sigma_8$ and $\Delta b\sigma_8$ depend on the survey volume. In this case, we repeated the entire analysis on 5 smaller sub-boxes, extracted from the original simulation snapshots, with increasing sides, $L_{\rm box} = 350, 450, 550$ and 650 Mpc h^{-1}. We found approximately linear relations between the estimated uncertainties and the survey volume. Considering the volume of surveys like Euclid, we expect that the uncertainties on both $f\sigma_8$ and $b\sigma_8$ will be about 10 times smaller relative to the values estimated in the current analysis. However, there are many complications affecting the analysis on real data, that might

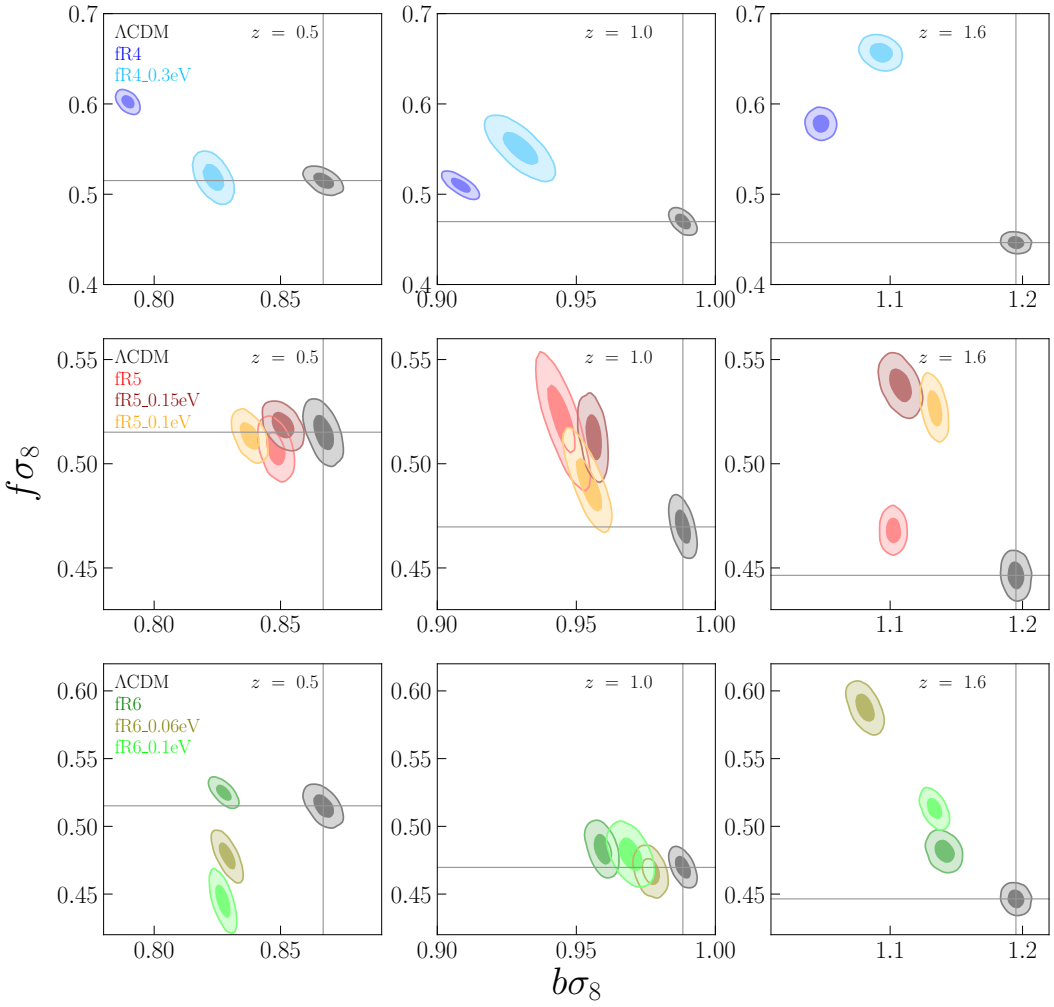

Figure 5.16: Posterior constraints at $1-2\sigma$ confidence levels in the $f\sigma_8 - b\sigma_8$ plane, marginalised over Σ_s, obtained from the MCMC analysis of the redshift-space monopole and quadrupole moments of the 2PCF for the MG models are shown by different colours, as labelled. Panels in the columns, from left to right, refer to $z = 0.5,\ 1$ and 1.6.

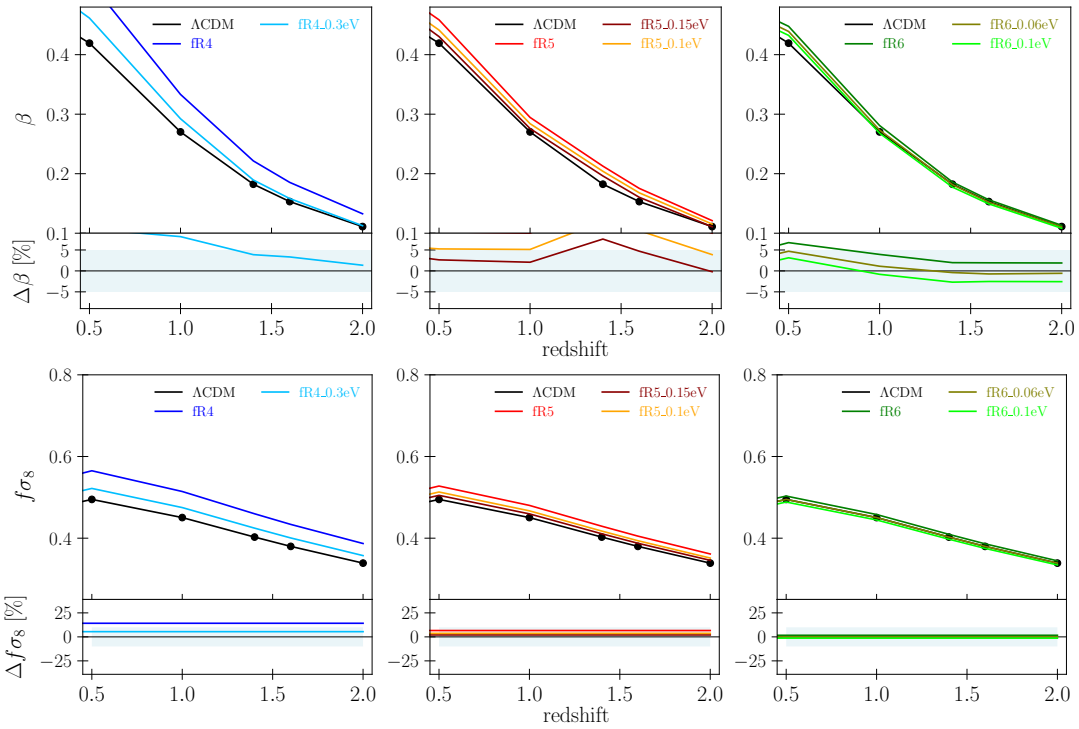

Figure 5.17: Theoretical expectation of the linear distortion parameter β (*upper panel*), and the growth rate $f\sigma_8$ (*lower panel*) as a function of the redshift for each family of mocks from the DUSTGRAIN-*pathfinder* runs assuming a flat ΛCDM model.

significantly increase the estimated uncertainties. Reliable forecasts should include both statistical and systematic uncertainties possibly caused by observational effects, such as e.g. redshift measurement errors, photometric and spectrophotometric calibration, sky brightness variations, geometric selections.

5.8. Discussion

We investigated the clustering and redshift-space distortions of CDM haloes in MG models, with and without massive neutrinos. The present work is a follow-up to the analyses presented in Marulli et al. (2012), who investigated the halo clustering properties in cDE cosmological scenarios. In particular, this work extended the analysis to $f(R)$ models, investigating at the same time the effects of including massive neutrinos. Specific combinations of parameters in $f(R)$ gravity and neutrino masses are considered to investigate possible cosmic degeneracies in the spatial properties of the LSS of the Universe. The family of MG models analysed in this work mimics the ΛCDM background expansion on large scales, being also consistent with solar system constraints (Hu and Sawicki, 2007).

In particular we studied whether redshift-space distortions in the 2PCF multipole moments can be effective in breaking these cosmic degeneracies. The analysis has been performed using mock halo catalogues at different redshifts extracted from the DUSTGRAIN-*pathfinder* runs, a set of N-body simulations of

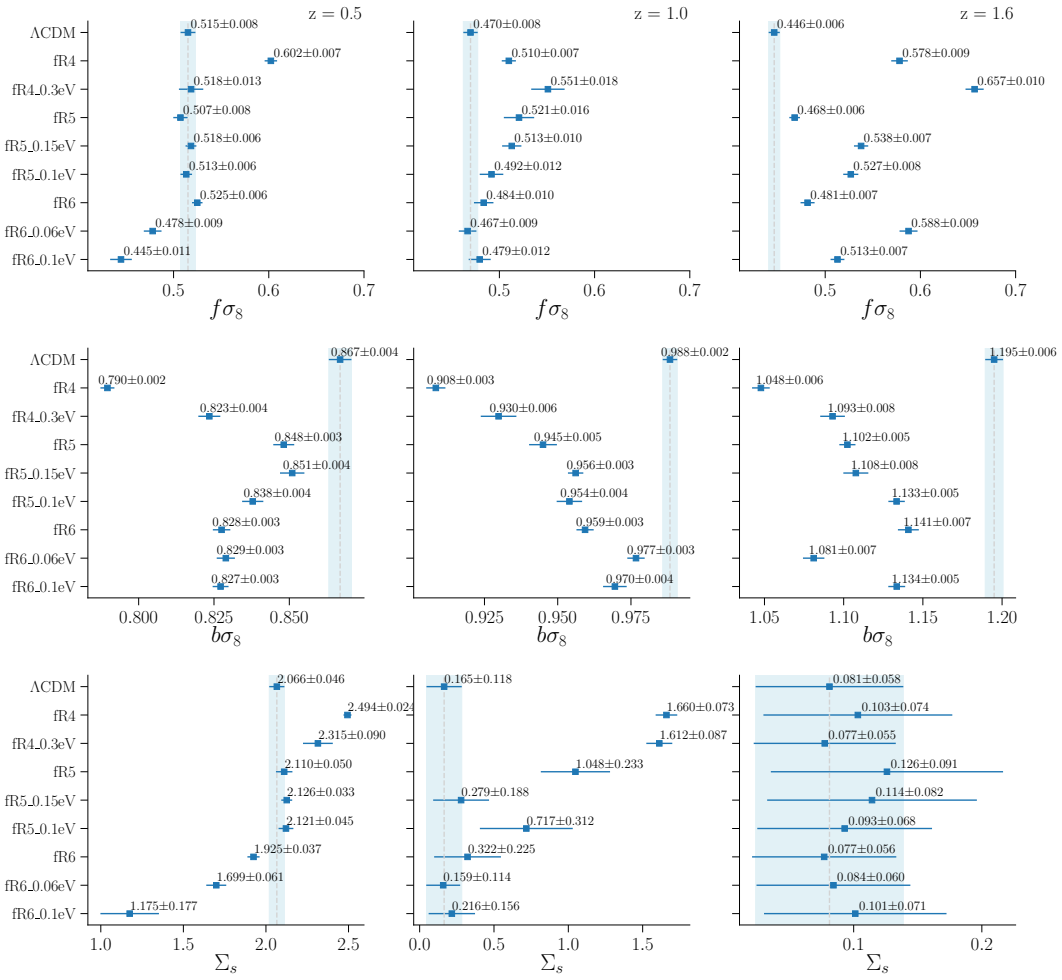

Figure 5.18: Posterior constraints at 1σ and 2σ confidence levels for $f\sigma_8$ (upper panels), $b\sigma_8$ (central panels) and Σ_s (bottom panels), at three different redshifts $z = 0.5, 1.0$ and 1.6 from left to right, for all models considered in this work, obtained from the MCMC analysis of the redshift-space monopole and quadrupole moments of CDM haloes. The vertical shaded areas are centred on ΛCDM results, for comparison.

$f(R)$ models with and without massive neutrinos (Giocoli, Baldi, and Moscardini, 2018; Peel et al., 2018a; Peel et al., 2018b; Merten et al., 2018). We considered intermediate scales, below $50h^{-1}\,\mathrm{Mpc}$, focusing on the first two even multipole moments of the 2PCF. We exploited a Bayesian statistical approach to assess posterior probability distributions for the three free parameters of the dispersion model $\{f\sigma_8,\ b\sigma_8,\ \Sigma_S\}$. The main result that came out from this analysis is that redshift-space distortions of 2PCF multipoles are effective probes to disentangle cosmic degeneracies, though only at large enough redshifts ($z \gtrsim 1$). In fact, the linear growth rate constraints obtained from all the analysed $f(R)$ mock catalogues are statistically distinguishable from ΛCDM predictions, at all redshifts but $z = 0.5$, as shown in Fig. 5.16 and 5.18.

CHAPTER 6

Modelling redshift space distortions: validation of statistical methods of clustering anisotropies

Since redshift-space distortions are considered one of the most powerful cosmological probe to explore the LSS, in this Chapter we validate it considering different statistical methods that are currently used to constrain the linear growth rate from the 2PCF. The content of this Chapter is an extended version of our paper (García-Farieta et al., 2019), in which we studied the clustering signal of mock catalogues extracted from large N-body simulations of the standard cosmological framework. The analysis consists in quantifying the systematic uncertainties on the growth rate and linear bias measurements due to the assumptions in the redshift-space distortion model, using both multipole moments and clustering wedges of the redshift-space 2PCF. We take into account the impact of redshift measurement errors, that introduce spurious clustering anisotropies.

Observational cosmology has had progressive improvements concerning both data acquisition and modelling. With the common goal of understanding structure formation and its evolution in the Universe, several projects have been carried on to explore the properties of cosmic tracers at different scales. The main properties of the large-scale structure of the Universe have been constrained both at very high redshifts, exploiting the Cosmic Microwave Background (CMB) power spectrum (Bennett et al., 2013; Planck Collaboration et al., 2018a), and in the local Universe thanks to increasingly large surveys of galaxies and galaxy clusters (e.g. Parkinson et al., 2012; Campbell et al., 2014; Guzzo et al., 2014; Alam et al., 2017). The unprecedented amount and quality of the data expected from the upcoming projects are focused on testing fundamental physics and solving questions that have remained unanswered for years. In particular, in

the era of large galaxy surveys, such as the Dark Energy Survey[1] (DES) (DES Collaboration et al., 2017), the extended Roentgen Survey with an Imaging Telescope Array (eROSITA) satellite mission[2] (Merloni, 2012), the NASA Wide Field Infrared Space Telescope (WFIRST) mission[3] (Spergel, 2013), the ESA Euclid mission[4] (Laureijs et al., 2011b; Amendola et al., 2018), the Large Synoptic Survey Telescope[5] (LSST) (Ivezic, 2008), and the Square Kilometre Array (SKA) (Maartens et al., 2015; Santos et al., 2015), we will have the opportunity to clarify some of the main open issues in the current understanding of the Universe, such as the physical nature of dark matter (DM) and dark energy (DE), and to test the gravity theory on the largest scales accessible (for a recent review see e.g. Silk, 2017). This constitutes sufficient motivation for the forthcoming generation of galaxy surveys, exploring the dark sector with increasingly large and accurate maps of galaxies and other cosmic tracers.

The impact of systematics on constraining cosmological parameters is perhaps the most important factor to consider from an observational point of view. In this context, systematics have been taken into account in several previous investigations, considering their impact on constraining cosmological parameters using cosmic shear tomography (Cardone et al., 2014), lensing statistics in ray-tracing simulations with photometric redshifts (Abruzzo and Haiman, 2019), cluster mass function in large weak lensing surveys (Corless and King, 2009), cosmography with strong and weak lensing (Mandelbaum et al., 2005; Acebron et al., 2017; Shirasaki and Yoshida, 2014), power spectra from cosmic shear analysis (Hikage et al., 2019), estimators from supernova cosmology (Nordin, Goobar, and Jönsson, 2008; Zhai and Wang, 2018), and involving the systematic errors on redshift-space distortions in Fourier space to test cosmological-scale gravity (Ishikawa et al., 2014). Recently, some theoretical tools have been proposed to deal with the effect of the unknown systematics, like the Bayesian conservative constraints (Bernal and Peacock, 2018). Robust constraints on cosmological parameters should also take into account the spurious effects in the measurements. In particular we investigate the impact of redshift measurement errors on the estimators that quantify the galaxy clustering and that are commonly used to derive constraints on cosmological parameters. This is important considering the limits of precision in the redshift expected from photometric and spectroscopic samples of future galaxy surveys.

In the following Sections, we present a systematic validation analysis of the main statistical techniques currently used to constrain the linear growth rate from redshift-space anisotropies in the 2PCF of cosmic tracers. We model the monopole and quadrupole multipole moments and the clustering wedges of the 2PCF, which encode most of the information on the large-scale structure distribution. Then, we investigate new RSD models based on perturbation

[1] http://www.darkenergysurvey.org
[2] http://www.mpe.mpg.de/eROSITA
[3] http://wfirst.gsfc.nasa.gov
[4] http://www.euclid-ec.org
[5] http://www.lsst.org

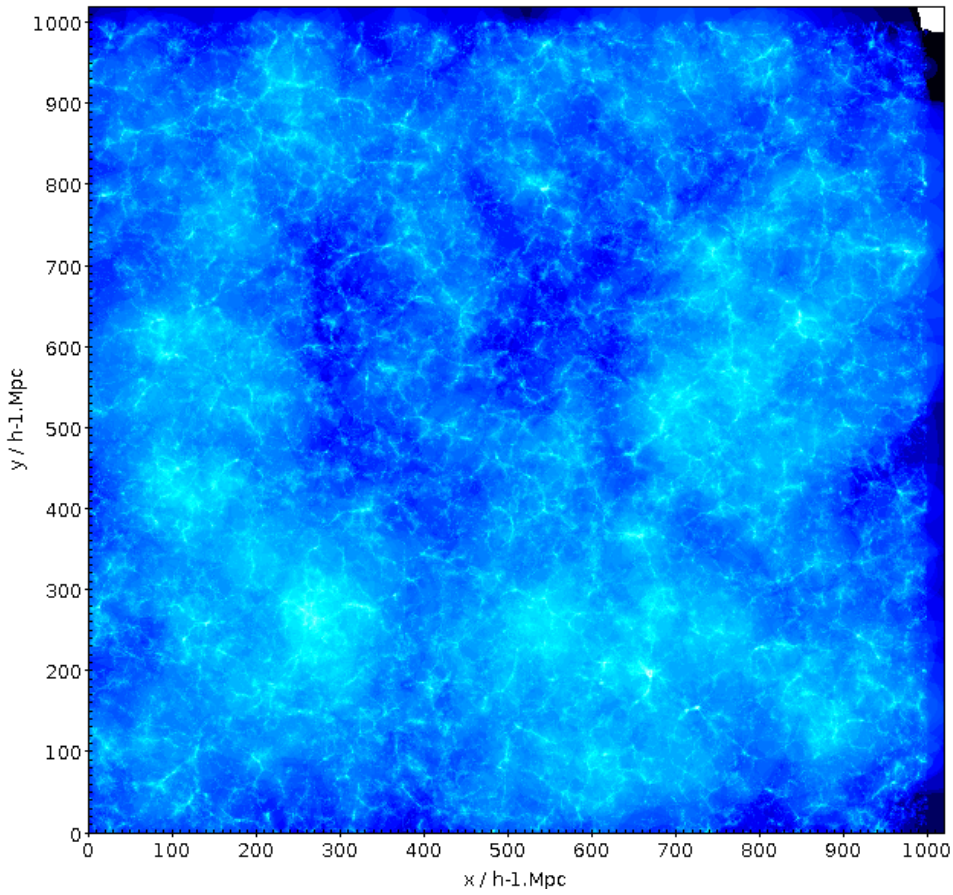

Figure 6.1: Density field map of a FOF sample from the MDPL2 simulation at redshift $z = 0$. The slice is $5h^{-1}$ Mpc thick and encloses the region of the most massive halo in the simulation. Taken from http://www.cosmosim.org/.

theory, named Scoccimarro (2004) and Taruya, Nishimichi, and Saito (2010) models, that we compare with the so-called dispersion model (Davis and Peebles, 1983; Peacock and Dodds, 1996). Moreover, we investigate also the impact of redshift measurement errors, which introduce spurious small-scale clustering anisotropies. We focus on the redshift range $0.5 \lesssim z \lesssim 2$, and consider mildly non-linear scales $10 < r[h^{-1}\,\mathrm{Mpc}] < 55$, where the assumptions in the RSD models considered in this work are expected to be reliable. In addition, we investigate the impact of considering only larger scales, $r > 30\ h^{-1}\,\mathrm{Mpc}$, where the models are supposed to be less biased.

6.1. N-body simulations and mock halo catalogues

The basics on N-body simulations have been presented in Chapter §5. In this Chapter we use a set of the halo catalogues extracted from the publicly available MDPL2 simulations belongs to the MultiDark suite (Riebe et al., 2013; Klypin et al., 2016) that is available at the CosmoSim database[6]. This

[6] http://www.cosmosim.org/

set of simulations have been widely used in several studies in recent years (see e.g. van den Bosch and Jiang, 2016; Rodríguez-Puebla et al., 2016; Klypin et al., 2016; Vega-Ferrero, Yepes, and Gottlöber, 2017; Zandanel et al., 2018; Topping et al., 2018; Wang et al., 2018; Ntampaka, Rines, and Trac, 2019; Granett et al., 2019). The MDPL2 simulation follows the dynamical evolution of 3840^3 dark matter particles, with mass resolution as low as $1.51 \times 10^9 M_\odot/h$, in a comoving box of $1000h^{-1}$ Mpc on a side assuming a ΛCDM cosmology consistent with Planck results (Planck Collaboration et al., 2014; Planck Collaboration et al., 2016d). The adopted cosmological parameters are: $\Omega_m = 0.307$, $\Omega_\Lambda = 0.693$, $\Omega_b = 0.048$, $\sigma_8 = 0.823$, $n = 0.96$ and $h = 0.678$. The dark matter haloes (Riebe et al., 2013) have been identified using a Friends-of-Friends (FoF) algorithm with a linking length of 0.2 times the mean interparticle distance (Knebe et al., 2011). A projection of the density field map of a FOF sample from the MDPL2 simulation at redshift $z = 0$ is shown in Fig. 6.1.

Our analysis will focus on mock catalogues constructed using the MDPL2 simulation and considering redshift errors to investigate the RSD on intermediate and non-linear scales. For the clustering analysis presented in this Chapter we make use of one realisation of the halo samples per each redshift considered, taking into account only the identified haloes that have more than N_{min} particles per halo, where N_{min} have been chosen according to the mass threshold fixed to $M_{\rm min} = 10^{12} M_\odot/h$, which corresponds to a minimum number of 665 particles per halo. For all the samples, we have restricted our analysis in the mass range $M_{\rm min} < M < M_{\rm max}$, where $M_{\rm max} = 2 \times 10^{15}, 1.3 \times 10^{15}, 7.4 \times 10^{14}, 5.4 \times 10^{14}, 4.0 \times 10^{14}, 3.6 \times 10^{14}, 3.1 \times 10^{14}\, M_\odot/h$, at $z = 0.523,\ 0.740,\ 1.032,\ 1.270,\ 1.535,\ 1.771,\ 2.028$, respectively.

6.2. Clustering of DM haloes

In this Section, we describe the methodology used to quantify the halo clustering through the 2PCF. Specifically, we characterise the anisotropic clustering either with the first two non-null multipole moments of the 2PCF, or with the clustering wedges. All the numerical computations in this Chapter have been performed with the CosmoBolognaLib (Marulli, Veropalumbo, and Moresco, 2016)[7].

6.2.1. The two-point correlation function

The methodology employed in this Section is similar to the one adopted in Chapter §5. As mentioned above, we compare the results obtained from the multipole moments with the one from the clustering wedges of the 2PCF, reason for which we recall the main equations of these formalisms (for details

[7]Specifically, we used the CosmoBolognaLib V5.3, which includes the new implemented RSD likelihood modules required for the current analysis. The software and its documentation are freely available at the GitHub repository: https://github.com/federicomarulli/CosmoBolognaLib.

see Chapter §3), and we give a more detailed description on the estimators.

Firstly, we characterise the spatial distribution of DM haloes in MDPL2 simulations in terms of its 2PCF in both real-space $\xi(r,\mu)$ and redshift-space $\xi(s,\mu)$. Since the full 2D 2PCF encodes a complete description of the halo clustering, we measure it by using the conventional Landy and Szalay (1993) estimator with an angular dependence given by

$$\hat{\xi}(r,\mu) = \frac{DD(r,\mu) - 2DR(r,\mu) + RR(r,\mu)}{RR(r,\mu)}, \tag{5.26}$$

with μ being the cosine of the angle between the line-of-sight (LOS) and the comoving separation r, and $DD(r,\mu), RR(r,\mu)$, and $DR(r,\mu)$ the normalised number of pairs of CDM haloes in data-data, random-random and data-random catalogues, respectively. We consider intermediate scales from $1h^{-1}$ Mpc to $55h^{-1}$ Mpc , in 80 linearly spaced bins, with random samples five times larger than the halo ones to keep the shot noise errors due to the finite number of random objects negligible.

As introduced in Chapter §3, the clustering anisotropies can be effectively quantified by decomposing the full 2D 2PCF either in its multipole moments or in the so-called wedges (Kazin, Sánchez, and Blanton, 2012; Sánchez et al., 2013; Sánchez et al., 2014; Sánchez et al., 2017). The coefficients of the Legendre expansion [see Eq. (5.27)], correspond to the l^{th} non-vanishing multipole moment of the 2PCF written as follows:

$$\xi_l(r) \equiv \frac{2l+1}{2}\int_{-1}^{+1} d\mu \xi(r,\mu) L_l(\mu). \tag{3.21}$$

We measure the multipole moments through the *direct estimator*, instead of the *integrated estimator* presented in the previous Chapter, see Eq. (5.28). Starting from the Landy and Szalay (1993) estimator, the *direct multipoles* actually take the form

$$\begin{aligned}\hat{\xi}_\ell(s) &= \frac{DD_\ell(s) + RR_\ell(s) - 2DR_\ell(s)}{RR_0(s)} \\ &= \frac{2\ell+1}{2}\int_{-1}^{+1} \mathrm{d}\mu \frac{DD(\mu,s) + RR(\mu,s) - 2DR(\mu,s)}{RR(\mu,s)} L_l(\mu) \\ &\quad \cdot \frac{RR(\mu,s)}{RR(s)},\end{aligned} \tag{6.1}$$

thus the pair-counter was performed directly in 1D bins considering that our random pairs do not depend on μ, i.e. $RR(r,\mu) = RR(r)$ instead of integrating over 2D bins (Kazin, Sánchez, and Blanton, 2012). In real-space the full clustering signal is encoded in the monopole moment $\xi_0(r)$, whereas in redshift-space we focus on the two first non-zero multipole moments, monopole $\xi_0(s)$ and quadrupole $\xi_2(s)$, since the odd multipoles vanish by symmetry at first order. On the other hand, the clustering wedges introduced by Kazin, Sánchez, and

Blanton (2012), correspond to the angle-averaged of the $\xi(s,\mu)$ over wide bins of μ expressed as

$$\xi_w(s) = \frac{1}{\Delta\mu}\int_{\mu_1}^{\mu_2} \xi(s,\mu)\mathrm{d}\mu, \tag{3.29}$$

where $\Delta\mu = \mu_2 - \mu_1$ is the wedge width. In this work we focus on the two clustering wedges with $\Delta\mu = 0.5$, that is the transverse wedge, $\xi_\perp(s) \equiv \xi_{1/2}(\mu_{min} = 0, s)$, and the radial (or LOS) wedge, $\xi_\parallel(s) \equiv \xi_{1/2}(\mu_{min} = 0.5, s)$, computed in the ranges $0 \leq \mu < 0.5$ and $0.5 \leq \mu \leq 1$, respectively. In real-space both wedges, radial $\xi_\parallel$ and transverse $\xi_\perp$, are identical between them and equal to the monopole signal $\xi_0(r)$ because there are no distortions in any direction. For consistency, in following Sections we present all our results using both descriptions, the multipole statistics and clustering wedges defined above.

The errors on the 2PCF measurements are estimated by using the bootstrap resampling method (Efron, 1979). Firstly, the original catalogue is divided into 27 sub-samples, which are then re-sampled in 100 different data sets with replacement, then the $\xi(r,\mu)$ is measured in each one of them (Barrow, Bhavsar, and Sonoda, 1984; Ling, Frenk, and Barrow, 1986).

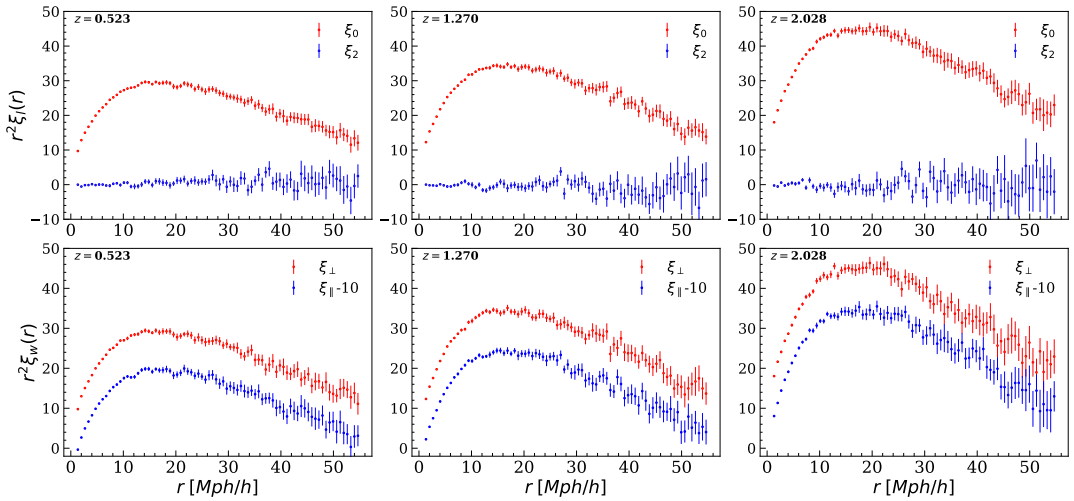

Figure 6.2: The real-space 2PCF of CDM haloes at three different redshifts, as indicated by the labels. *Upper panels*: the monopole ξ_0 and quadrupole ξ_2 moments. *Bottom panels*: the perpendicular $\xi_\perp$ and parallel $\xi_\parallel$ wedges; the latter are shifted by -10, for clarity reasons. The error bars are computed with bootstrap sampling.

6.2.2. Clustering in real space

The real-space 2PCF of DM haloes at three different redshifts, created from the FOF MDPL2 simulations, is shown in Fig. 6.2. In the upper panel the 2PCF was computed from the multipole statistics, monopole $\xi_0(r)$ (red) and quadrupole $\xi_2(r)$ (blue). As expected, the main signal is contained in the monopole, while the mean quadrupole is consistent with zero, at 1σ, at all scales. The lower panels show the 2PCF computed from clustering wedges, $\xi_\perp(r)$ (red) and $\xi_\parallel(r)$ (blue), the latter are rescaled by -10 for visualisation purposes. As mentioned

before, all of them are statistically equal since in real-space there are no clustering anisotropies from the simulations, all multipole moments with $l > 0$ are supposed to vanish and the clustering wedges for any width $\Delta\mu$ correspond to the $\xi_0(r)$ signal. In all cases, the error bars are computed with the bootstrap method.

The amplitude of the real-space clustering signal allows us to characterise the effective halo bias, $b_{\rm eff}$, which relates the halo clustering to the underlying mass distribution. From our mass-selected samples, the mean apparent effective bias of CDM haloes is defined as follows

$$\langle b(z) \rangle = \left\langle \sqrt{\frac{\xi_{\rm halo}}{\xi_{CDM}(\sigma_8)}} \right\rangle, \tag{5.29}$$

where ξ_{halo} is the measured halo bias of the MDPL2 sub samples and ξ_{CDM} is obtained by Fourier transforming of the non-linear matter power spectrum from the HALOFIT (Smith et al., 2003) implementation in CAMB (Lewis, Challinor, and Lasenby, 2000). Moreover, we consider the effective bias proposed by Tinker et al. (2010) in order to compare our results with theoretical predictions. In each case the effective bias is estimated by averaging the bias $b(M,\ z)$ of a set of CDM haloes with a given mass M and redshift, in the scale range $10h^{-1}\,{\rm Mpc} < r < 50h^{-1}\,{\rm Mpc}$, as following

$$b_{eff}(z) = \frac{\int_{M_{min}}^{M_{max}} n(M,z) b(M,z) dM}{\int_{M_{min}}^{M_{max}} n(M,z) dM}, \tag{5.30}$$

where the mass limits $[M_{min},\ M_{max}]$ have been defined in Section 6.1, while the mass function, $n(M,z)$, and the linear bias, $b(M,z)$ are estimated using the Tinker et al. (2008) model and the Tinker et al. (2010) model, respectively. The left panel of Fig. 6.3 shows the measured CDM halo bias as a function of scale with error bars propagated from the 2PCF and the horizontal line corresponds to the Tinker et al. (2010) prediction.

A scale dependent behaviour of the bias can be appreciated at scales smaller than $10h^{-1}\,{\rm Mpc}$ with deviations of about 4% with respect to the theoretical linear prediction. The right panel of Fig. 6.3 shows the evolution of the mean effective bias for scales larger than $10h^{-1}\,{\rm Mpc}$, with respect to the redshift, the dashed line refers to the theoretical ΛCDM predictions of Tinker et al. (2010) normalised to the σ_8 value of MDPL2 simulations. The error bars are computed by propagating the 2PCF errors estimated with bootstrap resampling. They show a very good agreement with respect to the Tinker et al. (2010) prediction as it can be appreciated in the bottom subpanel, where the blue line represents the difference between the two values and the cyan shaded region corresponds to 1σ deviation.

6.2.3. Dynamic distortions and clustering in redshift space

The patterns of the clustering in the density field are affected by the peculiar velocities of CDM haloes, which causes an enhancement of the 2PCF due to

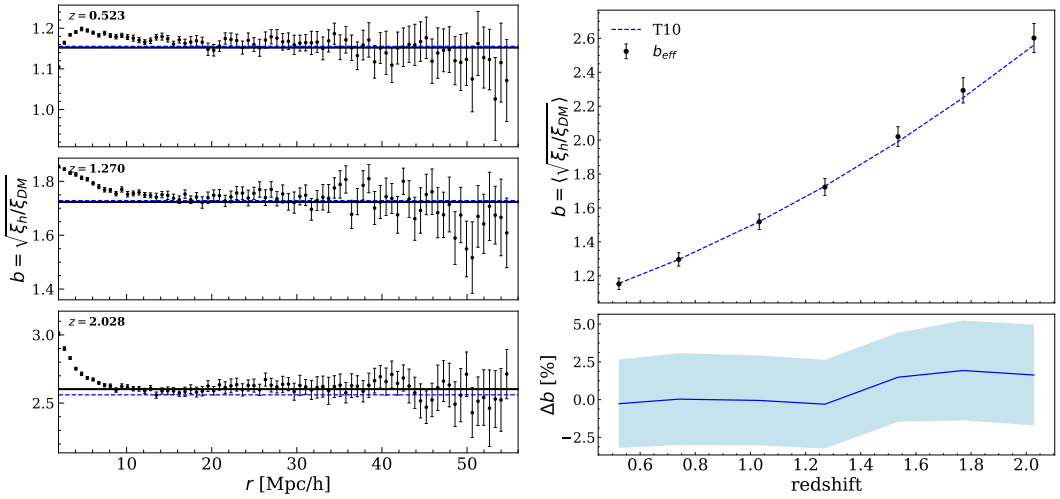

Figure 6.3: Effective halo bias $\langle b \rangle$ as a function of the comoving scale (left panel) and as a function of the redshift (right panel), computed as an average in the range $10h^{-1}\,\mathrm{Mpc} < r < 50h^{-1}\,\mathrm{Mpc}$ from the real-space correlation function. Dashed line show the theoretical ΛCDM effective bias predicted by Tinker et al. (2010).

redshift-space distortions. As it is well known, the observed redshift z_{obs} measured for real galaxy surveys can be expressed as a combination of three terms (e.g. Marulli et al., 2012): i) the cosmological redshift, z_c, due to the Hubble flow, ii) the redshift caused by the peculiar velocity along the LOS of the observer, and iii) an additional term due to the redshift measurement errors coming from the adopted instrumentation and calibration analysis. Indeed, neglecting the latter two terms introduces displacements between the matter distribution in real and redshift space (for a review see Hamilton, 1998; Scoccimarro, 2004).

Since we are interested in mimicking redshift surveys, we construct realistic mock catalogues of the CDM halo distribution in redshift-space from the MDPL2 simulations. First, we introduce a local observer at a random position in the simulation, then we transform the comoving coordinates of each DM halo into polar coordinates as a projection on the sky, and finally we estimate the observed redshifts assuming the following relation:

$$z_{\rm obs} = z_c + (1+z_c)\frac{\mathbf{v}\cdot\hat{\mathbf{r}}}{c} + \frac{\sigma_v}{c}\,, \tag{6.2}$$

where σ_v corresponds to the amplitude of a Gaussian noise in the measured redshift expressed in km/s and $\hat{\mathbf{r}}$ is a unit vector along the LOS, so that the contribution of peculiar motions is given by $\vec{v}_{\parallel} = \vec{v}\cdot\hat{\mathbf{r}}$. Finally, we return back to comoving Cartesian coordinates, mimicking the distortions in redshift space by replacing z_c with $z_{\rm obs}$ to estimate the comoving distance. As in Marulli et al. (2012), we consider the following values for the σ_v term: 0, 200, 500, 1000, 1250, 1500 km/s, whose effects in the redshift measurement of the mock catalogues correspond to the per cent uncertainties $\delta z = \{0,\ 0.07,\ 0.2,\ 0.3,\ 0.4,\ 0.5\}\%$. These values cover the sensible range extending from the case with negligible redshift errors ($\sigma_z = 0$), to the case with errors representative to those expected from

z	σ_v [km/s]				
	200	500	1000	1250	1500
0.523	0.44	1.09	2.19	2.74	3.28
0.740	0.38	0.96	1.92	2.39	2.87
1.032	0.33	0.82	1.64	2.05	2.46
1.270	0.29	0.73	1.47	1.84	2.20
1.535	0.26	0.66	1.31	1.64	1.97
1.771	0.24	0.60	1.20	1.50	1.80
2.028	0.22	0.55	1.10	1.38	1.65

Table 6.1: The ratios between the values of the Gaussian redshift errors considered in this work and the expected redshift errors in Euclid-like spectroscopic galaxy surveys.

next-generation spectroscopic surveys. Tab. 6.1 reports the ratios between the σ_v values considered in this work and the ones expected in Euclid-like spectroscopic galaxy surveys, that is $\sigma_z/(1+z) \sim 0.001$ (Laureijs et al., 2011b).

Fig. 6.4 shows the spatial distribution of DM haloes in polar coordinates for a mock sample at $z = 1.032$ including redshift measurement errors. The slight elongation increasing with σ_v in the halo distribution along the LOS due to redshift errors can be appreciated in the different panels.

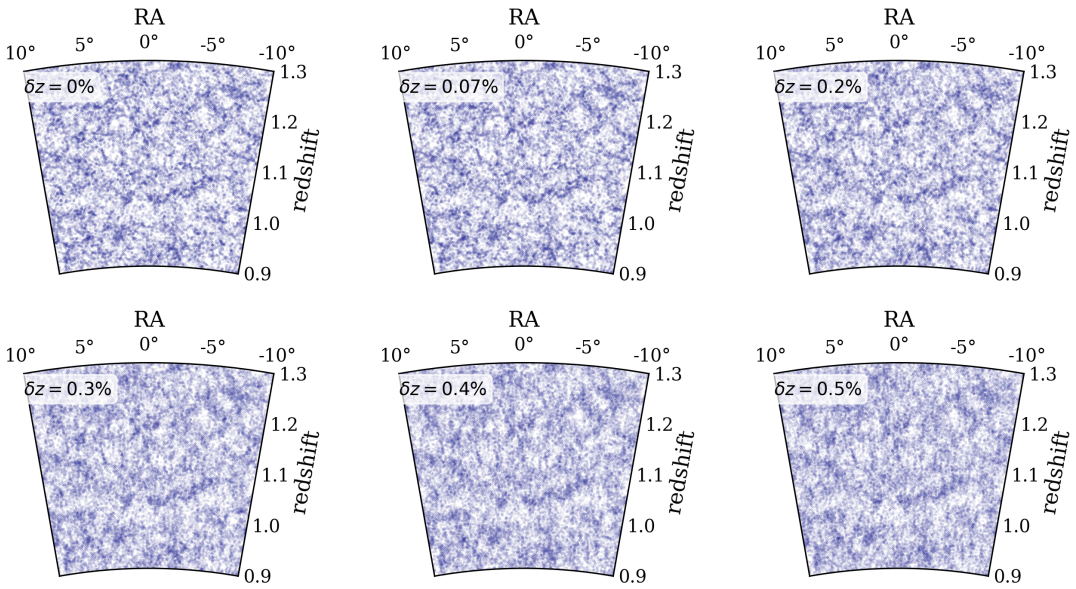

Figure 6.4: Spatial distribution of haloes in mock sub samples at $z = 1.032$ including redshift errors as indicated in the labels. Only haloes in a 2 degree declination slice are plotted.

Fig. 6.5 shows the 2PCF as a function of the transverse $s_\perp$ and parallel $s_\parallel$ separations to the LOS, at $z = 0.523,\ 1.032,\ 1.535$ for the MDPL2 mocks. The iso-correlation contours of $\xi(s_\perp, s_\parallel)$ are evaluated in the interval $[0.05,\ 3]$ for different values of the redshift measurement errors, δz as indicated in the panels.

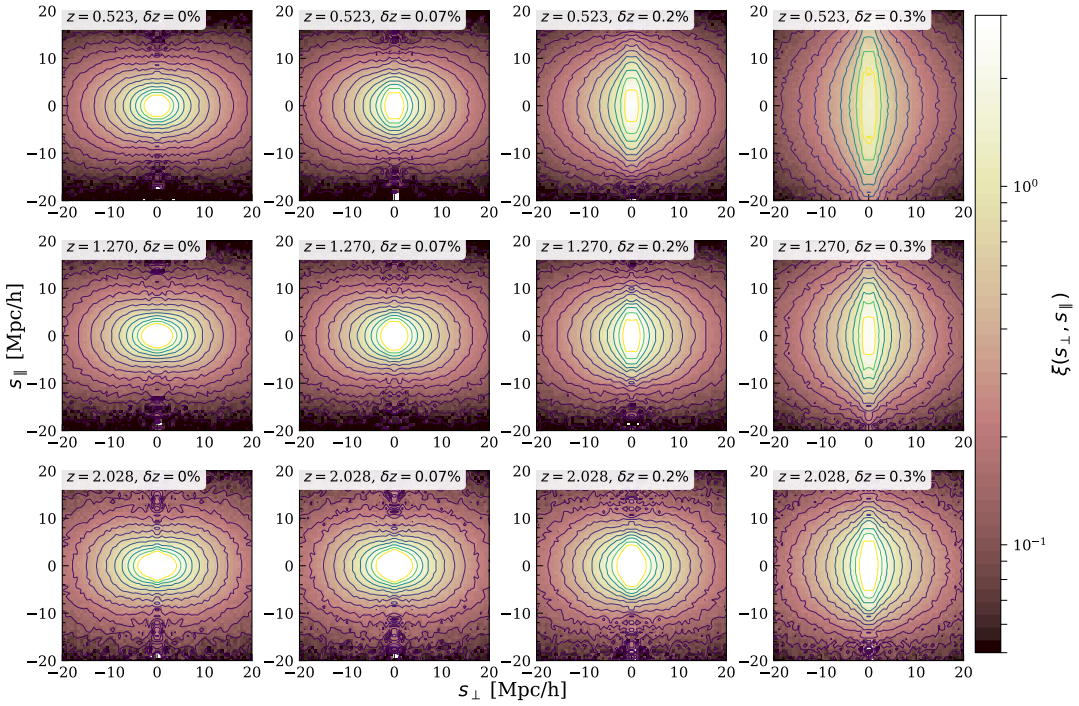

Figure 6.5: Iso-correlation contours of $\xi(s_\perp, s_\parallel)$ measured in the mock catalogues. Contours are drawn in correspondence of the correlation levels $\xi(s_\perp, s_\parallel) =$ 0.05, 0.07, 0.09, 0.13, 0.18, 0.24, 0.33, 0.45, 0.62, 0.85, 1.17, 1.6, 2.2, 3. Different panels refer to different amplitudes of the redshift errors, as indicated in the labels.

As it can be seen, redshift errors introduce spurious clustering anisotropies at small scales, enhancing the clustering signal along the LOS, analogously to the Fingers-of-God (FoG) elongations (Marulli et al., 2012).

In order to increase the signal-to-noise ratio, it is convenient to project the two-dimensional 2PCF correlation function, $\xi(s_\perp, s_\parallel)$, onto one-dimensional statistics, such as the multipole moments and the clustering wedges. In Figs. 6.6a and 6.6b we show the redshift-space monopole and quadrupole moments, and the redshift-space radial and transverse wedges, respectively. The case of the isolated monopole moment of the 2PCF was studied in a previous paper by Marulli et al. (2012). In agreement with the results of that paper, we found a suppression in the 2PCF monopole at small scales due to redshifts errors. The results for the clustering wedges are consistent with the multipole ones, showing a small-scale suppression in the transverse wedge, in the presence of redshift errors, while the radial wedge increases. As shown in Fig. 6.5 and discussed in detail in the next Sections, the spurious anisotropies caused by redshift errors in the multipole moments and wedges have a scale-dependent pattern similar to the FoG one caused by small-scale incoherent motions.

A first quantitative assessment on the impact of redshift errors in the estimates of the linear growth rate $f\sigma_8$ and the bias $b\sigma_8$ can be obtained from the multipole moments of the 2PCF by calculating the ratio of the monopole in redshift-space

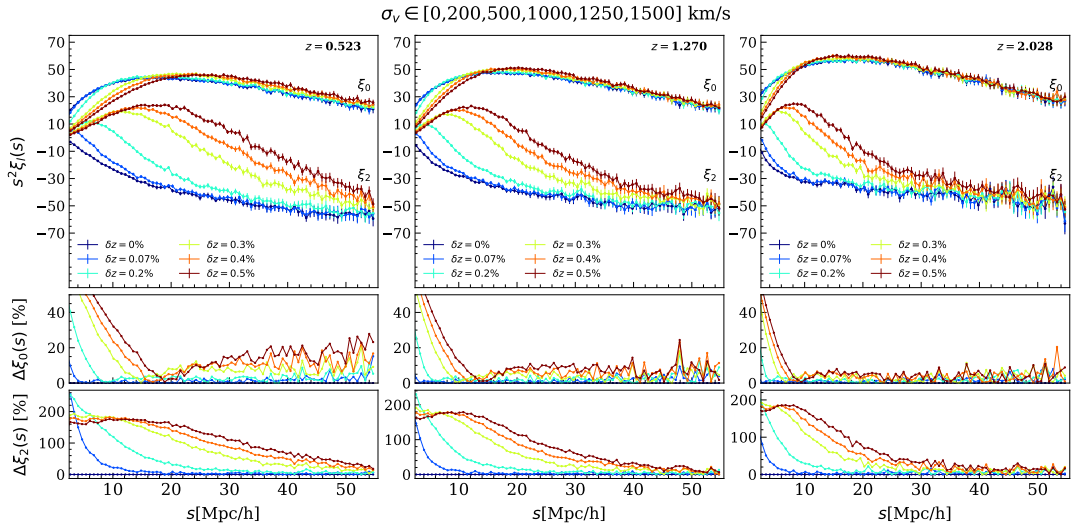

(a) Redshift-space 2PCF monopole and quadrupole of the MDPL2 DM haloes, at three different redshifts. The coloured lines correspond to the 2PCFs measured in mock catalogues with redshift errors, as indicated by the labels. The bottom panels show the percent relative difference with respect to the case with no redshift errors.

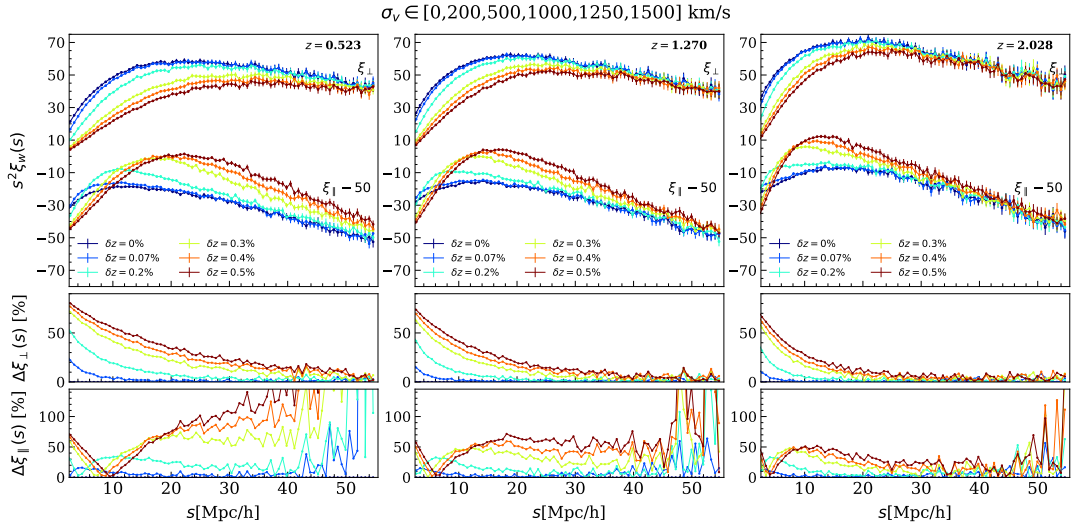

(b) Redshift-space 2PCF perpendicular and parallel wedges of the MDPL2 DM haloes, at three different redshifts. The coloured lines correspond to the 2PCFs measured in mock catalogues with redshift errors, as indicated by the labels. The bottom panels show the percent relative difference with respect to the case with no redshift errors.

Figure 6.6: Measured multipole moments and clustering wedges of the 2PCF from mock catalogues of the MDPL2 simulation.

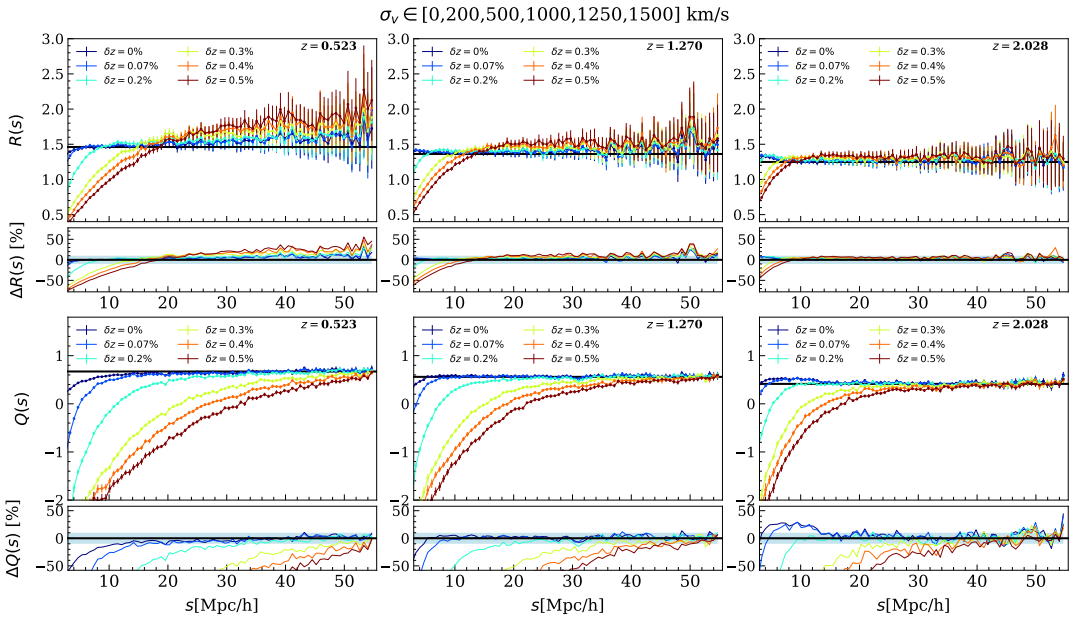

Figure 6.7: The ratio between the redshift-space and real-space monopole moments, $R(s)$ (*upper panels*), and between the redshift-space quadrupole and monopole, $Q(s)$ (*lower panels*), at three different redshifts and for different redshift errors, as indicated by the labels. Horizontal lines represent the theoretical predictions obtained assuming the Tinker et al. (2008) mass function and the Tinker et al. (2010) effective bias. The error bars are computed by propagating the 2PCF bootstrap errors and the subpanels show the relative percent differences with respect to the case with no redshift errors.

to the real-space correlation function $R(s)$ and from the quadrupole-to-monopole ratio $Q(s)$. By assuming the linear regime, these quantities are simply related to the distortion parameter β as follows:

$$R(s) = \frac{\xi_0(s)}{\xi_0(r)} = 1 + \frac{2\beta}{3} + \frac{\beta^2}{5}, \tag{3.27}$$

$$Q(s) = \frac{\xi_2(s)}{\xi_0(s) - \frac{3}{s^3}\int_0^s ds'\xi(s')s'^2} = \frac{\frac{4}{3}\beta + \frac{4}{7}\beta^2}{1 + \frac{2\beta}{3} + \frac{\beta^2}{5}}, \tag{3.28}$$

where ξ_0 and ξ_2 are the redshift-space monopole and quadrupole of the 2PCF, respectively. Fig. 6.7 shows the measurements of the $R(s)$ and $Q(s)$ estimators, as a function of redshift errors, and their theoretical prediction calculated by assuming the Tinker et al. (2010) linear bias. We find a good agreement between measurements and theoretical predictions in the case without redshift errors, for both estimators, at large enough scales (beyond $\sim 10h^{-1}\,\mathrm{Mpc}$). On the other hand, redshift errors introduce scale-dependent distortions in both these statistics. In particular, their effect is to increase (decrease) the $R(s)$ ratio above (below) a characteristic scale, whereas the $Q(s)$ is reduced, especially at small scales.

6.3. *Intermezzo*: implementing models of RSD

A short theoretical description on the modelling of clustering distortions induced by peculiar velocities has been already presented in Chapter §3. Here we discuss briefly the methodology followed in the implementation of the models for redshift-space distortions, from the linear theory to more elaborated prescriptions based on standard perturbation theory (SPT). Since the aim of this Chapter is focused on modelling RSD, we do not enter in a detailed description on the theoretical aspects of perturbation theory, that clearly is out of reach of this Thesis.

In order to extract information from the RSD signal, we model the clustering signal in configuration space. To get the theoretical model of the multipole moments or clustering wedges of the 2PCF, first of all, we consider the description of the clustering in Fourier space through the matter power spectrum $P(k,\mu)$. The complexity of the redshift-space power spectrum $P(k,\mu)$ depends on how the matter field, the velocity field and the galaxy bias are described to account for the non-linearities in the growth of cosmic structures, in this sense several approaches have been proposed in literature (for a review see e.g. Scoccimarro, 2004). Under the assumption of the plane-parallel approximation, meaning that the probed separation range is much smaller than the distance between sources and observer, and considering a linear bias, we focus on three specific models: i) the so-called dispersion model, ii) the Scoccimarro (2004) model, and iii) the TNS model (Taruya, Nishimichi, and Saito, 2010). Once the redshift-space power spectrum is computed, it can be decomposed in terms of its multipole moments $P_l(k)$ [see Eq. (3.14)], and finally by Fourier transforming, as shown by Eq. (3.20), the corresponding multipole moments and clustering wedges of the 2PCF can be obtained.

The Dispersion model was already introduced in Chapter §3 and discussed in the analysis presented in Section 5.6 of Chapter §5. Thus, in this Section we focus on the models based on perturbation theory, for which the power spectrum is given by

$$P(k,\mu) = \begin{cases} D_{FoG} b^2 \left[P_{\delta\delta} + 2\beta\mu^2 P_{\delta\theta} + \beta^2\mu^4 P_{\theta\theta}\right] & \text{Scoccimarro model} \\ D_{FoG} b^2 \left[P_{\delta\delta} + 2\beta\mu^2 P_{\delta\theta} + \beta^2\mu^4 P_{\theta\theta} + bC_A + b^2 C_B\right] & \text{TNS model,} \end{cases} \tag{6.3}$$

where D_{FoG} is a damping term that describes the velocity dispersion, $P_{\delta\delta}$, $P_{\delta\theta}$ and $P_{\theta\theta}$ denote the auto-power spectrum of density, the cross-power spectrum and the velocity-divergence spectrum, respectively [see Eq. (3.38)], and C_A, C_B are correction terms of the TNS model that depend on the bias and growth factor. Several motivations, regarding the pairwise velocities σ_{12}, suggest that

the D_{FoG} term can be modelled as a Gaussian or Lorentzian function following:

$$D_{FoG}(k,\mu,f,\sigma_{12}) = \begin{cases} \exp\left[-(k\mu f\sigma_{12})^2\right] & \text{Gaussian} \\ 1/[1+(k\mu f\sigma_{12})^2] & \text{Lorentzian;} \end{cases}$$

as it can be noted, the use of either a Gaussian or a Lorentzian damping results in the same effect at first order.

Since both the Scoccimarro (2004) model and the Taruya, Nishimichi, and Saito (2010) model take into account the non-linear mode coupling between the density and velocity divergence fields, the main issue is to compute, first, these individual contributions, $P_{\delta\delta}$, $P_{\delta\theta}$ and $P_{\theta\theta}$, and then the correction terms in the case of the TNS model. At scales close to linear-regime $P_{\delta\theta}$ and $P_{\theta\theta}$ tend to $P_{\delta\delta}$, in general, they can be computed from perturbation theory (Eulerian, Lagrangian or Time renormalization)[8], but also from fitting formulas (see e.g. Jennings, 2012; Pezzotta et al., 2017; Bel et al., 2019). $P_{\delta\delta}$ is the non-linear correction obtained directly from the HALOFIT non-linear model built-in Boltzmann codes, e.g. CAMB or CLASS codes, while for the contribution coming from the cross term and the velocity one, we used the following relations:

$$P_{\delta\theta}(k) = \begin{cases} \left(P_{\delta\delta}(k)P_L(k)e^{-k/k^*}\right)^{\frac{1}{2}}, & \text{Pezzotta et al. (2017) approx.,} \\ \left[P^{\rm HF}_{\delta\delta}(k)P^{\rm lin}_{\theta\theta}(k)\right]^{\frac{1}{2}} e^{-\frac{k}{k_\delta}-bk^6}, & \text{Bel et al. (2019) approx.,} \\ \exp(f(k))^2\left(P_L(k)+P_{1loop}(k)\right), & \text{Crocce et al., (2012),} \\ P_L(k)+2\int F_2(\boldsymbol{p},\boldsymbol{q})G_2(\boldsymbol{p},\boldsymbol{q})P(p)P(q)d^3q+ & \\ 3P(k)\int\left[F_3(k,q)+G_3(k,q)\right]P(q)d^3q, & \text{Scoccimarro (2004),} \end{cases} \tag{6.4}$$

and

$$P_{\theta\theta}(k) = \begin{cases} P_L(k)e^{-k/k^*}, & \text{Pezzotta et al. (2017) approx.,} \\ P^{\rm lin}_{\theta\theta}(k)e^{-\frac{k}{k_\theta}}, & \text{Bel et al. (2019) approx.,} \\ \exp(g(k))^2\left(P_L(k)+P_{1loop}(k)\right), & \text{Crocce et al., (2012),} \\ P_L(k)+2\int\left[G_2(\boldsymbol{p},\boldsymbol{q})\right]^2P(p)P(q)d^3q+ & \\ 6P(k)\int G_3(k,q)P(q)d^3q, & \text{Scoccimarro (2004),} \end{cases} \tag{6.5}$$

being P_L (k) the linear matter power spectrum. For the fitting formulas by Pezzotta et al. (2017), k^* is a parameter representing the typical damping scale of the velocity power spectra, which can be well described by $\frac{1}{k^*} = p_1\sigma_8^{p_2}$, where p_1 and p_2 are the free parameters of the fit. This description of the power spectrum naturally converges to $P_{\delta\delta}(k)$ in the linear regime, including a dependence on the redshift through $\sigma_8(z)$.

The fitting functions by Bel et al. (2019) extend the ones previously investigated by (Jennings, Baugh, and Pascoli, 2011; Jennings, 2012), considering a dependency on the amplitude of linear fluctuations measured by σ_8. In this case, $P^{\rm HF}_{\delta\delta}(k)$ refers to the non-linear density-density CDM power spectrum computed with HALOFIT (Takahashi et al., 2012), which is included in CAMB, while

[8] For the Eulerian scheme see (Bernardeau et al., 2002), for the Lagrangian see (Bernardeau and Valageas, 2008) and for Time renormalization see (Pietroni, 2008).

$P^{\rm lin}_{\theta\theta}(k)$ refers to the linear auto-spectrum of the velocity divergence which can be computed as $P^{\rm lin}_{\theta\theta}(k) = f^2(k)P^{\rm lin}_{\delta\delta}(k)$. Moreover, b, a_1, a_2, and a_3 are free parameters to be fitted, controlling the amplitude of the typical damping scales k_δ and k_θ so that $1/k_\theta = a_1 + a_2 k + a_3 k^2$.

The expressions for $P_{\theta\theta}(k)$ and $P_{\delta\delta}(k)$ by Crocce and Scoccimarro (2006a) are derived from the renormalized perturbative scheme, in terms of the functions $f(k)$ and $g(k)$, which represent the second-order correction of the non-linear propagator, while P_{1loop} is the one-loop power spectrum correction. Both terms can be computed with the MPTbreeze code[9] (Crocce, Scoccimarro, and Bernardeau, 2012). A detailed description of this formalism can be found in (Crocce and Scoccimarro, 2006b; Crocce and Scoccimarro, 2006a).

In the last scheme that we use, the auto-power spectra of density, the cross-power spectrum and the velocity-divergence, are obtained from the standard perturbation theory, as proposed originally by Scoccimarro (2004). The terms F_i and G_i in Eqs. (6.4) and (6.5) are named kernels and can be written as follows:

$$
\begin{aligned}
F_2(\boldsymbol{k},\boldsymbol{q}) &= \frac{\nu_2}{2} + \frac{1}{2}\hat{\boldsymbol{k}}\cdot\hat{\boldsymbol{q}}\left(\frac{k}{q}+\frac{q}{k}\right) + \frac{2}{7}\left(\hat{\boldsymbol{k}}_i\hat{\boldsymbol{k}}_j - \frac{1}{3}\delta_{ij}\right)\left(\hat{\boldsymbol{q}}_i\hat{\boldsymbol{q}}_j - \frac{1}{3}\delta_{ij}\right),\\
G_2(\boldsymbol{k},\boldsymbol{q}) &= \frac{\mu_2}{2} + \frac{1}{2}\hat{\boldsymbol{k}}\cdot\hat{\boldsymbol{q}}\left(\frac{k}{q}+\frac{q}{k}\right) + \frac{4}{7}\left(\hat{\boldsymbol{k}}_i\hat{\boldsymbol{k}}_j - \frac{1}{3}\delta_{ij}\right)\left(\hat{\boldsymbol{q}}_i\hat{\boldsymbol{q}}_j - \frac{1}{3}\delta_{ij}\right),\\
F_3(k,q) &= \frac{6k^6 - 79k^4q^2 + 50k^2q^4 - 21q^6}{63k^2q^4} + \frac{\left(q^2-k^2\right)^3\left(7q^2+2k^2\right)}{42k^3q^5}\ln\left|\frac{k+q}{k-q}\right|,\\
G_3(k,q) &= \frac{6k^6 - 41k^4q^2 + 2k^2q^4 - 3q^6}{21k^2q^4} + \frac{\left(q^2-k^2\right)^3\left(q^2+2k^2\right)}{14k^3q^5}\ln\left|\frac{k+q}{k-q}\right|,
\end{aligned}
$$

where $\nu_2 = 34/21$ and $\mu_2 = 26/21$ represent the second-order evolution in the spherical collapse dynamics. The origin of the other terms in the kernels has different physical motivations, which consider the mapping transformation from Lagrangian to Eulerian space and take into account the effect of tidal gravitational fields (for details see Scoccimarro, 2004).

Since the SPT consists on expanding the statistics of interest as a sum of infinite terms, where every term corresponds to a n-loop correction, we consider corrections up 1-loop order. The 0-loop correction corresponds to the linear power spectrum, $P^{(0)}(k) = P^L(k)$, whereas the 1-loop term is expressed as a sum of 2 different terms $P^{13}(k)$ and $P^{22}(k)$. Thus at 1-loop order the power spectrum is written as follows

$$
P^{1-\rm loop}_{xy}(k) = P^{\rm L}_{xy}(k) + P^{13}_{xy}(k) + P^{22}_{xy}(k), \tag{3.42}
$$

where the 1-loop corrections are defined by

$$
\begin{aligned}
\left\langle x_2(\vec{k}) y_2\left(\vec{k}'\right)\right\rangle &= (2\pi)^3\delta_D\left(\vec{k}+\vec{k}'\right)P^{22}_{xy}(k),\\
\left\langle x_1(\vec{k}) y_3\left(\vec{k}'\right) + x_3(\vec{k}) y_1\left(\vec{k}'\right)\right\rangle &= (2\pi)^3\delta_D\left(\vec{k}+\vec{k}'\right)P^{13}_{xy}(k),
\end{aligned}
\tag{6.6}
$$

[9] http://maia.ice.cat/crocce/mptbreeze/

where x and y can be δ or θ. Working these through, the extended expressions for the 1-loop corrections in terms of the linear power spectrum $P_0(k) = P^{\rm L}(k, z = 0)$ at redshift $z = 0$, are, for the 22 correction:

$$P^{22}_{\delta\delta}(k) = 2\frac{k^3}{(2\pi)^2}\int_0^\infty r^2 {\rm d}r \int_{-1}^1 P_0(kr)P_0\left(k\sqrt{1+r^2-2rx}\right) F_2^2(k,r,x){\rm d}x, \tag{6.7}$$

$$P^{22}_{\delta\theta}(k) = 2\frac{k^3}{(2\pi)^2}\int_0^\infty r^2 {\rm d}r \int_{-1}^1 P_0(kr)P_0\left(k\sqrt{1+r^2-2rx}\right) F_2(k,r,x)G_2(k,r,x){\rm d}x, \tag{6.8}$$

$$P^{22}_{\theta\theta}(k) = 2\frac{k^3}{(2\pi)^2}\int_0^\infty r^2 {\rm d}r \int_{-1}^1 P_0(kr)P_0\left(k\sqrt{1+r^2-2rx}\right) G_2^2(k,r,x){\rm d}x, \tag{6.9}$$

while for the 13 correction they are:

$$P^{13}_{\delta\delta}(k) = 2\frac{k^3}{(2\pi)^2}F_1(k)P_0(k)\int_0^\infty r^2 P_0(kr)F_3(k,r,x){\rm d}r, \tag{6.10}$$

$$\begin{aligned} P^{13}_{\delta\theta}(k) = &\frac{k^3}{(2\pi)^2}F_1(k)P_0(k)\int_0^\infty r^2 P_0(kr)G_3(k,r,x){\rm d}r \\ &+\frac{k^3}{(2\pi)^2}G_1(k)P_0(k)\int_0^\infty r^2 P_0(kr)F_3(k,r,x)dr \end{aligned} \tag{6.11}$$

$$P^{13}_{\theta\theta}(k) = 2\frac{k^3}{(2\pi)^2}G_1(k)P_0(k)\int_0^\infty r^2 P_0(kr)G_3(k,r,x){\rm d}r. \tag{6.12}$$

For a detailed description of the perturbation theory approach see e.g. Gil-Marín et al. (2012). The algorithms to compute all these quantities are provided by the *Cosmological Perturbation Theory Library* (henceforth `CPT Library`)[10] (Taruya, Nishimichi, and Saito, 2010), that we implemented and tested as subroutines in the CosmoBolognaLibrary. Thus, with the SPT power spectra computed up to 1-loop order we can input these to the Scoccimarro (2004) model and to the TNS model (Taruya, Nishimichi, and Saito, 2010) to calculate the redshift-space power spectrum as in Eq. (6.3). Regarding the TNS model, the corrections terms C_A and C_B, can be expressed in terms of the basic quantities of density δ and velocity divergence $\theta(\mathbf{k}) \equiv [-i\mathbf{k}\cdot\mathbf{v}(\mathbf{k})]/[af(a)H(a)]$, specifically they are rewritten as

$$\begin{aligned} C_A(k,\mu) = &(k\mu f)\int \frac{d^3\boldsymbol{p}}{(2\pi)^3}\frac{p_z}{p^2} \\ &\times [B_\sigma(\boldsymbol{p}, \boldsymbol{k}-\boldsymbol{p}, -\boldsymbol{k}) - B_\sigma(\boldsymbol{p}, \boldsymbol{k}, -\boldsymbol{k}-\boldsymbol{p})] \end{aligned} \tag{3.43}$$

$$C_B(k,\mu) = (k\mu f)^2\int \frac{d^3\boldsymbol{p}}{(2\pi)^3}F(\boldsymbol{p})F(\boldsymbol{k}-\boldsymbol{p}) \tag{3.44}$$

$$F(\boldsymbol{p}) = \frac{p_z}{p^2}\left[P_{\delta\theta}(p) + f\frac{p_z^2}{p^2}P_{\theta\theta}(p)\right] \tag{3.45}$$

[10] Cosmological Perturbation Theory Library (CPT Library) http://www2.yukawa.kyoto-u.ac.jp/~atsushi.taruya/cpt_pack.html

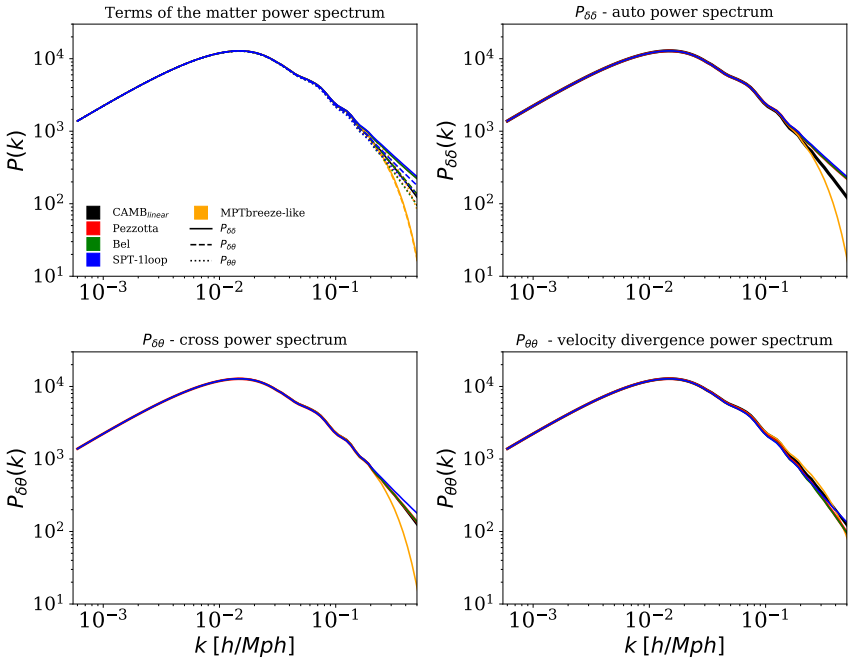

(a)

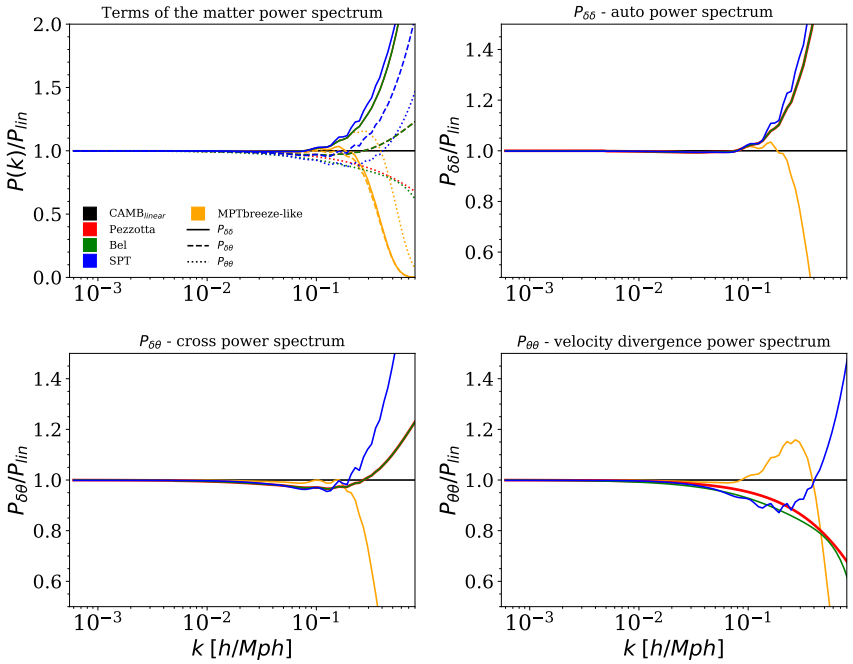

(b)

Figure 6.8: Comparison of the different schemes implemented in the CosmoBolognaLib to compute $P_{\delta\delta}(k)$, $P_{\delta\theta}(k)$ and $P_{\theta\theta}(k)$. The upper panels show each power spectrum, at $z = 0$, as a function of the wave number when a PLANCK18 cosmology is assumed. In the lower panels the relative differences are measured with respect to the linear power spectrum.

where B_σ is the cross bispectrum defined by

$$\left\langle \theta(\boldsymbol{k}_1) \left\{ \delta(\boldsymbol{k}_2) + f\frac{k_{2z}^2}{k_2^2}\theta(\boldsymbol{k}_2) \right\} \left\{ \delta(\boldsymbol{k}_3) + f\frac{k_{3z}^2}{k_3^2}\theta(\boldsymbol{k}_3) \right\} \right\rangle = (2\pi)^3 \delta_D(\boldsymbol{k}_1+\boldsymbol{k}_2+\boldsymbol{k}_3) B_\sigma(\boldsymbol{k}_1,\boldsymbol{k}_2,\boldsymbol{k}_3) . \tag{3.46}$$

Note that C_A and C_B terms are proportional to b^3 and b^4, respectively, actually they can be re-written as a power series expansion of b, f and μ and their respective contributions to the total power spectrum (Taruya, Nishimichi, and Saito, 2010; de la Torre and Guzzo, 2012).

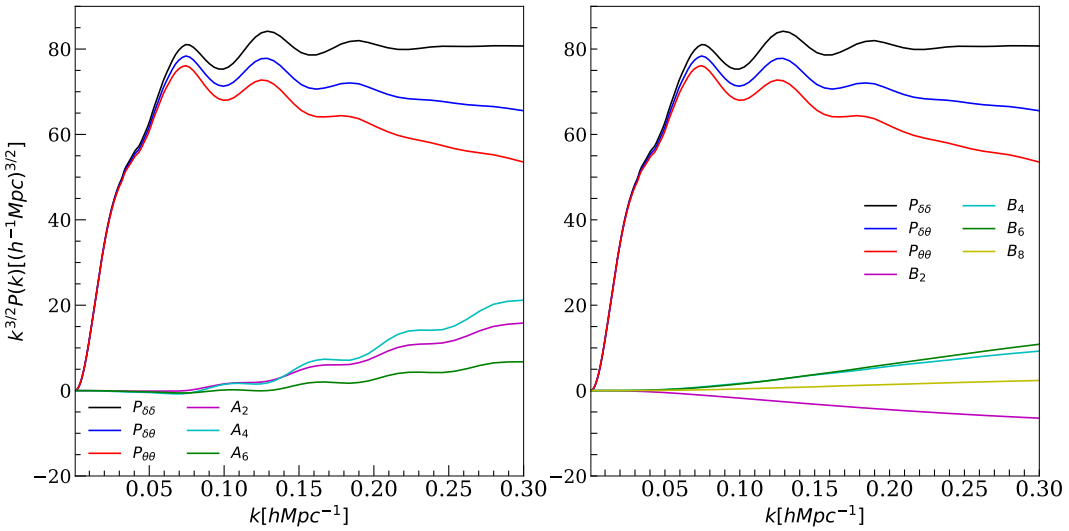

Figure 6.9: Contribution of the correction terms of the TNS model, at $z = 0$ for a PLANCK18 cosmology, with respect to the $P_{\delta\delta}$, $P_{\delta\theta}$ and $P_{\theta\theta}$ power spectrum. The A_i and B_i terms have been computed using the Standard Perturbation theory at 1-loop according to Eq. (6.13).

Fig. 6.8 shows the comparison between the different 'methods' that have been implemented in the CosmoBolognaLib to compute $P_{\delta\delta}(k)$, $P_{\delta\theta}(k)$ and $P_{\theta\theta}(k)$. The upper panels show each power spectrum, at $z = 0$, as a function of the wave number when a PLANCK18 cosmology is assumed. In the lower panels the relative differences are measured with respect to the linear power spectrum. As it can be noticed, all approaches are in agreement each other at linear regime. The results using the MPTbreeze method are the most deviated from the others since this method includes an exponential cut-off that dominates in the non-linear regime (see e.g. Lazanu et al., 2016). The Pezzotta et al. (2017) and Bel et al. (2019) fitting formulas are in very well agreement between them for the auto-power spectrum and the cross-power spectrum; the observed differences in the velocity divergence power spectrum are in the non-linear regime, where the Bel et al. (2019) approach predicts a lower value with respect to the predictions of the rest of the methods. Furthermore, the fitting formulas deviate significantly when $k > 10^{-1}$h/Mpc from the full prediction at 1-loop order from

SPT computed with the CPT Library.

Fig. 6.9 shows the contribution of the correction terms of the TNS model with respect to the $P_{\delta\delta}$, $P_{\delta\theta}$ and $P_{\theta\theta}$ power spectrum. Each power spectrum was computed using the SPT scheme implemented in the CPT Library and linked with the cosmology provided by the CosmoBolognaLib. As expected, the effect of the correction terms is more important at non-linear regime exhibiting an oscillating behaviour, as predicted by Taruya, Nishimichi, and Saito (2010). Using perturbation theory, the integrals in Eqs. (3.43) and (3.44) can be separated and written in a different fashion as follows

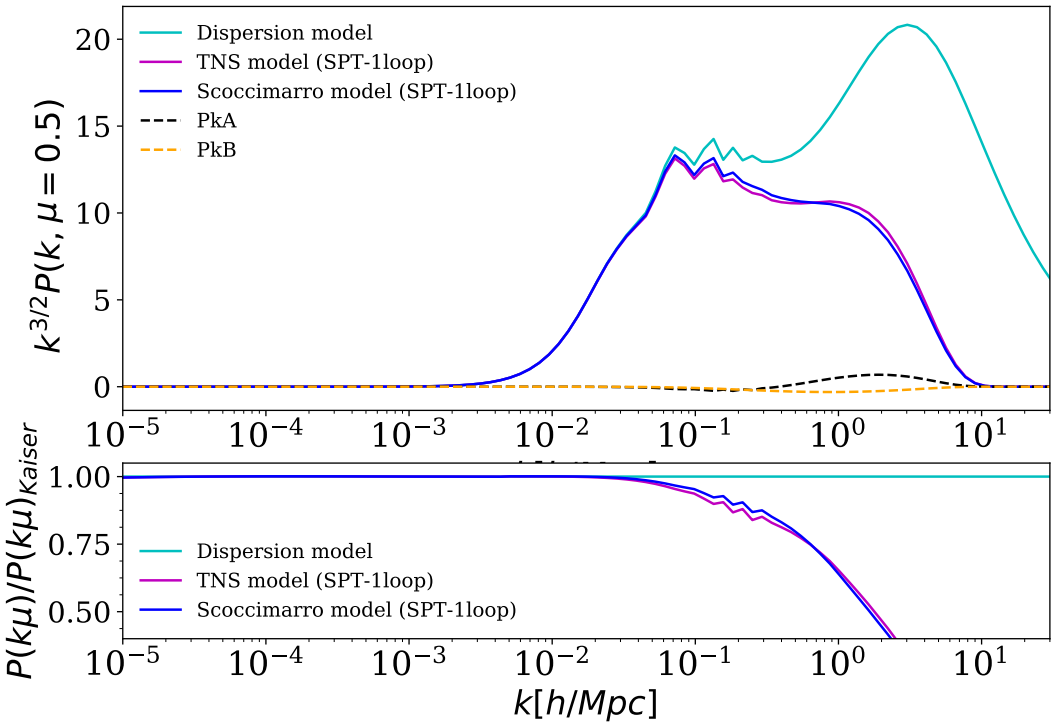

Figure 6.10: Total amplitude of the TNS correction terms ($C_A = PkA$ and $C_B = PkB$), computed using the SPT scheme from the CPT routines up 1-loop, compared with respect to the full redshift power spectrum from each RSD model: Dispersion, Scoccimarro and TNS models. The subpanel refers to the ratio between the power spectrum predicted by each one of the models and the Kaiser model.

$$A_2 = \mu^2(\beta P_{A11} + \beta^2 P_{A12}), \tag{6.13}$$
$$A_4 = \mu^4\beta^2(P_{A22} + \beta P_{A23}), \tag{6.14}$$
$$A_6 = \mu^6\beta^3 P_{A33}, \tag{6.15}$$
$$B_2 = \mu^2(\beta^2 P_{B12} + \beta^3 P_{B13} + \beta^4 P_{B14}), \tag{6.16}$$
$$B_4 = \mu^4(\beta^2 P_{B22} + \beta^3 P_{B23} + \beta^4 P_{B24}), \tag{6.17}$$
$$B_6 = \mu^6(\beta^3 P_{B33} + \beta^4 P_{B34}), \tag{6.18}$$
$$B_8 = \mu^8\beta 4 P_{B44}; \tag{6.19}$$

each term contributes to the total correction such that

$$C_A(k,\mu;f,b) = A_2 + A_4 + A_6 \tag{6.20}$$
$$C_B(k,\mu;f,b) = B_2 + B_4 + B_6 + B_8, \tag{6.21}$$

where the A_i and B_i terms are obtained from the implemented CPT routines.

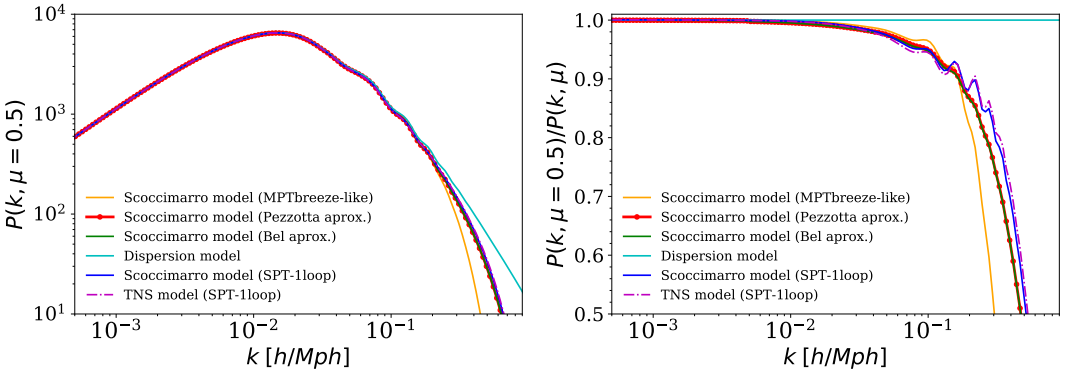

Figure 6.11: Total redshift power spectrum $P(k,\mu)$ predicted by different RSD models: i) Dispersion model, ii) Scoccimarro (2004) model and iii) TNS model (Taruya, Nishimichi, and Saito, 2010), making use of three different schemes: i) SPT from CPT Library, ii) Renormalized perturbation theory from MPTBreeze, and iii) fitting formulas. The cosmology assumed corresponds to PLANCK18 at $z = 0$.

The extended form of the P_{Amn} and P_{Bmn} terms can be found in the Appendix B. Fig. 6.10 displays the total effect of the TNS correction terms, at $z = 0$ for a PLANCK18 cosmology, compared to the full redshift power spectrum from each RSD model (Dispersion, Scoccimarro and TNS), computed using the SPT scheme integrated in the CPT Library, where $C_A = PkA$ and $C_B = PkB$. Both Scoccimarro (2004) and TNS (Taruya, Nishimichi, and Saito, 2010) models give a similar prediction of the power spectrum, where the TNS correction terms change the $P(k,\mu)$ amplitude slightly only at $k > 10^{-1}$ by less than 1%. On the other hand, at the same scales the Dispersion model has a larger amplitude with respect to the previous models. This overestimation in the power spectrum impacts the clustering analysis using RSD in configuration space, in such a way that the constraints on the growth rate parameter deviates from the theoretical expectation by at least 10% (Marulli et al., 2012; Marulli et al., 2017). A comparison of these results with the other schemes, MPTBreeze and fitting functions, is shown in Fig. 6.11, where the same behaviour can be appreciated. For the remaining part of the Thesis we focus only in the results derived using SPT up 1-loop; then in the following Sections the statistical analysis is performed considering that $P_{\delta\delta}$, $P_{\delta\theta}$, $P_{\theta\theta}$ and the TNS correction terms are computed using the CPT routines instead of the fitting formulas and MPTBreeze.

6.4. Modelling redshift-space distortions

In this Section we show the results of applying the RSD models, implemented in the previous Section, to each mock catalogue constructed from MDPL2 simulations considering the effect of possible redshift errors. The parametrisation of the RSD allows us to derive constraints on $f\sigma_8$ and $b\sigma_8$ parameters directly from the clustering. Thus, in order to extract this information from the RSD signal, we model both multipole moments (monopole and quadrupole) and clustering wedges (radial and transverse) by assuming the plane-parallel approximation and the non-linear correlation function derived from the dispersion, Scoccimarro (2004) and TNS (Taruya, Nishimichi, and Saito, 2010) models.

We exploit a full Markov Chain Monte Carlo (MCMC) statistical analysis to estimate posterior distribution constraints on the three free RSD model parameters $[f\sigma_8,\, b\sigma_8,\, \sigma_{12}]$. We consider a standard Gaussian likelihood defined as follows:

$$-2\ln\mathcal{L} = \sum_{i,j=1}^{N} \left[\xi_l^D(s_i) - \xi_l^M(s_i)\right] C_l^{-1}(s_i, s_j) \left[\xi_l^D(s_j) - \xi_l^M(s_j)\right] , \tag{6.22}$$

with N being the number of bins at which the multipole moments and the wedges are computed, and the superscripts D and M refer to data and model, respectively. The corresponding covariance matrix $C_l(s_i, s_j)$ is computed from the data with the bootstrap method given by

$$C_k\left(s_i, s_j\right) = \frac{1}{N_R - 1} \sum_{n=1}^{N_R} \left[\xi_k^n\left(s_i\right) - \bar{\xi}_k\left(s_i\right)\right] \left[\xi_k^n\left(s_j\right) - \bar{\xi}_k\left(s_j\right)\right] . \tag{6.23}$$

The indices i and j run over the 2PCF bins, while k refers either to the order of the multipole moments considered, in which case $k = l = 0,\ 2$, or to the clustering wedges, with $k = w = 0,\ 0.5$. In both cases, $\bar{\xi}_k = 1/N_R \sum_{n=1}^{N_R} \xi_k^n$ is the average multipole (wedge) of the 2PCF, and $N_R = 100$ is the number of realisations obtained by resampling the catalogues with the bootstrap method.

We perform the MCMC analysis on all the MDPL2 mock halo catalogues to get the global evolution of the constrained parameters. First we compare the constraints on $f\sigma_8$, $b\sigma_8$ and σ_{12} at $z = 1.032$, obtained with the Gaussian and Lorentzian damping factors. The results are shown in Fig. 6.12 for the redshift-space multipole moments and clustering wedges. As it can be appreciated, the systematic errors are lower when the damping factor is modelled with a Gaussian function. This effect is more significant when the redshift errors are large, i.e. $\delta z > 0.2\%$, in agreement with Marulli et al. (2012). Thus, in the following we will adopt the Gaussian form. Figs. 6.13 and 6.14 show the measured multipole moments and the clustering wedges compared to best-fit model predictions for the dispersion, Scoccimarro and TNS models, at $z = 0.523,\ 1.032,\ 2.028$, and for different redshift measurement errors as labelled in the panels.

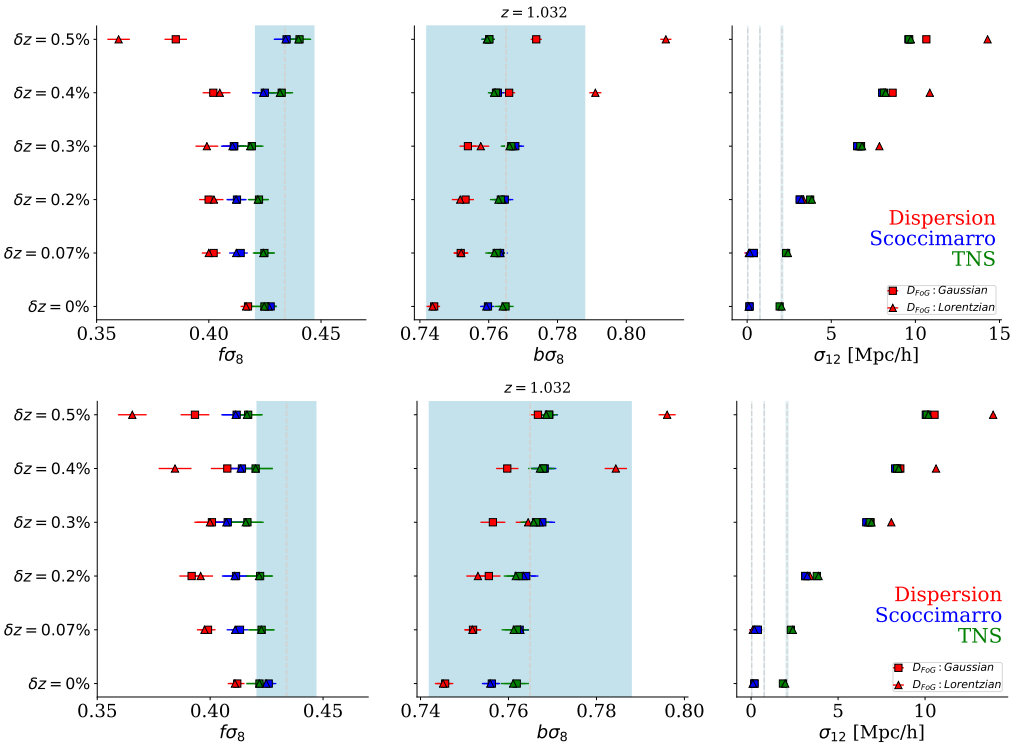

Figure 6.12: Constraints on $[f\sigma_8,\ b\sigma_8,\ \sigma_{12}]$ of the MDPL2 mock catalogue at $z = 1.032$ assuming the Gaussian and Lorentzian form of the damping factor for different values of redshift errors. The models: dispersion, Scoccimarro and TNS models, are differentiated by colour as labelled and the error bars show the 68% marginalised posterior uncertainties. The gray lines show the theoretical predictions, computed assuming the Tinker et al. (2010) effective bias. *Upper panel*: results from the redshift-space monopole and quadrupole moments; *lower panel*: results from the perpendicular and parallel wedges. The shaded area represents a 3% region, for comparison.

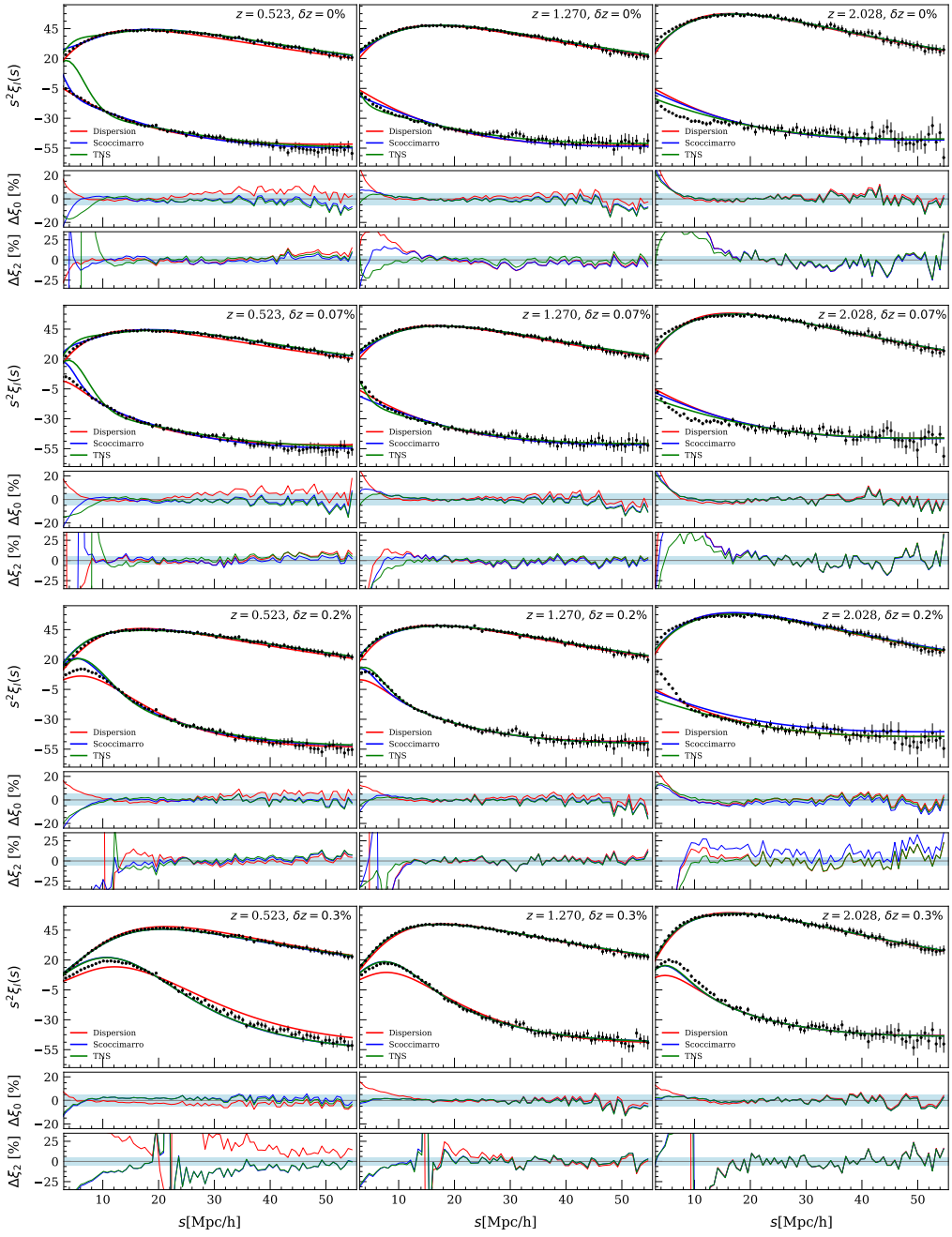

Figure 6.13: Redshift-space monopole, ξ_0, and quadrupole, ξ_2, moments of the MDPL2 mock catalogues, compared to the best-fit models – dispersion model (red), Scoccimarro model (blue) and TNS model (green). The results are shown at three different redshifts, and for different measurement redshift errors, as indicated by the labels. The subpanels show the relative percent differences with respect to the measurements. The shaded area represents a 3% difference for comparison.

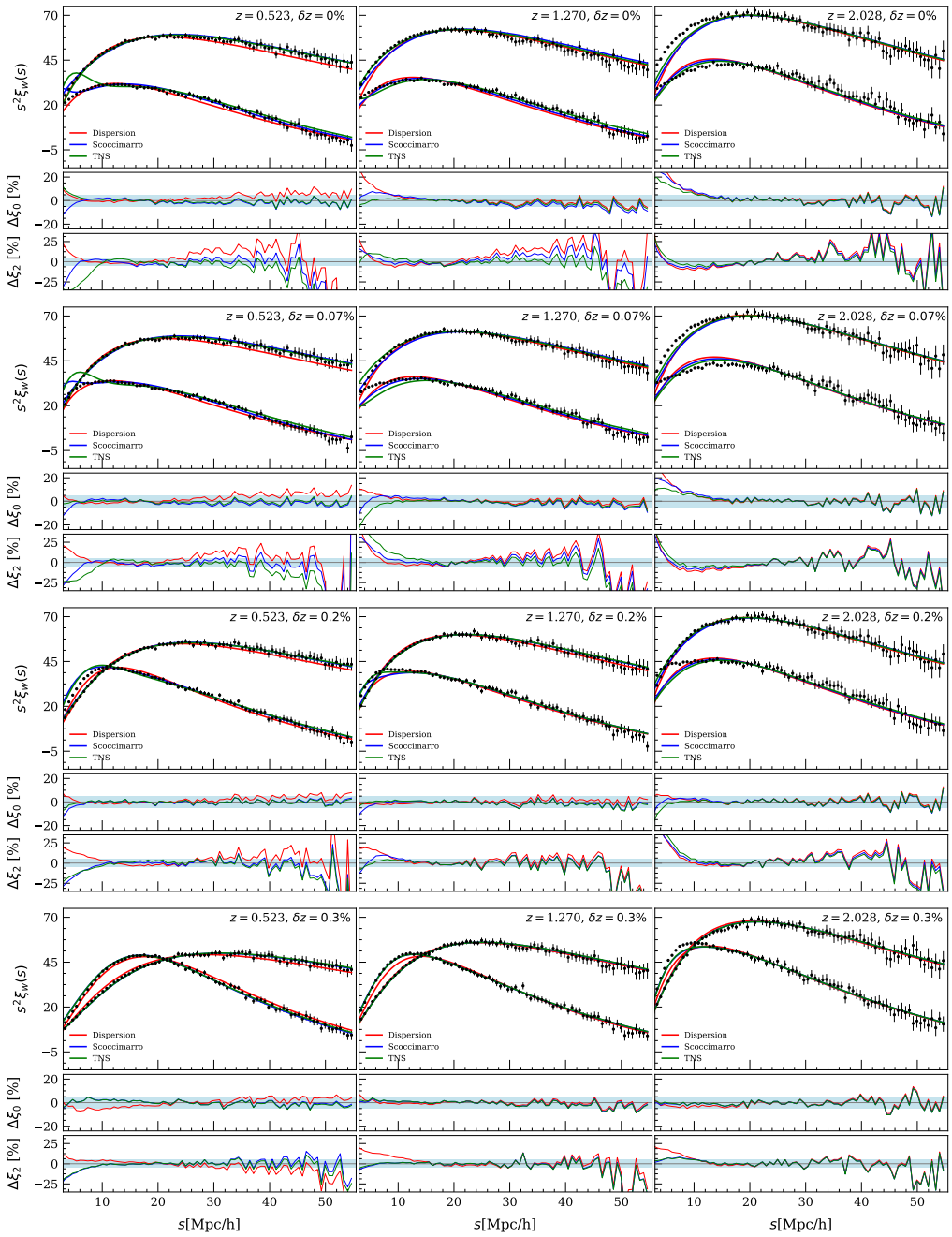

Figure 6.14: As Fig. 6.13 but for the redshift-space perpendicular, $\xi_{\perp}$, and parallel, $\xi_{\parallel}$, wedges of the MDPL2 mock catalogues.

6.5. Discussion

The global evolution of the marginalised posterior constraints on the parameters $[f\sigma_8, b\sigma_8, \sigma_{12}]$, as a function of redshift, can be appreciated in Figs. 6.15 and 6.16 for multipole moments and clustering wedges, respectively. The black lines represent the theoretical predictions, where $f\sigma_8$ was computed from CAMB, $b\sigma_8$ by assuming the Tinker et al. (2010) bias and the pairwise velocity dispersion σ_{12} corresponds to the best fit value obtained from the model considered (Dispersion, Soccimarro or TNS), when the remaining parameters are fixed to the theoretical expectation. For clarity, the results are divided by model conserving the same colour scheme in all plots when redshift errors are included as indicated by the labels. In the case with no redshift errors, we find a systematic bias in the $f\sigma_8$ constraints of about 10% at low redshifts ($z < 1$) for the dispersion model, in agreement with previous works, (see e.g. Bianchi et al., 2012; Marulli et al., 2012; Marulli et al., 2017). The Scoccimarro and TNS models provide more accurate constraints, with a systematic bias of about 8% and 5%, respectively. At high redshifts ($z \geq 1$) the agreement between $f\sigma_8$ measurements and the expected values improves. In particular, the Scoccimarro model recovers $f\sigma_8$ within 4%, while the TNS model within 3%. The constraints on $b\sigma_8$ are overall in good agreement for all models, being the TNS model the one with the lowest deviation with respect to the theoretical expectations, which is found to be less than 2% at all considered redshifts.

As we have seen in Fig. 6.5, the spurious anisotropies caused by the Gaussian redshift errors are similar to the FoG distortions. The combined effects of redshift errors and FoG are thus parameterised by the single damping term of the RSD models. Indeed, as shown in Figs. 6.15 and 6.16, the estimated value of the σ_{12} parameter of the damping term systematically increases as redshift errors increase. At $z \geq 1$, the $f\sigma_8$ and $b\sigma_8$ constraints are not significantly affected by the introduction of Gaussian redshift errors, up to $\delta z = 0.5\%$. On the other hand, at lower redshifts, the impact is more significant, as expected, though only for the largest redshift errors considered, $\delta z > 0.3\%$. This means that at $z \approx 0.5$ and including redshift errors around $\delta z = 0.3\%$ in the mocks, the relative error on the recovered $f\sigma_8$ decreases from 13% (8%, 7%) to 8% (3%, 5%) in the dispersion (Scoccimarro, TNS) model; at $z = 0.75$ the same parameter changes from 9% (6%, 3%) to 3% (4%, 1%) in the dispersion (Scoccimarro, TNS) model. The effect of the remaining δz values on $f\sigma_8$ constraints makes it fluctuate around the expected value for all models considered, meaning that true value can be recovered with a deviation of 3% even if there are redshift errors as the introduced ones in the mocks at high redshift. On the other hand the recovered $b\sigma_8$ is very stable as redshift changes, even for the distorted cases, being around a 3% of deviation for $\delta z < 0.5$ i.e. ~ 1500km/s. The global evolution of the constrained parameters suggests an increase proportional to δz, being the damping factor σ_{12} the most sensitive to the redshift errors. In fact, it has large variations in the relative error with respect to the theoretical value. This is expected since this term modulates the velocity dispersion and encodes the information to describe the squashing observed at small scales. This behaviour

can be also anticipated from the shape of the 2D 2PCF (see Fig. 6.5) and the best fit models displayed in Fig. 6.13 for multipole moments and 6.14 for wedges. At high redshift $z > 1$ we did not find a significant difference when clustering wedges are used instead of the multipole moments to get the constraints from redshift-space distortions. However, at low redshift $z < 1$, we observed that the constraints derived from clustering wedges have a smaller dispersion with respect to what obtained from the multipole moments. This can be also noticed from the first column of Fig. 6.16, where $f\sigma_8$ at $z = 0.5, 0.75$ has relative errors close to 3% as indicated by the shaded regions in the lower panels, for the three models studied. The same behaviour can be appreciated in Fig. 6.14 at scales smaller than $20h^{-1}$ Mpc for each mock catalogue.

The marginalised posterior constraints at 68% confidence level for $f\sigma_8$, $b\sigma_8$ and σ_{12}, obtained from the MCMC analysis of the redshift-space monopole and quadrupole moments, and of the perpendicular and parallel cluster wedges, are shown in Figs. 6.17 and 6.18, respectively. The posterior constraints show a notable agreement in the $f\sigma_8 - b\sigma_8$ plane at high redshift when multipole moments and clustering wedges are used. In both cases the Gaussian redshift errors cause shifts in the constraints that tend to increase $b\sigma_8$, while $f\sigma_8$ fluctuates close to the true value. This can be better seen in Figs. 6.19 and 6.20 for multipole moments and wedges respectively. The MCMC analysis shows that the $f\sigma_8 - b\sigma_8$ parameters obtained from the dispersion model are more sensitive to the Gaussian redshift errors than the ones obtained using the Scoccimarro and TNS models. In these models, the bias $b\sigma_8$ is quite stable around the central value with respect to the no distorted case, while $f\sigma_8$ changes in a similar way that the dispersion model, considering that, in any case the deviations are rather small. The global trend for each Gaussian redshift error δz considered is displayed in Fig. 6.21 for multipole moments and in Fig. 6.22 for clustering wedges. The models are displayed with the same colours used before [dispersion (red), Scoccimarro (blue) and TNS (green)] and the true values are highlighted with the stars for comparison.

A summary of the posterior constraints at 68% confidence level at three different redshifts $z = 0.523$, 1.270 and 2.028, is displayed in Fig. 6.23 (multipole moments) and in Fig. 6.24 (wedges), where the results for $f\sigma_8$ are shown in the first column, $b\sigma_8$ in the central column and σ_{12} in the last column. These plots confirm that the TNS model recover better the parameters being the least affected by the Gaussian errors after the whole MCMC analysis. Moreover, we compare the results obtained by fitting the 2PCF statistics in the comoving scale range $10 < r[h^{-1}\,\mathrm{Mpc}] < 55$ to the ones obtained at scales $r > 30\ h^{-1}\,\mathrm{Mpc}$. As expected, while the statistical uncertainties are larger in the latter scale, the systematic discrepancies are slightly reduced. In particular, the discrepancies of the TNS model on both the growth rate and the linear bias are reduced below 3%, at $z < 1.5$, for redshift errors up to $\delta z \sim 0.3\%$. On the other hand, at larger redshifts it seems more convenient to consider in the analysis also the small scales, which can be reliably described by all the RSD models considered.

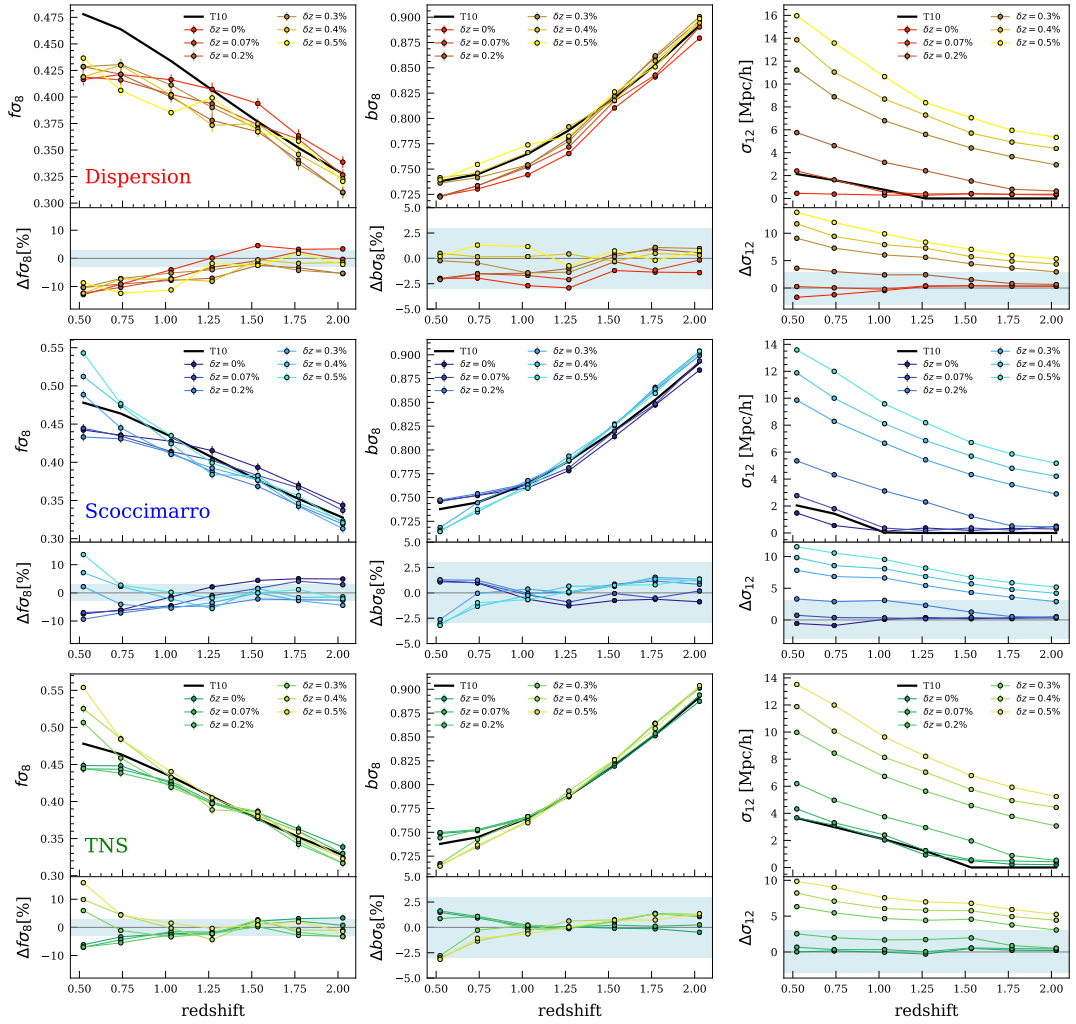

Figure 6.15: Best-fit constraints on $[f\sigma_8, b\sigma_8, \sigma_{12}]$ obtained from the redshift-space monopole and quadrupole moments, as a function of redshift, and for different values of redshift errors, as indicated by the labels. The error bars show the 68% marginalised posterior uncertainties. The black lines show the theoretical predictions, computed assuming the Tinker et al. (2010) effective bias. *Upper panels*: dispersion model; *central panels*: Scocimarro model; *lower panel*: TNS model. The subpanels show the relative percent differences with respect to the theoretical prediction. The shaded area represents a 3% difference for comparison.

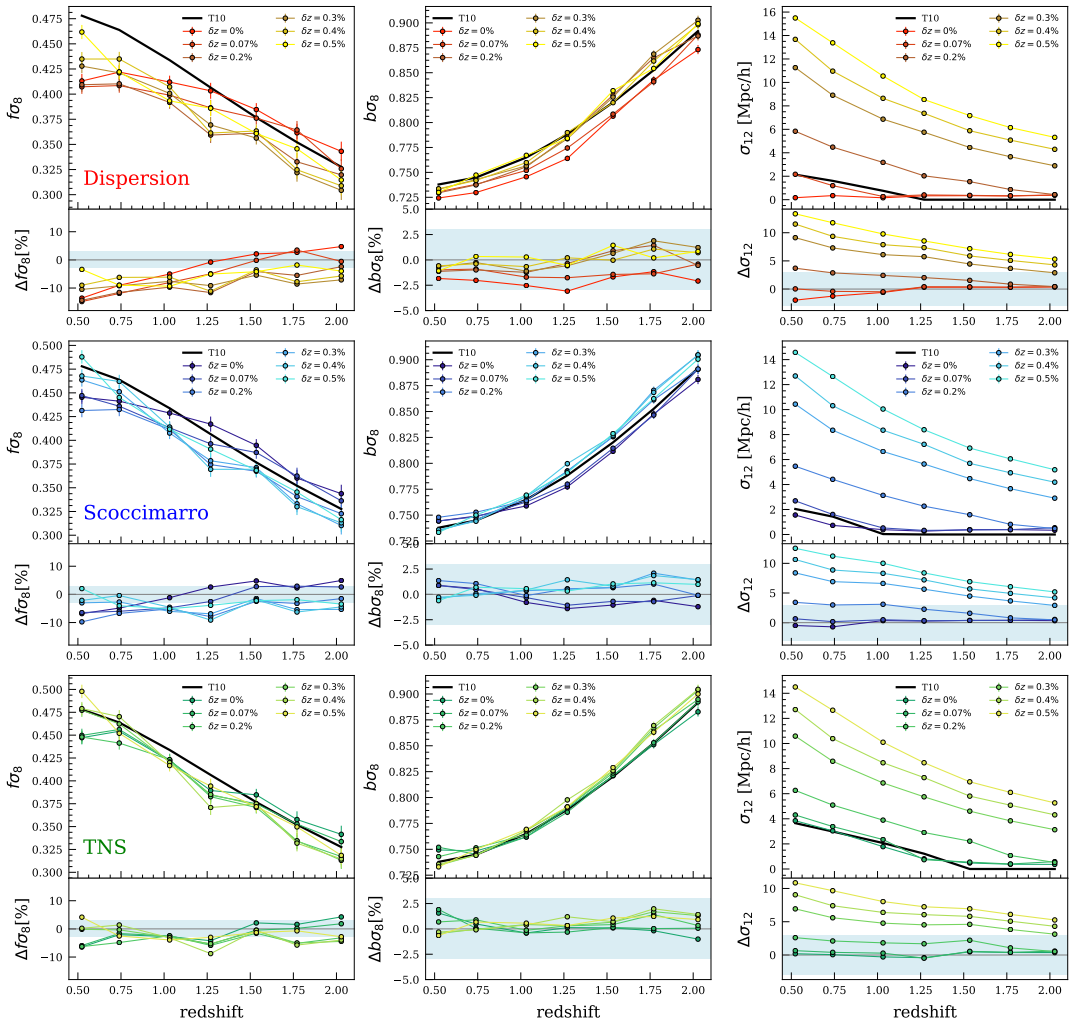

Figure 6.16: As Fig. 6.15, but using perpendicular and parallel clustering wedges.

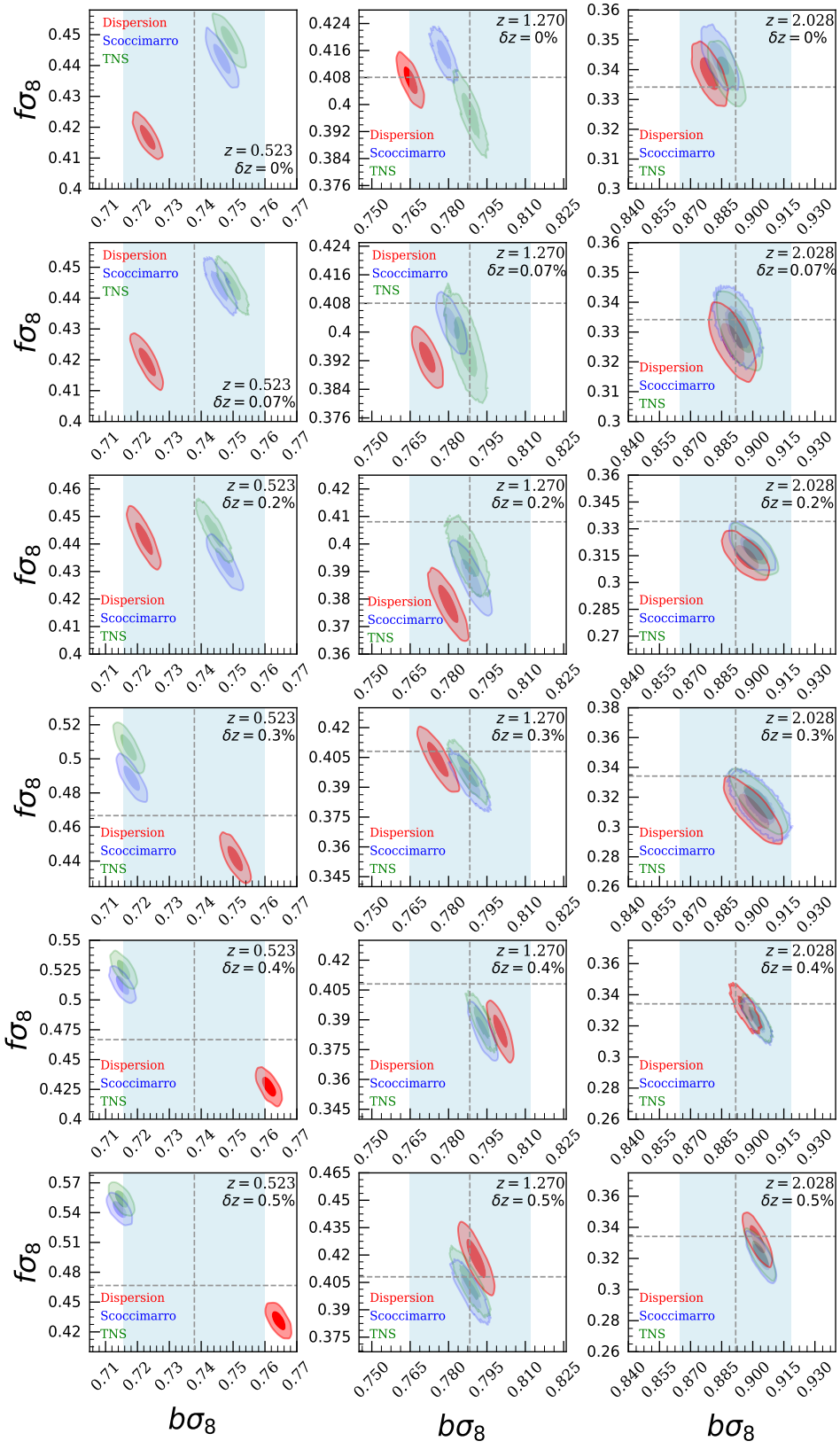

Figure 6.17: Posterior constraints at 68% and 95% confidence levels in the $f\sigma_8 - b\sigma_8$ plane, marginalised over the damping parameter σ_{12}, obtained from the MCMC analysis of the multipole moments monopole and quadrupole of the 2PCF in redshift-space for the models shown by different colours as labelled. Panels in the columns, from left to right, refer to $z = 0.523$, 1.27 and 2.028. From top to bottom, the rows increase the Gaussian redshift error considered in the mock catalogue from $\delta z = 0\%$ to 0.5% as labelled in each panel. The shaded area represents a 3% difference for comparison.

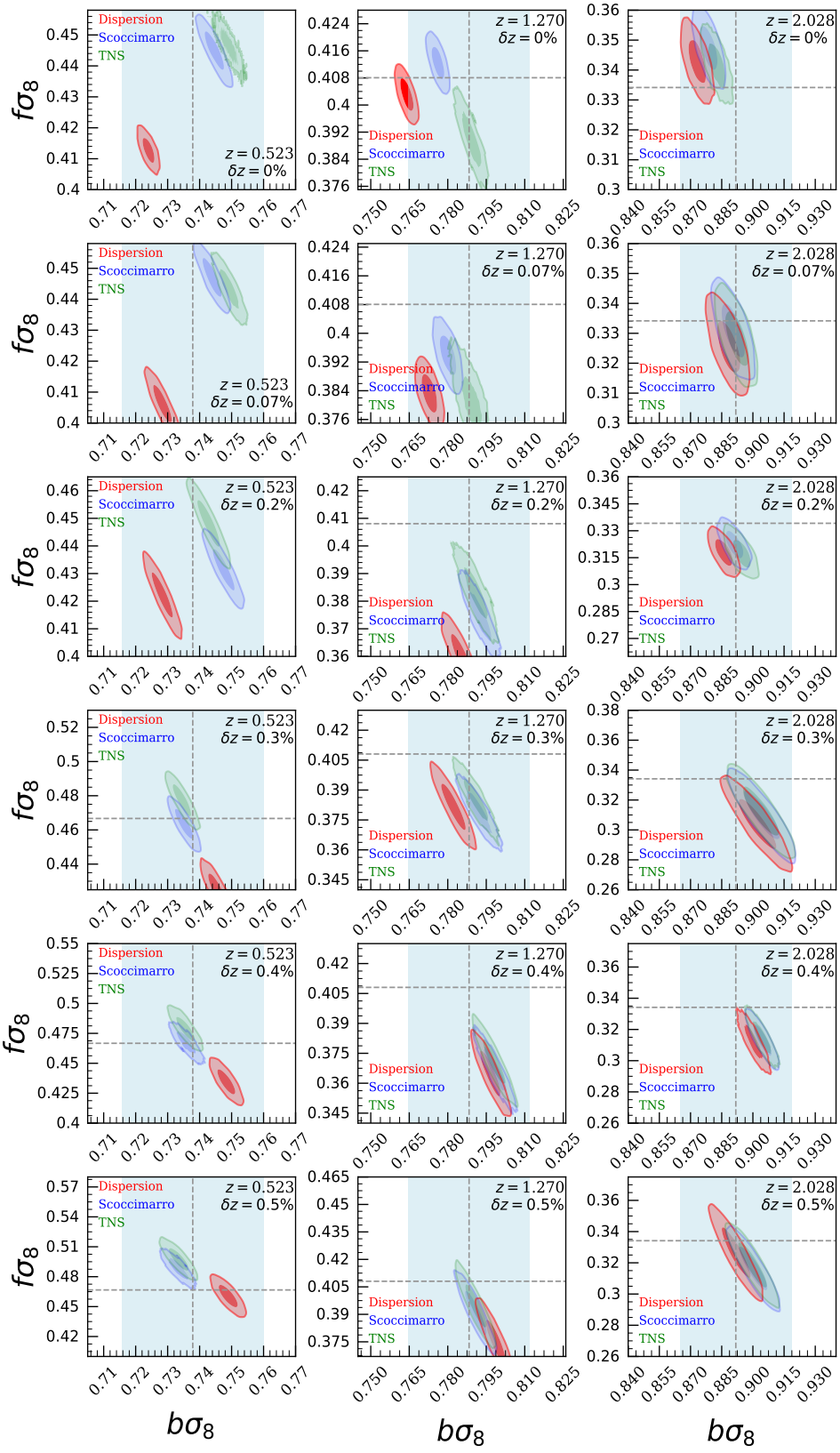

Figure 6.18: As Fig. 6.17 but for the MCMC analysis of the clustering wedges, transverse and parallel, of the 2PCF in redshift-space.

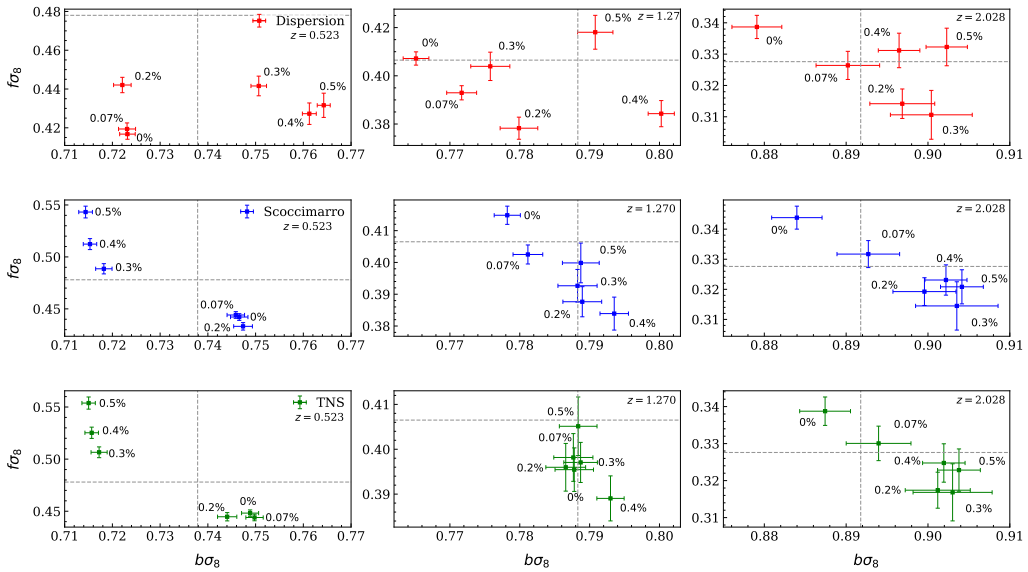

Figure 6.19: Impact of the Gaussian redshift errors on $f\sigma_8$ and $b\sigma_8$ obtained from the MCMC analysis of the monopole and quadrupole moments of the 2PCF in redshift-space as labelled. Panels in the columns, from left to right, refer to $z = 0.523$, 1.27 and 2.028, while the rows represent each one of the models considered to model the RSD: the dispersion (red), the Scoccimarro (blue) and the TNS (green) models. Dashed lines represent the theoretical expected values assuming Tinker et al. (2010) bias.

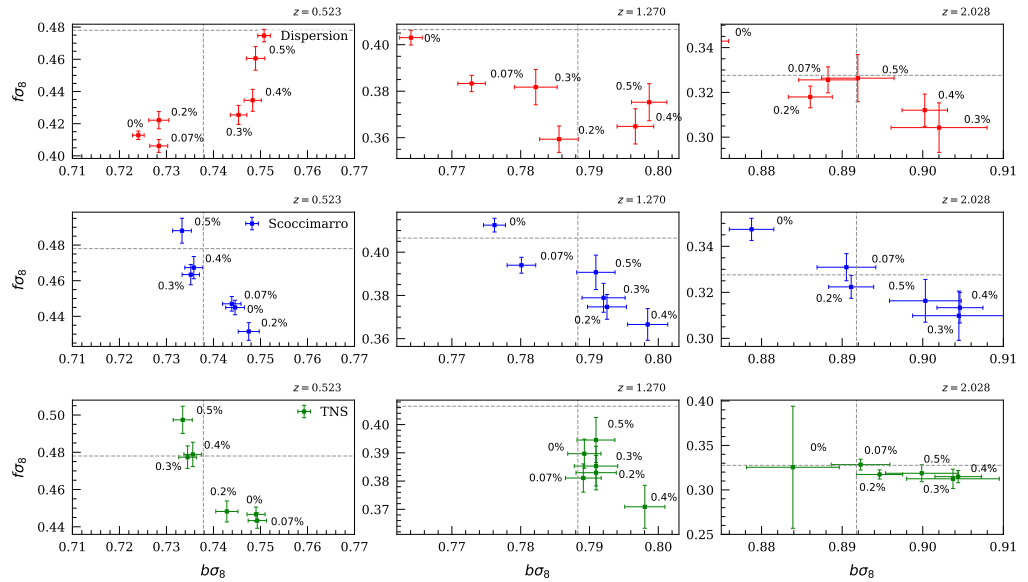

Figure 6.20: As Fig. 6.19 but for the MCMC analysis of the transverse and parallel clustering wedges of the 2PCF in redshift-space as labelled.

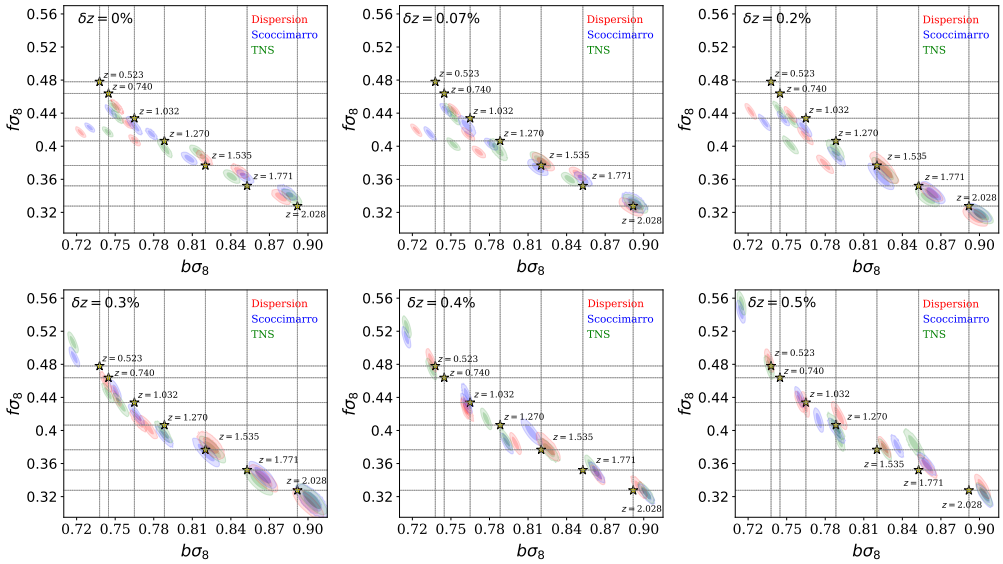

Figure 6.21: Impact of the Gaussian redshift errors, as labelled in each panel, on $f\sigma_8$ and $b\sigma_8$ constraints obtained from the MCMC analysis of the monopole and quadrupole moments of the 2PCF in redshift-space. The contours are shown for all redshifts considered in this work as labelled, where the colours correspond to the dispersion (red), the Scoccimarro (blue) and the TNS (green) models. Dashed lines represent the theoretical expected values assuming Tinker et al. (2010) bias, being the intersections highlighted by stars.

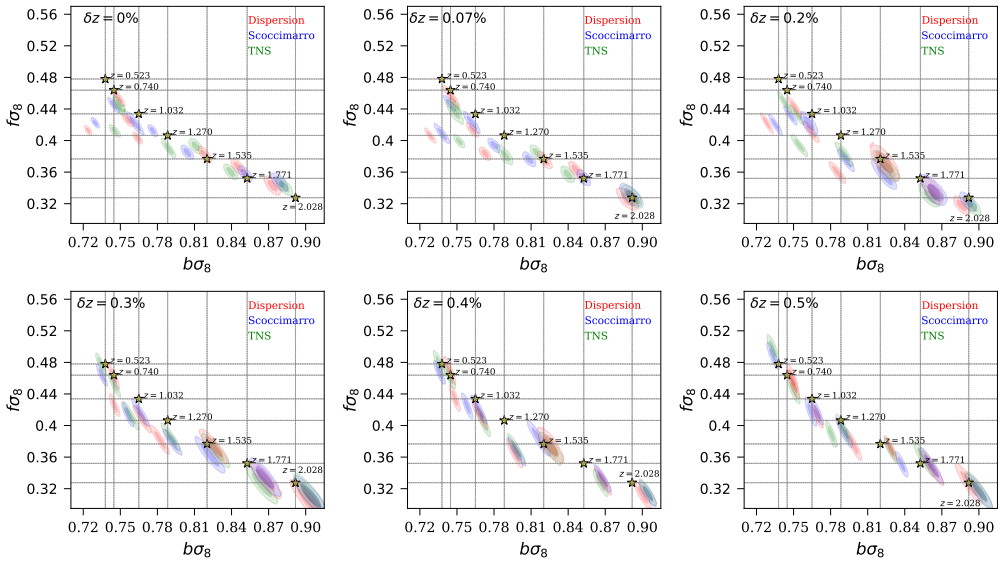

Figure 6.22: As Fig. 6.21 but for the MCMC analysis of the transverse and parallel clustering wedges of the 2PCF in redshift-space.

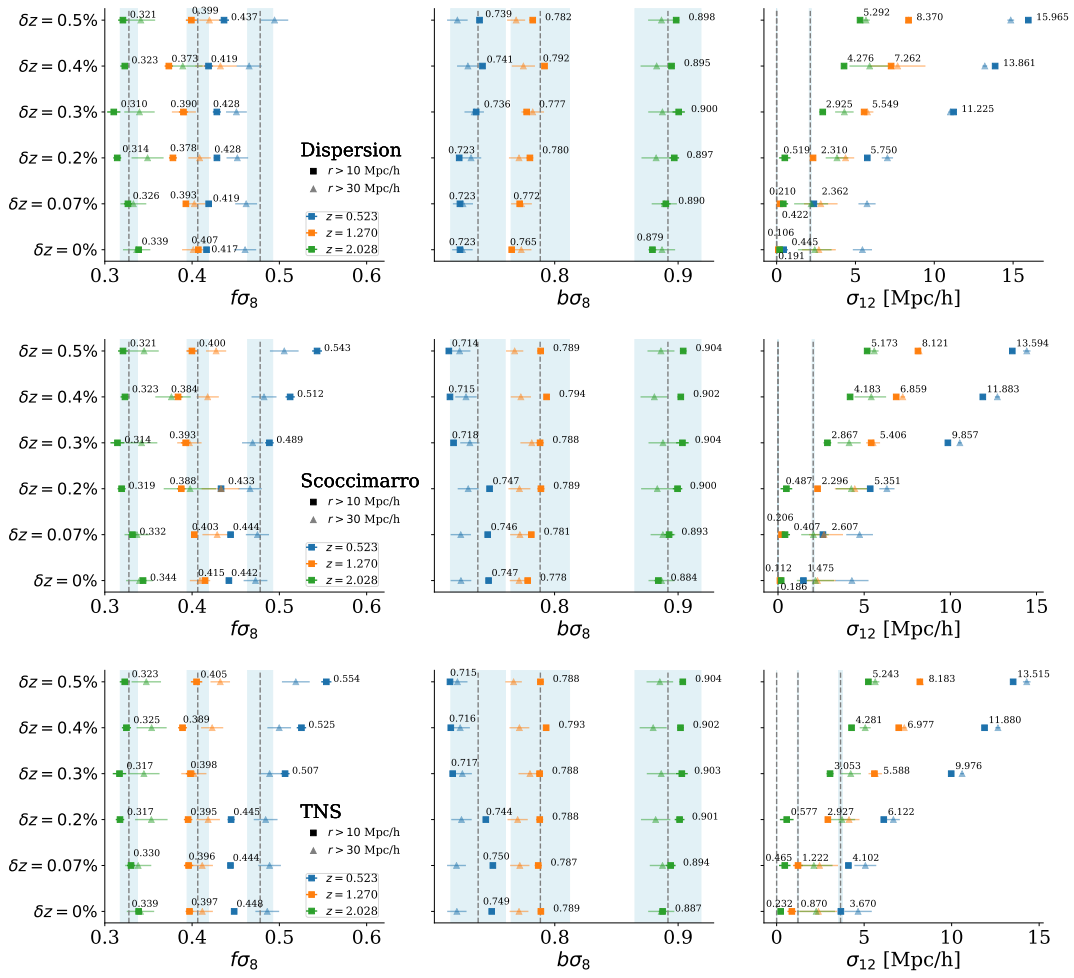

Figure 6.23: Summary of the posterior constraints at 68% confidence level for $f\sigma_8$ (first column), $b\sigma_8$ (central column) and σ_{12} (last column), obtained from the MCMC analysis of the redshift-space monopole and quadrupole moments of CDM haloes. The results are shown at three different redshifts $z = 0.523$ (blue), $z = 1.270$ (orange) and $z = 2.028$ (green), for the models considered in this work. The panels, from top to bottom, refer to the dispersion (first row), Scoccimarro (central row) and TNS (bottom row) models. The vertical gray lines are centred on theoretical expectations, with the shaded area reporting a 3% region, for comparison.

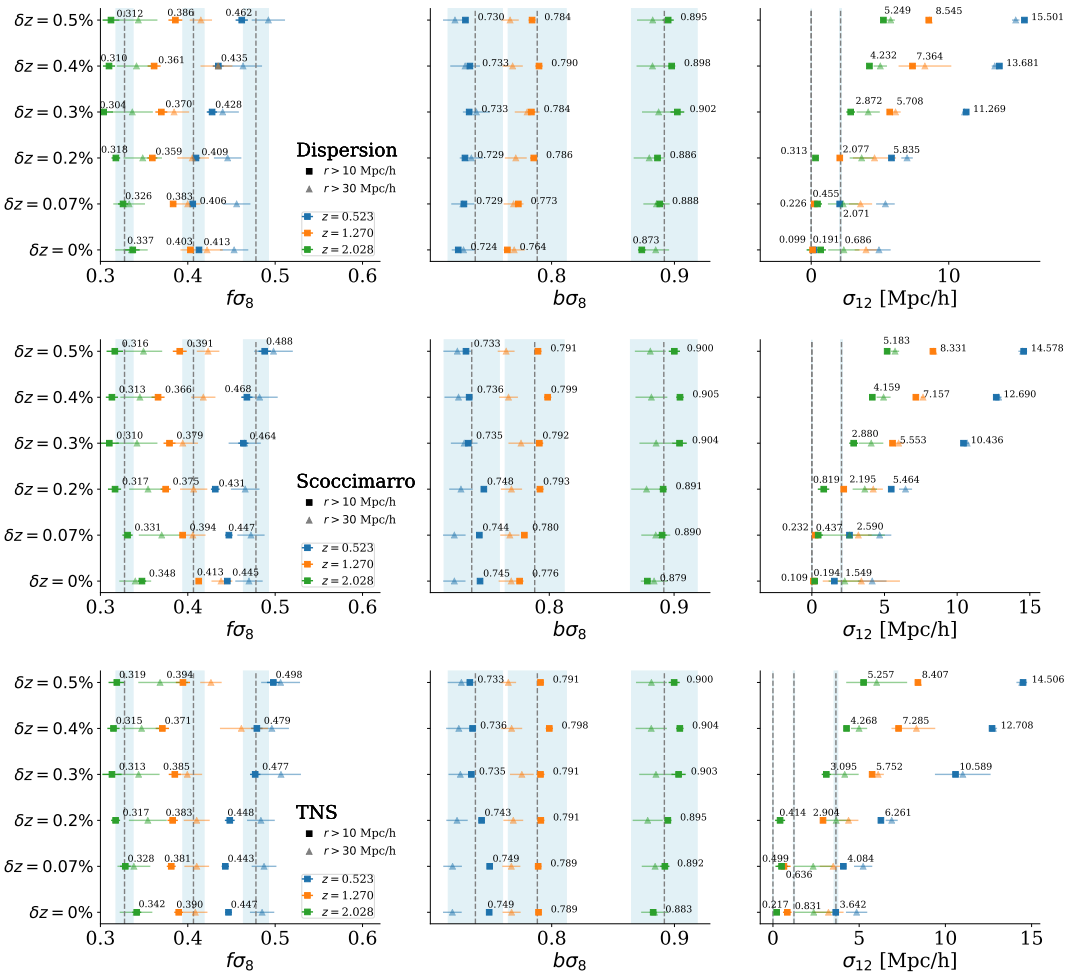

Figure 6.24: As Fig. 6.23 but for the MCMC analysis of the clustering wedges, transverse and parallel, of redshift-space 2PCF of CDM haloes.

CHAPTER 7

Conclusions

Motivated by the current issues in cosmology, in this Thesis we have investigated the large scale structure of Universe in different scenarios with the goal of constraining its cosmological parameters. To explore reliable evidence beyond the standard ΛCDM model, we have analysed statistically: *i)* some of the well established models of dark energy by combining recent observational data from CMB, BAO and growth rate of LSS and *ii)* predictions obtained from N-body simulations focusing on the clustering and RSD in the context of modify gravity models with massive neutrinos. Additionally, since RSD have been proven to be a powerful method to estimate cosmological parameters, we have implemented, tested and compared RSD models based on phenomenological approximations as well as schemes based on cosmological perturbation theory, investigating the robustness of this methodology at several scales and including realistic systematics.

In Chapter §2 we have introduced the theoretical framework of modern cosmology, which is based on the Einstein's General Relativity and then we proceeded presenting the standard ΛCDM model. We emphasize on the structure formation and on the statistical description of the density field as well as the measurements of galaxy clustering. Then, in Chapter §3 we discuss in detail the redshift-space distortions and the differences between clustering in real and redshift space, considering that in the recent years, the spatial distribution of matter on cosmological scales, has become one of the most efficient probes to investigate the properties of the Universe, such as test gravity theories on large scales, to explore the dark sector and the origin of the accelerated expansion of the universe, as well as a probe to constrain alternative cosmological models.

Moreover, we have illustrated that despite the current data are in well agreement with the standard model, there are some unsatisfactory properties of the cosmological constant, the so-called fine-tuning and the coincidence problems, that motivate different frameworks for Dark Energy and Modified Gravity in

which extra degrees of freedom can help alleviate these issues. In Chapter §4, we use the most recent observational data from CMB (Planck 2018 final data release) and LSS (SDSS, WiggleZ, VIPERS) to constrain dynamical dark energy models. The CMB shift parameter, which traditionally has been used to determine the main cosmological parameters of the standard model ΛCDM is employed in addition to data from redshift-space distortions through the growth parameter $A(z) = f(z)\sigma_8(z)$ to constrain the mass variance σ_8. BAO data is also used to study the history of the cosmological expansion and the main properties of DE. From the evolution of the deceleration parameter $q(z)$, we found new evidence on results indicated in previous works (Bonilla and Castillo, 2018), showing a slowdown behaviour of $q(z)$ at low redshifts ($z < 0.5$), made evident by the change of sign in the jerk parameter $j(z)$. This behaviour is present only in models with DE density varying with time and it is related to the dynamics of the DE density, being in principle a sign that allows us to distinguish this kind of models from a cosmological constant. Then, by using the Akaike and Bayesian Information Criterion (AIC, BIC) we performed an exclusion analysis of the different models classifying those that are better suited to the observational data; we found that the interactive dark energy (IDE) models are the most favoured by observational data, when information from SNIa and Hz is included. The analysis shows that the IDE model is followed closely by EDE and ΛCDM models, which in some cases fit better the observational data with individual probes.

In the context of models based on modified gravity and massive neutrino cosmologies, presented in Chapter §5, we investigated the spatial properties of the large-scale structure by exploiting the DUSTGRAIN-*pathfinder* simulations that follow, simultaneously, the effects of $f(R)$ gravity and massive neutrinos. These are two of the most interesting scenarios that have been recently explored to account for possible observational deviations from the standard ΛCDM model. In particular, we studied whether redshift-space distortions in the 2PCF multipole moments can be effective breaking the cosmic degeneracy between these two effects. We analysed the redshift-space distortions in the clustering of dark matter haloes at different redshifts, focusing on the monopole and quadrupole moments of the two-point correlation function, both in real and redshift space. The deviations with respect to ΛCDM model have been quantified in terms of the linear growth rate parameter. We found that multipole moments of the 2PCF from redshift-space distortions provide a useful probe to discriminate between ΛCDM and modified gravity models, especially at high redshifts ($z \gtrsim 1$), even in the presence of massive neutrinos. The linear growth rate constraints that we obtain from all the analysed $f(R) + m_\nu$ mock catalogues are statistically distinguishable from ΛCDM predictions at all redshifts but $z = 0.5$.

Finally, in order to test the ability of redshift-space distortions to constrain cosmological parameters, such as the linear growth rate, we presented in Chapter §6 the results on the systematic validation of the state-of-the-art methods used to model the galaxy two-point correlation function. The numerical recipes were tested on mock halo catalogues extracted from large N-body simulations of the

standard cosmological scenario, specifically we use the MDPL2 simulations belongs to the MultiDark suite, in the redshift range $0.5 < z < 2$. We have consider both the monopole and quadrupole multipole moments of the redshift-space two-point correlation function, as well as the radial and transverse clustering wedges, in the comoving scale range $10 < r[h^{-1}\,\mathrm{Mpc}\,] < 55$. In our analysis, we quantified the systematic uncertainties on the growth rate and linear bias measurements due to the different assumptions in the redshift-space distortion modelling. Moreover, we investigate the impact of redshift measurement errors, up to $\delta z \sim 0.5\%$, which introduce spurious clustering anisotropies. To perform the Bayesian analysis, we have implemented in the CosmoBolongaLib, both the dispersion model and two widely-used models based on perturbation theory, that is the Scoccimarro (2004) model and the Taruya, Nishimichi, and Saito (2010) model. We also revisited briefly the schemes currently used for perturbation theory computations up 1-loop, which have become important tools in theoretical cosmology, such as fitting formulas, standard perturbation theory and renormalized perturbation theory. These schemes provide a more accurate description of the redshift matter power spectrum in terms of the auto-spectrum, cross-spectrum and the velocity divergence, all of them were implemented and tested in the last version of the CosmoBolongaLib. After applying our methodology to the mock samples, we conclude that, at $z < 1$, the linear growth rate measured with the dispersion model is underestimated by about 10%, in agreement with previous findings, while the Scoccimarro and TNS models provide slightly better constraints, with a systematic bias of about 8% and 5%, respectively. At $z \geq 1$, all the RSD models considered provide constraints in good agreement with expectations. The TNS model is the one which performs better, with growth rate uncertainties below 3%. Limiting the analysis at $r > 30\,h^{-1}\,\mathrm{Mpc}$, the statistical uncertainties become larger, as expected, while the systematic discrepancies are slightly reduced. In particular, the systematics of the TNS model on both the growth rate and the linear bias are reduced below 3%, at $z < 1.5$, for redshift errors up to $\delta z \sim 0.3\%$. Furthermore, Gaussian redshift errors introduce spurious anisotropies, whose effect combines with the one of the small-scale as incoherent motions responsible of the FoG distortions. The effect of redshift errors is degenerate with the one of small-scale random motions, and can be marginalised in the statistically analysis, not introducing a significant bias in the linear growth constraints, especially at $z \geq 1$.

APPENDIX A

Homogeneity scale in the context of fractal analysis

This section is based on the paper by García-Farieta and Casas-Miranda (2018). The fractal analysis is an useful mathematical tool that quantifies galactic clustering using data from galaxy surveys by calculating quantities such as the fractal dimension. This makes possible to establish relationships between these values and other statistical descriptors. The possible cosmological implications of fractal analysis of the galaxy distribution are discussed in detail by Baryshev et al. (1998) and Martinez (1991).

The concept of dimension is associated with the number of degrees of freedom to specify any point within a distribution of points in a metric space. Topologically, the dimension indicates how much space a set occupies near each of its points (Falconer, 2004). The *self-similar dimension* can be explained by a further fragmentation of a set, and the ratio of the number of identical parts where each part is scaled down by the ratio r. For any set $X \in R^n$ that supports division into a finite number of subsets $N(k)$, where all of them are consistent with each other by translations and rotations, and it is a reduced copy of the initial set by a factor $r = 1/k$. The self-similar dimension of X is defined as the unique value D satisfying the equation $N(k) = k^D$ (Mandelbrot, 1983), i.e.,

$$D = \frac{\log N}{\log(k)}. \tag{A.1}$$

Here D is not necessarily an integer number. When the object cannot be subdivided into exact copies of itself we can use the *box-counting dimension*. In this case a set $\mathscr{A}$ is covered by a grid or regular boxes with side $\delta > 0$, all equal to each other, then the number of boxes $N(\delta)$ needed to cover the figure is determined. The *mass-radius fractal dimension* D_m is defined by a power law. In particular this dimension is the measure of the total mass contained in a sphere of radius R whose center is a point of the set, and the mass contained

as a function of the radial size is determined as

$$M(R) = FR^{D_m}, \tag{A.2}$$

where the factor F is a function that may be different for fractals with identical dimension, and the density number of galaxies decreases as $n(R) \approx R^{D_m-d}$ for a set in $\mathbb{R}^d$ (Martinez and Saar, 2010).

A more general geometric estimator is given by the multifractal description (Saslaw, 2000), that provides the most detailed description possible of the fractal properties of a distribution of points. For each center of a point distribution, the number of particles $n_i(r)$ contained within a sphere of radius r measured from the position of the ith particle is given by

$$n_i(r) = \sum_{j=1}^{N} \Theta(r - |\mathbf{x_i} - \mathbf{x_j}|), \tag{A.3}$$

where the sum is over all particles in the sample, and N is the total number of particles. The coordinates of each particle in the three-dimensional space are denoted as $\mathbf{x_j}$, $j \neq i$, and Θ is the Heaviside function. The number of particles $n_i(r)$ around each galaxy taken as the center, with coordinates $\mathbf{x_i}$, is determined by counting the particles around the center that are located within a comoving sphere of radius r (Célérier and Thieberger, 2005), that is, a sphere expanding with the Hubble flow, where the distance between two points remains fixed as the universe expands.

The correlation dimension is defined similarly to the mass-radius fractal dimension (Seshadri, 2005). To characterize the distribution, we must have all the information about the statistical moments in order to define the generalized dimension. The generalized correlation integral $C_q(r)$ is defined as

$$C_q(r) = \frac{1}{NM} \sum_{i=1}^{M} [n_i(r)]^{q-1}, \tag{A.4}$$

where q is called the structure parameter and corresponds to an arbitrary real number, and M is the number of particles used as centers. According to Murante et al. (1997), from the correlation integral it is possible to perform a power series expansion of $\log(r)$ [equation (A.5)] and thus to calculate directly the multifractal dimension D_q. It is sufficient to keep the first two terms on the right side of equation (A.5), which is simplified so that a simple relation between the generalized correlation integral and generalized fractal dimension is obtained as in equation (A.6) (Chacón, 2014):

$$\log[C_q^{1/(q-1)}] = D_q \log(r) + \log(F_q) + \mathcal{O}\left(\frac{1}{\log(r)}\right), \tag{A.5}$$

$$C_q(r)^{1/(q-1)} = F_q r^{D_q}. \tag{A.6}$$

Thus the generalised fractal dimension can be defined in the same way as the mass-radius fractal dimension, such that D_q is given by

$$D_q = \frac{1}{q-1}\frac{d\log C_q(r)}{d\log r}. \tag{A.7}$$

For some values of q such that $q_i \neq q_j$ which satisfy $D_{q_i} = D_{q_j}$, i.e., D_q is independent of q and r, the distribution is called monofractal because its dimension is constant. In addition, if D_q is equal to the Euclidean dimension, the distribution is homogeneous. For $q \geq 1$, D_q explores the scaling behaviour in high-density environments within the distribution, which are associated mainly with clusters and superclusters, whereas for $q < 1$, D_q explores the behaviour in low-density environments, i.e., those associated with *voids* (Sarkar et al., 2009).

Based on this formalism several investigations have reported a value of the homogeneity scale, such as Zheng et al. (1988) for *CfA survey data*, Xia, Deng, and Zou (1992) for the *IRAS survey*, and Seshadri (1999) for *the Campanas redshift survey*. Chacón-Cardona and Casas-Miranda (2012) performed a multifractal analysis of dark matter halos from the *Millennium* simulation (Springel et al., 2005). They found a transition to homogeneity between 100 and 120 Mpc/h in strong agreement with the ΛCDM model. For analysis with the WiggleZ survey, Scrimgeour et al. (2012) report a transition to homogeneity at $r_H = 71 \pm 8\ Mpc/h$ with $z \leq 0.2$; this indicates that the galaxy distribution does not behave as a fractal object. This result is also consistent with Hogg et al. (2005), Yadav et al. (2005) and Sarkar et al. (2009), who report a transition to homogeneity at $\sim 70\ Mpc/h$. Wu, Lahav, and Rees (1999) and Yadav et al. (2005) are in agreement with this value for the homogeneity scale. In all cases the effects of the geometry of the surveys must be taken into account according to (Yadav, Bagla, and Khandai, 2010; Pan and Coles, 2002). In particular, the fractal calculations may be affected by the presence of holes and borders in the catalogues that are inherent to the process of observation using astronomical instruments.

Recently García-Farieta and Casas-Miranda (2018) investigated if the effect of cumulative holes in the masks of BOSS (SDSS-III) can produce variations in the scale of cosmic homogeneity. The results show that observational holes cause a shift in the homogeneity scale r_H, in particular for percentages of holes between $0 - 10\%$ the homogeneity scale is reached at (83 ± 1)Mpc/h with a dimension in the range $2.83^{\pm 0.09} \leq D_q \leq 2.855^{\pm 0.09}$. The correlation dimension D_2 is related to the homogeneity scale r_H and the usual two-point correlation function for a sample displaying cosmic homogeneity (Peebles, 1980; Peebles, 1989; Pan and Coles, 2000). Fig. A.1 shows the spectrum of fractal dimension D_q and its dependency with radial distance for synthetic samples. For $q = 2$ the dimension tends to $D = 3$ as r increases, at scales below 50 Mpc/h the distribution it is highly noisy indicating that it is grouped into small spatial regions. In high-density regions there is a strong tendency to homogeneity because the values of the fractal dimension are very close to the physical space dimension. $D_{q\geq 2}$ increases at large r values to reach homogeneity in agreement

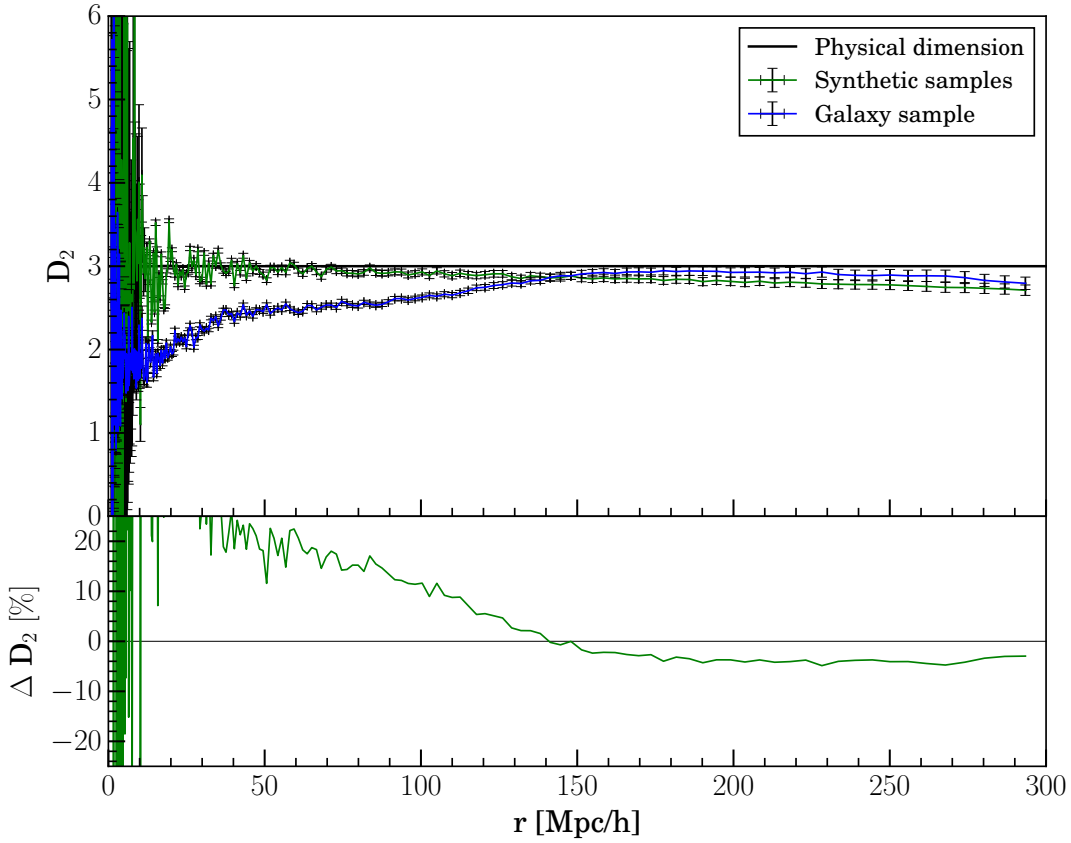

Figure A.1: Upper panel: Multifractal spectrum of $D_2(r)$ (structure parameter $q = 2.0$), as a function of the comoving distance r for all synthetic samples (green line) and for the galaxy sample (blue line). Lower panel: percentage difference in fractal dimension between synthetic and galaxy samples, where $\Delta D_2 = 100(D_{2_{synth}} - D_{2_{gal}})/D_{2_{gal}}$.

with other analysis, this means that on average the space is statistically filled at depths greater than r_H.

APPENDIX B

Correction terms of the TNS model

The correction terms C_A and C_B for the TNS model (Taruya, Nishimichi, and Saito, 2010) are derived from perturbation theory. Following Taruya, Nishimichi, and Saito (2010) and de la Torre and Guzzo (2012), for a biased tracer, these terms can be written as follows

$$C_A(k,\mu,f,b) = \sum_{m,n=1}^{3} b^{3-n} f^n \mu^{2m} P_{Amn}(k) \tag{B.1}$$

$$C_B(k,\mu,f,b) = \sum_{m=1}^{4}\sum_{i=1}^{2} b^{4-a-b}(-f)^{a+b}\mu^{2n} P_{Bnab}(k), \tag{B.2}$$

where f is the growth rate, b the bias of the tracer and

$$\begin{aligned} P_{Amn}(k) = \frac{k^3}{(2\pi)^2}\Bigg[\int_0^\infty dr \int_{-1}^{+1} dx \,(A_{mn}(r,x)P(k) \\ +\widetilde{A}_{mn}(r,x)P(kr)\Big) \times \frac{P\left(k\sqrt{1+r^2-2rx}\right)}{(1+r^2-2rx)^2} \\ +P(k)\int_0^\infty dr a_{mn}(r)P(kr)\Bigg], \end{aligned} \tag{B.3}$$

$$\begin{aligned} P_{Bnab}(k) = \frac{k^3}{(2\pi)^2}\int_0^\infty dr \int_{-1}^{+1} dx B^n_{ab}(r,x) \\ \frac{P_{a2}\left(k\sqrt{1+r^2-2rx}\right)P_{b2}(kr)}{(1+r^2-2rx)^a}, \end{aligned} \tag{B.4}$$

where the non-vanishing functions $A_{mn}(r,x)$, $\widetilde{A}_{mn}(r,x)$, $a_{mn}(r,x)$ and $B_{ab}(r,x)$ have been provided by Taruya, Nishimichi, and Saito (2010), as follows

$$A_{11} = -\frac{r^3}{7}\left\{x + 6x^3 + r^2x(-3 + 10x^2) + r\left(-3 + x^2 - 12x^4\right)\right\},$$

$$A_{12} = \frac{r^4}{14}(x^2 - 1)(-1 + 7rx - 6x^2),$$

$$A_{22} = \frac{r^3}{14}\left\{r^2x(13 - 41x^2) - 4(x + 6x^3) + r\left(5 + 9x^2 + 42x^4\right)\right\},$$

$$A_{23} = A_{12},$$

$$A_{33} = \frac{r^3}{14}(1 - 7rx + 6x^2)\left\{-2x + r(-1 + 3x^2)\right\},$$

for A_{mn},

$$\widetilde{A}_{11} = \frac{1}{7}(x + r - 2rx^2)(3r + 7x - 10rx^2),$$

$$\widetilde{A}_{12} = \frac{r}{14}(x^2 - 1)(3r + 7x - 10rx^2),$$

$$\widetilde{A}_{22} = \frac{1}{14}\left\{28x^2 + rx(25 - 81x^2) + r^2(1 - 27x^2 + 54x^4)\right\},$$

$$\widetilde{A}_{23} = \frac{r}{14}(1 - x^2)(r - 7x + 6rx^2),$$

$$\widetilde{A}_{33} = \frac{1}{14}(r - 7x + 6rx^2)(-2x - r + 3rx^2),$$

for $\widetilde{A}_{mn}$, and

$$a_{11} = -\frac{1}{84r}\left[2r(19 - 24r^2 + 9r^4) - 9(r^2 - 1)^3 \log\left|\frac{r+1}{r-1}\right|\right],$$

$$a_{12} = \frac{1}{112r^3}\left[2r(r^2 + 1)(3 - 14r^2 + 3r^4) - 3(r^2 - 1)^4 \log\left|\frac{r+1}{r-1}\right|\right],$$

$$a_{22} = \frac{1}{336r^3}\left[2r(9 - 185r^2 + 159r^4 - 63r^6) + 9(r^2 - 1)^3(7r^2 + 1) \log\left|\frac{r+1}{r-1}\right|\right],$$

$$a_{23} = a_{12},$$

$$a_{33} = \frac{1}{336r^3}\left[2r(9 - 109r^2 + 63r^4 - 27r^6) + 9(r^2 - 1)^3(3r^2 + 1) \log\left|\frac{r+1}{r-1}\right|\right].$$

for a_{mn}. Whereas the non-vanishing contributions for B^n_{ab} are

$$B^1_{11} = \frac{r^2}{2}(x^2 - 1),$$

$$B_{12}^1 = \frac{3r^2}{8}(x^2-1)^2,$$

$$B_{21}^1 = \frac{3r^4}{8}(x^2-1)^2,$$

$$B_{22}^1 = \frac{5r^4}{16}(x^2-1)^3,$$

$$B_{11}^2 = \frac{r}{2}(r+2x-3rx^2),$$

$$B_{12}^2 = -\frac{3r}{4}(x^2-1)(-r-2x+5rx^2),$$

$$B_{21}^2 = \frac{3r^2}{4}(x^2-1)(-2+r^2+6rx-5r^2x^2),$$

$$B_{22}^2 = -\frac{3r^2}{16}(x^2-1)^2(6-30rx-5r^2+35r^2x^2),$$

$$B_{12}^3 = \frac{r}{8}\left\{4x(3-5x^2)+r(3-30x^2+35x^4)\right\},$$

$$B_{21}^3 = \frac{r}{8}\left[-8x+r\left\{-12+36x^2+12rx(3-5x^2)\right.\right.$$
$$\left.\left.+r^2(3-30x^2+35x^4)\right\}\right],$$

$$B_{22}^3 = \frac{3r}{16}(x^2-1)\left[-8x+r\left\{-12+60x^2\right.\right.$$
$$\left.\left.+20rx(3-7x^2)+5r^2(1-14x^2+21x^4)\right\}\right],$$

$$B_{22}^4 = \frac{r}{16}\left[8x(-3+5x^2)-6r(3-30x^2+35x^4)\right.$$
$$+6r^2x(15-70x^2+63x^4)$$
$$\left.+r^3\left\{5-21x^2(5-15x^2+11x^4)\right\}\right].$$

By using the Kaiser term of the TNS model, i.e. ignoring the damping terms $D(k,\mu,f,\sigma_{12})$, the corresponding multipole moments of the correlation function are then given by (de la Torre and Guzzo, 2012):

$$
\begin{aligned}
\xi_0^s(s) = {} & b^2\xi_{\delta\delta} + bf\frac{2}{3}\xi_{\delta\theta} + f^2\frac{1}{5}\xi_{\theta\theta} \\
& + b^2 f\frac{1}{3}\xi_{A11} + bf^2\frac{1}{3}\xi_{A12} + bf^2\frac{1}{5}\xi_{A22} + f^3\frac{1}{5}\xi_{A23} \\
& + f^3\frac{1}{7}\xi_{A33} + b^2f^2\frac{1}{3}\xi_{B111} - bf^3\frac{1}{3}\left(\xi_{B112} + \xi_{B121}\right) \\
& + f^4\frac{1}{3}\xi_{B122} + b^2f^2\frac{1}{5}\xi_{B211} - bf^3\frac{1}{5}\left(\xi_{B212} + \xi_{B221}\right) \\
& + f^4\frac{1}{5}\xi_{B222} - bf^3\frac{1}{7}\left(\xi_{B312} + \xi_{B321}\right) + f^4\frac{1}{7}\xi_{B322} \\
& + f^4\frac{1}{9}\xi_{B422}, \qquad \text{(B.5)} \\
\xi_2^s(s) = {} & bf\frac{4}{3}\xi^{(2)}_{\delta\theta} + f^2\frac{4}{7}\xi^{(2)}_{\theta\theta} \\
& + b^2 f\frac{2}{3}\xi^{(2)}_{A11} + bf^2\frac{2}{3}\xi^{(2)}_{A12} + bf^2\frac{4}{7}\xi^{(2)}_{A22} + f^3\frac{4}{7}\xi^{(2)}_{A23} \\
& + f^3\frac{10}{21}\xi^{(2)}_{A33} + b^2f^2\frac{2}{3}\xi^{(2)}_{B111} - bf^3\frac{2}{3}\left(\xi^{(2)}_{B112} + \xi^{(2)}_{B121}\right) \\
& + f^4\frac{2}{3}\xi^{(2)}_{B122} + b^2f^2\frac{4}{7}\xi^{(2)}_{B211} - bf^3\frac{4}{7}\left(\xi^{(2)}_{B212} + \xi^{(2)}_{B221}\right) \\
& + f^4\frac{4}{7}\xi^{(2)}_{B222} - bf^3\frac{10}{21}\left(\xi^{(2)}_{B312} + \xi^{(2)}_{B321}\right) + f^4\frac{10}{21}\xi^{(2)}_{B322} \\
& + f^4\frac{40}{99}\xi^{(2)}_{B422}, \qquad \text{(B.6)}
\end{aligned}
$$

where ξ_{Amn} and ξ_{Bnab} are the Fourier conjugate pairs of P_{Amn} and P_{Bnab} in Eqs. (B.3) and (B.4), and $\xi_X^{(l)}$ is the l-th multipole moment of the correlation function associated to P_X as defined in Eq. (3.20). For the order $l = 2$, the latter were already found by Hamilton (1992) and Cole, Fisher, and Weinberg (1994), by using recurrence relations and the integral forms of spherical Bessel functions, so that

$$\xi_X^{(2)}(r) = \xi_X(r) - 3X_2(r) \qquad \text{(B.7)}$$

(B.8)

where,

$$X_n(r) = r^{-(n+1)}\int_0^r \xi_X(r')r'^n dr'. \qquad \text{(B.9)}$$

Bibliography

Abazajian, K. N., J. F. Beacom, and N. F. Bell (July 2002). "Stringent constraints on cosmological neutrino-antineutrino asymmetries from synchronized flavor transformation". In: *Phys. Rev. D* 66.1, 013008, p. 013008. DOI: 10.1103/PhysRevD.66.013008. eprint: astro-ph/0203442.

Abbott, B. P. et al. (Feb. 2016). "Observation of Gravitational Waves from a Binary Black Hole Merger". In: *Phys. Rev. Lett.* 116.6, 061102, p. 061102. DOI: 10.1103/PhysRevLett.116.061102. arXiv: 1602.03837 [gr-qc].

Abbott, T. M. C. et al. (Aug. 2018). "Dark Energy Survey year 1 results: Cosmological constraints from galaxy clustering and weak lensing". In: *Phys. Rev. D* 98 (4), p. 043526. DOI: 10.1103/PhysRevD.98.043526. URL: https://link.aps.org/doi/10.1103/PhysRevD.98.043526.

Abruzzo, Matthew W. and Zoltán Haiman (June 2019). "The impact of photometric redshift errors on lensing statistics in ray-tracing simulations". In: *Mon. Not. R. Astron. Soc.* 486.2, pp. 2730–2753. DOI: 10.1093/mnras/stz1016. arXiv: 1810.12312 [astro-ph.CO].

Acebron, Ana et al. (Sept. 2017). "Hubble Frontier Fields: systematic errors in strong lensing models of galaxy clusters - implications for cosmography". In: *Mon. Not. R. Astron. Soc.* 470.2, pp. 1809–1825. DOI: 10.1093/mnras/stx1330. arXiv: 1704.05380 [astro-ph.CO].

Adler, R. J. (1981). *The Geometry of Random Fields*. Ed. by Robert E. O'Malley. Society for Industrial and Applied Mathematics.

Agarwal, Shankar and Hume A. Feldman (2011). "The effect of massive neutrinos on the matter power spectrum". In: *Monthly Notices of the Royal Astronomical Society* 410.3, pp. 1647–1654. DOI: 10.1111/j.1365-2966.2010.17546.x. eprint: /oup/backfile/content_public/journal/mnras/410/3/10.1111/j.1365-2966.2010.17546.x/2/mnras0410-1647.pdf. URL: http://dx.doi.org/10.1111/j.1365-2966.2010.17546.x.

Akaike, H. (1974). "A New Look at the Statistical Model Identification". In: *IEEE Transactions on Automatic Control* 19, pp. 716–723.

Alam, Shadab et al. (Sept. 2017). "The clustering of galaxies in the completed SDSS-III Baryon Oscillation Spectroscopic Survey: cosmological analysis of the DR12 galaxy sample". In: *Mon. Not. R. Astron. Soc.* 470.3, pp. 2617–2652. DOI: 10.1093/mnras/stx721. arXiv: 1607.03155 [astro-ph.CO]. URL: http://dx.doi.org/10.1093/mnras/stx721.

Albrecht, Andreas et al. (Sept. 2006). "Report of the Dark Energy Task Force". In: *arXiv e-prints*, astro-ph/0609591, astro–ph/0609591. arXiv: astro-ph/0609591 [astro-ph].

Albrecht, Andreas et al. (Jan. 2009). "Findings of the Joint Dark Energy Mission Figure of Merit Science Working Group". In: *arXiv e-prints*, arXiv:0901.0721, arXiv:0901.0721. arXiv: 0901.0721 [astro-ph.IM].

Alimi, Jean-Michel et al. (June 2012). "DEUS Full Observable ΛCDM Universe Simulation: the numerical challenge". In: *arXiv e-prints*, arXiv:1206.2838, arXiv:1206.2838. arXiv: 1206.2838 [astro-ph.CO].

Alpher, R. A., H. Bethe, and G. Gamow (Apr. 1948). "The Origin of Chemical Elements". In: *Phys. Rev.* 73 (7), pp. 803–804. DOI: 10.1103/PhysRev.73.803. URL: https://link.aps.org/doi/10.1103/PhysRev.73.803.

Alsing, Justin, Alan Heavens, and Andrew H. Jaffe (2017). "Cosmological parameters, shear maps and power spectra from CFHTLenS using Bayesian hierarchical inference". In: *Monthly Notices of the Royal Astronomical Society* 466.3, pp. 3272–3292. DOI: 10.1093/mnras/stw3161. eprint: /oup/backfile/content_public/journal/mnras/466/3/10.1093_mnras_stw3161/7/stw3161.pdf. URL: http://dx.doi.org/10.1093/mnras/stw3161.

Amendola, L., C. Quercellini, and E. Giallongo (Feb. 2005). "Constraints on perfect fluid and scalar field dark energy models from future redshift surveys". In: *Mon. Not. R. Astron. Soc.* 357, pp. 429–439. DOI: 10.1111/j.1365-2966.2004.08558.x. eprint: astro-ph/0404599.

Amendola, L. et al. (Apr. 2018). "Cosmology and fundamental physics with the Euclid satellite". In: *Living Reviews in Relativity* 21, 2, p. 2. DOI: 10.1007/s41114-017-0010-3. arXiv: 1606.00180.

Amendola, Luca (Aug. 2000). "Coupled quintessence". In: *Phys. Rev. D* 62.4, 043511, p. 043511. DOI: 10.1103/PhysRevD.62.043511. arXiv: astro-ph/9908023 [astro-ph].

Amendola, Luca et al. (Sept. 2013). "Cosmology and fundamental physics with the Euclid satellite". In: *Living Reviews in Relativity* 16.1, 6, p. 6. DOI: 10.12942/lrr-2013-6. arXiv: 1206.1225 [astro-ph.CO].

Anderson, D and K Burnham (2004). "Model selection and multi-model inference". In: *Second. NY: Springer-Verlag* 63.

Anderson, L. et al. (June 2014). "The clustering of galaxies in the SDSS-III Baryon Oscillation Spectroscopic Survey: baryon acoustic oscillations in the Data Releases 10 and 11 Galaxy samples". In: *Mon. Not. R. Astron. Soc.* 441, pp. 24–62. DOI: 10.1093/mnras/stu523. arXiv: 1312.4877.

Andrae, Rene, Tim Schulze-Hartung, and Peter Melchior (Dec. 2010). "Dos and don'ts of reduced chi-squared". In: *arXiv e-prints*, arXiv:1012.3754, arXiv:1012.3754. arXiv: 1012.3754 [astro-ph.IM].

Armendariz-Picon, C., V. Mukhanov, and Paul J. Steinhardt (Nov. 2000). "Dynamical Solution to the Problem of a Small Cosmological Constant and Late-Time Cosmic Acceleration". In: *Phys. Rev. Lett.* 85.21, pp. 4438–4441. DOI: 10.1103/PhysRevLett.85.4438. arXiv: astro-ph/0004134 [astro-ph].

Armendariz-Picon, Christian, V Mukhanov, and Paul J Steinhardt (May 2001). "Essentials of k-essence". In: *Physical Review D* 63.10, 103510, p. 103510. DOI: 10.1103/PhysRevD.63.103510. arXiv: astro-ph/0006373 [astro-ph].

Arnouts, S. et al. (1999). "Measuring and modelling the redshift evolution of clustering: the Hubble Deep Field North". In: *Monthly Notices of the*

Royal Astronomical Society 310.2, pp. 540–556. DOI: 10.1046/j.1365-8711.1999.02978.x. eprint: /oup/backfile/content_public/journal/mnras/310/2/10.1046/j.1365-8711.1999.02978.x/2/310-2-540.pdf. URL: http://dx.doi.org/10.1046/j.1365-8711.1999.02978.x.

Baldi, Marco et al. (2014). "Cosmic degeneracies - I. Joint N-body simulations of modified gravity and massive neutrinos". In: *Monthly Notices of the Royal Astronomical Society* 440.1, pp. 75–88. DOI: 10.1093/mnras/stu259. eprint: /oup/backfile/content_public/journal/mnras/440/1/10.1093_mnras_stu259/2/stu259.pdf. URL: http://dx.doi.org/10.1093/mnras/stu259.

Barrow, J. D., S. P. Bhavsar, and D. H. Sonoda (Sept. 1984). "A bootstrap resampling analysis of galaxy clustering". In: *Mon. Not. R. Astron. Soc.* 210, 19P–23P. DOI: 10.1093/mnras/210.1.19P.

Barrow, John D., Rachel Bean, and João Magueijo (Aug. 2000). "Can the Universe escape eternal acceleration?" In: *Mon. Not. R. Astron. Soc.* 316.3, pp. L41–L44. DOI: 10.1046/j.1365-8711.2000.03778.x. arXiv: astro-ph/0004321 [astro-ph].

Bartolo, N. et al. (Nov. 2004). "Non-Gaussianity from inflation: theory and observations". In: *Phys. Rept.* 402.3-4, pp. 103–266. DOI: 10.1016/j.physrep.2004.08.022. arXiv: astro-ph/0406398 [astro-ph].

Baryshev, Yurij V et al. (1998). "On the fractal structure of galaxy distribution and its implications for cosmology". In: *Fractals* 6.03, pp. 231–243.

Bassett, Bruce and Renée Hlozek (2010). "Baryon acoustic oscillations". In: *Dark Energy: Observational and Theoretical Approaches, Edited by Pilar Ruiz-Lapuente. Published: Cambridge, UK ; New York by Cambridge University Press, 2010. ISBN 9780521518888 (hardback), p.246.* Ed. by Pilar Ruiz-Lapuente. Cambridge University Press. Chap. 9, p. 246.

Battye, Richard A. and Adam Moss (Feb. 2014). "Evidence for Massive Neutrinos from Cosmic Microwave Background and Lensing Observations". In: *Phys. Rev. Lett.* 112 (5), p. 051303. DOI: 10.1103/PhysRevLett.112.051303. URL: https://link.aps.org/doi/10.1103/PhysRevLett.112.051303.

Bel, J. et al. (Mar. 2014). "The VIMOS Public Extragalactic Redshift Survey (VIPERS). Ω_0 from the galaxy clustering ratio measured at z ~1". In: *Astron. Astrophys.* 563, A37, A37. DOI: 10.1051/0004-6361/201321942. arXiv: 1310.3380 [astro-ph.CO].

Bel, J. et al. (Feb. 2019). "Accurate fitting functions for peculiar velocity spectra in standard and massive-neutrino cosmologies". In: *Astron. Astrophys.* 622, A109, A109. DOI: 10.1051/0004-6361/201834513. arXiv: 1809.09338 [astro-ph.CO].

Bellomo, Nicola et al. (2017). "Hiding neutrino mass in modified gravity cosmologies". In: *Journal of Cosmology and Astroparticle Physics* 2017.02, p. 043. URL: http://stacks.iop.org/1475-7516/2017/i=02/a=043.

Bennett, C. L. et al. (Oct. 2013). "Nine-year Wilkinson Microwave Anisotropy Probe (WMAP) Observations: Final Maps and Results". In: *Astrophys. J. Suppl.* 208.2, 20, p. 20. DOI: 10.1088/0067-0049/208/2/20. arXiv: 1212.5225 [astro-ph.CO].

Bernal, José Luis and John A. Peacock (July 2018). "Conservative cosmology: combining data with allowance for unknown systematics". In: *Journal of Cosmology and Astro-Particle Physics* 2018.7, 002, p. 002. DOI: 10.1088/1475-7516/2018/07/002. arXiv: 1803.04470 [astro-ph.CO].

Bernal, José Luis, Licia Verde, and Adam G. Riess (2016). "The trouble with H 0". In: *Journal of Cosmology and Astroparticle Physics* 2016.10, p. 019. URL: http://stacks.iop.org/1475-7516/2016/i=10/a=019.

Bernardeau, F. et al. (2002). "Large-scale structure of the Universe and cosmological perturbation theory". In: *Physics Reports* 367.1, pp. 1 –248. ISSN: 0370-1573. DOI: https://doi.org/10.1016/S0370-1573(02)00135-7. URL: http://www.sciencedirect.com/science/article/pii/S0370157302001357.

Bernardeau, Francis and Patrick Valageas (Oct. 2008). "Propagators in Lagrangian space". In: *Phys. Rev. D* 78.8, 083503, p. 083503. DOI: 10.1103/PhysRevD.78.083503. arXiv: 0805.0805 [astro-ph].

Beutler, F. et al. (July 2012). "The 6dF Galaxy Survey: z$\sim$ 0 measurements of the growth rate and σ_8". In: *Mon. Not. R. Astron. Soc.* 423.4, pp. 3430–3444. DOI: 10.1111/j.1365-2966.2012.21136.x. arXiv: 1204.4725 [astro-ph.CO].

Beutler, Florian et al. (Oct. 2011). "The 6dF Galaxy Survey: baryon acoustic oscillations and the local Hubble constant". In: *Mon. Not. R. Astron. Soc.* 416.4, pp. 3017–3032. DOI: 10.1111/j.1365-2966.2011.19250.x. arXiv: 1106.3366 [astro-ph.CO].

Beutler, Florian et al. (Sept. 2014). "The clustering of galaxies in the SDSS-III Baryon Oscillation Spectroscopic Survey: testing gravity with redshift space distortions using the power spectrum multipoles". In: *Mon. Not. R. Astron. Soc.* 443.2, pp. 1065–1089. DOI: 10.1093/mnras/stu1051. arXiv: 1312.4611 [astro-ph.CO]. URL: http://dx.doi.org/10.1093/mnras/stu1051.

Bianchi, D. et al. (Dec. 2012). "Statistical and systematic errors in redshift-space distortion measurements from large surveys". In: *Monthly Notices of the Royal Astronomical Society* 427.3, pp. 2420–2436. ISSN: 0035-8711. DOI: 10.1111/j.1365-2966.2012.22110.x. eprint: http://oup.prod.sis.lan/mnras/article-pdf/427/3/2420/3855345/427-3-2420.pdf. URL: https://doi.org/10.1111/j.1365-2966.2012.22110.x.

Blake, C. et al. (Sept. 2012). "The WiggleZ Dark Energy Survey: joint measurements of the expansion and growth history at $z < 1$". In: *Mon. Not. R. Astron. Soc.* 425, pp. 405–414. DOI: 10.1111/j.1365-2966.2012.21473.x. arXiv: 1204.3674.

Blake, C. et al. (Dec. 2013a). "Galaxy And Mass Assembly (GAMA): improved cosmic growth measurements using multiple tracers of large-scale structure". In: *Mon. Not. R. Astron. Soc.* 436, pp. 3089–3105. DOI: 10.1093/mnras/stt1791. arXiv: 1309.5556 [astro-ph.CO].

Blake, Chris and Karl Glazebrook (2003). "Probing Dark Energy Using Baryonic Oscillations in the Galaxy Power Spectrum as a Cosmological Ruler". In: *The Astrophysical Journal* 594.2, p. 665. URL: http://stacks.iop.org/0004-637X/594/i=2/a=665.

Blake, Chris et al. (2011). "The WiggleZ Dark Energy Survey: mapping the distance–redshift relation with baryon acoustic oscillations". In: *Monthly*

Notices of the Royal Astronomical Society 418.3, pp. 1707–1724. DOI: 10.1111/j.1365-2966.2011.19592.x. eprint: /oup/backfile/content_public/journal/mnras/418/3/10.1111_j.1365-2966.2011.19592.x/1/mnras0418-1707.pdf. URL: http://dx.doi.org/10.1111/j.1365-2966.2011.19592.x.

Blake, Chris et al. (Aug. 2011). "The WiggleZ Dark Energy Survey: testing the cosmological model with baryon acoustic oscillations at z= 0.6". In: *Mon. Not. R. Astron. Soc.* 415.3, pp. 2892–2909. DOI: 10.1111/j.1365-2966.2011.19077.x. arXiv: 1105.2862 [astro-ph.CO].

Blake, Chris et al. (Dec. 2013b). "Galaxy And Mass Assembly (GAMA): improved cosmic growth measurements using multiple tracers of large-scale structure". In: *Mon. Not. R. Astron. Soc.* 436.4, pp. 3089–3105. DOI: 10.1093/mnras/stt1791. arXiv: 1309.5556 [astro-ph.CO].

Boisseau, B. et al. (Sept. 2000). "Reconstruction of a Scalar-Tensor Theory of Gravity in an Accelerating Universe". In: *Phys. Rev. Lett.* 85.11, pp. 2236–2239. DOI: 10.1103/PhysRevLett.85.2236. arXiv: gr-qc/0001066 [gr-qc].

Bolotin, Y. L., D. A. Erokhin, and O. A. Lemets (Sept. 2012). "Expanding Universe: slowdown or speedup?" In: *Physics Uspekhi* 55.27, A02. DOI: 10.3367/UFNe.0182.201209c.0941. arXiv: 1108.0203 [astro-ph.CO].

Bond, J. R., G. Efstathiou, and M. Tegmark (Nov. 1997). "Forecasting cosmic parameter errors from microwave background anisotropy experiments". In: *Mon. Not. R. Astron. Soc.* 291, pp. L33–L41. DOI: 10.1093/mnras/291.1.L33. eprint: astro-ph/9702100.

Bondi, H. (Feb. 1948). "Review of Cosmology". In: *Monthly Notices of the Royal Astronomical Society* 108.1, pp. 104–120. ISSN: 0035-8711. DOI: 10.1093/mnras/108.1.104. eprint: http://oup.prod.sis.lan/mnras/article-pdf/108/1/104/8077153/mnras108-0104.pdf. URL: https://doi.org/10.1093/mnras/108.1.104.

Bonilla, Alexander and Jairo Castillo (Jan. 2018). "Constraints on Dark Energy Models from Galaxy Clusters and Gravitational Lensing Data". In: *Universe* 4.1, p. 21. DOI: 10.3390/universe4010021. arXiv: 1711.09291 [astro-ph.CO].

Bonilla, Alexander and Jorge Enrique García-Farieta (2019). "Exploring the dark universe: Constraints on dynamical dark energy models from CMB, BAO and growth rate measurements". In: *International Journal of Modern Physics D* 28.09, p. 1950118. DOI: 10.1142/S0218271819501189.

Bonvin, Camille et al. (Feb. 2018). "Redshift-space distortions from vector perturbations". In: *J. Cosm. Astro-Particle Phys.* 2018.2, 028, p. 028. DOI: 10.1088/1475-7516/2018/02/028. arXiv: 1712.00052 [astro-ph.CO].

Brandbyge, Jacob and Steen Hannestad (2009). "Grid based linear neutrino perturbations in cosmological N -body simulations". In: *Journal of Cosmology and Astroparticle Physics* 2009.05, p. 002. URL: http://stacks.iop.org/1475-7516/2009/i=05/a=002.

— (2010). "Resolving cosmic neutrino structure: a hybrid neutrino N -body scheme". In: *Journal of Cosmology and Astroparticle Physics* 2010.01, p. 021. URL: http://stacks.iop.org/1475-7516/2010/i=01/a=021.

Brandbyge, Jacob et al. (2008). "The effect of thermal neutrino motion on the non-linear cosmological matter power spectrum". In: *Journal of Cosmology and Astroparticle Physics* 2008.08, p. 020. URL: http://stacks.iop.org/1475-7516/2008/i=08/a=020.

Brandbyge, Jacob et al. (2010). "Neutrinos in non-linear structure formation - the effect on halo properties". In: *Journal of Cosmology and Astroparticle Physics* 2010.09, p. 014. URL: http://stacks.iop.org/1475-7516/2010/i=09/a=014.

Cabré, Anna and Enrique Gaztañaga (Mar. 2009). "Clustering of luminous red galaxies - I. Large-scale redshift-space distortions". In: *Mon. Not. R. Astron. Soc.* 393.4, pp. 1183–1208. DOI: 10.1111/j.1365-2966.2008.14281.x. arXiv: 0807.2460 [astro-ph].

Cai, Rong-Gen and Anzhong Wang (Mar. 2005). "Cosmology with interaction between phantom dark energy and dark matter and the coincidence problem". In: *J. Cosm. Astro-Particle Phys.* 2005.3, 002, p. 002. DOI: 10.1088/1475-7516/2005/03/002. arXiv: hep-th/0411025 [hep-th].

Cai, Yan-Chuan et al. (Nov. 2016). "Redshift-space distortions around voids". In: *Mon. Not. R. Astron. Soc.* 462.3, pp. 2465–2477. DOI: 10.1093/mnras/stw1809. arXiv: 1603.05184 [astro-ph.CO].

Caldera-Cabral, Gabriela, Roy Maartens, and L. Arturo Ureña-López (Mar. 2009). "Dynamics of interacting dark energy". In: *Phys. Rev. D* 79.6, 063518, p. 063518. DOI: 10.1103/PhysRevD.79.063518. arXiv: 0812.1827 [gr-qc].

Caldwell, R. R., Rahul Dave, and Paul J. Steinhardt (Feb. 1998). "Cosmological Imprint of an Energy Component with General Equation of State". In: *Phys. Rev. Lett.* 80.8, pp. 1582–1585. DOI: 10.1103/PhysRevLett.80.1582. arXiv: astro-ph/9708069 [astro-ph].

Caldwell, Robert R (Oct. 2002). "A phantom menace? Cosmological consequences of a dark energy component with super-negative equation of state". In: *Physics Letters B* 545.1, pp. 23–29. DOI: 10.1016/S0370-2693(02)02589-3. arXiv: astro-ph/9908168 [astro-ph].

Campbell, Lachlan A. et al. (Sept. 2014). "The 6dF Galaxy Survey: Fundamental Plane data". In: *Mon. Not. R. Astron. Soc.* 443.2, pp. 1231–1251. DOI: 10.1093/mnras/stu1198. arXiv: 1406.4867 [astro-ph.GA].

Cárdenas, Víctor H., Carla Bernal, and Alexand er Bonilla (Aug. 2013). "Cosmic slowing down of acceleration using f_{gas}". In: *Mon. Not. R. Astron. Soc.* 433.4, pp. 3534–3538. DOI: 10.1093/mnras/stt983. arXiv: 1306.0779 [astro-ph.CO].

Cardone, Vincenzo F. et al. (Mar. 2014). "The power spectrum of systematics in cosmic shear tomography and the bias on cosmological parameters". In: *Mon. Not. R. Astron. Soc.* 439.1, pp. 202–220. DOI: 10.1093/mnras/stt2357. arXiv: 1307.4857 [astro-ph.CO].

Carmeli, M. and T. Kuzmenko (Oct. 2001). "Value of the cosmological constant: Theory versus experiment". In: *20th Texas Symposium on relativistic astrophysics*. Ed. by J. C. Wheeler and H. Martel. Vol. 586. American Institute of Physics Conference Series, pp. 316–318. DOI: 10.1063/1.1419571. eprint: astro-ph/0102033.

Castorina, Emanuele et al. (2014). "Cosmology with massive neutrinos II: on the universality of the halo mass function and bias". In: *Journal of Cosmology and Astroparticle Physics* 2014.02, p. 049. URL: http://stacks.iop.org/1475-7516/2014/i=02/a=049.

Castorina, Emanuele et al. (2015). "DEMNUni: the clustering of large-scale structures in the presence of massive neutrinos". In: *Journal of Cosmology and Astroparticle Physics* 2015.07, p. 043. URL: http://stacks.iop.org/1475-7516/2015/i=07/a=043.

Célérier, M. N. and R. Thieberger (Sept. 2005). "Fractal Dimensions of the Galaxy Distribution Varying by Steps?" In: *22nd Texas Symposium on Relativistic Astrophysics*. Ed. by P. Chen et al., pp. 364–367. eprint: astro-ph/0504442.

Chacón, César Alexander (2014). "Study of the fractal structure of the Large-scale matter distribution in the Universe". PhD thesis. Universidad Nacional de Colombia - Sede Bogotá, Departamento de Física, Colombia.

Chacón-Cardona, César A and Rigoberto A Casas-Miranda (2012). "Millennium Simulation Dark Matter Haloes: Multi-fractal and Lacunarity Analysis with Homogeneity Transition". In: *arXiv preprint arXiv:1209.2637*.

Chen, Lu, Qing-Guo Huang, and Ke Wang (Feb. 2019). "Distance priors from Planck final release". In: *J. Cosm. Astro-Particle Phys.* 2019.2, 028, p. 028. DOI: 10.1088/1475-7516/2019/02/028. arXiv: 1808.05724 [astro-ph.CO].

Chevallier, Michel and David Polarski (Jan. 2001). "Accelerating universes with scaling dark matter". In: *International Journal of Modern Physics D* 10.02, pp. 213–223. DOI: 10.1142/S0218271801000822. arXiv: gr-qc/0009008 [gr-qc].

Chiang, Chi-Ting, Marilena LoVerde, and Francisco Villaescusa-Navarro (Nov. 2018). "First detection of scale-dependent linear halo bias in N-body simulations with massive neutrinos". In: *arXiv e-prints*, arXiv:1811.12412, arXiv:1811.12412. arXiv: 1811.12412 [astro-ph.CO].

Chiba, Takeshi, Takahiro Okabe, and Masahide Yamaguchi (July 2000). "Kinetically driven quintessence". In: *Physical Review D* 62.2, 023511, p. 023511. DOI: 10.1103/PhysRevD.62.023511. arXiv: astro-ph/9912463 [astro-ph].

Cleveland, B. T. et al. (Mar. 1998). "Measurement of the Solar Electron Neutrino Flux with the Homestake Chlorine Detector". In: *Astrophys. J.* 496, pp. 505–526. DOI: 10.1086/305343.

Clowes, Roger G et al. (2013). "A structure in the early Universe at z∼1.3 that exceeds the homogeneity scale of the RW concordance cosmology". In: *Monthly Notices of the Royal Astronomical Society* 429.4, pp. 2910–2916.

Cognola, G. et al. (Feb. 2009). "Initial and final de Sitter universes from modified f(R) gravity". In: *Phys. Rev. D* 79.4, 044001, p. 044001. DOI: 10.1103/PhysRevD.79.044001. arXiv: 0810.4989 [gr-qc].

Cohen, Andrew G., David B. Kaplan, and Ann E. Nelson (June 1999). "Effective Field Theory, Black Holes, and the Cosmological Constant". In: *Phys. Rev. Lett.* 82.25, pp. 4971–4974. DOI: 10.1103/PhysRevLett.82.4971. arXiv: hep-th/9803132 [hep-th].

Coil, A. L. (2013). "The Large-Scale Structure of the Universe". In: *Planets, Stars and Stellar Systems. Volume 6: Extragalactic Astronomy and Cosmology.*

Ed. by T. D. Oswalt and W. C. Keel. Springer, Dordrecht. Chap. 8, p. 387. DOI: 10.1007/978-94-007-5609-0_8.

Coil, Alison L (2013). "The Large-Scale Structure of the Universe". In: *Planets, Stars and Stellar Systems*. Springer, pp. 387–421.

Coil, Alison L. (2013). "The Large-Scale Structure of the Universe". In: *Planets, Stars and Stellar Systems Vol. 6, by Oswalt, Terry D.; Keel, William C., ISBN 978-94-007-5608-3. Springer Science+Business Media Dordrecht, 2013, p. 387*. Ed. by Terry D. Oswalt and William C. Keel. Vol. 6. Springer, Dordrecht. Chap. 8, p. 387. DOI: 10.1007/978-94-007-5609-0_8.

Cole, S., K. B. Fisher, and D. H. Weinberg (July 1995). "Constraints on Omega from the IRAS redshift surveys". In: *Mon. Not. R. Astron. Soc.* 275, pp. 515–526. DOI: 10.1093/mnras/275.2.515. eprint: astro-ph/9412062.

Cole, S. et al. (Sept. 2005). "The 2dF Galaxy Redshift Survey: power-spectrum analysis of the final data set and cosmological implications". In: *Mon. Not. R. Astron. Soc.* 362, pp. 505–534. DOI: 10.1111/j.1365-2966.2005.09318.x. eprint: astro-ph/0501174.

Cole, Shaun, Karl B. Fisher, and David H. Weinberg (1994). "Fourier analysis of redshift-space distortions and the determination of Ω". In: *Monthly Notices of the Royal Astronomical Society* 267.3, pp. 785–799. DOI: 10.1093/mnras/267.3.785. eprint: /oup/backfile/content_public/journal/mnras/267/3/10.1093/mnras/267.3.785/2/mnras267-0785.pdf. URL: http://dx.doi.org/10.1093/mnras/267.3.785.

Cole, Shaun et al. (2005). "The 2dF Galaxy Redshift Survey: power-spectrum analysis of the final data set and cosmological implications". In: *Monthly Notices of the Royal Astronomical Society* 362.2, pp. 505–534.

Collett, Thomas E. et al. (2018). "A precise extragalactic test of General Relativity". In: *Science* 360.6395, pp. 1342–1346. ISSN: 0036-8075. DOI: 10.1126/science.aao2469. eprint: http://science.sciencemag.org/content/360/6395/1342.full.pdf. URL: http://science.sciencemag.org/content/360/6395/1342.

Cooke, Ryan J. et al. (Jan. 2014). "Precision Measures of the Primordial Abundance of Deuterium". In: *Astrophys. J.* 781.1, 31, p. 31. DOI: 10.1088/0004-637X/781/1/31. arXiv: 1308.3240 [astro-ph.CO].

Copeland, Edmund J., M. Sami, and Shinji Tsujikawa (Jan. 2006). "Dynamics of Dark Energy". In: *International Journal of Modern Physics D* 15.11, pp. 1753–1935. DOI: 10.1142/S021827180600942X. arXiv: hep-th/0603057 [hep-th].

Copi, Craig J., David N. Schramm, and Michael S. Turner (Jan. 1995). "Big-Bang Nucleosynthesis and the Baryon Density of the Universe". In: *Science* 267.5195, pp. 192–199. DOI: 10.1126/science.7809624. arXiv: astro-ph/9407006 [astro-ph].

Corless, Virginia L. and Lindsay J. King (June 2009). "Cosmology with the cluster mass function: mass estimators and shape systematics in large weak lensing surveys". In: *Mon. Not. R. Astron. Soc.* 396.1, pp. 315–324. DOI: 10.1111/j.1365-2966.2009.14542.x. arXiv: 0901.3434 [astro-ph.CO].

Costa, André A. et al. (Jan. 2017). "Constraints on interacting dark energy models from Planck 2015 and redshift-space distortion data". In: *J. Cosm.*

Astro-Particle Phys. 2017.1, 028, p. 028. DOI: 10.1088/1475-7516/2017/01/028. arXiv: 1605.04138 [astro-ph.CO].

Costanzi, Matteo et al. (Dec. 2013). "Cosmology with massive neutrinos III: the halo mass function and an application to galaxy clusters". In: *J. Cosm. Astro-Particle Phys.* 2013.12, 012, p. 012. DOI: 10.1088/1475-7516/2013/12/012. arXiv: 1311.1514 [astro-ph.CO].

Costanzi, Matteo et al. (2014). "Neutrino constraints: what large-scale structure and CMB data are telling us?" In: *Journal of Cosmology and Astroparticle Physics* 2014.10, p. 081. URL: http://stacks.iop.org/1475-7516/2014/i=10/a=081.

Cowan C. L., Jr. et al. (July 1956). "Detection of the Free Neutrino: A Confirmation". In: *Science* 124.3212, pp. 103–104. DOI: 10.1126/science.124.3212.103.

Crocce, Martín and Román Scoccimarro (Mar. 2006a). "Memory of initial conditions in gravitational clustering". In: *Phys. Rev. D* 73.6, 063520, p. 063520. DOI: 10.1103/PhysRevD.73.063520. arXiv: astro-ph/0509419 [astro-ph].

— (Mar. 2006b). "Renormalized cosmological perturbation theory". In: *Phys. Rev. D* 73.6, 063519, p. 063519. DOI: 10.1103/PhysRevD.73.063519. arXiv: astro-ph/0509418 [astro-ph].

Crocce, Martín., Román. Scoccimarro, and Francis Bernardeau (Dec. 2012). "MPTBREEZE: a fast renormalized perturbative scheme". In: *Mon. Not. R. Astron. Soc.* 427.3, pp. 2537–2551. DOI: 10.1111/j.1365-2966.2012.22127.x. arXiv: 1207.1465 [astro-ph.CO].

Cuesta, Antonio J., Viviana Niro, and Licia Verde (2016). "Neutrino mass limits: Robust information from the power spectrum of galaxy surveys". In: *Physics of the Dark Universe* 13, pp. 77 –86. ISSN: 2212-6864. DOI: https://doi.org/10.1016/j.dark.2016.04.005. URL: http://www.sciencedirect.com/science/article/pii/S2212686416300267.

da Ângela, J., P. J. Outram, and T. Shanks (Aug. 2005). "Constraining β(z) and $\Omega^0{}_m$ from redshift-space distortions in z$\backsim$3 galaxy surveys". In: *Mon. Not. R. Astron. Soc.* 361.3, pp. 879–886. DOI: 10.1111/j.1365-2966.2005.09212.x. arXiv: astro-ph/0505469 [astro-ph].

Dalal, Neal et al. (Oct. 2001). "Testing the Cosmic Coincidence Problem and the Nature of Dark Energy". In: *Phys. Rev. Lett.* 87.14, 141302, p. 141302. DOI: 10.1103/PhysRevLett.87.141302. arXiv: astro-ph/0105317 [astro-ph].

Davis, M. and P. J. E. Peebles (Apr. 1983). "A survey of galaxy redshifts. V - The two-point position and velocity correlations". In: *Astrophys. J.* 267, pp. 465–482. DOI: 10.1086/160884.

Davis, M. et al. (May 1985). "The evolution of large-scale structure in a universe dominated by cold dark matter". In: *Astrophys. J.* 292, pp. 371–394. DOI: 10.1086/163168.

Davis, Marc et al. (1982). "A survey of galaxy redshifts. II-The large scale space distribution". In: *The Astrophysical Journal* 253, pp. 423–445.

Davis, MPPJE and PJE Peebles (1983). "A survey of galaxy redshifts. V-The two-point position and velocity correlations". In: *The Astrophysical Journal* 267, pp. 465–482.

De Felice, Antonio and Shinji Tsujikawa (June 2010). "f(R) Theories". In: *Living Reviews in Relativity* 13.1, 3, p. 3. DOI: 10.12942/lrr-2010-3. arXiv: 1002.4928 [gr-qc].

de la Torre, S. and L. Guzzo (Nov. 2012). "Modelling non-linear redshift-space distortions in the galaxy clustering pattern: systematic errors on the growth rate parameter". In: *Mon. Not. R. Astron. Soc.* 427.1, pp. 327–342. DOI: 10.1111/j.1365-2966.2012.21824.x. arXiv: 1202.5559 [astro-ph.CO].

de la Torre, S. et al. (Sept. 2013). "The VIMOS Public Extragalactic Redshift Survey (VIPERS) . Galaxy clustering and redshift-space distortions at z $\sim$ 0.8 in the first data release". In: *Astron. Astrophys.* 557, A54, A54. DOI: 10.1051/0004-6361/201321463. arXiv: 1303.2622 [astro-ph.CO].

Delubac, Timothée et al. (2015). "Baryon Acoustic Oscillations in the Lyα forest of BOSS DR11 quasars". In: *Astronomy & Astrophysics* 574, A59.

DES Collaboration et al. (Aug. 2017). "Dark Energy Survey Year 1 Results: Cosmological Constraints from Galaxy Clustering and Weak Lensing". In: *ArXiv e-prints: 1708.01530*. arXiv: 1708.01530.

Desjacques, Vincent, Donghui Jeong, and Fabian Schmidt (Feb. 2018). "Large-scale galaxy bias". In: *Phys. Rept.* 733, pp. 1–193. DOI: 10.1016/j.physrep.2017.12.002. arXiv: 1611.09787 [astro-ph.CO].

Despali, G. et al. (Mar. 2016). "The universality of the virial halo mass function and models for non-universality of other halo definitions". In: *Mon. Not. R. Astron. Soc.* 456, pp. 2486–2504. DOI: 10.1093/mnras/stv2842. arXiv: 1507.05627.

Di Valentino, E. et al. (Apr. 2018). "Exploring cosmic origins with CORE: Cosmological parameters". In: *Journal of Cosmology and Astro-Particle Physics* 2018.4, 017, p. 017. DOI: 10.1088/1475-7516/2018/04/017. arXiv: 1612.00021 [astro-ph.CO].

Dicke, R. H. et al. (July 1965). "Cosmic Black-Body Radiation." In: *Astrophys. J.* 142, pp. 414–419. DOI: 10.1086/148306.

Dimopoulos, Savas et al. (Mar. 2007). "Testing General Relativity with Atom Interferometry". In: *Phys. Rev. Lett.* 98.11, 111102, p. 111102. DOI: 10.1103/PhysRevLett.98.111102. arXiv: gr-qc/0610047 [gr-qc].

Dodelson, Scott (2003). *Modern Cosmology*. Academic Press.

Dolag, K. et al. (Feb. 2008). "Simulation Techniques for Cosmological Simulations". In: *Space Science Reviews* 134.1, pp. 229–268. ISSN: 1572-9672. DOI: 10.1007/s11214-008-9316-5. URL: https://doi.org/10.1007/s11214-008-9316-5.

Dolgov, A. D. et al. (June 2002). "Cosmological bounds on neutrino degeneracy improved by flavor oscillations". In: *Nuclear Physics B* 632, pp. 363–382. DOI: 10.1016/S0550-3213(02)00274-2. eprint: hep-ph/0201287.

Doran, Michael and Georg Robbers (June 2006). "Early dark energy cosmologies". In: *J. Cosm. Astro-Particle Phys.* 2006.6, 026, p. 026. DOI: 10.1088/1475-7516/2006/06/026. arXiv: astro-ph/0601544 [astro-ph].

Duffy, Alan R (2014). "Probing the nature of dark energy through galaxy redshift surveys with radio telescopes". In: *Annalen der Physik* 526.7-8, pp. 283–293.

Dvali, G., G. Gabadadze, and M. Porrati (July 2000). "4D gravity on a brane in 5D Minkowski space". In: *Physics Letters B* 485.1-3, pp. 208–214. DOI: 10.1016/S0370-2693(00)00669-9. arXiv: hep-th/0005016 [hep-th].

Efron, B. (Jan. 1979). "Bootstrap Methods: Another Look at the Jackknife". In: *Ann. Statist.* 7.1, pp. 1–26. DOI: 10.1214/aos/1176344552. URL: https://doi.org/10.1214/aos/1176344552.

Einstein, Albert (1917). "Cosmological Considerations in the General Theory of Relativity". In: *Sitzungsber. Preuss. Akad. Wiss. Berlin (Math. Phys.)* 1917, pp. 142–152.

Eisenstein, D. J. and W. Hu (Mar. 1998). "Baryonic Features in the Matter Transfer Function". In: *Astrophys. J.* 496, pp. 605–614. DOI: 10.1086/305424. eprint: astro-ph/9709112.

Eisenstein, Daniel J. et al. (Nov. 2005). "Detection of the Baryon Acoustic Peak in the Large-Scale Correlation Function of SDSS Luminous Red Galaxies". In: *Astrophys. J.* 633.2, pp. 560–574. DOI: 10.1086/466512. arXiv: astro-ph/0501171 [astro-ph].

Eke, Vincent R et al. (2004). "Galaxy groups in the 2dFGRS: the group-finding algorithm and the 2PIGG catalogue". In: *Monthly Notices of the Royal Astronomical Society* 348.3, pp. 866–878.

Enqvist, Kari et al. (2015). "Decaying dark matter and the tension in σ_8". In: *Journal of Cosmology and Astroparticle Physics* 2015.09, p. 067. URL: http://stacks.iop.org/1475-7516/2015/i=09/a=067.

Falconer, Kenneth (2004). *Fractal geometry: mathematical foundations and applications*. John Wiley & Sons.

Fisher, Karl B. and Adi Nusser (1996). "The non-linear redshift-space power spectrum: Ω from redshift surveys". In: *Monthly Notices of the Royal Astronomical Society* 279.1, pp. L1–L5. DOI: 10.1093/mnras/279.1.L1. eprint: /oup/backfile/content_public/journal/mnras/279/1/10.1093/mnras/279.1.l1/2/279-1-l1.pdf. URL: http://dx.doi.org/10.1093/mnras/279.1.L1.

Font-Ribera, Andreu et al. (May 2014). "Quasar-Lyman α forest cross-correlation from BOSS DR11: Baryon Acoustic Oscillations". In: *J. Cosm. Astro-Particle Phys.* 2014.5, 027, p. 027. DOI: 10.1088/1475-7516/2014/05/027. arXiv: 1311.1767 [astro-ph.CO].

Friedmann, A. (1922). "Über die Krümmung des Raumes". In: *Zeitschrift fur Physik* 10, pp. 377–386. DOI: 10.1007/BF01332580.

Frieman, J. A., M. S. Turner, and D. Huterer (Sept. 2008). "Dark Energy and the Accelerating Universe". In: *Annu. Rev. Astron. Astrophys.* 46, pp. 385–432. DOI: 10.1146/annurev.astro.46.060407.145243. arXiv: 0803.0982.

Fu, Xiangyun, Puxun Wu, and Hongwei Yu (July 2010). "The growth factor of matter perturbations in f(R) gravity". In: *European Physical Journal C* 68.1-2, pp. 271–276. DOI: 10.1140/epjc/s10052-010-1324-4. arXiv: 1012.2249 [gr-qc].

García-Aspeitia, Miguel A, Juan A Magaña, and Tonatiuh Matos (Mar. 2012). "Braneworld model of dark matter: structure formation". In: *General Relativity and Gravitation* 44.3, pp. 581–601. DOI: 10.1007/s10714-011-1294-3. arXiv: 1102.0825 [gr-qc].

García-Farieta, Jorge Enrique et al. (Sept. 2019). "Validating the methodology for constraining the linear growth rate from clustering anisotropies". In: *arXiv e-prints*, arXiv:1909.08016, arXiv:1909.08016. arXiv: 1909.08016 [astro-ph.CO].

García-Farieta, J.E. and R.A. Casas-Miranda (2018). "Effect of observational holes in fractal analysis of galaxy survey masks". In: *Chaos, Solitons & Fractals* 111, pp. 128 –137. ISSN: 0960-0779. DOI: \url{https://doi.org/10.1016/j.chaos.2018.04.018}. URL: \url{http://www.sciencedirect.com/science/article/pii/S0960077918301632}.

García-Farieta, Jorge Enrique et al. (July 2019). "Clustering and redshift-space distortions in modified gravity models with massive neutrinos". In: *Monthly Notices of the Royal Astronomical Society*. ISSN: 0035-8711. DOI: 10.1093/mnras/stz1850. eprint: http://oup.prod.sis.lan/mnras/advance-article-pdf/doi/10.1093/mnras/stz1850/28914901/stz1850.pdf. URL: https://doi.org/10.1093/mnras/stz1850.

Gaztañaga, E. et al. (Dec. 2005). "Statistical analysis of galaxy surveys - II. The three-point galaxy correlation function measured from the 2dFGRS". In: *Mon. Not. R. Astron. Soc.* 364, pp. 620–634. DOI: 10.1111/j.1365-2966.2005.09583.x. eprint: astro-ph/0506249.

Gil-Marín, Héctor et al. (Nov. 2012). "Perturbation theory approach for the power spectrum: from dark matter in real space to massive haloes in redshift space". In: *Journal of Cosmology and Astro-Particle Physics* 2012.11, 029, p. 029. DOI: 10.1088/1475-7516/2012/11/029. arXiv: 1209.3771 [astro-ph.CO].

Giocoli, C., G. Tormen, and F. C. van den Bosch (June 2008). "The population of dark matter subhaloes: mass functions and average mass-loss rates". In: *Mon. Not. R. Astron. Soc.* 386, pp. 2135–2144. DOI: 10.1111/j.1365-2966.2008.13182.x. arXiv: 0712.1563.

Giocoli, Carlo, Marco Baldi, and Lauro Moscardini (2018). "Weak lensing light-cones in modified gravity simulations with and without massive neutrinos". In: *Monthly Notices of the Royal Astronomical Society* 481.2, pp. 2813–2828. DOI: 10.1093/mnras/sty2465. eprint: /oup/backfile/content_public/journal/mnras/481/2/10.1093_mnras_sty2465/1/sty2465.pdf. URL: http://dx.doi.org/10.1093/mnras/sty2465.

Granett, Benjamin R. et al. (May 2019). "Measuring the growth of structure by matching dark matter haloes to galaxies with VIPERS and SDSS". In: *arXiv e-prints*, arXiv:1905.10375, arXiv:1905.10375. arXiv: 1905.10375 [astro-ph.CO].

Guo, Zong-Kuan, Nobuyoshi Ohta, and Shinji Tsujikawa (July 2007). "Probing the coupling between dark components of the universe". In: *Phys. Rev. D* 76.2, 023508, p. 023508. DOI: 10.1103/PhysRevD.76.023508. arXiv: astro-ph/0702015 [astro-ph].

Guzzo, L. et al. (Jan. 2008). "A test of the nature of cosmic acceleration using galaxy redshift distortions". In: *Nature* 451.7178, pp. 541–544. DOI: 10.1038/nature06555. arXiv: 0802.1944 [astro-ph].

Guzzo, L. et al. (June 2014). "The VIMOS Public Extragalactic Redshift Survey (VIPERS). An unprecedented view of galaxies and large-scale structure at 0.5

< z < 1.2". In: *Astron. Astrophys.* 566, A108, A108. DOI: 10.1051/0004-6361/201321489. arXiv: 1303.2623 [astro-ph.CO].

Guzzo, L et al. (2014). "The VIMOS Public Extragalactic Redshift Survey (VIPERS)-An unprecedented view of galaxies and large-scale structure at 0.5< z< 1.2". In: *Astronomy & Astrophysics* 566, A108.

Hagstotz, S. et al. (Feb. 2019). "Breaking cosmic degeneracies: Disentangling neutrinos and modified gravity with kinematic information". In: *arXiv e-prints*. arXiv: 1902.01868.

Hagstotz, Steffen et al. (June 2018). "Joint halo mass function for modified gravity and massive neutrinos I: simulations and cosmological forecasts". In: *arXiv e-prints*, arXiv:1806.07400, arXiv:1806.07400. arXiv: 1806.07400 [astro-ph.CO].

Hamana, Takashi et al. (2015). "Cosmological constraints from Subaru weak lensing cluster counts". In: *Publications of the Astronomical Society of Japan* 67.3, p. 34. DOI: 10.1093/pasj/psv034. eprint: /oup/backfile/content_public/journal/pasj/67/3/10.1093/pasj/psv034/2/psv034.pdf. URL: http://dx.doi.org/10.1093/pasj/psv034.

Hamaus, Nico et al. (Nov. 2015). "Probing cosmology and gravity with redshift-space distortions around voids". In: *J. Cosm. Astro-Particle Phys.* 2015.11, 036, p. 036. DOI: 10.1088/1475-7516/2015/11/036. arXiv: 1507.04363 [astro-ph.CO].

Hamaus, Nico et al. (July 2017). "Multipole analysis of redshift-space distortions around cosmic voids". In: *J. Cosm. Astro-Particle Phys.* 2017.7, 014, p. 014. DOI: 10.1088/1475-7516/2017/07/014. arXiv: 1705.05328 [astro-ph.CO].

Hamilton, A. J. S. (Jan. 1992). "Measuring Omega and the real correlation function from the redshift correlation function". In: *Astrophys. J. Lett.* 385, pp. L5–L8. DOI: 10.1086/186264.

— (Nov. 1993). "Toward Better Ways to Measure the Galaxy Correlation Function". In: *Astrophys. J.* 417, p. 19. DOI: 10.1086/173288.

Hamilton, A. J. S. (1998). "Linear Redshift Distortions: A Review". In: *The Evolving Universe: Selected Topics on Large-Scale Structure and on the Properties of Galaxies*. Dordrecht: Springer Netherlands, pp. 185–275.

Hamilton, A. J. S. (Jan. 1998). "Linear Redshift Distortions: a Review". In: *The Evolving Universe*. Ed. by Donald Hamilton. Vol. 231. Astrophysics and Space Science Library, p. 185. DOI: 10.1007/978-94-011-4960-0_17. arXiv: astro-ph/9708102 [astro-ph].

Hamilton, A. J. S., M. Tegmark, and N. Padmanabhan (Sept. 2000). "Linear redshift distortions and power in the IRAS Point Source Catalog Redshift Survey". In: *Mon. Not. R. Astron. Soc.* 317, pp. L23–L27. DOI: 10.1046/j.1365-8711.2000.03888.x. eprint: astro-ph/0004334.

Hawkins, Ed et al. (Nov. 2003). "The 2dF Galaxy Redshift Survey: correlation functions, peculiar velocities and the matter density of the Universe". In: *Mon. Not. R. Astron. Soc.* 346.1, pp. 78–96. DOI: 10.1046/j.1365-2966.2003.07063.x. arXiv: astro-ph/0212375 [astro-ph].

Hawley, DL and PJE Peebles (1975). "Distribution of observed orientations of galaxies". In: *The Astronomical Journal* 80, pp. 477–491.

He, Jian-hua (Nov. 2013). "Weighing neutrinos in $f(R)$ gravity". In: *Phys. Rev. D* 88 (10), p. 103523. DOI: 10.1103/PhysRevD.88.103523. URL: https://link.aps.org/doi/10.1103/PhysRevD.88.103523.

He, Jian-hua et al. (2018). "No evidence for modifications of gravity from galaxy motions on cosmological scales". In: *Nature Astronomy*. Exported from https://app.dimensions.ai on 2019/02/03, pp. 1–6. DOI: 10.1038/s41550-018-0573-2. URL: https://app.dimensions.ai/details/publication/pub.1107129377andhttp://arxiv.org/pdf/1809.09019.

Hellwing, Wojciech A. et al. (Sept. 2016). "The effect of baryons on redshift space distortions and cosmic density and velocity fields in the EAGLE simulation". In: *Mon. Not. R. Astron. Soc.* 461.1, pp. L11–L15. DOI: 10.1093/mnrasl/slw081. arXiv: 1603.03328 [astro-ph.CO].

Hikage, Chiaki et al. (Apr. 2019). "Cosmology from cosmic shear power spectra with Subaru Hyper Suprime-Cam first-year data". In: *Publ. Astron. Soc. Japan* 71.2, 43, p. 43. DOI: 10.1093/pasj/psz010. arXiv: 1809.09148 [astro-ph.CO].

Hinshaw, G et al. (2013). "Nine-year Wilkinson Microwave Anisotropy Probe (WMAP) observations: cosmological parameter results". In: *The Astrophysical Journal Supplement Series* 208.2, p. 19.

Hogg, David W. (May 1999). "Distance measures in cosmology". In: *arXiv e-prints*, astro-ph/9905116, astro–ph/9905116. arXiv: astro-ph/9905116 [astro-ph].

Hogg, David W et al. (2005). "Cosmic homogeneity demonstrated with luminous red galaxies". In: *The Astrophysical Journal* 624.1, p. 54.

Howlett, Cullan et al. (May 2015). "The clustering of the SDSS main galaxy sample - II. Mock galaxy catalogues and a measurement of the growth of structure from redshift space distortions at z = 0.15". In: *Mon. Not. R. Astron. Soc.* 449.1, pp. 848–866. DOI: 10.1093/mnras/stu2693. arXiv: 1409.3238 [astro-ph.CO].

Hu, Wayne and Ignacy Sawicki (Sept. 2007). "Models of $f(R)$ cosmic acceleration that evade solar system tests". In: *Phys. Rev. D* 76 (6), p. 064004. DOI: 10.1103/PhysRevD.76.064004. URL: https://link.aps.org/doi/10.1103/PhysRevD.76.064004.

Hu, Wayne and Naoshi Sugiyama (Nov. 1996). "Small-Scale Cosmological Perturbations: an Analytic Approach". In: *Astrophys. J.* 471, p. 542. DOI: 10.1086/177989. arXiv: astro-ph/9510117 [astro-ph].

Hubble, Edwin (1934). "The distribution of extra-galactic nebulae". In: *The Astrophysical Journal* 79, p. 8.

Hubble, Edwin P (1926). "Extragalactic nebulae." In: *The Astrophysical Journal* 64, pp. 321–369.

Hudson, M. J. and S. J. Turnbull (June 2012). "The Growth Rate of Cosmic Structure from Peculiar Velocities at Low and High Redshifts". In: *Astrophys. J. Lett.* 751, L30, p. L30. DOI: 10.1088/2041-8205/751/2/L30. arXiv: 1203.4814.

Hut, P (1977). "Cosmological tests of general relativity". In: *Nature* 267.5607, pp. 128–130.

Iorio, Lorenzo (July 2003). "The Impact of the Static Part of the Earth's Gravity Field on Some Tests of General Relativity with Satellite Laser Ranging". In: *Celestial Mechanics and Dynamical Astronomy* 86.3, pp. 277–294. arXiv: gr-qc/0203050 [gr-qc].

Ishikawa, Takashi et al. (Oct. 2014). "On the systematic errors of cosmological-scale gravity tests using redshift-space distortion: non-linear effects and the halo bias". In: *Mon. Not. R. Astron. Soc.* 443.4, pp. 3359–3367. DOI: 10.1093/mnras/stu1382. arXiv: 1308.6087 [astro-ph.CO].

Ivezic, Z. et al. (May 2008). "LSST: from Science Drivers to Reference Design and Anticipated Data Products". In: *ArXiv e-prints: 0805.2366*. arXiv: 0805.2366.

Jackson, J. C. (1972). "A Critique of Rees's Theory of Primordial Gravitational Radiation". In: *Monthly Notices of the Royal Astronomical Society* 156.1, 1P–5P. DOI: 10.1093/mnras/156.1.1P. eprint: /oup/backfile/content_public/journal/mnras/156/1/10.1093_mnras_156.1.1p/3/mnras156-001p.pdf. URL: http://dx.doi.org/10.1093/mnras/156.1.1P.

Jennings, E., C. M. Baugh, and S. Pascoli (Jan. 2011). "Modelling redshift space distortions in hierarchical cosmologies". In: *Mon. Not. R. Astron. Soc.* 410.3, pp. 2081–2094. DOI: 10.1111/j.1365-2966.2010.17581.x. arXiv: 1003.4282 [astro-ph.CO].

Jennings, Elise (Nov. 2012). "An improved model for the non-linear velocity power spectrum". In: *Mon. Not. R. Astron. Soc.* 427.1, pp. L25–L29. DOI: 10.1111/j.1745-3933.2012.01338.x. arXiv: 1207.1439 [astro-ph.CO].

Jennings, Elise et al. (Sept. 2012). "Redshift-space distortions in f(R) gravity". In: *Monthly Notices of the Royal Astronomical Society* 425.3, pp. 2128–2143. ISSN: 0035-8711. DOI: 10.1111/j.1365-2966.2012.21567.x. eprint: http://oup.prod.sis.lan/mnras/article-pdf/425/3/2128/3061734/425-3-2128.pdf. URL: https://dx.doi.org/10.1111/j.1365-2966.2012.21567.x.

Jing, Y. P. and G. Börner (Dec. 2004). "The Pairwise Velocity Dispersion of Galaxies: Luminosity Dependence and a New Test of Galaxy Formation Models". In: *Astrophys. J.* 617.2, pp. 782–793. DOI: 10.1086/425679. arXiv: astro-ph/0406077 [astro-ph].

Jones, D. O. et al. (2018). "Measuring Dark Energy Properties with Photometrically Classified Pan-STARRS Supernovae. II. Cosmological Parameters". In: *The Astrophysical Journal* 857.1, p. 51. URL: http://stacks.iop.org/0004-637X/857/i=1/a=51.

Joudaki, Shahab et al. (2018). "KiDS-450 + 2dFLenS: Cosmological parameter constraints from weak gravitational lensing tomography and overlapping redshift-space galaxy clustering". In: *Monthly Notices of the Royal Astronomical Society* 474.4, pp. 4894–4924. DOI: 10.1093/mnras/stx2820. eprint: /oup/backfile/content_public/journal/mnras/474/4/10.1093_mnras_stx2820/1/stx2820.pdf. URL: http://dx.doi.org/10.1093/mnras/stx2820.

Joyce, Austin, Lucas Lombriser, and Fabian Schmidt (2016). "Dark Energy Versus Modified Gravity". In: *Annual Review of Nuclear and Particle Science* 66.1, pp. 95–122. DOI: 10.1146/annurev-nucl-102115-044553. eprint:

https://doi.org/10.1146/annurev-nucl-102115-044553. URL: https://doi.org/10.1146/annurev-nucl-102115-044553.

Kaiser, N. (July 1987). "Clustering in real space and in redshift space". In: *Mon. Not. R. Astron. Soc.* 227, pp. 1–21. DOI: 10.1093/mnras/227.1.1.

Kaiser, Nick (July 1987). "Clustering in real space and in redshift space". In: *Monthly Notices of the Royal Astronomical Society* 227.1, pp. 1–21. ISSN: 0035-8711. DOI: 10.1093/mnras/227.1.1. eprint: http://oup.prod.sis.lan/mnras/article-pdf/227/1/1/18522208/mnras227-0001.pdf. URL: https://doi.org/10.1093/mnras/227.1.1.

Kanipe, J. (May 1995). "The Pillars of Cosmology: A Short History and Assessment". In: *Astrophys. & Space Science.* 227, pp. 109–118. DOI: 10.1007/BF00678071.

Kass, Robert E. and Adrian E. Raftery (1995). "Bayes Factors". In: *Journal of the American Statistical Association* 90.430, pp. 773–795. ISSN: 01621459. URL: http://www.jstor.org/stable/2291091.

Kazin, Eyal A., Ariel G. Sánchez, and Michael R. Blanton (Feb. 2012). "Improving measurements of H(z) and D_A (z) by analysing clustering anisotropies". In: *Mon. Not. R. Astron. Soc.* 419, pp. 3223–3243. DOI: 10.1111/j.1365-2966.2011.19962.x. arXiv: 1105.2037 [astro-ph.CO].

Kerscher, Martin, István Szapudi, and Alexander S. Szalay (May 2000). "A Comparison of Estimators for the Two-Point Correlation Function". In: *Astrophys. J. Lett.* 535.1, pp. L13–L16. DOI: 10.1086/312702. arXiv: astro-ph/9912088 [astro-ph].

Kirkman, David et al. (Nov. 2003). "The Cosmological Baryon Density from the Deuterium-to-Hydrogen Ratio in QSO Absorption Systems: D/H toward Q1243+3047". In: *Astrophys. J. Suppl.* 149.1, pp. 1–28. DOI: 10.1086/378152. arXiv: astro-ph/0302006 [astro-ph].

Kirshner, RP et al. (1983). "A deep survey of galaxies". In: *The Astronomical Journal* 88, pp. 1285–1300.

Klypin, Anatoly et al. (Apr. 2016). "MultiDark simulations: the story of dark matter halo concentrations and density profiles". In: *Mon. Not. R. Astron. Soc.* 457.4, pp. 4340–4359. DOI: 10.1093/mnras/stw248. arXiv: 1411.4001 [astro-ph.CO].

Knebe, A. et al. (Aug. 2011). "Haloes gone MAD: The Halo-Finder Comparison Project". In: *Mon. Not. R. Astron. Soc.* 415, pp. 2293–2318. DOI: 10.1111/j.1365-2966.2011.18858.x. arXiv: 1104.0949.

Knebe, Alexander (2005). "How to Simulate the Universe in a Computer". In: *Publications of the Astronomical Society of Australia* 22.3, 184–189. DOI: 10.1071/AS04059. eprint: astro-ph/0412565.

Kramer, M. et al. (Oct. 2006). "Tests of General Relativity from Timing the Double Pulsar". In: *Science* 314.5796, pp. 97–102. DOI: 10.1126/science.1132305. arXiv: astro-ph/0609417 [astro-ph].

Kumar, Suresh and Rafael C. Nunes (Dec. 2016). "Probing the interaction between dark matter and dark energy in the presence of massive neutrinos". In: *Phys. Rev. D* 94 (12), p. 123511. DOI: 10.1103/PhysRevD.94.123511. URL: https://link.aps.org/doi/10.1103/PhysRevD.94.123511.

Landy, S. D. and A. S. Szalay (July 1993). "Bias and variance of angular correlation functions". In: *Astrophys. J.* 412, pp. 64–71. DOI: 10.1086/172900.

Laureijs, R. et al. (Oct. 2011a). "Euclid Definition Study Report". In: *ArXiv e-prints*. arXiv: 1110.3193 [astro-ph.CO].

Laureijs, R. et al. (Oct. 2011b). "Euclid Definition Study Report". In: *arXiv e-prints*, arXiv:1110.3193, arXiv:1110.3193. arXiv: 1110.3193 [astro-ph.CO].

Laureijs, René et al. (2012). "Euclid: ESA's mission to map the geometry of the dark universe". In: *SPIE Astronomical Telescopes+ Instrumentation*. International Society for Optics and Photonics, 84420T–84420T.

Lazanu, Andrei et al. (Apr. 2016). "Matter bispectrum of large-scale structure: Three-dimensional comparison between theoretical models and numerical simulations". In: *Phys. Rev. D* 93.8, 083517, p. 083517. DOI: 10.1103/PhysRevD.93.083517. arXiv: 1510.04075 [astro-ph.CO].

Lemaître, G. (1927). "Un Univers homogène de masse constante et de rayon croissant rendant compte de la vitesse radiale des nébuleuses extra-galactiques". In: *Annales de la Société Scientifique de Bruxelles* 47, pp. 49–59.

Lesgourgues, Julien and Sergio Pastor (2006). "Massive neutrinos and cosmology". In: *Physics Reports* 429.6, pp. 307 –379. ISSN: 0370-1573. DOI: https://doi.org/10.1016/j.physrep.2006.04.001. URL: http://www.sciencedirect.com/science/article/pii/S0370157306001359.

— (2012). "Neutrino mass from cosmology". In: *Advances in High Energy Physics* 2012.

Lesgourgues, Julien and Sergio Pastor (June 2014). "Neutrino cosmology and Planck". In: *New Journal of Physics* 16.6, 065002, p. 065002. DOI: 10.1088/1367-2630/16/6/065002. arXiv: 1404.1740 [hep-ph].

Lesgourgues, Julien et al. (2013). *Neutrino cosmology*. Cambridge University Press.

Lewis, Antony, Anthony Challinor, and Anthony Lasenby (2000). "Efficient Computation of Cosmic Microwave Background Anisotropies in Closed Friedmann-Robertson-Walker Models". In: *The Astrophysical Journal* 538.2, p. 473. URL: http://stacks.iop.org/0004-637X/538/i=2/a=473.

Li, C. et al. (Apr. 2007). "Luminosity dependence of the spatial and velocity distributions of galaxies: semi-analytic models versus the Sloan Digital Sky Survey". In: *Mon. Not. R. Astron. Soc.* 376, pp. 984–996. DOI: 10.1111/j.1365-2966.2007.11518.x. eprint: astro-ph/0701218.

Liddle, Andrew R. (July 2004). "How many cosmological parameters?" In: *Mon. Not. R. Astron. Soc.* 351.3, pp. L49–L53. DOI: 10.1111/j.1365-2966.2004.08033.x. arXiv: astro-ph/0401198 [astro-ph].

Lilje, P. B. and G. Efstathiou (Feb. 1989). "Gravitationally induced velocity fields in the universe. I - Correlation functions". In: *Mon. Not. R. Astron. Soc.* 236, pp. 851–864. DOI: 10.1093/mnras/236.4.851.

Linder, E. V. (Aug. 2005). "Cosmic growth history and expansion history". In: *Phys. Rev. D* 72.4, 043529, pp. 043529–+. DOI: 10.1103/PhysRevD.72.043529. arXiv: astro-ph/0507263 [astro-ph].

Linder, E. V. (June 2008). "Redshift distortions as a probe of gravity". In: *Astroparticle Physics* 29, pp. 336–339. DOI: 10.1016/j.astropartphys.2008.03.002. arXiv: 0709.1113.

Linder, Eric V. (Mar. 2003). "Exploring the Expansion History of the Universe". In: *Phys. Rev. Lett.* 90.9, 091301, p. 091301. DOI: 10.1103/PhysRevLett.90.091301. arXiv: astro-ph/0208512 [astro-ph].

Linder, Eric V. (2017). "Cosmic growth and expansion conjoined". In: *Astroparticle Physics* 86, pp. 41 –45. ISSN: 0927-6505. DOI: https://doi.org/10.1016/j.astropartphys.2016.11.002. URL: http://www.sciencedirect.com/science/article/pii/S092765051630161X.

Ling, E. N., C. S. Frenk, and J. D. Barrow (Dec. 1986). "Uncertainties in the cluster-cluster correlation function". In: *Mon. Not. R. Astron. Soc.* 223, 21P–27P. DOI: 10.1093/mnras/223.1.21P.

Lu, Jia-Shu et al. (2015). "Constraining absolute neutrino masses via detection of galactic supernova neutrinos at JUNO". In: *Journal of Cosmology and Astroparticle Physics* 2015.05, p. 044. URL: http://stacks.iop.org/1475-7516/2015/i=05/a=044.

Lu, Jianbo et al. (Dec. 2016). "Cosmic constraint on massive neutrinos in viable f(R) gravity with producing ΛCDM background expansion". In: *The European Physical Journal C* 76.12, p. 679. ISSN: 1434-6052. DOI: 10.1140/epjc/s10052-016-4525-7. URL: https://doi.org/10.1140/epjc/s10052-016-4525-7.

Ma, Chung-Pei (1999). "Redshift Evolution of the Nonlinear Two-Point Correlation Function". In: *The Astrophysical Journal* 510.1, p. 32. URL: http://stacks.iop.org/0004-637X/510/i=1/a=32.

Maartens, Roy et al. (Jan. 2015). "Cosmology with the SKA – overview". In: *arXiv e-prints*, arXiv:1501.04076, arXiv:1501.04076. arXiv: 1501.04076 [astro-ph.CO].

Magaña, Juan, Víctor H. Cárdenas, and Verónica Motta (Oct. 2014). "Cosmic slowing down of acceleration for several dark energy parametrizations". In: *J. Cosm. Astro-Particle Phys.* 2014.10, 017, p. 017. DOI: 10.1088/1475-7516/2014/10/017. arXiv: 1407.1632 [astro-ph.CO].

Magaña, Juan et al. (July 2017). "Testing cosmic acceleration for w(z) parametrizations using f_{gas} measurements in galaxy clusters". In: *Mon. Not. R. Astron. Soc.* 469.1, pp. 47–61. DOI: 10.1093/mnras/stx750. arXiv: 1703.08521 [astro-ph.CO].

Mandelbaum, Rachel et al. (Aug. 2005). "Systematic errors in weak lensing: application to SDSS galaxy-galaxy weak lensing". In: *Mon. Not. R. Astron. Soc.* 361.4, pp. 1287–1322. DOI: 10.1111/j.1365-2966.2005.09282.x. arXiv: astro-ph/0501201 [astro-ph].

Mandelbrot, Benoit B (1983). "The fractal geometry of nature/Revised and enlarged edition". In: *New York, WH Freeman and Co., 1983, 495 p.* 1.

Marcondes, R. J. F. (2016). "Interacting dark energy models in Cosmology and large-scale structure observational tests". PhD thesis. Instituto de Física, University of São Paulo, São Paulo. URL: https://arxiv.org/abs/1610.01272.

Martínez, V. J. and E. Saar (2002). *Statistics of the Galaxy Distribution*. Chapman.

Martinez, Vicent J (1991). "Fractal aspects of galaxy clustering". In: *Applying Fractals in Astronomy*. Springer, pp. 135–159.

Martinez, Vicent J and Enn Saar (2010). *Statistics of the galaxy distribution*. CRC Press.

Martino, Ivan de, Mariafelicia De Laurentis, and Salvatore Capozziello (2015). "Constraining $f(R)$ Gravity by the Large-Scale Structure". In: *Universe* 1.2, pp. 123–157. ISSN: 2218-1997. DOI: 10.3390/universe1020123. URL: http://www.mdpi.com/2218-1997/1/2/123.

Marulli, F. et al. (Mar. 2017). "Redshift-space distortions of galaxies, clusters, and AGN. Testing how the accuracy of growth rate measurements depends on scales and sample selections". In: *Astron. Astrophys.* 599, A106, A106. DOI: 10.1051/0004-6361/201526885. arXiv: 1505.01170 [astro-ph.CO].

Marulli, F. et al. (Nov. 2018). "The XXL Survey. XVI. The clustering of X-ray selected galaxy clusters at z 0.3". In: *Astron. Astrophys.* 620, A1, A1. DOI: 10.1051/0004-6361/201833238. arXiv: 1807.04760 [astro-ph.CO].

Marulli, Federico, Marco Baldi, and Lauro Moscardini (Mar. 2012). "Clustering and redshift-space distortions in interacting dark energy cosmologies". In: *Mon. Not. R. Astron. Soc.* 420.3, pp. 2377–2386. DOI: 10.1111/j.1365-2966.2011.20199.x. arXiv: 1110.3045 [astro-ph.CO]. URL: http://dx.doi.org/10.1111/j.1365-2966.2011.20199.x.

Marulli, Federico, Alfonso Veropalumbo, and Michele Moresco (Jan. 2016). "CosmoBolognaLib: C++ libraries for cosmological calculations". In: *Astronomy and Computing* 14, pp. 35–42. ISSN: 2213-1337. DOI: 10.1016/j.ascom.2016.01.005. arXiv: 1511.00012. URL: http://www.sciencedirect.com/science/article/pii/S2213133716300014.

Marulli, Federico et al. (Nov. 2011). "Effects of massive neutrinos on the large-scale structure of the Universe". In: *Mon. Not. R. Astron. Soc.* 418.1, pp. 346–356. DOI: 10.1111/j.1365-2966.2011.19488.x. arXiv: 1103.0278 [astro-ph.CO]. URL: http://dx.doi.org/10.1111/j.1365-2966.2011.19488.x.

Marulli, Federico et al. (Nov. 2012). "Cosmology with clustering anisotropies: disentangling dynamic and geometric distortions in galaxy redshift surveys". In: *Mon. Not. R. Astron. Soc.* 426.3, pp. 2566–2580. DOI: 10.1111/j.1365-2966.2012.21875.x. arXiv: 1203.1002 [astro-ph.CO].

Matarrese, Sabino et al. (1997). "Redshift evolution of clustering". In: *Monthly Notices of the Royal Astronomical Society* 286.1, pp. 115–132. DOI: 10.1093/mnras/286.1.115. eprint: /oup/backfile/content_public/journal/mnras/286/1/10.1093/mnras/286.1.115/3/286-1-115.pdf. URL: http://dx.doi.org/10.1093/mnras/286.1.115.

McGill, C. (Feb. 1990). "The redshift projection. I - Caustics and correlation functions". In: *Mon. Not. R. Astron. Soc.* 242, pp. 428–438. DOI: 10.1093/mnras/242.3.428.

Meng, X.-L. et al. (July 2015). "Utility of observational Hubble parameter data on dark energy evolution". In: *arXiv e-prints*. arXiv: 1507.02517.

Merloni, A. et al. (Sept. 2012). "eROSITA Science Book: Mapping the Structure of the Energetic Universe". In: *ArXiv e-prints: 1209.3114*. arXiv: 1209.3114 [astro-ph.HE].

Merten, Julian et al. (Oct. 2018). "On the dissection of degenerate cosmologies with machine learning". In: *ArXiv e-prints*, arXiv:1810.11027, arXiv:1810.11027. arXiv: 1810.11027 [astro-ph.CO].

Misner, Charles W, Kip S Thorne, and John A Wheeler (1973). "Gravitation". In: *San Francisco: WH Freeman and Co., 1973* 1.

Moresco, M. and F. Marulli (Oct. 2017). "Cosmological constraints from a joint analysis of cosmic growth and expansion". In: *Mon. Not. R. Astron. Soc.* 471, pp. L82–L86. DOI: 10.1093/mnrasl/slx112. arXiv: 1705.07903.

Moresco, Michele (Apr. 2015). "Raising the bar: new constraints on the Hubble parameter with cosmic chronometers at $z \sim 2$". In: *Monthly Notices of the Royal Astronomical Society: Letters* 450.1, pp. L16–L20. ISSN: 1745-3925. DOI: 10.1093/mnrasl/slv037. eprint: http://oup.prod.sis.lan/mnrasl/article-pdf/450/1/L16/3083577/slv037.pdf. URL: https://doi.org/10.1093/mnrasl/slv037.

Moresco, Michele et al. (May 2016). "A 6% measurement of the Hubble parameter at z$\sim$0.45: direct evidence of the epoch of cosmic re-acceleration". In: *Journal of Cosmology and Astro-Particle Physics* 2016.5, 014, p. 014. DOI: 10.1088/1475-7516/2016/05/014. arXiv: 1601.01701 [astro-ph.CO].

Moscardini, Lauro and Klaus Dolag (2011). "Cosmology with Numerical Simulations". In: *Dark Matter and Dark Energy: A Challenge for Modern Cosmology*. Ed. by Sabino Matarrese et al. Dordrecht: Springer Netherlands, pp. 217–237. ISBN: 978-90-481-8685-3. DOI: 10.1007/978-90-481-8685-3_4. URL: https://doi.org/10.1007/978-90-481-8685-3_4.

Motohashi, Hayato, Alexei A. Starobinsky, and Jun'ichi Yokoyama (Mar. 2013). "Cosmology Based on $f(R)$ Gravity Admits 1 eV Sterile Neutrinos". In: *Phys. Rev. Lett.* 110 (12), p. 121302. DOI: 10.1103/PhysRevLett.110.121302. URL: https://link.aps.org/doi/10.1103/PhysRevLett.110.121302.

Mukhanov, Viatcheslav (2005). *Physical foundations of cosmology*. Cambridge University Press.

Murante, G et al. (1997). "Density singularities and cosmic structures". In: *Monthly Notices of the Royal Astronomical Society* 291.4, pp. 585–592.

Narikawa, Tatsuya and Kazuhiro Yamamoto (Feb. 2010). "Characterizing the linear growth rate of cosmological density perturbations in an f(R) model". In: *Phys. Rev. D* 81.4, 043528, p. 043528. DOI: 10.1103/PhysRevD.81.043528. arXiv: 0912.1445 [astro-ph.CO].

Nesseris, S. and L. Perivolaropoulos (Dec. 2005). "Comparison of the legacy and gold type Ia supernovae dataset constraints on dark energy models". In: *Phys. Rev. D* 72.12, 123519, p. 123519. DOI: 10.1103/PhysRevD.72.123519. arXiv: astro-ph/0511040 [astro-ph].

— (Jan. 2007). "Crossing the phantom divide: theoretical implications and observational status". In: *J. Cosm. Astro-Particle Phys.* 2007.1, 018, p. 018. DOI: 10.1088/1475-7516/2007/01/018. arXiv: astro-ph/0610092 [astro-ph].

Nesseris, Savvas et al. (July 2011). "The WiggleZ Dark Energy Survey: constraining the evolution of Newton's constant using the growth rate of structure". In: *J. Cosm. Astro-Particle Phys.* 2011.7, 037, p. 037. DOI: 10.1088/1475-7516/2011/07/037. arXiv: 1107.3659 [astro-ph.CO].

Nojiri, Shin'ichi, Sergei D. Odintsov, and Diego Sáez-Gómez (Oct. 2009). "Cosmological reconstruction of realistic modified F(R) gravities". In: *Physics Letters B* 681.1, pp. 74–80. DOI: 10.1016/j.physletb.2009.09.045. arXiv: 0908.1269 [hep-th].

Nordin, Jakob, Ariel Goobar, and Jakob Jönsson (Feb. 2008). "Quantifying systematic uncertainties in supernova cosmology". In: *Journal of Cosmology and Astro-Particle Physics* 2008.2, 008, p. 008. DOI: 10.1088/1475-7516/2008/02/008. arXiv: 0801.2484 [astro-ph].

Ntampaka, Michelle, Ken Rines, and Hy Trac (June 2019). "Cluster Cosmology with the Velocity Distribution Function of the HeCS-SZ Sample". In: *arXiv e-prints*, arXiv:1906.07729, arXiv:1906.07729. arXiv: 1906.07729 [astro-ph.CO].

Oka, Akira et al. (Apr. 2014). "Simultaneous constraints on the growth of structure and cosmic expansion from the multipole power spectra of the SDSS DR7 LRG sample". In: *Mon. Not. R. Astron. Soc.* 439.3, pp. 2515–2530. DOI: 10.1093/mnras/stu111. arXiv: 1310.2820 [astro-ph.CO].

Okumura, Teppei et al. (June 2016). "The Subaru FMOS galaxy redshift survey (FastSound). IV. New constraint on gravity theory from redshift space distortions at z∼1.4". In: *Publ. Astron. Soc. Japan* 68.3, 38, p. 38. DOI: 10.1093/pasj/psw029. arXiv: 1511.08083 [astro-ph.CO].

Pacaud, F. et al. (Nov. 2018). "The XXL Survey. XXV. Cosmological analysis of the C1 cluster number counts". In: *Astron. Astrophys.* 620, A10, A10. DOI: 10.1051/0004-6361/201834022. arXiv: 1810.01624.

Padmanabhan, T. (May 1993). *Structure Formation in the Universe*. Cambridge University Press, p. 499.

Pan, Jun and Peter Coles (2000). "Large-scale cosmic homogeneity from a multifractal analysis of the PSCz catalogue". In: *Monthly Notices of the Royal Astronomical Society* 318.4, p. L51. DOI: 10.1046/j.1365-8711.2000.03965.x.

— (2002). "Boundary corrections in fractal analysis of galaxy surveys". In: *Monthly Notices of the Royal Astronomical Society* 330.3, pp. 719–730. DOI: 10.1046/j.1365-8711.2002.05114.x.

Parker, Leonard and Alpan Raval (Sept. 1999). "Nonperturbative effects of vacuum energy on the recent expansion of the universe". In: *Physical Review D* 60.6, 063512, p. 063512. DOI: 10.1103/PhysRevD.60.063512. arXiv: gr-qc/9905031 [gr-qc].

Parkinson, David et al. (Nov. 2012). "The WiggleZ Dark Energy Survey: Final data release and cosmological results". In: *Phys. Rev. D* 86.10, 103518, p. 103518. DOI: 10.1103/PhysRevD.86.103518. arXiv: 1210.2130 [astro-ph.CO].

Peacock, J. A. and S. J. Dodds (Apr. 1994). "Reconstructing the Linear Power Spectrum of Cosmological Mass Fluctuations". In: *Mon. Not. R. Astron. Soc.* 267, p. 1020. DOI: 10.1093/mnras/267.4.1020. arXiv: astro-ph/9311057 [astro-ph].

Peacock, J. A. and S. J. Dodds (June 1996). "Non-linear evolution of cosmological power spectra". In: *Mon. Not. R. Astron. Soc.* 280.3, pp. L19–L26. DOI: 10.1093/mnras/280.3.L19. arXiv: astro-ph/9603031 [astro-ph].

Peacock, John A (1999). *Cosmological physics*. Cambridge university press.

Peacock, John A. et al. (Mar. 2001). "A measurement of the cosmological mass density from clustering in the 2dF Galaxy Redshift Survey". In: *Nature* 410.6825, pp. 169–173. arXiv: astro-ph/0103143 [astro-ph].

Peebles, P. J. E. and M. G. Hauser (Nov. 1974). "Statistical Analysis of Catalogs of Extragalactic Objects. III. The Shane-Wirtanen and Zwicky Catalogs". In: *Astrophys. J. Suppl.* 28, p. 19. DOI: 10.1086/190308.

Peebles, P. J. E. and J. T. Yu (Dec. 1970). "Primeval Adiabatic Perturbation in an Expanding Universe". In: *Astrophys. J.* 162, p. 815. DOI: 10.1086/150713.

Peebles, Phillip James Edwin (1980). *The large-scale structure of the universe*. Princeton university press.

— (1993). *Principles of physical cosmology*. Princeton University Press.

Peebles, PJE (1989). "The fractal galaxy distribution". In: *Physica D: Nonlinear Phenomena* 38.1, pp. 273–278.

Peebles, PJE and Edward J Groth (1975). "Statistical analysis of catalogs of extragalactic objects. V-Three-point correlation function for the galaxy distribution in the Zwicky catalog". In: *The Astrophysical Journal* 196, pp. 1–11.

Peel, A. et al. (Nov. 2018a). "Breaking degeneracies in modified gravity with higher (than 2nd) order weak-lensing statistics". In: *Astron. Astrophys.* 619, A38, A38. DOI: 10.1051/0004-6361/201833481. arXiv: 1805.05146.

Peel, Austin et al. (Oct. 2018b). "Distinguishing standard and modified gravity cosmologies with machine learning". In: *ArXiv e-prints*, arXiv:1810.11030, arXiv:1810.11030. arXiv: 1810.11030 [astro-ph.CO].

Penzias, A. A. and R. W. Wilson (July 1965). "A Measurement of Excess Antenna Temperature at 4080 Mc/s." In: *Astrophys. J.* 142, pp. 419–421. DOI: 10.1086/148307.

Percival, W. J. et al. (Oct. 2004a). "The 2dF Galaxy Redshift Survey: spherical harmonics analysis of fluctuations in the final catalogue". In: *Mon. Not. R. Astron. Soc.* 353.4, pp. 1201–1218. DOI: 10.1111/j.1365-2966.2004.08146.x. arXiv: astro-ph/0406513 [astro-ph].

Percival, W. J. et al. (Oct. 2004b). "The 2dF Galaxy Redshift Survey: spherical harmonics analysis of fluctuations in the final catalogue". In: *Mon. Not. R. Astron. Soc.* 353, pp. 1201–1218. DOI: 10.1111/j.1365-2966.2004.08146.x. eprint: arXiv:astro-ph/0406513.

Percival, Will J. and Martin White (Feb. 2009). "Testing cosmological structure formation using redshift-space distortions". In: *Mon. Not. R. Astron. Soc.* 393.1, pp. 297–308. DOI: 10.1111/j.1365-2966.2008.14211.x. arXiv: 0808.0003 [astro-ph].

Percival, Will J. et al. (2007). "Measuring the Matter Density Using Baryon Oscillations in the SDSS". In: *The Astrophysical Journal* 657.1, p. 51. URL: http://stacks.iop.org/0004-637X/657/i=1/a=51.

Percival, Will J. et al. (Feb. 2010). "Baryon acoustic oscillations in the Sloan Digital Sky Survey Data Release 7 galaxy sample". In: *Mon. Not. R. Astron.*

Soc. 401.4, pp. 2148–2168. DOI: 10.1111/j.1365-2966.2009.15812.x. arXiv: 0907.1660 [astro-ph.CO].

Perlmutter, S. et al. (June 1999). "Measurements of Ω and Λ from 42 High-Redshift Supernovae". In: *Astrophys. J.* 517, pp. 565–586. DOI: 10.1086/307221. eprint: astro-ph/9812133.

Perlmutter, S. et al. (1999). "Measurements of Ω and Λ from 42 High-Redshift Supernovae". In: *The Astrophysical Journal* 517.2, p. 565. URL: http://stacks.iop.org/0004-637X/517/i=2/a=565.

Pettorino, Valeria, Luca Amendola, and Christof Wetterich (Apr. 2013). "How early is early dark energy?" In: *Phys. Rev. D* 87.8, 083009, p. 083009. DOI: 10.1103/PhysRevD.87.083009. arXiv: 1301.5279 [astro-ph.CO].

Pezzotta, A. et al. (July 2017). "The VIMOS Public Extragalactic Redshift Survey (VIPERS). The growth of structure at $0.5 < z < 1.2$ from redshift-space distortions in the clustering of the PDR-2 final sample". In: *Astron. Astrophys.* 604, A33, A33. DOI: 10.1051/0004-6361/201630295. arXiv: 1612.05645 [astro-ph.CO].

Pietroni, Massimo (Oct. 2008). "Flowing with time: a new approach to non-linear cosmological perturbations". In: *J. Cosm. Astro-Particle Phys.* 2008.10, 036, p. 036. DOI: 10.1088/1475-7516/2008/10/036. arXiv: 0806.0971 [astro-ph].

Planck Collaboration et al. (Nov. 2014). "Planck 2013 results. XVI. Cosmological parameters". In: *Astron. Astrophys.* 571, A16, A16. DOI: 10.1051/0004-6361/201321591. arXiv: 1303.5076.

Planck Collaboration et al. (2016a). "Planck 2015 results - XI. CMB power spectra, likelihoods, and robustness of parameters". In: *A&A* 594, A11. DOI: 10.1051/0004-6361/201526926. URL: https://doi.org/10.1051/0004-6361/201526926.

Planck Collaboration et al. (2016b). "Planck 2015 results - XIII. Cosmological parameters". In: *A&A* 594, A13. DOI: 10.1051/0004-6361/201525830. URL: https://doi.org/10.1051/0004-6361/201525830.

Planck Collaboration et al. (2016c). "Planck 2015 results - XXIV. Cosmology from Sunyaev-Zeldovich cluster counts". In: *A&A* 594, A24. DOI: 10.1051/0004-6361/201525833. URL: https://doi.org/10.1051/0004-6361/201525833.

Planck Collaboration et al. (Sept. 2016d). "Planck 2015 results. XIII. Cosmological parameters". In: *Astron. Astrophys.* 594, A13, A13. DOI: 10.1051/0004-6361/201525830. arXiv: 1502.01589 [astro-ph.CO].

Planck Collaboration et al. (July 2018a). "Planck 2018 results. I. Overview and the cosmological legacy of Planck". In: *arXiv e-prints*, arXiv:1807.06205, arXiv:1807.06205. arXiv: 1807.06205 [astro-ph.CO].

Planck Collaboration et al. (July 2018b). "Planck 2018 results. VI. Cosmological parameters". In: *arXiv e-prints*, arXiv:1807.06209, arXiv:1807.06209. arXiv: 1807.06209 [astro-ph.CO].

— (July 2018c). "Planck 2018 results. VI. Cosmological parameters". In: *arXiv e-prints*, arXiv:1807.06209, arXiv:1807.06209. arXiv: 1807.06209 [astro-ph.CO].

Poulin, Vivian et al. (June 2018). "Implications of an extended dark energy cosmology with massive neutrinos for cosmological tensions". In: *Phys. Rev.*

D 97 (12), p. 123504. DOI: 10.1103/PhysRevD.97.123504. URL: https://link.aps.org/doi/10.1103/PhysRevD.97.123504.

Poulin, Vivian et al. (June 2019). "Early Dark Energy can Resolve the Hubble Tension". In: *Phys. Rev. Lett.* 122.22, 221301, p. 221301. DOI: 10.1103/PhysRevLett.122.221301. arXiv: 1811.04083 [astro-ph.CO].

Press, W. H. and P. Schechter (Feb. 1974). "Formation of Galaxies and Clusters of Galaxies by Self-Similar Gravitational Condensation". In: *Astrophys. J.* 187, pp. 425–438. DOI: 10.1086/152650.

Puchwein, Ewald, Marco Baldi, and Volker Springel (2013). "Modified-Gravity-gadget: a new code for cosmological hydrodynamical simulations of modified gravity models". In: *Monthly Notices of the Royal Astronomical Society* 436.1, pp. 348–360. DOI: 10.1093/mnras/stt1575. eprint: /oup/backfile/content_public/journal/mnras/436/1/10.1093_mnras_stt1575/2/stt1575.pdf. URL: http://dx.doi.org/10.1093/mnras/stt1575.

Quartin, Miguel et al. (2008). "Dark interactions and cosmological fine-tuning". In: *Journal of Cosmology and Astroparticle Physics* 2008.05, p. 007.

Raccanelli, A., W. J. Percival, and L. Samushia (Feb. 2012). "Interpreting large-scale redshift-space distortion measurements". In: *Monthly Notices of the Royal Astronomical Society* 420.3, pp. 2102–2119. ISSN: 0035-8711. DOI: 10.1111/j.1365-2966.2011.20169.x. eprint: http://oup.prod.sis.lan/mnras/article-pdf/420/3/2102/3011995/mnras0420-2102.pdf. URL: https://dx.doi.org/10.1111/j.1365-2966.2011.20169.x.

Ratra, Bharat and P. J. E. Peebles (June 1988). "Cosmological consequences of a rolling homogeneous scalar field". In: *Phys. Rev. D* 37 (12), pp. 3406–3427. DOI: 10.1103/PhysRevD.37.3406. URL: https://link.aps.org/doi/10.1103/PhysRevD.37.3406.

Reid, B. A. et al. (Nov. 2012). "The clustering of galaxies in the SDSS-III Baryon Oscillation Spectroscopic Survey: measurements of the growth of structure and expansion rate at z = 0.57 from anisotropic clustering". In: *Mon. Not. R. Astron. Soc.* 426, pp. 2719–2737. DOI: 10.1111/j.1365-2966.2012.21779.x. arXiv: 1203.6641.

Reid, Beth A and Martin White (2011). "Towards an accurate model of the redshift-space clustering of haloes in the quasi-linear regime". In: *Monthly Notices of the Royal Astronomical Society* 417.3, pp. 1913–1927.

Riebe, K. et al. (Aug. 2013). "The MultiDark Database: Release of the Bolshoi and MultiDark cosmological simulations". In: *Astronomische Nachrichten* 334, pp. 691–708. DOI: 10.1002/asna.201211900.

Riemer-Sørensen, Signe et al. (2013). "Simultaneous Constraints on the Number and Mass of Relativistic Species". In: *The Astrophysical Journal* 763.2, p. 89. URL: http://stacks.iop.org/0004-637X/763/i=2/a=89.

Riess, A. G. et al. (Sept. 1998). "Observational Evidence from Supernovae for an Accelerating Universe and a Cosmological Constant". In: *Astron. J.* 116, pp. 1009–1038. DOI: 10.1086/300499. eprint: astro-ph/9805201.

Riess, Adam G. et al. (1998). "Observational Evidence from Supernovae for an Accelerating Universe and a Cosmological Constant". In: *The Astronomical Journal* 116.3, p. 1009. URL: http://stacks.iop.org/1538-3881/116/i=3/a=1009.

Riess, Adam G. et al. (2016). "A 2.4% Determination of the Local Value of the Hubble Constant". In: *The Astrophysical Journal* 826.1, p. 56. URL: http://stacks.iop.org/0004-637X/826/i=1/a=56.

Robertson, H. P. (Nov. 1935). "Kinematics and World-Structure". In: *Astrophys. J.* 82, p. 284. DOI: 10.1086/143681.

Rodríguez-Puebla, Aldo et al. (Oct. 2016). "Halo and subhalo demographics with Planck cosmological parameters: Bolshoi-Planck and MultiDark-Planck simulations". In: *Mon. Not. R. Astron. Soc.* 462.1, pp. 893–916. DOI: 10.1093/mnras/stw1705. arXiv: 1602.04813 [astro-ph.CO].

Roncarelli, M., C. Carbone, and L. Moscardini (Feb. 2015). "The effect of massive neutrinos on the Sunyaev-Zel'dovich and X-ray observables of galaxy clusters". In: *Mon. Not. R. Astron. Soc.* 447, pp. 1761–1773. DOI: 10.1093/mnras/stu2546. arXiv: 1409.4285.

Ross, N. P., T. Shanks, and J. Cruz da Ângela (Dec. 2007). "The 2dF-SDSS LRG and QSO (2SLAQ) Survey: LRG Clustering and Redshift-Space Distortions". In: *Cosmic Frontiers*. Ed. by N. Metcalfe and T. Shanks. Vol. 379. Astronomical Society of the Pacific Conference Series, p. 68.

Ross, Nicholas P. et al. (Oct. 2007). "The 2dF-SDSS LRG and QSO Survey: the LRG 2-point correlation function and redshift-space distortions". In: *Mon. Not. R. Astron. Soc.* 381.2, pp. 573–588. DOI: 10.1111/j.1365-2966.2007.12289.x. arXiv: astro-ph/0612400 [astro-ph].

Saini, Tarun Deep et al. (Aug. 2000). "Reconstructing the Cosmic Equation of State from Supernova Distances". In: *Phys. Rev. Lett.* 85.6, pp. 1162–1165. DOI: 10.1103/PhysRevLett.85.1162. arXiv: astro-ph/9910231 [astro-ph].

Saito, Shun, Masahiro Takada, and Atsushi Taruya (May 2008). "Impact of Massive Neutrinos on the Nonlinear Matter Power Spectrum". In: *Phys. Rev. Lett.* 100 (19), p. 191301. DOI: 10.1103/PhysRevLett.100.191301. URL: https://link.aps.org/doi/10.1103/PhysRevLett.100.191301.

— (Oct. 2009). "Nonlinear power spectrum in the presence of massive neutrinos: Perturbation theory approach, galaxy bias, and parameter forecasts". In: *Phys. Rev. D* 80 (8), p. 083528. DOI: 10.1103/PhysRevD.80.083528. URL: https://link.aps.org/doi/10.1103/PhysRevD.80.083528.

Samushia, L., W. J. Percival, and A. Raccanelli (Mar. 2012). "Interpreting large-scale redshift-space distortion measurements". In: *Mon. Not. R. Astron. Soc.* 420.3, pp. 2102–2119. DOI: 10.1111/j.1365-2966.2011.20169.x. arXiv: 1102.1014 [astro-ph.CO].

Sánchez, Ariel G. et al. (Aug. 2013). "The clustering of galaxies in the SDSS-III Baryon Oscillation Spectroscopic Survey: cosmological constraints from the full shape of the clustering wedges". In: *Mon. Not. R. Astron. Soc.* 433.2, pp. 1202–1222. DOI: 10.1093/mnras/stt799. arXiv: 1303.4396 [astro-ph.CO].

Sánchez, Ariel G. et al. (May 2014). "The clustering of galaxies in the SDSS-III Baryon Oscillation Spectroscopic Survey: cosmological implications of the full shape of the clustering wedges in the data release 10 and 11 galaxy samples". In: *Mon. Not. R. Astron. Soc.* 440.3, pp. 2692–2713. DOI: 10.1093/mnras/stu342. arXiv: 1312.4854 [astro-ph.CO].

Sánchez, Ariel G. et al. (2017). "The clustering of galaxies in the completed SDSS-III Baryon Oscillation Spectroscopic Survey: Cosmological implications of the configuration-space clustering wedges". In: *Monthly Notices of the Royal Astronomical Society* 464.2, pp. 1640–1658. DOI: 10.1093/mnras/stw2443. eprint: /oup/backfile/content_public/journal/mnras/464/2/10.1093_mnras_stw2443/4/stw2443.pdf. URL: http://dx.doi.org/10.1093/mnras/stw2443.

Sánchez, Ariel G. et al. (Jan. 2017). "The clustering of galaxies in the completed SDSS-III Baryon Oscillation Spectroscopic Survey: Cosmological implications of the configuration-space clustering wedges". In: *Mon. Not. R. Astron. Soc.* 464.2, pp. 1640–1658. DOI: 10.1093/mnras/stw2443. arXiv: 1607.03147 [astro-ph.CO].

Santos, M. et al. (Apr. 2015). "Cosmology from a SKA HI intensity mapping survey". In: *Advancing Astrophysics with the Square Kilometre Array (AASKA14)*, p. 19. arXiv: 1501.03989 [astro-ph.CO].

Sargent, WLW and EL Turner (1977). "A statistical method for determining the cosmological density parameter from the redshifts of a complete sample of galaxies". In: *The Astrophysical Journal* 212, pp. L3–L7.

Sarkar, Prakash et al. (2009). "The scale of homogeneity of the galaxy distribution in SDSS DR6". In: *Monthly Notices of the Royal Astronomical Society: Letters* 399.1, pp. L128–L131.

Saslaw, William C. (2000). *The distribution of the galaxies: gravitational clustering in cosmology*. Cambridge University Press.

Satpathy, Siddharth et al. (2017). "The clustering of galaxies in the completed SDSS-III Baryon Oscillation Spectroscopic Survey: on the measurement of growth rate using galaxy correlation functions". In: *Monthly Notices of the Royal Astronomical Society* 469.2, pp. 1369–1382. DOI: 10.1093/mnras/stx883. eprint: /oup/backfile/content_public/journal/mnras/469/2/10.1093_mnras_stx883/1/stx883.pdf. URL: http://dx.doi.org/10.1093/mnras/stx883.

Schmidt, B. P. et al. (Nov. 1998). "The High-Z Supernova Search: Measuring Cosmic Deceleration and Global Curvature of the Universe Using Type IA Supernovae". In: *Astrophys. J.* 507, pp. 46–63. DOI: 10.1086/306308. eprint: astro-ph/9805200.

Schneider, Peter (2007). *Extragalactic astronomy and cosmology: an introduction*. Springer.

Schwarz, G. (July 1978). "Estimating the Dimension of a Model". In: *Annals of Statistics* 6, pp. 461–464.

Scoccimarro, R. (Dec. 2000). "The Bispectrum: From Theory to Observations". In: *Astrophys. J.* 544, pp. 597–615. DOI: 10.1086/317248. eprint: astro-ph/0004086.

Scoccimarro, Román (Oct. 2004). "Redshift-space distortions, pairwise velocities, and nonlinearities". In: *Phys. Rev. D* 70.8, 083007 (8), p. 083007. DOI: 10.1103/PhysRevD.70.083007. arXiv: astro-ph/0407214 [astro-ph]. URL: https://link.aps.org/doi/10.1103/PhysRevD.70.083007.

Scoccimarro, Roman, HMP Couchman, and Joshua A Frieman (1999). "The bispectrum as a signature of gravitational instability in redshift space". In: *ApJ* 517.2, p. 531.

Scrimgeour, Morag I et al. (2012). "The WiggleZ Dark Energy Survey: the transition to large-scale cosmic homogeneity". In: *Monthly Notices of the Royal Astronomical Society* 425.1, pp. 116–134.

Seldner, M et al. (1977). "New reduction of the Lick catalog of galaxies". In: *The Astronomical Journal* 82, pp. 249–256.

Seljak, U., A. Slosar, and P. McDonald (Oct. 2006). "Cosmological parameters from combining the Lyman-α forest with CMB, galaxy clustering and SN constraints". In: *J. Cosm. Astro-Particle Phys.* 10, 014, p. 014. DOI: 10.1088/1475-7516/2006/10/014. eprint: astro-ph/0604335.

Seo, H.-J. and D. J. Eisenstein (Dec. 2003). "Probing Dark Energy with Baryonic Acoustic Oscillations from Future Large Galaxy Redshift Surveys". In: *Astrophys. J.* 598, pp. 720–740. DOI: 10.1086/379122. eprint: astro-ph/0307460.

Seo, Hee-Jong and Daniel J. Eisenstein (Aug. 2007). "Improved Forecasts for the Baryon Acoustic Oscillations and Cosmological Distance Scale". In: *Astrophys. J.* 665.1, pp. 14–24. DOI: 10.1086/519549. arXiv: astro-ph/0701079 [astro-ph].

Seshadri, TR (1999). "Multi-fractal analysis of the galaxy distribution in the Las Campanas redshift survey". In: *Pramana* 53.6, pp. 989–993.

— (2005). "Fractal analysis of galaxy surveys". In: *Bulletin of the Astronomical Society of India* 33, p. 1.

Shane, CD, CA Wirtanen, and Uli Steinlin (1959). "The distribution of extra-galactic nebulae, III". In: *The Astronomical Journal* 64, p. 197.

Shapley, Harlow and Adelaide Ames (1932). "A survey of the external galxies brighter than the thirteenth magnitude". In: *Annals of Harvard College Observatory* 88, pp. 41–76.

Shi, Feng et al. (Dec. 2016). "Mapping the Real-space Distributions of Galaxies in SDSS DR7. I. Two-point Correlation Functions". In: *Astrophys. J.* 833.2, 241, p. 241. DOI: 10.3847/1538-4357/833/2/241. arXiv: 1608.02313 [astro-ph.CO].

Shi, K., Y. F. Huang, and T. Lu (Nov. 2012). "A comprehensive comparison of cosmological models from the latest observational data". In: *Mon. Not. R. Astron. Soc.* 426.3, pp. 2452–2462. DOI: 10.1111/j.1365-2966.2012.21784.x. arXiv: 1207.5875 [astro-ph.CO].

Shirasaki, Masato and Naoki Yoshida (May 2014). "Statistical and Systematic Errors in the Measurement of Weak-Lensing Minkowski Functionals: Application to the Canada-France-Hawaii Lensing Survey". In: *Astrophys. J.* 786.1, 43, p. 43. DOI: 10.1088/0004-637X/786/1/43. arXiv: 1312.5032 [astro-ph.CO].

Silk, Joseph (Jan. 2017). "Challenges in Cosmology from the Big Bang to Dark Energy, Dark Matter and Galaxy Formation". In: *14th International Symposium on Nuclei in the Cosmos (NIC2016)*, p. 010101. DOI: 10.7566/JPSCP.14.010101. arXiv: 1611.09846 [astro-ph.CO].

Simpson, Fergus and John A. Peacock (Feb. 2010). "Difficulties distinguishing dark energy from modified gravity via redshift distortions". In: *Phys. Rev.*

D 81 (4), p. 043512. DOI: 10.1103/PhysRevD.81.043512. URL: https://link.aps.org/doi/10.1103/PhysRevD.81.043512.

Smith, R. E. et al. (2003). "Stable clustering, the halo model and non-linear cosmological power spectra". In: *Monthly Notices of the Royal Astronomical Society* 341.4, pp. 1311–1332. DOI: 10.1046/j.1365-8711.2003.06503.x. eprint: /oup/backfile/content_public/journal/mnras/341/4/10.1046/j.1365-8711.2003.06503.x/2/341-4-1311. URL: http://dx.doi.org/10.1046/j.1365-8711.2003.06503.x.

Smoot, G. F. (May 1999). "COBE observations and results". In: *3K cosmology*. Ed. by L. Maiani, F. Melchiorri, and N. Vittorio. Vol. 476. American Institute of Physics Conference Series, pp. 1–10. DOI: 10.1063/1.59326. eprint: astro-ph/9902027.

Smoot, G. F. et al. (Sept. 1992). "Structure in the COBE differential microwave radiometer first-year maps". In: *Astrophys. J. Lett.* 396, pp. L1–L5. DOI: 10.1086/186504.

Song, Yong-Seon and Will J. Percival (Oct. 2009). "Reconstructing the history of structure formation using redshift distortions". In: *J. Cosm. Astro-Particle Phys.* 2009.10, 004, p. 004. DOI: 10.1088/1475-7516/2009/10/004. arXiv: 0807.0810 [astro-ph].

Sotiriou, Thomas P. (Sept. 2006). "f(R) gravity and scalar tensor theory". In: *Classical and Quantum Gravity* 23.17, pp. 5117–5128. DOI: 10.1088/0264-9381/23/17/003. arXiv: gr-qc/0604028 [gr-qc].

Sotiriou, Thomas P. and Valerio Faraoni (Jan. 2010). "f(R) theories of gravity". In: *Reviews of Modern Physics* 82.1, pp. 451–497. DOI: 10.1103/RevModPhys.82.451. arXiv: 0805.1726 [gr-qc].

Spergel, D. et al. (May 2013). "Wide-Field InfraRed Survey Telescope-Astrophysics Focused Telescope Assets WFIRST-AFTA Final Report". In: *ArXiv e-prints: 1305.5422*. arXiv: 1305.5422 [astro-ph.IM].

Springel, V. et al. (June 2005). "Simulations of the formation, evolution and clustering of galaxies and quasars". In: *Nature* 435, pp. 629–636. DOI: 10.1038/nature03597. eprint: astro-ph/0504097.

Springel, Volker (2005). "The cosmological simulation code gadget-2". In: *Monthly Notices of the Royal Astronomical Society* 364.4, pp. 1105–1134. DOI: 10.1111/j.1365-2966.2005.09655.x. eprint: /oup/backfile/content_public/journal/mnras/364/4/10.1111_j.1365-2966.2005.09655.x/1/364-4-1105.pdf. URL: http://dx.doi.org/10.1111/j.1365-2966.2005.09655.x.

Springel, Volker et al. (2005). "Simulations of the formation, evolution and clustering of galaxies and quasars". In: *Nature* 435.7042, pp. 629–636.

Stabenau, Hans F. and Bhuvnesh Jain (Oct. 2006). "N-body simulations of alternative gravity models". In: *Phys. Rev. D* 74.8, 084007, p. 084007. DOI: 10.1103/PhysRevD.74.084007. arXiv: astro-ph/0604038 [astro-ph].

Steinhardt, Paul J., Limin Wang, and Ivaylo Zlatev (June 1999). "Cosmological tracking solutions". In: *Phys. Rev. D* 59.12, 123504, p. 123504. DOI: 10.1103/PhysRevD.59.123504. arXiv: astro-ph/9812313 [astro-ph].

Susskind, Leonard (Nov. 1995). "The world as a hologram". In: *Journal of Mathematical Physics* 36.11, pp. 6377–6396. DOI: 10.1063/1.531249. arXiv: hep-th/9409089 [hep-th].

Suzuki, N. et al. (Feb. 2012). "The Hubble Space Telescope Cluster Supernova Survey. V. Improving the Dark-energy Constraints above z > 1 and Building an Early-type-hosted Supernova Sample". In: *Astrophys. J.* 746.1, 85, p. 85. DOI: 10.1088/0004-637X/746/1/85. arXiv: 1105.3470 [astro-ph.CO].

't Hooft, G. (Oct. 1993). "Dimensional Reduction in Quantum Gravity". In: *arXiv e-prints*, gr-qc/9310026, gr–qc/9310026. arXiv: gr-qc/9310026 [gr-qc].

't Hooft, Gerard (Apr. 2001). "The Holographic Principle". In: *Basics and Highlights in Fundamental Physics*, pp. 72–100. DOI: 10.1142/9789812811585_0005. arXiv: hep-th/0003004 [hep-th].

Takahashi, Ryuichi et al. (Dec. 2012). "Revising the Halofit Model for the Nonlinear Matter Power Spectrum". In: *Astrophys. J.* 761.2, 152, p. 152. DOI: 10.1088/0004-637X/761/2/152. arXiv: 1208.2701 [astro-ph.CO].

Tansella, Vittorio et al. (Nov. 2018). "Redshift-space distortions from vector perturbations. II. Anisotropic signal". In: *Phys. Rev. D* 98.10, 103515, p. 103515. DOI: 10.1103/PhysRevD.98.103515. arXiv: 1807.00731 [astro-ph.CO].

Taruya, Atsushi, Takahiro Nishimichi, and Shun Saito (Sept. 2010). "Baryon acoustic oscillations in 2D: Modeling redshift-space power spectrum from perturbation theory". In: *Phys. Rev. D* 82.6, 063522, p. 063522. DOI: 10.1103/PhysRevD.82.063522. arXiv: 1006.0699 [astro-ph.CO].

Tinker, J. L. et al. (Dec. 2010). "The Large-scale Bias of Dark Matter Halos: Numerical Calibration and Model Tests". In: *Astrophys. J.* 724, pp. 878–886. DOI: 10.1088/0004-637X/724/2/878. arXiv: 1001.3162.

Tinker, Jeremy et al. (Dec. 2008). "Toward a Halo Mass Function for Precision Cosmology: The Limits of Universality". In: *Astrophys. J.* 688.2, pp. 709–728. DOI: 10.1086/591439. arXiv: 0803.2706 [astro-ph].

Tojeiro, Rita et al. (Aug. 2012). "The clustering of galaxies in the SDSS-III Baryon Oscillation Spectroscopic Survey: measuring structure growth using passive galaxies". In: *Mon. Not. R. Astron. Soc.* 424.3, pp. 2339–2344. DOI: 10.1111/j.1365-2966.2012.21404.x. arXiv: 1203.6565 [astro-ph.CO].

Tonry, John L. et al. (Sept. 2003). "Cosmological Results from High-zSupernovae". In: *The Astrophysical Journal* 594.1, pp. 1–24. DOI: 10.1086/376865. URL: https://doi.org/10.1086/376865.

Topping, Michael W. et al. (Jan. 2018). "Understanding Large-scale Structure in the SSA22 Protocluster Region Using Cosmological Simulations". In: *Astrophys. J.* 852.2, 134, p. 134. DOI: 10.3847/1538-4357/aa9f0f. arXiv: 1709.06572 [astro-ph.GA].

Tormen, G. (June 1998). "The assembly of matter in galaxy clusters". In: *Mon. Not. R. Astron. Soc.* 297, pp. 648–656. eprint: arXiv:astro-ph/9802290.

Tormen, G., L. Moscardini, and N. Yoshida (June 2004). "Properties of cluster satellites in hydrodynamical simulations". In: *Mon. Not. R. Astron. Soc.* 350, pp. 1397–1408. DOI: 10.1111/j.1365-2966.2004.07736.x. eprint: arXiv:astro-ph/0304375.

Tsujikawa, Shinji (July 2007). "Matter density perturbations and effective gravitational constant in modified gravity models of dark energy". In: *Phys. Rev. D* 76.2, 023514, p. 023514. DOI: 10.1103/PhysRevD.76.023514. arXiv: 0705.1032 [astro-ph].

Turner, Monica L. et al. (Oct. 2017). "A comparison of observed and simulated absorption from H I, C IV, and Si IV around z ≈ 2 star-forming galaxies suggests redshift-space distortions are due to inflows". In: *Mon. Not. R. Astron. Soc.* 471.1, pp. 690–705. DOI: 10.1093/mnras/stx1616. arXiv: 1703.00086 [astro-ph.GA].

Turok, Neil (June 2002). "A critical review of inflation". In: *Classical and Quantum Gravity* 19.13, pp. 3449–3467. DOI: 10.1088/0264-9381/19/13/305.

Tutusaus, Isaac et al. (2016). "Dark sectors of the Universe: A Euclid survey approach". In: *Physical Review D* 94.12, p. 123515.

Upadhye, Amol (May 2019). "Neutrino mass and dark energy constraints from redshift-space distortions". In: *J. Cosm. Astro-Particle Phys.* 2019.5, 041, p. 041. DOI: 10.1088/1475-7516/2019/05/041. arXiv: 1707.09354 [astro-ph.CO].

Ursino, E. et al. (July 2011). "Expected properties of the two-point autocorrelation function of the intergalactic medium". In: *Mon. Not. R. Astron. Soc.* 414.4, pp. 2970–2984. DOI: 10.1111/j.1365-2966.2011.18597.x. arXiv: 1009.5519 [astro-ph.CO].

Uzan, Jean-Philippe (May 2006). "The acceleration of the universe and the physics behind it". In: *arXiv e-prints*, astro-ph/0605313, astro–ph/0605313. arXiv: astro-ph/0605313 [astro-ph].

Uzan, Jean-Philippe (2011). "Testing general relativity: from local to cosmological scales". In: *Philosophical Transactions of the Royal Society of London A: Mathematical, Physical and Engineering Sciences* 369.1957, pp. 5042–5057. ISSN: 1364-503X. DOI: 10.1098/rsta.2011.0293. eprint: http://rsta.royalsocietypublishing.org/content/369/1957/5042.full.pdf. URL: http://rsta.royalsocietypublishing.org/content/369/1957/5042.

van den Bosch, F. C. and F. Jiang (May 2016). "Statistics of dark matter substructure - II. Comparison of model with simulation results". In: *Mon. Not. R. Astron. Soc.* 458, pp. 2870–2884. DOI: 10.1093/mnras/stw440.

Vargas-Magaña, Mariana et al. (2018). "The clustering of galaxies in the completed SDSS-III Baryon Oscillation Spectroscopic Survey: theoretical systematics and Baryon Acoustic Oscillations in the galaxy correlation function". In: *Monthly Notices of the Royal Astronomical Society* 477.1, pp. 1153–1188. DOI: 10.1093/mnras/sty571. eprint: /oup/backfile/content_public/journal/mnras/477/1/10.1093_mnras_sty571/1/sty571.pdf. URL: http://dx.doi.org/10.1093/mnras/sty571.

Vega-Ferrero, Jesús, Gustavo Yepes, and Stefan Gottlöber (May 2017). "On the shape of dark matter haloes from MultiDark Planck simulations". In: *Mon. Not. R. Astron. Soc.* 467.3, pp. 3226–3238. DOI: 10.1093/mnras/stx282. arXiv: 1603.02256 [astro-ph.CO].

Verde, L. et al. (Sept. 2002). "The 2dF Galaxy Redshift Survey: the bias of galaxies and the density of the Universe". In: *Mon. Not. R. Astron. Soc.*

335, pp. 432–440. DOI: 10.1046/j.1365-8711.2002.05620.x. eprint: astro-ph/0112161.

Viel, Matteo, Martin G. Haehnelt, and Volker Springel (2010). "The effect of neutrinos on the matter distribution as probed by the intergalactic medium". In: *Journal of Cosmology and Astroparticle Physics* 2010.06, p. 015. URL: http://stacks.iop.org/1475-7516/2010/i=06/a=015.

Villaescusa-Navarro, F. et al. (Mar. 2014). "Cosmology with massive neutrinos I: towards a realistic modeling of the relation between matter, haloes and galaxies". In: *J. Cosm. Astro-Particle Phys.* 3, 011, p. 011. DOI: 10.1088/1475-7516/2014/03/011. arXiv: 1311.0866.

Villaescusa-Navarro, Francisco et al. (2013). "Non-linear evolution of the cosmic neutrino background". In: *Journal of Cosmology and Astroparticle Physics* 2013.03, p. 019. URL: http://stacks.iop.org/1475-7516/2013/i=03/a=019.

Villaescusa-Navarro, Francisco et al. (July 2018). "The Imprint of Neutrinos on Clustering in Redshift Space". In: *The Astrophysical Journal* 861.1, p. 53. DOI: 10.3847/1538-4357/aac6bf.

Wagner, Christian, Licia Verde, and Raul Jimenez (2012). "Effects of the Neutrino Mass Splitting on the Nonlinear Matter Power Spectrum". In: *The Astrophysical Journal Letters* 752.2, p. L31. URL: http://stacks.iop.org/2041-8205/752/i=2/a=L31.

Walker, T. P. et al. (July 1991). "Primordial nucleosynthesis redux". In: *Astrophys. J.* 376, pp. 51–69. DOI: 10.1086/170255.

Wang, L. and P. J. Steinhardt (Dec. 1998). "Cluster Abundance Constraints for Cosmological Models with a Time-varying, Spatially Inhomogeneous Energy Component with Negative Pressure". In: *Astrophys. J.* 508, pp. 483–490. DOI: 10.1086/306436. eprint: astro-ph/9804015.

Wang, Shuang et al. (Apr. 2016). "A Comprehensive Investigation on the Slowing Down of Cosmic Acceleration". In: *Astrophys. J.* 821.1, 60, p. 60. DOI: 10.3847/0004-637X/821/1/60. arXiv: 1509.03461 [astro-ph.CO].

Wang, Yang et al. (Dec. 2018). "The Three Hundred Project: The Influence of Environment on Simulated Galaxy Properties". In: *Astrophys. J.* 868.2, 130, p. 130. DOI: 10.3847/1538-4357/aae52e. arXiv: 1809.05244 [astro-ph.GA].

Wang, Yun (May 2008). "Differentiating dark energy and modified gravity with galaxy redshift surveys". In: *J. Cosm. Astro-Particle Phys.* 2008.5, 021, p. 021. DOI: 10.1088/1475-7516/2008/05/021. arXiv: 0710.3885 [astro-ph].

Weinberg, Steven (Jan. 1989). "The cosmological constant problem". In: *Rev. Mod. Phys.* 61 (1), pp. 1–23. DOI: 10.1103/RevModPhys.61.1. URL: https://link.aps.org/doi/10.1103/RevModPhys.61.1.

— (2001). "The cosmological constant problems". In: *Sources and Detection of Dark Matter and Dark Energy in the Universe*. Springer, pp. 18–26.

— (2008). *Cosmology*. OUP Oxford. ISBN: 9780198526827. URL: http://www.oup.com/uk/catalogue/?ci=9780198526827.

Wetterich, C. (June 1988). "Cosmology and the fate of dilatation symmetry". In: *Nuclear Physics B* 302, pp. 668–696. DOI: 10.1016/0550-3213(88)90193-9. arXiv: 1711.03844 [hep-th].

White, M. (Dec. 2005). "Baryon oscillations". In: *Astroparticle Physics* 24, pp. 334–344. DOI: 10.1016/j.astropartphys.2005.07.007. eprint: astro-ph/0507307.

Will, Clifford M. (June 2014). "The Confrontation between General Relativity and Experiment". In: *Living Reviews in Relativity* 17.1, p. 4. ISSN: 1433-8351. DOI: 10.12942/lrr-2014-4. URL: https://doi.org/10.12942/lrr-2014-4.

Wolz, Laura et al. (Sept. 2012). "On the validity of cosmological Fisher matrix forecasts". In: *J. Cosm. Astro-Particle Phys.* 2012.9, 009, p. 009. DOI: 10.1088/1475-7516/2012/09/009. arXiv: 1205.3984 [astro-ph.CO].

Wong, Y. Y. (July 2002). "Analytical treatment of neutrino asymmetry equilibration from flavor oscillations in the early universe". In: *Phys. Rev. D* 66.2, 025015, p. 025015. DOI: 10.1103/PhysRevD.66.025015. eprint: hep-ph/0203180.

Wong, Yvonne Y. Y. (Oct. 2008). "Higher order corrections to the large scale matter power spectrum in the presence of massive neutrinos". In: *J. Cosm. Astro-Particle Phys.* 2008.10, 035, p. 035. DOI: 10.1088/1475-7516/2008/10/035. arXiv: 0809.0693 [astro-ph].

— (Nov. 2011). "Neutrino Mass in Cosmology: Status and Prospects". In: *Annual Review of Nuclear and Particle Science* 61.1, pp. 69–98. DOI: 10.1146/annurev-nucl-102010-130252. arXiv: 1111.1436 [astro-ph.CO].

Wright, Bill S., Hans A. Winther, and Kazuya Koyama (2017). "COLA with massive neutrinos". In: *Journal of Cosmology and Astroparticle Physics* 2017.10, p. 054. URL: http://stacks.iop.org/1475-7516/2017/i=10/a=054.

Wright, Bill S. et al. (June 2019). "Investigating the degeneracy between modified gravity and massive neutrinos with redshift-space distortions". In: *J. Cosm. Astro-Particle Phys.* 2019.6, 040, p. 040. DOI: 10.1088/1475-7516/2019/06/040. arXiv: 1902.10692 [astro-ph.CO].

Wu, Kelvin KS, Ofer Lahav, and Martin J Rees (1999). "The large-scale smoothness of the Universe". In: *Nature* 397.6716, pp. 225–230.

Xia, Xiao-Yang, Zu-Gan Deng, and Zhen-Long Zou (1992). "Fractal dimensions in the large-scale distribution of IRAS galaxies." In: *Science in China A: Mathematics* 35, pp. 326–335.

Xu, Xiaoying et al. (2012). "A 2 per cent distance to z = 0.35 by reconstructing baryon acoustic oscillations – II. Fitting techniques". In: *Monthly Notices of the Royal Astronomical Society* 427.3, pp. 2146–2167. DOI: 10.1111/j.1365-2966.2012.21573.x. eprint: /oup/backfile/content_public/journal/mnras/427/3/10.1111/j.1365-2966.2012.21573.x/2/427-3-2146.pdf. URL: http://dx.doi.org/10.1111/j.1365-2966.2012.21573.x.

Xu, Xiaoying et al. (2013). "Measuring DA and H at z=0.35 from the SDSS DR7 LRGs using baryon acoustic oscillations". In: *Monthly Notices of the Royal Astronomical Society* 431.3, pp. 2834–2860. DOI: 10.1093/mnras/stt379. eprint: /oup/backfile/content_public/journal/mnras/431/3/10.1093/mnras/stt379/2/stt379.pdf. URL: http://dx.doi.org/10.1093/mnras/stt379.

Xu, Yue-Yao and Xin Zhang (Nov. 2016). "Comparison of dark energy models after Planck 2015". In: *European Physical Journal C* 76.11, 588, p. 588. DOI: 10.1140/epjc/s10052-016-4446-5. arXiv: 1607.06262 [astro-ph.CO].

Yadav, Jaswant et al. (2005). "Testing homogeneity on large scales in the Sloan Digital Sky Survey data release one". In: *Monthly Notices of the Royal Astronomical Society* 364.2, pp. 601–606.

Yadav, Jaswant K, JS Bagla, and Nishikanta Khandai (2010). "Fractal dimension as a measure of the scale of homogeneity". In: *Monthly Notices of the Royal Astronomical Society* 405.3, pp. 2009–2015.

Yèche, Christophe et al. (2017). "Constraints on neutrino masses from Lyman-alpha forest power spectrum with BOSS and XQ-100". In: *Journal of Cosmology and Astroparticle Physics* 2017.06, p. 047. URL: http://stacks.iop.org/1475-7516/2017/i=06/a=047.

Yepes, Gustavo (Jan. 2001). "The Universe in a Computer: The Importance of Numerical Simulations in Cosmology". In: *Historical Development of Modern Cosmology*. Ed. by Vicent J. Martínez, Virginia Trimble, and María Jesús Pons-Bordería. Vol. 252. Astronomical Society of the Pacific Conference Series, p. 355.

Zandanel, Fabio et al. (Oct. 2018). "MultiDark clusters: galaxy cluster mock light-cones, eROSITA, and the cluster power spectrum". In: *Mon. Not. R. Astron. Soc.* 480.1, pp. 987–1005. DOI: 10.1093/mnras/sty1901. arXiv: 1804.07063 [astro-ph.CO].

Zennaro, M et al. (2018). "Cosmological constraints from galaxy clustering in the presence of massive neutrinos". In: *Monthly Notices of the Royal Astronomical Society* 477.1, pp. 491–506. DOI: 10.1093/mnras/sty670. eprint: /oup/backfile/content_public/journal/mnras/477/1/10.1093_mnras_sty670/1/sty670.pdf. URL: http://dx.doi.org/10.1093/mnras/sty670.

Zhai, Zhongxu and Yun Wang (Nov. 2018). "Robust and model-independent cosmological constraints from distance measurements". In: *arXiv e-prints*, arXiv:1811.07425, arXiv:1811.07425. arXiv: 1811.07425 [astro-ph.CO].

Zhang, H. et al. (July 2008). "Probing the nature of cosmic acceleration". In: *Physics Letters B* 665, pp. 319–324. DOI: 10.1016/j.physletb.2008.06.041. arXiv: 0806.4082.

Zhang, Hongsheng, Xin-Zhou Li, and Hyerim Noh (Nov. 2010). "Semi-holographic universe". In: *Physics Letters B* 694.3, pp. 177–180. DOI: 10.1016/j.physletb.2010.09.039. arXiv: 1010.1362 [gr-qc].

Zhang, Ming-Jian and Jun-Qing Xia (Apr. 2018). "Physical condition for the slowing down of cosmic acceleration". In: *Nuclear Physics B* 929, pp. 438–451. DOI: 10.1016/j.nuclphysb.2018.02.020. arXiv: 1701.04973 [astro-ph.CO].

Zheng, Wen et al. (1988). "Fractal structure in the large scale distribution of galaxies". In: *Chinese astronomy and astrophysics* 12.4, pp. 269–275.

Zwicky, F. (Oct. 1937). "On the Masses of Nebulae and of Clusters of Nebulae". In: *ApJ* 86, p. 217.

Zwicky, Fritz and E Herzog (1966). "Catalogue of Galaxies and of Clusters of Galaxies". In: *Caltech*.